

**Development and Characterisation of
Metal Oxide Gas Sensors**

Enobong Effiong Basse

PhD

2014

**Development and Characterisation of
Metal Oxide Gas Sensors**

Enobong Effiong Bassey

A thesis submitted to
Auckland University of Technology
in fulfilment of the requirements for the degree of
Doctor of Philosophy (PhD)

2014

Faculty of Design and Creative Technologies

Abstract

There is an increasing interest among researchers of environmental sensors to improve the functionality and portability of chemical sensor devices, while applying simple materials and innovative techniques. Nanotechnology, which is at the cross-road of science, technology and arts, has provided the platform for this multidisciplinary technological development. The research described in this thesis involves the design, fabrication and characterisation of chemical sensors for the analysis of trace volatile hydrocarbons. The objective of this study is the systematic investigation of the sensing-dependence of the composition of veritable materials used in the preparation of nanocomposites, characterisation of their nanostructures, and development of their sensing mechanism based on their surface-gas interaction behaviour.

This research involved the preparation of five chemical sensors using 100:0, 75:25, 50:50, 25:75 and 0:100 molar ratios of tin dioxide and zinc oxide. These sensors were labelled as SnO₂, S₃Z₁, SZ, S₁Z₃ and ZnO sensors, respectively. The samples were prepared using the radio frequency (RF) magnetron sputtering under the same conditions. A similar set of samples were annealed. Both as-fabricated and annealed samples were characterised using field emission - scanning electron microscope (FE-SEM), energy dispersive X-ray spectroscopy (EDS) and atomic force microscope (AFM). Nanostructural analysis revealed the nanocrystalline images to have minor hillocks on a relatively dense film surface. The unannealed samples exhibited more rounded protrusions than the annealed samples. The grain heights of the as-fabricated samples were higher than the annealed samples, while there was reduction in surface roughness as a result of annealing. The grain size was observed to increase from pure SnO₂ and ZnO samples toward the SZ samples. Also, the SZ samples were observed to reflect the lowest surface roughness parameters, while the S₁Z₃ samples showed the highest surface roughness values.

The sensor signals, usually quantised in raw form, were smoothed using the Savitzky-Golay filter, before characterisation of the sensitivity of the sensors. Experimental investigation proved that gas sensitivity increased with increasing gas concentration

and increasing temperature for all sensors. The best sensitivities were displayed by S_1Z_3 , followed by S_3Z_1 sensor devices, while ZnO was more sensitive than SnO₂. This behaviour was attributed to the high photocatalytic activity of pure ZnO and coupled SnO₂-ZnO nanocomposites than pure SnO₂.

This fact was collaborated with the results of the thermodynamic analysis of each sensor. For both methanol and ethanol, the activation energy of SnO₂ was higher than that of ZnO, while the activation energy of S_1Z_3 sensor devices was the lowest. It was observed that ethanol was more sensitive than methanol, indicating a possibility for good selectivity of the sensors. Statistical analysis confirmed that sensor type, gas concentration and temperature influenced respective sensor sensitivity; but the effects were varied depending on the sensing conditions and sensor types.

With the development and simulation of modified chemisorption and linear models, excellent sensitivity behaviours were observed at extended concentration range. These results collaborated the facts that S_1Z_3 and S_3Z_1 sensors were the best sensors. At higher concentrations however, the SZ sensors were observed to improve in sensitivity. With these behaviours, different sensing mechanisms were proposed for each chemical sensor. It is proposed that this result is a very significant contribution to the state-of-knowledge in the domain of scientific endeavour.

Dedication

This PhD Thesis is dedicated to the loving memory of my beloved mother,

Mrs Antonia Anselm Bassey (Late)

Mum, you have been a source of inspiration and love to me.
I will always appreciate your invaluable sacrifices and legacies.

Acknowledgements

I would like to express my sincere gratitude to my primary supervisor, Professor Philip Sallis, for his commitment, immense interest, infectious knowledge, patience and moral support. Also, my thanks go to my second supervisor, Professor Krishnamachar Prasad, for his research attitude and guidance. Without them, this thesis would not have been successful.

With gratitude, I would also like to acknowledge the several financial supports from the Faculty of Design and Creative Technologies (DCT), Engineering Research and Innovation Cluster (ERIC), Geoinformatics Research Centre (GRC), School of Computer and Mathematical Sciences, School of Engineering, the Auckland University of Technology (AUT). These sources of funding have enabled me to undertake this research and attend international conferences.

I acknowledge Professor Nakavanta Bhat and the Centre for Nano Science and Engineering (CeNSE), Indian Institute of Science (IISc), Bangalore, for the facilitation of the fabrication and characterisation of the sensor devices. I would like to thank Professor Thomas Neitzert for facilitating the ERIC support. Also, I am very grateful to Dr Jacqueline Whalley, and other members of the GRC, for insightful discussions and friendship. Gratefully, I appreciate all their contributions.

I would like to extend my deepest gratitude to my entire family for their love, interest and encouragement. To my dad, Mr Anselm Bassey (JP), your unflinching confidence in me has been my source of inspiration. To my uncle, Mr Joseph Bassey, your seemingly-unlimited reserves of love, positivity and humane sacrifice have challenged me beyond comprehension. My sincere appreciation to all of you.

I thank my wife, Uyaietop, for her assistance in taking care of my kids. To my lovely kids, Enobong Jr, Uyaiabasi and Uwakmfon, I dedicate this thesis. Your learning profiles are a reflection of the different sensory environments you have assimilated in your growth paths. I am persuaded that this doctoral thesis will be a source of

inspiration to you. I really appreciate the individual sacrifices you have made during my period of doctoral study.

Most importantly, I am very grateful to the Almighty God for His love, inspiration, guidance and provisions. Without You, I would have given up a long time ago. Lord, I will always be grateful.

Finally, without the support and fellowship of many other good friends and family (too many to mention), this doctoral study would not have been completed sanity-intact; therefore, I thank you all.

Table of Contents

| | |
|---|-------------|
| Abstract | ii |
| Dedication | iv |
| Acknowledgements | v |
| Attestation of Authorship | xii |
| List of Conference Publications | xiii |
| List of Figures | xv |
| List of Tables | xxi |
| Acronyms and Abbreviations | xxii |
| Chapter One: Introduction | 1 |
| 1.1 Introduction | 1 |
| 1.2 Motivation | 1 |
| 1.3 Objective of Research | 2 |
| 1.4 Thesis Organisation..... | 3 |
| 1.5 Keywords | 4 |
| Chapter Two: Fundamentals of Chemical Sensor | 5 |
| 2.1 Operating Principles and Sensory Analysis | 5 |
| 2.2 Classification of Sensors | 5 |

| | |
|--|----|
| 2.3 Chemical Sensors | 7 |
| 2.4 Types of Chemical Sensors | 9 |
| 2.5 Solid State Gas Sensors..... | 9 |
| 2.5.1 Catalytic sensors | 10 |
| 2.6 Metal Oxide Nanostructured Sensors (MOX)..... | 11 |
| 2.6.1 Categories of Metal Oxide Nanostructures | 14 |
| 2.7 Dimensionalities of Nanostructures | 15 |
| 2.7.1 Zero-Dimensional (0D) Nanostructures | 17 |
| 2.7.2 One-Dimensional (1D) Nanostructures | 18 |
| 2.7.3 Two-Dimensional (2D) Nanostructures | 20 |
| 2.7.4 Three-Dimensional (3D) Nanostructures | 21 |
| 2.8 Properties of SnO ₂ and ZnO Devices..... | 22 |
| 2.8.1 Material Properties and Crystalline Structure | 22 |
| 2.8.2 Mechanical Properties | 24 |
| 2.8.3 Electronic Properties and Band Structures | 24 |
| 2.8.4 Work Function, Surface Coverage and Ionisation Potential | 30 |
| 2.8.5 Bulk Properties | 31 |
| 2.8.6 Surface Properties..... | 33 |
| 2.8.7 Transport Properties | 35 |
| 2.9 Sensor Performance Characteristics..... | 39 |
| 2.9.1 Calibration Curve | 39 |
| 2.9.2 Base Line | 39 |
| 2.9.3 Response and Sensitivity | 40 |
| 2.9.4 Selectivity/Specificity..... | 42 |
| 2.9.5 Detection Time | 42 |
| 2.9.6 Response Time | 43 |
| 2.9.7 Recovery or Decay Time..... | 43 |
| 2.9.8 Reversibility | 43 |
| 2.9.9 Stability and Long-Term Effect..... | 44 |
| 2.9.10 Reproducibility | 44 |
| 2.9.11 Drift | 45 |
| 2.9.12 Detection Limit..... | 46 |
| 2.10 Parameters for Characterisation of Sensor Behaviour | 46 |
| 2.10.1 Reception Function..... | 46 |
| 2.10.2 Transducer Function | 47 |
| 2.10.3 Geometrical Aspect | 47 |
| 2.10.4 Film thickness..... | 48 |
| 2.10.5 Grain Size | 48 |
| 2.11 Conclusion | 50 |

Chapter Three: Sensing Mechanism, Surface Chemistry and Transport Phenomena.....51

3.1 Sensing Mechanism 51

3.2 Surface Chemistry: Adsorption Mechanism 52

 3.2.1 Physisorption 53

 3.2.2 Hydrogen Bonding 55

 3.2.3 Chemisorption 56

 3.2.4 Ionosorption..... 59

 3.2.5 Adsorption of Oxygen 60

 3.2.6 Adsorption of Water Vapour 64

3.3 Types of Adsorption-Desorption Models..... 68

 3.3.1 Langmuir Model 68

 3.3.2 Brunauer, Emmet and Teller (BET) Model..... 72

 3.3.3 Freundlich Model 73

 3.3.4 Wolkenstein Model 74

 3.3.5 Kolmogorov Model 77

3.4 Electronic Conduction and Surface States 79

3.5 Transport Phenomena..... 80

 3.5.1 Charge Transfer Model and Space Charge Region 84

3.6 Surface Reaction Processes by Metal Oxide Semiconductors 87

 3.6.1 Surface Reactions with Reducing Gases 88

3.7 Surface Reaction Process and Conduction Model of Coupled SnO₂ and ZnO Nanocomposite..... 93

3.8 Conclusion 98

Chapter Four: Materials Design, Fabrication and Characterisation of Metal Oxide Gas Sensors.....99

4.1 Introduction 99

4.2 Experimental Procedures 99

4.3 Preparation/Cleaning of the Wafer/Substrate..... 101

 4.3.1 Piranha Cleaning 101

 4.3.2 Thermal Oxidation..... 102

4.4 Preparation of Metal Oxide Target 102

 4.4.1 Preparation of Molar Concentrations 102

 4.4.2 Sintering 104

4.5 Thin Film Deposition: Radio Frequency (RF) Magnetron Sputtering..... 105

| | |
|---|------------|
| 4.6 Post-Deposition Treatment: Annealing..... | 108 |
| 4.7 Interdigital Patterning..... | 109 |
| 4.7.1 Optimisation of Interdigital Patterning Process | 109 |
| 4.7.2 Shadow Mask Patterning | 110 |
| 4.8 Thin Film Characterisation | 111 |
| 4.8.1 Film Thickness | 111 |
| 4.8.2 Field Emission - Scanning Electron Microscope (FE-SEM) | 111 |
| 4.8.3 Energy Dispersive Spectroscopy (EDS)..... | 113 |
| 4.8.4 Atomic Force Microscope (AFM)..... | 113 |
| 4.9 Gas Sensing..... | 114 |
| 4.9.1 Gas Sensing System | 114 |
| 4.9.2 Gas Sensing Measurement Procedure | 117 |
| 4.10 Conclusion | 119 |
| Chapter Five: Metal Oxide Thin Film Characterisation..... | 120 |
| 5.1 Introduction..... | 120 |
| 5.2 Film Thickness..... | 120 |
| 5.3 FE-SEM and Energy Dispersive Spectroscopy (EDS) | 123 |
| 5.4 Atomic Force Microscope (AFM) | 131 |
| 5.5 Proposed Binary Phase Structure and Solubility of Coupled SnO ₂ -ZnO Nanocomposites | 137 |
| 5.6 Conclusion | 138 |
| Chapter Six: Gas Sensor Signal Processing and Gas Sensitivity Behaviour | 139 |
| 6.1 Sensor Response Data Normalisation | 139 |
| 6.2 Characterisation of Gas Response..... | 139 |
| 6.2.1 Effects of Sensor Composition and Gas Concentration on Sensitivity | 142 |
| 6.2.2 Sensitivity Profile in Time Domain..... | 156 |
| 6.2.3 Sensitivity Difference Behaviour | 162 |
| 6.2.4 Transient Response Curve Analysis..... | 163 |
| 6.3 Proposed Sensing Mechanism..... | 169 |
| 6.4 Summary and Conclusion | 170 |

| | |
|---|------------|
| Chapter Seven: Analysis of Gas Sensitivity and Simulation of Sensor Behaviour | 173 |
| 7.1 Introduction | 173 |
| 7.2 Sensitivity Analysis..... | 174 |
| 7.2.1 Factorial Analysis of Sensitivity to Methanol Based on Sensor Type, Gas Concentration and Operating Temperature..... | 175 |
| 7.2.2 Factorial Analysis of Sensitivity to Methanol and Ethanol Based on Sensor Type, Gas Type and Operating Temperature..... | 180 |
| 7.3 Modified Chemisorption Model..... | 185 |
| 7.3.1 Parameter Identification | 192 |
| 7.3.2 Simulation of Sensor Behaviour Using the Modified Chemisorption (Power) Simulation | 192 |
| 7.4 Linear Regression Model | 195 |
| 7.4.1 Linear Modelling of Sensitivity to Methanol | 195 |
| 7.4.2 Simulation of Sensor Behaviour Using the Linear Simulation | 196 |
| 7.5 Thermodynamics of Sensor - Gas Interaction..... | 197 |
| 7.6 Adsorption-Desorption Kinetics | 199 |
| 7.6.1 Feature Extraction | 200 |
| 7.7 Sensing Mechanism | 203 |
| 7.8 Practical Application of Sensor Devices..... | 205 |
| 7.9 Summary and Conclusion | 206 |
| | |
| Chapter Eight: Summary, Conclusion and Outlook | 208 |
| 8.1 Summary and Conclusion | 208 |
| 8.2 Outlook for Future Work | 210 |
| | |
| References | 212 |
| | |
| Appendix A: Gas Sensor Signal Pre-Processing and Processing..... | 240 |
| Appendix B: More Gas Sensitivity Results..... | 258 |

Attestation of Authorship

“I hereby declare that this submission is my own work and that, to the best of my knowledge and belief, it contains no material previously published or written by another person (except where explicitly defined in the acknowledgements), nor material which to a substantial extent has been submitted for the award of any other degree or diploma of a university or other institution of higher learning.”



Enobong Effiong Bassey

List of Conference Publications

The following conference publications were presented in the course of the thesis:

1. Bassey, E., Whalley, J., Sallis, P., and Prasad, K. (2014) "*Wavelet transform smoothing filters for metal oxide gas sensor signal cleaning.*" 8th International Conference on Sensing Technology (ICST 2014), September 2-4, Liverpool John Moores University, United Kingdom
2. Bassey, E., Whalley, J., and Sallis, P. (2014) "*An evaluation of wavelet transform smoothing filters for gas sensor signal cleaning.*" The Fourth International Conference on Advanced Communications and Computation (INFOCOMP 2014), July 20 - 24, Paris, France
3. Bassey, E. E., Prasad, K., and Sallis, P. (2013). "*Surface Structure and Particle Analysis of Combined SnO₂ and ZnO Nanoparticles Prepared for Gas Sensing.*" The 8th Pacific Rim International Conference on Advanced Materials and Processing (PRICM-8), August 4-9, Waikoloa, Hawaii, USA
4. Bassey, E. E., Prasad, K., and Sallis, P. (2013). "*Analysis of SnO₂/ZnO Nanostructures Prepared for Gas Sensing.*" 15th International Symposium on Olfaction and Electronic Nose, July 2-5, EXCO, Daegu, Korea
5. Bassey, E. E., Prasad, K., and Sallis, P. (2013). "*Characterisation of SnO₂ and ZnO Nanostructures.*" IEEE Instrumentation and Measurement Society New Zealand Chapter 5th Annual Workshop on Smart Sensors – Instrumentation and Measurement, February 18-19, University of Waikato, Hamilton, New Zealand
6. Bassey, E. E., Sallis, P., and Prasad, K. (2012). "*An Optimal Design of a Chemical Sensor for Phenol Characterisation in Environmental System.*" 2012 International Conference on Nanoscience and Nanotechnology (ICONN 2012), February 5-9, Perth, Australia

7. Bassey, E. E., Sallis, P., and Prasad, K. (2011). "*Design of a Chemical Sensor for Phenol Characterisation in Environmental Systems.*" International Conference "Nanoscale Materials and Devices for Energy Conversion, Storage and Biosensors" (Nanoenergy11), April 3-6, Natal, Brasil

8. Bassey, E. E., Sallis, P., and Prasad, K. (2011) "*Modification of Gold Nanoparticles for the Development of a Chemical Sensor.*" IEEE Instrumentation and Measurement Society New Zealand Chapter Workshop on Smart Sensors, Measurement and Instrumentation, March 10-11, Auckland University of Technology, Auckland, New Zealand

9. Bassey, E. E., Sallis, P., and Prasad, K. (2010). "*Incorporation of chemical sensors in wireless network systems.*" IEEE Instrumentation and Measurement Society New Zealand Chapter Workshop on Sensor and Instrumentation in Environmental, Health and Agricultural Applications, September 1-2, Massey University, Wellington, New Zealand

List of Figures

| | |
|--|----|
| Figure 2-1: Typical classification of chemical sensor (Korotcenkov 2011)..... | 6 |
| Figure 2-2: Typical chemical sensor system..... | 8 |
| Figure 2-3: Conduction processes and the corresponding energy bands for a <i>n</i> -type MOX material (left) described by a depletion layer and for a <i>p</i> -type MOX material (right) with accumulation layer (Bârsan 2011)..... | 13 |
| Figure 2-4: A summary of a few of the electronic, chemical, and optical processes occurring on metal oxides that can benefit from reduction in size to the nanometer range (Kolmakov and Moskovits 2004)..... | 15 |
| Figure 2-5: Dimensionality classification of nanostructures (Pokropivny and Skorokhod 2007)..... | 16 |
| Figure 2-6: Various organising schemes for self-construction of nanostructures by oriented attachment (Yang and Zeng 2004)..... | 17 |
| Figure 2-7: A schematic summary of the kinds of quasi-one-dimensional metaloxide nanostructures (Kolmakov and Moskovits 2004): (A) nanowires and nanorods; (B) core-shell structures with metallic inner core, semiconductor, or metal-oxide; (C) nanotubules/nanopipes and hollow nanorods; (D) heterostructures; (E) nanobelts/nanoribbons; (F) nanotapes, (G) dendrites, (H) hierarchical nanostructures; (I) nanosphere assembly; (J) nanosprings..... | 18 |
| Figure 2-8: Crystalline structure of SnO ₂ and ZnO. | 23 |
| Figure 2-9: Origin of energy bands by combination of atomic orbitals (Gründler 2007)..... | 25 |
| Figure 2-10: The electronic band structure of SnO ₂ calculated using the GGA-PBE approximation (Falabretti and Robertson 2007). | 27 |
| Figure 2-11: NL-EPM band structure of wurtzite ZnO (Bertazzi et al. 2007)..... | 28 |
| Figure 2-12: Density of states of the first eight conduction bands (top) and of the first six valence bands (bottom) of wurtzite ZnO corresponding to the proposed NL-EPM band structure (Goano et al. 2007). | 29 |
| Figure 2-13: Schematic band diagram of SnO ₂ bulk. Two vacancy donor level E _{D1} and E _{D2} are located 0.03 and 0.15 eV below the conduction band (E _c = 0eV). The bandgap (E _g) is 3.6 eV (Schmid et al. 2004). | 34 |
| Figure 2-14: Response and recovery time..... | 43 |

| | |
|--|----|
| Figure 2-15: Receptor and transducer functions of semiconductor metal oxide gas sensors (Kim et al. 2013): (a) reception function by chemisorption and reaction between reducing gases (CO) and oxygen adions (O ⁻) at the surface; (b) transducer function by electronic charge transport through the grains and across grain boundaries; and (c) the sensor element comprises of the sensing layer, electrodes for electrical measurements, substrate and integrated microheater. | 47 |
| Figure 3-1: Lennards-Jones potential energy diagram for chemisorption, hydrogen bonding and physisorption on the surface (Harbeck 2005). | 54 |
| Figure 3-2: Model of intergranular grains contact/boundary of a thin film <i>n</i> -type semiconductor metal oxide gas sensor surface and oxygen ionosorption (Ding et al. 2001). | 59 |
| Figure 3-3: Sensor scheme (a) sensor structure, and (b) equivalent electrical circuit (Bejaoui et al. 2013). | 60 |
| Figure 3-4: Oxygen species detected at different temperatures at surfaces with with IR (infrared analysis), TPD (temperature programmed desorption), EPR (electron paramagnetic resonance) (Gurlo et al. 2005). | 63 |
| Figure 3-5: Water-related species formed at different temperatures at SnO ₂ surfaces with IR, TPD, EPR (Gurlo et al. 2005). | 65 |
| Figure 3-6: Characteristics of several Langmuir isotherms for different K [K = b(T)] values (Hildenbrand 2003). | 70 |
| Figure 3-7: Schematic layout of a typical resistive gas sensor. The sensitive metal oxide layer is deposited over the metal electrodes onto the substrate (Barsan and Weimar 2001). | 81 |
| Figure 3-8: Schematic representation of a compact sensing layer with geometry and energy band representations; z_0 is the thickness of the depleted surface layer; z_g is the layer thickness and qV_s the band bending. (a) represents a partly depleted compact layer (“thicker”), and (b) represents a completely depleted layer (“thinner”) [Modified from (Barsan and Weimar 2001); (Min 2003)]. | 82 |
| Figure 3-9: Schematic representation of a porous sensing layer with geometry and surface energy band-case with necks between grains (z_n is the neck diameter; z_0 is the thickness of the depletion layer): (a) represents the case of only partly depleted necks whereas (b) represents large grains where the neck contact is completely depleted (Gurlo et al. 2005). | 83 |
| Figure 3-10: Different conduction mechanisms and changes upon O ₂ and CO exposure to a sensing layer in overview. This survey shows geometries, electronic band pictures and equivalent circuits. EC minimum of the conduction band; EV maximum of the valence band; EF Fermi level; LD Debye length (Barsan et al. 2007). | 83 |

| | |
|---|-----|
| Figure 3-11: Band bending on <i>n</i> -type semiconductor during ionosorption of oxygen [modified from (Gurlo 2006; Schmid et al. 2004)]. | 85 |
| Figure 3-12: Schematic representation of the sensitive layer for semiconductor; brown colour indicates low resistance while yellow indicates high resistance elements: (a) <i>n</i> -type materials, and (b) <i>p</i> -type materials (Weimar and Barsan 2009). | 88 |
| Figure 3-13: Microstructure and energy band model of a gas sensitive SnO ₂ film (Licznanski 2004). | 90 |
| Figure 3-14: Schematic representation of (a) adsorption of atmospheric oxygen on the sample surface, and (b) reaction of alcohol molecules with the adsorbed oxygen species (active sites) (Mishra et al. 2013). | 91 |
| Figure 3-15: A schematic diagram illustrating the principle of charge separation and photocatalytic activity for the couple oxides (Zhang et al. 2004b). A similar mechanism is presented by (Zheng et al. 2012). | 95 |
| Figure 3-16: Schematic of the band energy level of ZnO–SnO ₂ hetero-junction used for gas sensing (Mondal et al. 2014). | 95 |
| Figure 3-17: Band alignment diagram of the SnO ₂ –ZnO photocatalyst (Uddin et al. 2012). | 97 |
| Figure 3-18: Schematic of the formation process of ZnO–SnO ₂ composite. (a) SEM image of the meta-stable [ZnSn(OH) ₆] intermediate and (b) morphology of ZnO–SnO ₂ composite (Mondal et al. 2014). | 98 |
| Figure 4-1: Flow-diagram of gas fabrication, characterisation and sensing. | 100 |
| Figure 4-2: 25-Ton Manual Laboratory Press (Table-Top). | 103 |
| Figure 4-3: Tecport Sputter Coater. | 106 |
| Figure 4-4: Tecport sputter coater open chamber. | 107 |
| Figure 4-5: Interdigital patterned structure (a) photolithography, and (b) shadow mask. | 110 |
| Figure 4-6: Carl Zeiss ULTRA 55. | 112 |
| Figure 4-7: Q150R Rotary-Pumped Sputter Coater/SEM Carbon Coater. | 112 |
| Figure 4-8: AFM (Bruker Dimension Icon with ScanAsyst). | 114 |
| Figure 4-9: Gas sensing system. | 115 |
| Figure 4-10: Gas Chamber (Internal). | 116 |
| Figure 4-11: KIN-TEK Model 491 MB Module. | 116 |

| | |
|---|-----|
| Figure 4-12: Typical sensor digital signal..... | 118 |
| Figure 5-1: Film thickness plot (UA: Unannealed; A: Annealed). | 121 |
| Figure 5-2: Elemental composition of samples (a) SnO ₂ , (b) SZ, and (c) ZnO..... | 124 |
| Figure 5-3: Film surface cross-section..... | 125 |
| Figure 5-4: FE-SEM images films deposited for 30 min. | 126 |
| Figure 5-5: Particle size of (a) as-fabricated, (b) annealed nanostructures..... | 127 |
| Figure 5-6: Grain size plot (UA: Unannealed; A: Annealed). | 128 |
| Figure 5-7: SnO ₂ –ZnO as-fabricated samples..... | 130 |
| Figure 5-8: ZnO samples deposited for 20 min. | 131 |
| Figure 5-9: Surface roughness characterisation. | 132 |
| Figure 5-10: Representation of AFM images of films as-deposited samples (a) SnO ₂ , (b) SZ, and (c) ZnO. | 134 |
| Figure 5-11: Annealed SnO ₂ and ZnO deposited for 20 min (a) SnO ₂ , and (b) ZnO. | 135 |
| Figure 6-1: Typical sensor response (SnO ₂ sensor response behaviour with 200 ppm methanol)..... | 140 |
| Figure 6-2: Typical sensitivity – sensor type plots (200 ppm ethanol)..... | 141 |
| Figure 6-3: Sensitivity-temperature plots of SnO ₂ with methanol and ethanol. | 143 |
| Figure 6-4: Sensitivity-concentration plots of SnO ₂ with methanol. | 144 |
| Figure 6-5: Sensitivity-temperature plots with 100 ppm methanol. | 144 |
| Figure 6-6: Sensitivity difference – temperature plots of SnO ₂ | 145 |
| Figure 6-7: Sensitivity-temperature plots of S ₃ Z ₁ with methanol and ethanol..... | 147 |
| Figure 6-8: Sensitivity difference - temperature plots of S ₃ Z ₁ | 148 |
| Figure 6-9: Sensor sensitivity to methanol and ethanol at 150 °C. | 148 |
| Figure 6-10: Sensitivity-temperature plots of SZ with methanol and ethanol. | 150 |
| Figure 6-11: Sensitivity difference - concentration plots of SZ with methanol..... | 150 |
| Figure 6-12: Sensor sensitivity to methanol and ethanol at 250 °C..... | 151 |
| Figure 6-13: Sensitivity-temperature plots of S ₁ Z ₃ methanol and ethanol. | 153 |

| | |
|---|-----|
| Figure 6-14: Sensitivity difference – temperature plots of S_{1Z3} | 154 |
| Figure 6-15: Sensitivity-temperature plots of ZnO methanol and ethanol. | 155 |
| Figure 6-16: Sensitivity difference - temperature plots of ZnO..... | 155 |
| Figure 6-17: Sensitivity-time profile for 100ppm methanol at 150 °C. | 157 |
| Figure 6-18: Sensitivity vs. temperature plots with 150 ppm methanol. | 157 |
| Figure 6-19: Sensitivity-time profile for 150 ppm methanol at 250 °C. | 158 |
| Figure 6-20: Sensitivity-time profile for 200 ppm methanol at 350 °C..... | 159 |
| Figure 6-21: Sensitivity-time profile for 200 ppm ethanol at 350 °C..... | 160 |
| Figure 6-22: Sensitivity difference – sensor type plots of 200 ppm ethanol. | 162 |
| Figure 6-23: Sensitivity difference – sensor type plots of 200 ppm methanol. | 163 |
| Figure 6-24: Response and recovery time plots of 200 ppm methanol at 350 °C. ... | 164 |
| Figure 6-25: Response and recovery time plots of 150 ppm methanol at 150 °C. ... | 165 |
| Figure 6-26: Response and recovery time plots of 200 ppm ethanol at 350 °C. | 166 |
| Figure 7-1: Boxplot of sensitivity versus methanol concentration (across all sensor types and operating temperatures)..... | 176 |
| Figure 7-2: Boxplot of sensitivity versus temperature (across all sensor types and gas concentrations). | 177 |
| Figure 7-3: Boxplot of sensitivity versus sensor type (across all operating temperatures and methanol gas concentrations)..... | 178 |
| Figure 7-4: Estimated marginal mean of sensitivity to methanol. | 179 |
| Figure 7-5: Boxplot of sensitivity versus sensor type with 200 ppm methanol and ethanol. | 180 |
| Figure 7-6: Boxplot of sensitivity versus gas type with 200 ppm methanol and ethanol. | 181 |
| Figure 7-7: Boxplot of sensitivity versus temperature with 200 ppm methanol and ethanol. | 182 |
| Figure 7-8: Plot of estimated marginal means of sensitivity with 200 ppm methanol and ethanol. | 183 |
| Figure 7-9: Boxplot of sensitivity versus sensor type with 200 ppm ethanol..... | 184 |
| Figure 7-10: Boxplot of sensitivity versus sensor type with 200 ppm methanol..... | 185 |

| | |
|--|-----|
| Figure 7-11: Schematic of sensing reaction process on the surface of metal oxide semiconductor (Zeng et al. 2012)..... | 186 |
| Figure 7-12: Log-log plot of sensitivity versus concentration at (a) 150 °C, (b) 250 °C, and (c) 350 °C..... | 191 |
| Figure 7-13: Simulated sensitivity at 350 °C (power model). | 193 |
| Figure 7-14: Simulated sensitivity of SnO ₂ sensors (power model)..... | 194 |
| Figure 7-15: Simulated sensitivity of SZ sensors (power model)..... | 194 |
| Figure 7-16: Simulated sensitivity at 250 °C (linear model)..... | 196 |
| Figure 7-17: Resistance versus temperature plot of 200 ppm ethanol. | 198 |
| Figure 7-18: Plot of activation energy versus sensor type. | 198 |
| Figure 7-19: Gas adsorption-desorption cycle. | 201 |
| Figure 7-20: Adsorption-desorption cycles of SnO ₂ , SZ and ZnO sensors. | 202 |

List of Tables

| | |
|---|-----|
| Table 2-1: Structural data of zinc oxide (Ellmer 2011) | 23 |
| Table 4-1: Basic properties of SnO ₂ and ZnO | 103 |
| Table 4-2: Molar fraction compositions of the metal oxide mixtures..... | 104 |
| Table 4-3: Process parameters for Tecport RF magnetron sputtering of MOX thin films..... | 106 |
| Table 4-4: Process parameters for Tecport magnetron sputtering of Ti/Pt pattern.. | 110 |
| Table 6-1: Coefficient of determination (R ²)..... | 142 |
| Table 7-1: Table of power model parameters | 192 |
| Table 7-2: Coefficient of determination (power model) | 195 |
| Table 7-3: Table of linear model parameters | 196 |

Acronyms and Abbreviations

| Roman Symbol | Meaning |
|------------------------|---|
| ΔG | Change in Gibbs free energy |
| ΔH | Change in a enthalpy |
| ΔS | Change in entropy |
| <i>AFM</i> | Atomic Force Microscopy |
| <i>C</i> | Concentration |
| <i>CB</i> | Conduction band |
| <i>D</i> | Stability |
| <i>d</i> | Distance between the interacting particles |
| <i>DFT</i> | Density functional theory |
| <i>DL</i> | Detection limit |
| <i>E</i> | Energy of the system |
| <i>E_a</i> | Activation energy |
| <i>E_d</i> | Energy of dissociation |
| <i>EDS</i> | Energy Dispersive Spectroscopy |
| <i>F</i> | F-Distribution |
| <i>FE-SEM</i> | Field Emission-Scanning Electron Microscopy |
| <i>G</i> | Conductivity |
| <i>h</i> | Hour |
| <i>k</i> | Boltzmann constant |
| <i>K'</i> | Kinetic parameters, association constant |
| <i>k_{ads}</i> | Rate constant for adsorption |
| <i>k_{des}</i> | Rate constant for desorption |
| <i>LD</i> | Debye length (or depletion layer) |
| <i>M</i> | Mean |
| <i>m</i> | Mass |
| <i>MOX</i> | Metal oxide |
| <i>N</i> | Concentration of charge carries |
| <i>N</i> | Number of surface adsorption sites |
| <i>p_{gas}</i> | Gas partial pressure |
| <i>Q</i> | Reproducibility |
| <i>qVS</i> | Surface band bending |
| <i>R</i> | Resistance |
| <i>r</i> | Distance between two atoms in a molecule |
| \mathcal{R} | Universal gas constant |

| Roman Symbol | Meaning (Cont'd) |
|---------------------|---------------------------------------|
| R_n | Layer resistance for n-type material |
| R_p | Layer resistance for p-type material |
| S | Sensor signal response or sensitivity |
| SD | Standard deviation |
| T | Temperature |
| V | Volume |
| V_s | Potential of Schottky barrier |
| w | Weight |
| W | Number of quantum-mechanical levels |

| Greek Symbol | Meaning |
|---------------------|-------------------------------------|
| Γ_s | Integral of surface conductivity |
| ε | Dielectric constant of the material |
| ε_{pot} | Depth of potential |
| ζ | Drift |
| η | Partial Eta Squared (effect size) |
| θ | Fractional surface coverage |
| v | Volume |
| ρ | Density |
| ϱ | Grain size |
| σ | Conductivity |
| τ_{det} | Detection time |
| τ_{rec} | Recovery time |
| τ_{res} | Response time |
| Φ | Surface potential |

This list of acronyms and abbreviations is certainly incomplete. Common chemical formulas such as SnO₂, ZnO, and trade names such as MATLAB™, are left as they are or explained at the points of their use in this thesis. Common nomenclatures, symbols, variables and parameters used in various equations, tables and figures, are not listed. These, and other acronyms and symbols which are used sparingly in the thesis, are defined at the appropriate places in the thesis.

Chapter One

Introduction

1.1 Introduction

Innovations in the design and construction of modern sensors and sensor technologies incorporate a multidisciplinary platform of nanotechnology¹ of science and technology ([Russell et al. 2007](#)), ranging from biology; solid state physics; chemistry; electrical and electronics engineering; chemical and biomedical engineering; petroleum exploration, production and processing; sensory technology; physiology; psychology; social economics; marketing and management. Profound interest in miniaturisation of electronic components has led to improved portability of devices with improved functionality. In this blend of methods and techniques, nanotechnology and microelectronics have governed the development of a new generation of high-density, smart and innovative multi-analyte sensing devices to meet the rising demand for highly sensitive and highly selective smart sensor systems capable of simultaneously detecting multiple species and transmission/interpretation of signals in real-time for effective decision making.

1.2 Motivation

The increase in variety of applications of chemical sensors has sustained interest in functional improvement and miniaturisation of sensing systems. Metal oxide semiconductors have offered a veritable material for development of a dynamic range of interface circuit nano devices. Among the metal oxides, tin dioxide (SnO₂) and zinc oxide (ZnO) have stood out the most, in their versatile applications. Nanocomposites of SnO₂ and ZnO are expected to have significantly enhanced gas sensing properties.

¹ Nanotechnology is the understanding and control of matter at dimensions between approximately 1 and 100 nm, where unique phenomena enable novel applications; encompassing nanoscale science, engineering, and technology, nanotechnology involves imaging, measuring, modelling, and manipulating matter at this length scale ([Russell et al. 2007](#)).

Evidenced by published experimental results in the corpus of literature relating to this research domain, nanocomposites and their sensing mechanisms are still poorly understood. Their surface reactions have not been correlated with their nanostructures sufficiently, such that adequate robustness of results can be observed in terms of their scalability and generalisability. The research described in this thesis seeks to systematically investigate the sensing-dependence on the molar composition of the nanocomposite, and analyse the structural characteristics of the coupled SnO₂ and ZnO, to develop their sensing mechanism based on their adsorption-desorption behaviour.

It is proposed that this work will provide results that are both robust in terms of scientific adequacy and informative in terms of the state-of-knowledge advancement in this research domain. Establishing the potential for producing a reliable method for carrying out experiments to produce such results has an inherent question as to possibility. This, in itself, is the primary research question for the research presented in this thesis.

1.3 Objective of Research

The objectives of this research include the following:

1. Explore and develop an understanding of the sensing mechanism of the different combinations of coupled SnO₂ and ZnO nanocomposite nanostructure.
2. Advance the understanding of the relationship between nanocomposites combinations to their gas sensing behaviour in hydrocarbon environment. By gradual changes in the molar concentration of SnO₂ and ZnO, the entire spectrum (0-100%) of the combination is analysed, and related to the proposed sensing model. Effects of molar composition variation in the sensors will be related to the sensitivity of the resulting sensors.
3. Develop the relationship between surface morphology of the thin films (based on microstructure and chemical composition) with the reaction mechanism(s), signal response and possibly photocatalytic activity. This will be done by a critical analysis of the surface and particle characteristics of nanostructures of their thin films as investigated using field emission scanning electron microscopy (FE-SEM), atomic force microscopy (AFM), and energy dispersive spectroscopy (EDS). The

observations from nano-characterisation are collaborated with the sensing mechanism to propose the behaviour of the sensors towards geo-environmental hydrocarbon gases.

1.4 Thesis Organisation

Chapter 1 introduces this dissertation, providing the motivation, research objectives, and thesis organisation.

Chapter 2 presents the fundamentals of chemical sensors, discusses the operating principles of metal oxide based gas sensors, classes of chemical sensors, properties of SnO₂ and ZnO nanostructures, and sensor performance characteristics.

Chapter 3 describes the detailed surface reaction process between metal oxide semiconductors and target gases. The chapter is presented in sections covering sensing mechanism, surface chemistry and transport phenomena as related to metal oxide (MOX) semiconductor conduction processes.

Chapter 4 presents detailed description of the experimental design, fabrication and characterisation techniques for development and synthesis of gas sensor devices. This includes an overview of general deposition techniques to synthesis thin films of SnO₂ and ZnO and their nanocomposites, with special focus on sputtering processes, and description of the various characterisation techniques.

Chapter 5 presents the characterisation of films using FE-SEM, EDS and AFM. Post treatment of thin film, and film structural and electrical characterisation methods are presented, and possible effects on the sensitivity of the sensor are remarked.

Chapter 6 describes sensor signals processing. It involves exploration of different signal filtering methods to extract the desired digital signal while maintaining the shape and resolution of the signal. The sensor signals are processed and analysed for pattern recognition. The response behaviour is observed as it changes with variations in the

composition of the sensors, the gas concentration and the operating temperatures. A possible model of the sensitivity behaviour is proposed.

In Chapter 7, sensitivity analysis is undertaken to determine the effect of sensor type, gas concentration and temperature on sensor sensitivity, along with their relationship to sensor sensitivity itself, using factorial design. Modified chemisorption, power, and linear models are presented, and applied to simulate the behaviour of the sensors with different gas concentrations and operating temperatures. Sensing mechanisms are presented for each sensor, based on the results observed and the models of the gas-sensor behaviour. Environmental considerations for effective practical (real-life) applications of the sensors are presented.

Chapter 8 summarises the conclusions obtained from the research, and presents the outlook for future research to advance the field.

1.5 Keywords

Sensors, Nanoparticles, Nanostructures, Metal Oxides, SnO₂, ZnO, Hydrocarbon, Liquefied Petroleum Gas, Ethanol, Methanol, Hydrogen, Volatile Organic Gases, Gas Detectors, Design, Fabrication and Characterisation, Electrical and Electronics Engineering, Chemical Engineering, Petroleum Engineering, Biochemical Engineering, Solid-State Engineering, Photocatalysis.

Chapter Two

Fundamentals of Chemical Sensor

2.1 Operating Principles and Sensory Analysis

Sensory analysis is the technique for determination of stimuli from the five (human) senses. The sensory organs can be classified into two sensor types: physical and chemical sensors. The physical sensors measure touch, sight and hearing. The chemical sensors measure olfaction and taste. Olfaction is analysed in humans during mastication (retro nasal way) or inhalation, while taste is analysed as sweet, salty, sour, or bitter.

The basic principle of chemical sensory analyses is that chemical compounds readily oxidise or reduce at solid electrodes. This normally results in the deposition of polymeric adherent film on the electrodes. Three electrodes are normally involved in the electrochemical detection of an active analyte; working, reference and counter electrodes. The working electrode serves as a transducer, responding to the excitation signal and the concentration of the active analyte, and permitting the flow of electrons or sufficient currents to affect appreciable changes of bulk composition within the ordinary duration of the measurement. The reference electrode maintains a virtually invariant potential under the conditions prevailing in an electrochemical measurement and permits the observation, measurement and control of the potential of the working electrode. The counter electrode merely carries the electrons or current through the cell; no interesting reaction occurs at its surface.

2.2 Classification of Sensors

Previous attempts have been made to present a comprehensive classification of sensor and sensor technology. A typical chemical sensor classification is presented in Figure 2-1. [White \(1987\)](#) presented a comprehensive classification scheme for sensors based on the measurands, technological aspects, detection means, conversion phenomena, sensor materials and fields of application. Possible measurands could be electric, magnetic,

electromagnetic, acoustic, chemical, optical, heat, temperature, mechanical, radiation, biological, etc. Technological applications could be industrial (and non-industrial) process control, measurement, and automation, such as aircraft, medical products, automobiles, and consumer electronics. His categorisation scheme facilitated easy comparison of sensor for adaptation and applications amongst users.

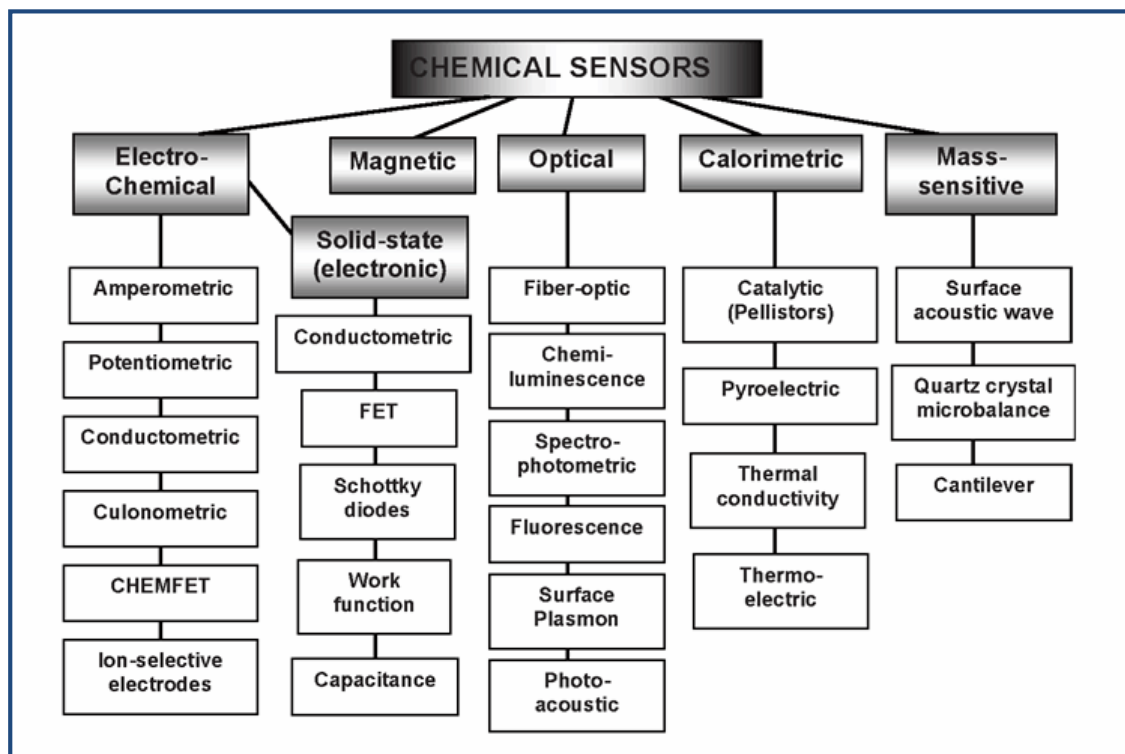


Figure 2-1: Typical classification of chemical sensor (Korotcenkov 2011).

Classification could also be based on specifications: accuracy, sensitivity, stability, response time, hysteresis, frequency response, input (stimulus) range, resolution, linearity, hardness (to environmental conditions, etc.), cost (price, size, weight, construction materials), operating temperature, etc (Patel 2014a).

Michahelles and Schiele (2003) organised sensor technology into uses, based on identification of six dimension (User ID, Object Use, Location, Bio Sign/Emotions, Activity and Interaction Among Humans) of sensing to represent the sensing goals for physical interaction. They developed the conceptual framework that allows categorisation of existing sensors and evaluation of their utility in various applications. Their framework

could be used as a guide to application designers in choosing meaningful sensor subsets and evaluating existing applications while designing new systems.

Other approaches could be applied in the classification of sensors, such as hardware and software, mechanism, etc. [Zook and Schroeder \(2006\)](#) classified sensing mechanisms, in terms of elemental transduction processes (ETPs) mechanisms, into four distinct categories: energy conversion, energy dispersion, energy modulation, and property modulation.

2.3 Chemical Sensors

A chemical sensor is defined as a device that transforms chemical information, ranging from the concentration of a specific sample component to total composition analysis, into an analytically useful signal ([Patel 2014b](#)). They are miniaturised portable devices developed for selective and typical continuous (reversible) real-time and on-line determination of the concentration of a specific substance compounds or ions even in complex samples in a single stage, without preliminary sample preparation ([McDonagh et al. 2008](#)). The devices transform chemical and/or physical information, such as the concentration of a specific sample component or total composition analysis, into an analytical useful signal, as the analytes interact with the receptors (sensing materials). Typically, the basic component of the chemical sensor is the sensing element, which is a chemical (or analyte) recognition system (receptor), and the physiochemical transducer, which is an analytical signal converter of chemical or biochemical reaction to physical parameter. These two components are connected in series. Depending on the complexity of the process, additional elements could be incorporated; particularly, units for signal implication and signal conditioning ([Gründler 2007](#)).

The chemical sensor is operated as a result of a sequence of events between the receptors and the targets, including electrical, optical, magnetic, thermal, colorimetric, electrochemical, and piezoelectrical properties of the analyte. The chemical recognition system (receptor) interacts with the analyte in selective chemical reactions, and transforms the chemical information into a form of energy which may be measured by

the transducer. The interaction is at the interface between the analyte and the receptor by equilibrium or catalytic reactions by processes of interaction equilibriums or chemical reaction equilibriums. The specific processes are adsorption, ion exchange and liquid-liquid extraction or partition equilibrium. The physiochemical transducer transforms the non-electric (biochemical or chemical) information into an analytical electric quantity, such as voltage, current or resistance. A typical chemical sensor is shown in Figure 2-2.

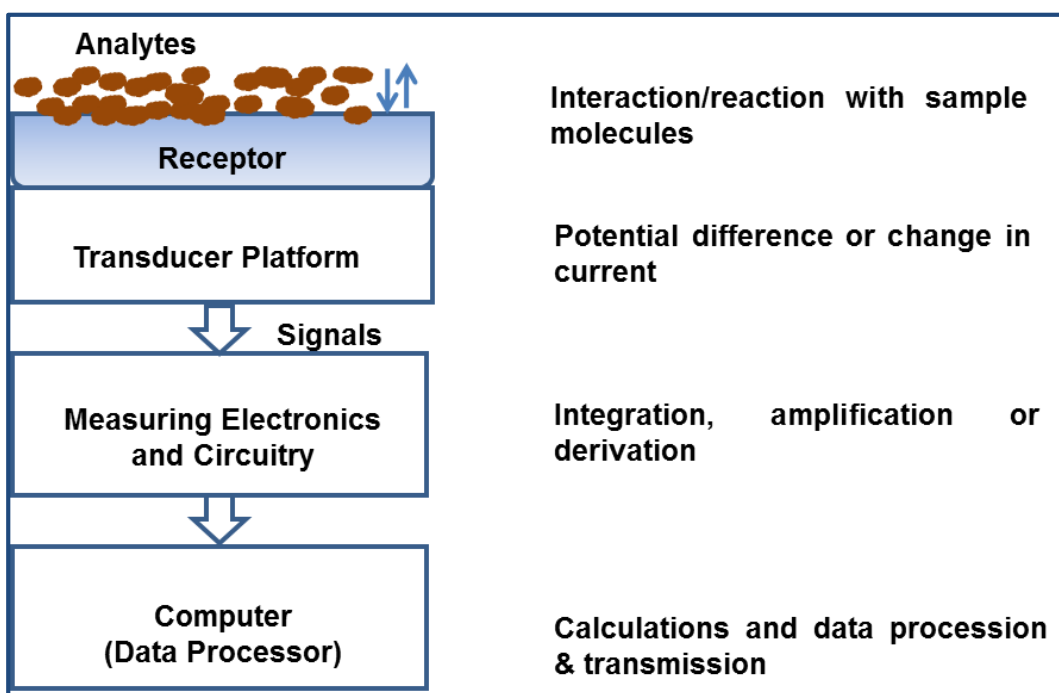


Figure 2-2: Typical chemical sensor system.

The chemical sensing phenomenon could be confined to the surface of the sensing layer or take place in the whole volume of the sensitive coating. Surface interaction requires the active species to be adsorbed at the surface or interface (gas/solid or liquid/solid); while the volume interaction implies that the species get adsorbed and partitioned between sample phase and the bulk of the sensitive material. In the sensing process, chemical interactions range from very weak physisorption through strong chemisorption to charge transfer and chemical reactions (see Chapter 3 for details). In physisorption, the chemical is only physically absorbed or adsorbed (London or Van-der-Waals dispersion forces) with interaction energy of 0-30kJ/mol ([Baltes et al. 2005](#)). In chemisorption

(interaction energy > 120 kJ/mol), the chemical sticks to the surface and forms a covalent bond in the process.

2.4 Types of Chemical Sensors

In chemical sensor, gas molecules react with the objective sensing materials on the sensor surface by activating a positive change in physical properties, i.e., mass, volume, or other. These changes are detected by chemical sensors, and the change is converted into an electronic signal by a transducer. Different forms of chemical reaction and their mode of electrical signal transformation results in different types of chemical sensors. These include: voltammetric ([Winqvist 2008](#)), amperometric ([Iwuoha et al. 2007](#); [Tvrdikova et al. 2012](#)), potentiometric ([Janata 2009](#); [Kale et al. 2003](#)), conductometric ([Calvo and Otero 2008](#); [Fraden 2004](#)), impedancemetric ([Achmann et al. 2009](#); [Fergus 2007](#)), calorimetric or chemoresistors ([Calvo and Otero 2008](#); [Kopparthy et al. 2012](#)), chromatographic (or electrophoresis or spectrophotometric) ([Gründler 2007](#); [Urschey et al. 2003](#)), field effect transistor ([Liu et al. 2009](#); [Mukherjee and Majumder 2009](#)), biochemical ([Anzai 2004](#); [Stanca et al. 2003](#)), carbon nanotube ([Gomez De Arco 2010](#); [Iijima 1991](#)), polymer conducting ([Adhikari and Majumdar 2004](#); [Lu et al. 2010](#)) sensors.

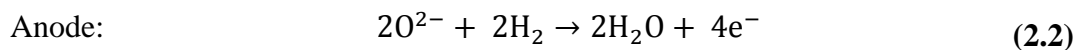
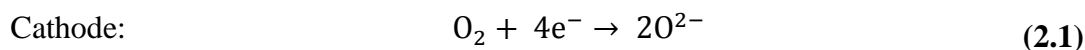
2.5 Solid State Gas Sensors

Solid state sensors operate by measuring the changes in the physical property of the devices relative to chemical reactions (i.e., adsorption/desorption processes) on the surface of a sensing element. The major physical property is conductivity change of gas-sensing material; its conductivity change can be transduced as a measurable electrical signal in the form of a change in conductance, capacitance, work function, mass, optical characteristics or reaction energy released by the gas/solid interaction. The read-out of the measured value is performed via electrodes, diode arrangements, transistors, surface wave components, thickness-mode transducers or optical arrangements ([Capone et al. 2003](#); [Korotcenkov 2007](#)).

A vital characteristic of solid state gas sensors is the reversible interaction of the gas with the surface of a solid-state material. These properties have generated great industrial and

scientific interests in solid state sensors because of their small sizes, economical cost, high sensitivities in detecting trace concentrations of chemical compounds, possibility of on-line real-time operation and possible bench production. Their high potential applications have increased to replace use of conventional analytical systems such as laboratory reaction processes, gas chromatography or optical detection is prohibitively expensive.

[Moseley \(1997\)](#) classified solid state gas sensors into three major categories: solid electrolytes, catalytic combustion, and resistance modulation of semiconducting oxides. **Solid electrolytes** are materials that allow the conduction of ions but not the conduction of electrons. Similar to liquid electrolytes, they support the function of electrochemical cells, in which chemical reactions are only allowed to proceed to completion if separate paths are provided for the flow of ions (through the electrolyte) and electrons (through an electronic conductor). The reactions at the electrodes are depicted as follows:



Electronic current transportation through an external load in a solid oxide fuel cell, flux of oxygen ions and consumption of hydrogen in the solid electrolyte are the major factors that support these reactions.

2.5.1 Catalytic sensors

Catalytic sensors (also called catalytic pellistor sensor) are used for the detection of combustible gases in ambient air environments, using a catalyst (e.g. platinum) to sustain such a reaction at a reasonable temperature. Usually, the sensor consists of a pellistor (i.e., detector) and a compensator. The catalytic palletised resistor (i.e., pellistor) surface is constructed around a platinum coil (microheater) that heats the catalyst to a sufficiently high temperature, at which any flammable gas molecules present burns and release combustion heat ([Artursson et al. 2002](#)). The compensator consists of a coil of fine platinum wire embedded in an alumina bead to acts as the reference resistance to the

sensor signal. Its effect is to eliminate the effects of environmental factors and inhibit oxidation process of any other substances other than the effects of the flammable volatile gas in the catalytic sensor. The working principle of the catalytic sensor is similar to the chemical reaction: when the flammable gas comes in contact with the catalyst surface it is oxidised, releases heat, and causes the resistance (or voltage) of the wire to change as a result of the temperature increase. [Kolev et al. \(1998\)](#) developed a three-dimensional thermal mathematical model of a pellistor based on the fundamental physical laws of heat transfer and employing a few clearly stated simplifying assumptions concerning the convective heat transfer in ambient air. They solved the model numerically using the implicit alternating-direction finite difference method.

2.6 Metal Oxide Nanostructured Sensors (MOX)

The exceptional physical, chemical, optical, electrical, electronic, and magnetic properties of metal oxides and their ability to behave as semiconductors² ([Gas'kov and Rumyantseva 2001](#)), have been the hallmark of their applications as sensors. Metal oxide semiconductors are chemo-resistive sensors made from metal oxides nanoparticles. The sensing element, normally comprising a semiconducting material presenting a high surface-to-bulk ratio, is deployed on a heated insulating substrate between two metallic electrodes ([Moseley 1997](#)). Changes in the density of charge carriers are observed as a result of reactions involving gas molecules and the semiconductor surface. Sensor signal is recorded as conductance (or resistance) of the device changes progressively with changing atmospheric composition.

Comparatively, the solid electrolytes, catalytic reaction and gas-sensing process on a metal oxide are analogous to each other as their reaction processes involve surface adsorption and chemical reaction in ambient gas environment. Currently, there is increasing need to establish a correlation between electro-physical (band gap, electro-conductivity, type of conductivity, oxygen diffusion), thermodynamic, surface, electronic, structural properties, catalytic activity and gas-sensing characteristics of metal

² Semiconductors are materials that are electrically insulating at a temperature of absolute zero but that becomes conducting for temperatures below its melting point ([Gas'kov and Rumyantseva 2001](#)).

oxides designed for solid-state sensors. This interest has led to the application of different functions and parameters in the development of various sensors for diverse applications. Despite the variety in design approaches of solid state sensors, operation principles are basically similar in characterisation of sensing parameters. For example, [Di Natale et al. \(2009\)](#) compared the sensing behaviour of quartz microbalances (QMB) and ChemFET transducers functionalised with the same sensing layers in the modification of cobalt tetraphenylporphyrin complex. They observed that QMB translates a change of mass into a shift of the frequency of an electric signal, which is intrinsically not dependent on the interaction mechanism, because any interaction with volatiles, both by physisorption or chemisorption, induces a change of the mass of the sensing layer.

Metal oxide semiconductors based on catalytic sensors mechanism have been developed and applied to gas sensing with familiar characteristics ([Holmberg et al. 1997](#)). As nanostructures, metal oxide exhibit unique electron and phonon confinement, high surface-to-volume ratios, modified surface work function, small grain size, high surface reaction activity, high catalytic efficiency and strong adsorption ability ([Solanki et al. 2011](#)). Typically, most metal oxide semiconductors are made from the chemical combination of transition/post-transition metals with oxygen. Such metal oxides as SnO₂, ZnO, Cu₂O, CdO, CeO₂, In₂O₃, TiO₂, Fe₂O₃, WO₃, MgO, Ga₂O₃, etc., have been applied for gas sensing. Their superiority above chemical sensor is characterised by their excellent sensitivity, reliability, durability, and response-recovery time.

There are two type of semiconducting metal oxides materials; based on their oxygen ionosorption behaviour, they are classified as *n*-type and *p*-type semiconductors (Figure 2-3). The *n*-type material builds a surface depletion layer, which has a lower concentration of free charge carriers (electrons) and by that exhibits higher resistivity ([Bârsan 2011](#)). Electronic transport takes place through the layers, perpendicular to the surface; i.e., from one grain to the other over the grain-grain barrier.

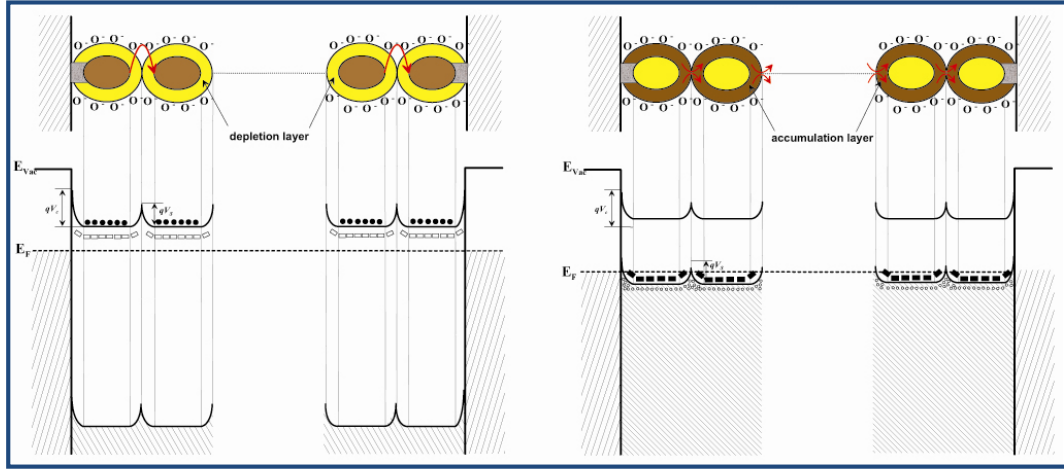


Figure 2-3: Conduction processes and the corresponding energy bands for a n -type MOX material (left) described by a depletion layer and for a p -type MOX material (right) with accumulation layer (Bârsan 2011).

Assuming negligible concentration of electrons in the depletion layer (i.e., the Schottky approximation holds), the relation between layer resistance, R_n , and the surface band bending qV_s is given as (Bârsan 2011):

$$R_n \approx \exp\left(\frac{qV_s}{kT}\right) \quad (2.3)$$

For the p -type material, the effect of oxygen ionosorption involves the appearance of a surface accumulation layer with a higher concentration of free charge carriers (holes) and thus, a lower resistivity. Thus, there is a possibility to have a lower resistance path around the grains, parallel to the surface. The relation between the resistance, R_p , and the surface band bending, qV_s , is given as (Bârsan 2011; Hübner et al. 2011):

$$R_p \approx \exp\left(\frac{qV_s}{2kT}\right) \quad (2.4)$$

Comparing Equations (2.3) and (2.4), it can be seen that different types of semiconducting MOX can exhibit the same chemistry of the porous sensing layers (i.e., the same change of the band bending or same surface reactivity), but transduce different electrical changes into a sensor signal. By considering the sensor signal as the relative change of the electrical conductance/resistance determined by target analyte exposure, $S_{n,p}$, a different type of conduction mechanism will determine a very different sensor signal for the same

surface reactivity as shown in the following relationship between the sensor signals in the two cases:

$$S_p = \sqrt{S_n} \quad (2.5)$$

The detection mechanism of metal oxide nanostructures is based on a modulation of their electrical conduction properties by surface adsorbed gas molecules. The details of the surface chemistry, conduction models and sensing mechanism are discussed in Chapter 3.

2.6.1 Categories of Metal Oxide Nanostructures

The interest in smaller and enhanced performance microelectronics has pushed the limits in the miniaturisation technology of metal oxides into nanostructures. In the Greek system, the word “nano”, depicts a number in the one billionth of any unit (i.e., 10^{-9}). In terms of material sizes, nanostructures are defined as materials that have at least one dimension smaller than 100 nm ([Gas'kov and Rumyantseva 2001](#); [Kuchibhatla et al. 2007](#)). They can be categorised into the following groups:

- a) Atomic clusters or nanoparticles
- b) Nanolayers
- c) Nanotubes and nanorods
- d) Nanocrystals
- e) Nanocomposites

[Kolmakov and Moskovits \(2004\)](#) showed that an increase in quantum confinement effects³ ([Semonin et al. 2012](#)) with decreasing nanostructure dimensions is also expected to have a potential impact on the performance of the materials in various electronic, chemical, and optical processes applications (Figure 2-4).

³ Quantum confinement effects becomes relevant when 1D of the nanostructure approaches the de Broglie wavelength of electrons and holes in the bulk semiconductor, $\lambda_e = (h/m_{\text{eff}}kT)$, where m_{eff} is the effective mass of the electron (or hole for λ_h), h is Plank's constant ([Semonin et al. 2012](#)). For most semiconductors λ_e, λ_h are 10 – 100 nm.

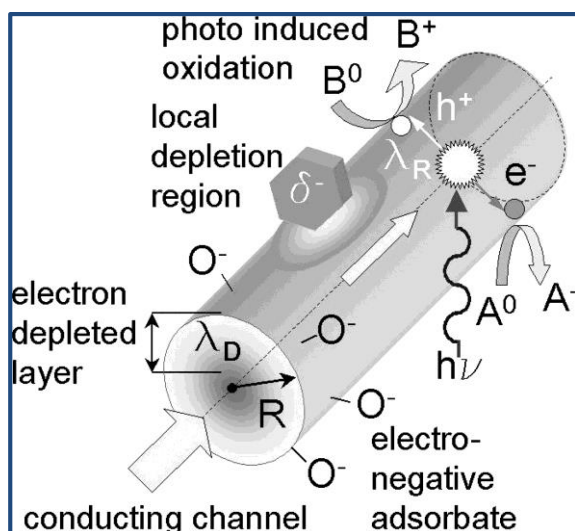


Figure 2-4: A summary of a few of the electronic, chemical, and optical processes occurring on metal oxides that can benefit from reduction in size to the nanometer range ([Kolmakov and Moskovits 2004](#))

2.7 Dimensionalities of Nanostructures

A general classification of the nanostructure dimensionality, adapted from [Pokropivny and Skorokhod \(2007\)](#), is presented in Figure 2-5. The major characteristic in the discrimination of nanostructures is their dimensionality. The shape of nanostructures were first classified by [Gleiter \(2000\)](#) and [Shevchenko et al. \(2004\)](#) on the basis dimensionality.

Unfortunately, their classification of nanostructures did not take into consideration the zero-dimensional (0D), one-dimensional (1D), two-dimensional (2D), and three-dimensional (3D) structures. An expanded classification was presented by ([Kustov and Nefedov 2008](#); [Pokropivny and Skorokhod 2007](#); [Tiwari et al. 2012](#)) as 0D (point), 1D (line), 2D, and 3D nanostructures; while [Comini et al. \(2009b\)](#) distinguished 2D and 3D in terms of deposition technique as thin film and thick film, respectively.

Within the nanocrystals, the grains (crystallites) are co-axis and their size is in the nano range. The structure of nanocomposites is made of two or more phases, where one of the phases is presented in zero, one-, two-, or three-dimensional states ([Errana 2011](#)).

Dimensionality classification of nanostructures ($L < 100 - 500 \text{ nm}$)

Designation: dimensionality of NS \rightarrow **kDlmn.e** \leftarrow dimensionality of elementary units
 $k > l, m, n \quad \{k, l, m, n\} = \{0, 1, 2, 3\}$

Elementary building units :

| | | |
|--|---|-----------------|
| 1. 0D Molecules, clusters, fullerenes, rings, metacarb, thoroids, domens, particles, powders, grains, schwarztons | 2. 1D nanotubes, fibers, filaments, whiskers, spirals, belts, springs, horns, columns, needles, pillars, helicoids, wires, ribbons | 3. 2D layers |
|--|---|-----------------|

0D-nanostructures :

| | |
|------------------------------------|--|
| 4. 0D0 uniform particles arrays | 5. 0D00 heterogeneous particles arrays, "core-shell" dendrimers, onions |
|------------------------------------|--|

1D-nanostructures :

| | | | | |
|--------------------------------------|---------------------------|--|--|---|
| 6. 1D0 molecular chains, polymers | 7. 1D00 heteropolymers | 8. 1D1 bundles, ropes, cables, corals | 9. 1D11 heterochains, heterocables, saws, hair, heterobundles, junctions, combs, bows | 10. 1D10 beads, pea-pods, fullereno-fibers |
|--------------------------------------|---------------------------|--|--|---|

2D-nanostructures :

| | | | | | |
|-----------------------------------|---|---|---|---|---|
| 11. 2D0 fullerene films | 12. 2D1 nanostraw, PhC, fibers films | 13. 2D2 tiling, mosaic, layered films | 14. 2D00 heterofilms of heteroparticles, fullereno-powders | 15. 2D10 films of pods, fullereno-fibers | 16. 2D11 films of fibers and nanotubes, PhC-waveguides |
| 17. 2D20 fullereno-plate films | 18. 2D21 bridges, fiber-layer films | 19. 2D22 hetero-layers, MOS-structures | 20. 2D210 fullerene-fiber-layer films | | |

3D-nanostructures :

| | | | |
|---|--|---|--|
| 21. 3D0 Fullerites, clathrates, powder skeletons, log | 22. 3D1 skeletons of fibers, nanotubes | 23. 3D2 layer skeletons, buildings, honeycombs, foams | 24. 3D00 sols, colloids, smogs, heteroparticles composites |
| 25. 3D10 skeletons of fibers-powders | 26. 3D11 skeletons of heterofibers, nanotubes | 27. 3D20 intercalates, skeletons of layers and powders | 28. 3D21 Cross-bar-layers, layer-fiber skeletons |
| 29. 3D22 heterolayers | 30. 3D30 opals, dispersions, particles, pores, fullerenes in matrix | 31. 3D31 membranes, PhC, fiber composites, waveguides | 32. 3D32 friction pairs, contacts, interfaces, cavities, grain boundaries |
| 33. 3D210 composites of layers, fibers and particles in matrix | 34. 3D310 membranes + impurities, powder-fiber composites | 35. 3D320 powder-layers composites | 36. 3D321 layers-fibers-composites in matrix, VCSEL |

Notices :

1. Interfaces between building units not regarded as additional 2D-NSs
2. Inverse NSs with cavity building units not regarded as separate ones
3. The classification may be extended with account of fourfold combinations

Figure 2-5: Dimensionality classification of nanostructures ([Pokropivny and Skorokhod 2007](#)).

2.7.1 Zero-Dimensional (0D) Nanostructures

Zero-dimensional (0D) nanostructures have all dimensions in the nanometer range (≤ 100 nm). They are nanostructures, such as atomic clusters, uniform particles arrays (quantum dots), nanodots, heterogeneous particles arrays, core-shell quantum dots, onions, hollow spheres and nanolenses ([Tiwari et al. 2012](#)). The major methods of synthesis are thermodynamic equilibrium and kinetic approach ([Cao and Wang 2004](#)). In the thermodynamic approach, synthesis process consists of (a) generation of supersaturation, (b) nucleation, and (c) subsequent growth. In the kinetic approach, formation of nanoparticles is achieved by either limiting the amount of precursors available for the growth such as used in molecular beam epitaxy, or confining the process in a limited space such as aerosol synthesis or micelle synthesis. When the characteristic dimension of the nanoparticles is sufficiently small and quantum effects are observed, quantum dots are the common term used to describe such nanoparticles ([Cao and Wang 2004](#)).

The evolution of nanostructures from 0D to 3D is depicted in Figure 2-6.

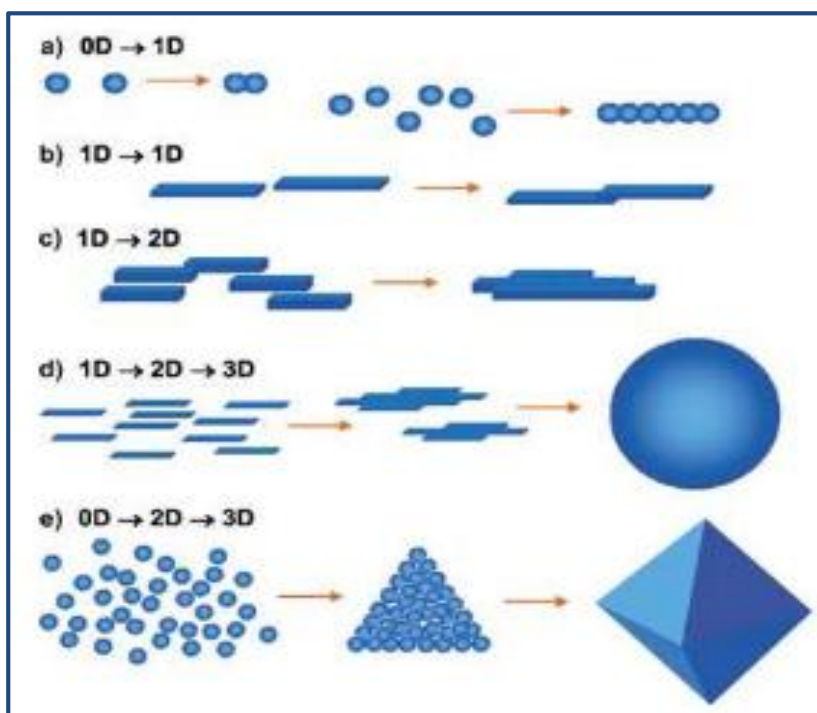


Figure 2-6: Various organising schemes for self-construction of nanostructures by oriented attachment ([Yang and Zeng 2004](#)).

2.7.2 One-Dimensional (1D) Nanostructures

One-dimensional (1D) Nanostructures are systems with the lateral dimension in nanometer scale and one dimension outside the nanometer range. Such systems include nanowires, nanoribbons, nanosheets, nanobelts, nanotubes, nanorods and heterostructures. These materials exhibit very large surface-to-volume ratios, good nanosize, strain induced grain-growth confinement, and simultaneous presence of monoclinic phase, while the oxygen ion vacancies stabilise the tetragonal phase at room temperature in nanocrystalline system ([Kuchibhatla et al. 2007](#)). They possess highly anisotropic morphologies with the smallest dimension structure that can efficiently transport electrical carriers. The different kinds of 1D nanostructures are presented in Figure 2-7.

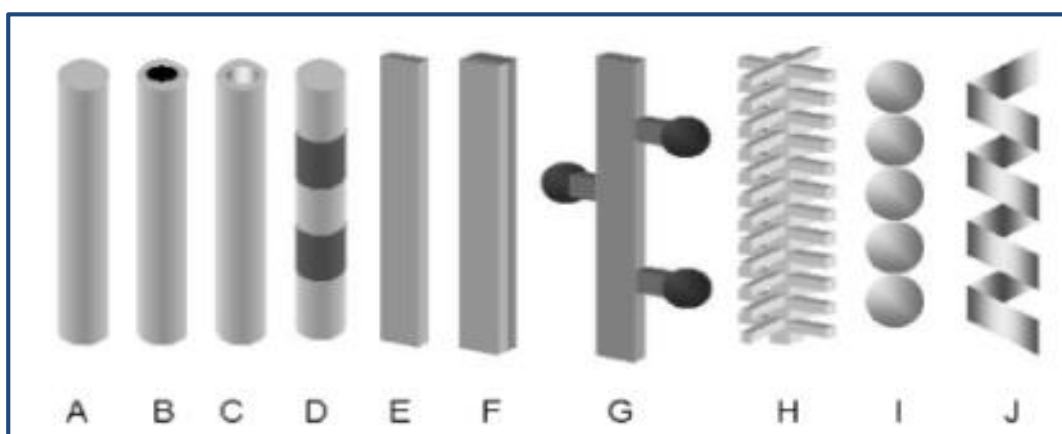


Figure 2-7: A schematic summary of the kinds of quasi-one-dimensional metaloxide nanostructures ([Kolmakov and Moskovits 2004](#)): (A) nanowires and nanorods; (B) core-shell structures with metallic inner core, semiconductor, or metal-oxide; (C) nanotubules/nanopipes and hollow nanorods; (D) heterostructures; (E) nanobelts/nanoribbons; (F) nanotapes, (G) dendrites, (H) hierarchical nanostructures; (I) nanosphere assembly; (J) nanosprings.

One-dimensional nanostructures have been synthesised from materials, such as metals, Group II–VI and Group III–V semiconductors, sulphides, nitrides, etc., using a variety of synthetic techniques, such as solution process, vapour–solid process, vapour–liquid–solid process, and template directed process ([Shen and Chen 2009](#)). [Yang and Kim \(2002\)](#) applied the Langmuir – Blodgett (LB) technique to the assembly of 1D nanostructures such as nanorods and nanowires, and rendered the nanostructures hydrophobic by surfactant surface functionalization before the LB experiments. However, the common

synthetic methods for 1D nanostructures have been classified as follows ([Kuchibhatla et al. 2007](#)):

- a) Anisotropic growth dictated by the crystallographic structure of a solid material.
- b) Anisotropic growth controlled and directed by various templates.
- c) Anisotropic growth kinetically controlled by supersaturation or through the use of an appropriate capping agent, and
- d) Miscellaneous methods with potential to yield controlled 0D nanostructures.

There is comparability of the Debye screening length of nanostructured metal oxides with their lateral dimensions and provision of a long semiconducting channel ([Sun et al. 2012](#)); this improves the efficiency of transducing surface chemical processes into electrical signals.

The mechanical properties of 1D nanostructure are discussed by [Ramírez et al. \(2008\)](#). Nanostructure modulus are essential for making predictions of composite elastic properties as a function of nanostructure morphology, orientation, or volume fraction incorporated into the composite matrix. A comparison of the mechanical properties of SnO₂ and ZnO nanostructured is presented based on varistors⁴ ([Ramírez et al. 2008](#)). They observed that SnO₂ possess superior thermomechanical properties (values of static and dynamic modulus, bending strength and thermal conductivity) than the ZnO-based varistors due to the homogeneous microstructure.

[Pan et al. \(2012\)](#) presented a comprehensive review of the rational synthesis and unique applications of 1D SnO₂ nanostructures and their optical and electrical properties. Applications include nanoscale gas sensor, lithium-ion batteries and optoelectronic devices.

ZnO nanostructures, such as nanowires ([Huang et al. 2001](#)), nanorods ([Zhu et al. 2011](#)), nanosheets ([Wang 2003](#)), nanoplates ([Morin et al. 2011](#)), nanorings ([Kong et al. 2004](#)),

⁴ Varistors are materials whose resistance varies with the applied electric field, resulting in nonohmic I–V characteristics. This property allows their use in the protection of electric and electronic circuits. It is an important application in lightning rod ([Ramírez et al. 2008](#)).

and network of 1D and 2D nanostructures ([Zhang et al. 2004a](#)) were synthesised with metal catalyst or self-catalyst such as Au, Co, Sn and Ni etc. [Wang et al. \(2007\)](#) discussed the mechanical, electrical and optical properties, as well as the underlying mechanism for piezoelectric devices and systems made from aligned ZnO nanostructures. They examined the bending modules, elastic deformation, electron transport and plastic limit based on the aligned morphology and their relationship to development of further applications, such as nanogenerator, self-powered nanodevices and nanosystems for in situ, real-time and implantable biosensing and biodetection, self-powering for defence and commercial applications, and remote sensing.

One-dimensional nanoscale building blocks can be ordered and rationally assembled into appropriate 2D or 3D architectures to offer fundamental scientific opportunities for investigating the influence of size and dimensionality with respect to their collective optical, magnetic, and electronic properties ([Yang and Kim 2002](#)).

2.7.3 Two-Dimensional (2D) Nanostructures

Two-dimensional nanostructures are systems in which two dimensions are outside the nanometer range. The simplest form of a 2D nanostructure is a plane or thin film with a depth less than 100 nm and two other dimensions larger than nanometric dimensions. In spite of its external dimensions, this nanostructure can show interior nanostructural dimensions, for example, nanocrystals (or nanograins) with nanoscale dimension ([Aliofkhazraei and Sabour Rouhaghdam 2010](#)). These nanostructures include multilayer thin film and coatings.

[Deng et al. \(2005\)](#) synthesised ultrabroad and ultralong transparent ZnO nanosheets via a vapour-solid mechanism under PbO atmosphere, forming (001) crystal planes as the narrowest facets of nanosheets. [Comini et al. \(2004\)](#) proposed the use of 2D nanostructures of SnO₂ in the form of nanobelts for NO₂ and ethanol sensing. Their theoretical explanation inferred that the crucial parameter in the sensing mechanism (i.e., the depletion layer depth) is not strongly affected by the dimensionality chosen for the system, in the considered range of dimensions. But at lower sizes, their model foresees a

change in the sensing properties depending on the dimensionality. Compared to the 3D counterpart, the electrical responses and basic requirements of the 2D nanostructure as a chemoresistive sensor is superior ([Comini et al. 2004](#)).

2.7.4 Three-Dimensional (3D) Nanostructures

Three-dimensional nanostructures are bulk systems with three dimensions outside the nanometer range (≥ 100 nm), such as fullerenes, nanotubes, nanoflowers, nanocrystalline and nanocomposite materials. Despite of the reinforcing materials in the nanocomposite materials being in the nanometric scale, the entire nanoarchitecture of the matrix demonstrate dimensions outside the nanometer range. 3D metal oxide nanostructures have higher surface area and supply enough absorption sites for all involved molecules in a small space. Their 3D porosity provides improved transport of the molecules ([Tiwari et al. 2012](#)).

[Matsui \(2010\)](#) reported on the fabrication of 3D nanostructure using the focused ion beam - chemical vapour deposition mechanism. [Ponzoni et al. \(2006\)](#) fabricated 3D hierarchical tungsten oxides (WO_{3-x}) nanowire network for gas sensing, with possibilities to modify into thin and thick film technology for outdoor applications. [Mei et al. \(2012\)](#) prepared 3D aloe-like SnO_2 nanostructures with a large amount of nanosheets by hydrothermal method for ethanol sensing. Their sensor promises to efficiently detect ethanol at ppb level.

ZnO of different 3D nanostructures have been fabricated in form such as graphene hybrid planar reticular morphology with stacking blowballs for field emitters ([Ding et al. 2012](#)), high-density rose-like microspheres along interconnected nanosheets network and large-scale hexagonal microdisks ([Ahsanulhaq et al. 2008](#)), flower-like ([Zhao et al. 2011](#)), and leaf-like platelets dendritic mesostructure ([Li et al. 2007b](#)). Further detail on discussion of materials classified as **mesostructured materials** is presented by [Solovyov \(2013\)](#).

2.8 Properties of SnO₂ and ZnO Devices

Tin dioxide (SnO₂) and zinc oxide (ZnO) are *n*-type semiconductors with excellent physical, electronic, optical, thermal and energetic properties. The *n*-type behaviour is attributed to oxygen deficiency, upon which the donors could be singly or doubly ionised oxygen-deficient. These properties, and their small grain size nanoparticles, very high surface-to-volume ratio and very great surface activities, have increased their versatility and applications in many disciplines such as solid state gas sensors, photonics, catalysis, semiconductors, optical devices, transparent conduction electrodes, low emission windows coatings, microelectronics and rechargeable lithium ion batteries.

2.8.1 Material Properties and Crystalline Structure

Tin and zinc group are IIB-IVB metals, and form transparent conducting oxides (SnO₂ and ZnO). Naturally, SnO₂ occurs as the mineral cassiterite. It is a white, diamagnetic solid amphoteric (i.e., reacts with acid and base) material. It is the most stable compound of tin oxides; another compound is tin (II) oxide (SnO). Others intermediate and less stable tin oxides are Sn₂O₃ ([Giefers et al. 2005](#)) or Sn₃O₄ ([Damaschio et al. 2010](#)). However, there is still no conformity about the correct chemical formula of the intermediate oxide between Sn₂O₃ and Sn₃O₄ ([Giefers et al. 2005](#)). SnO₂ is insoluble in water. It has a melting point of 1630 °C, sublimates at 1800-1900 °C, and exhibits a density of 6.95 gcm⁻³ at 300 K (i.e., 25 °C) ([Delgado 2002](#)). Structurally, it is a polar crystal of rutile structure with space group D_{4h} (tetragonal unit cell P4₂/mnm) ([Kykyneshi et al. 2011](#)). The crystal structure has lattice parameters of $a = 4.737 \text{ \AA}$, and $c = 3.185 \text{ \AA}$ with an axial ratio of 1:0.672 ([Kuchibhatla et al. 2007](#)). The tin and oxygen atoms have an octahedral coordination; i.e., each tin atom is surrounded by six oxygen atoms in an octahedral array, and each oxygen atom is surrounded by three tin atoms in a planar array (Figure 2-8a).

ZnO is an *n*-type semiconductor of the group-II^b element ₃₀Zn and the group-VI element ₈O; with the following electron configuration: the zinc configuration is (1s)²(2s)²(2p)⁶(3s)²(3p)⁶ (3d)¹⁰(4s)²; the oxygen configuration is (1s)²(2s)²(2p)⁴ ([Geurts 2010](#)). It has a wide direct band gap of about 3.37 eV at room temperature. As a zinc

monochalcogenide, it occurs as a crystal; the most stable form is as hexagonal wurtzite. It is a coarse white odourless solid with polar surfaces. The structure of ZnO can be described as a number of alternating planes composed of tetrahedrally coordinated O^{2-} and Zn^{2+} ions, stacked alternately along the c -axis (Wang 2004). As the lattice parameters (C6mc space group), this result in a hexagonal structure of ZnO, with $a = 0.3296$ and $c = 0.52065$ nm (Kuchibhatla et al. 2007). Figure 2-8b shows the hexagonal wurtzite structure of ZnO. The O and Zn atoms are shown as large grey and small black spheres, respectively.

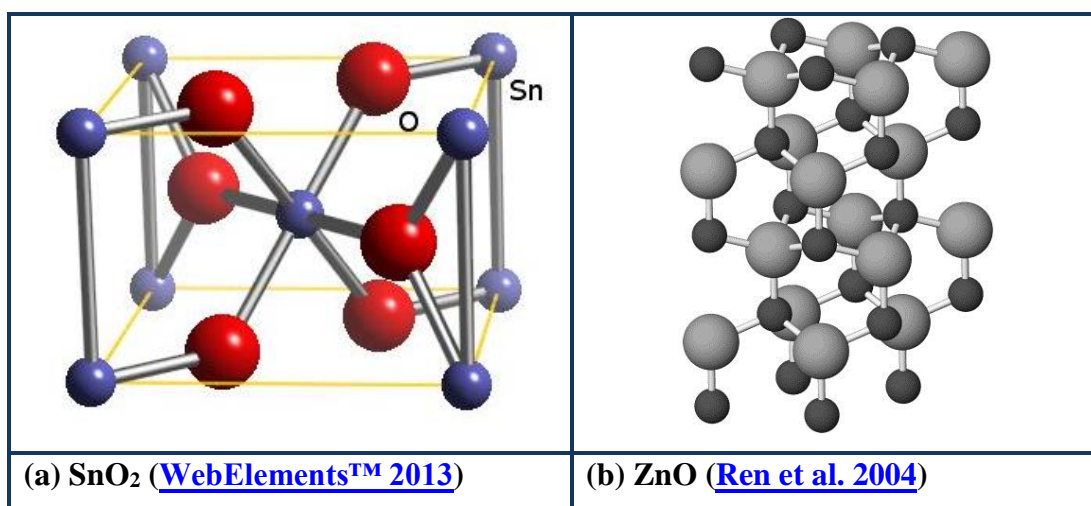


Figure 2-8: Crystalline structure of SnO₂ and ZnO.

Ellmer (2011) summarised some structural properties of ZnO in Table 2-1.

Table 2-1: Structural data of zinc oxide (Ellmer 2011)

| | |
|-----------------------------|--|
| Lattice (normal conditions) | Hexagonal, wurtzite (B4-type, P6 ₃ mc) |
| Lattice constants | $a = 0.32498$ nm, $c = 0.52066$ nm, $c/a = 1.6021$, $u = 0.3832$ |
| Density | 5.67 g cm ⁻³ , 4.2×10^{22} ZnO molecules/cm ³ |
| Hardness | 4.5 (Mohs), 5 GPa |
| Bulk modulus | 142.4 GPa |
| Lattice (high pressure) | Cubic, NaCl (B1-type, Fm ³ m) |

Its crystal lattice involves a sp^3 hybridisation of the electron states, leading to four equivalent orbitals, directed in tetrahedral geometry. The tetrahedral coordination in ZnO structure results in non-centrosymmetry; thus, the hexagonal structure have no inversion

symmetry (i.e., the structure cannot transform into itself at any coordinate), and consequently exhibit piezoelectricity and pyroelectricity properties. In the resulting semiconducting crystal, the bonding sp^3 states constitute the valence band, while the conduction band originates from its antibonding counterpart ([Geurts 2010](#)). ZnO decomposes at 1975 °C, and has solubility in water of 0.16 mg/100ml at 30 °C.

2.8.2 Mechanical Properties

Mechanical properties, one of the most highly structure-dependent properties of MOX, are of primary importance in their applications as sensor. The most studied mechanical properties are Young's modulus, strength, elastic properties, hardness, adhesion, etc ([Zabels et al. 2010](#)). These parameters play a major part in the mechanical characterisation of performance, stress, reliability, stability of sensor working devices, and might provide useful information about their predictable durability and appropriate working environments.

Generally, mechanical properties are determined using nanoindentation (i.e., depth sensing indentation) ([Martyniuk 2006](#)). The hardness and Young's modulus as a function of displacement of the indenter can be calculated from the measured load–displacement data ([Zabels et al. 2010](#)). Values of hardness and Young's modulus, from nanoindentation were observed to change progressively from values characteristics of thin film at shallow indents to values characteristic of the substrate at increasing depth ([Martyniuk 2006](#)).

2.8.3 Electronic Properties and Band Structures

Electronic properties of metal oxides are characterised by tunneling currents, purely ballistic transport, the coulomb blockade effects, the energy band model ([Kuchibhatla et al. 2007](#)). The band structure of semiconductor determines the relationship between the energy and the momentum of the carrier. Using the energy band model, metal oxide semiconductors can be characterised by the gap (i.e., the **band gap**) that separates or overlaps the conduction and valance bands. [Gründler \(2007\)](#) presented the entire spectrum of the electronic band structure from conductors (e.g., metals), semiconductors to non-conductors (e.g., free atoms) as shown in electronic band structure (Figure 2-9).

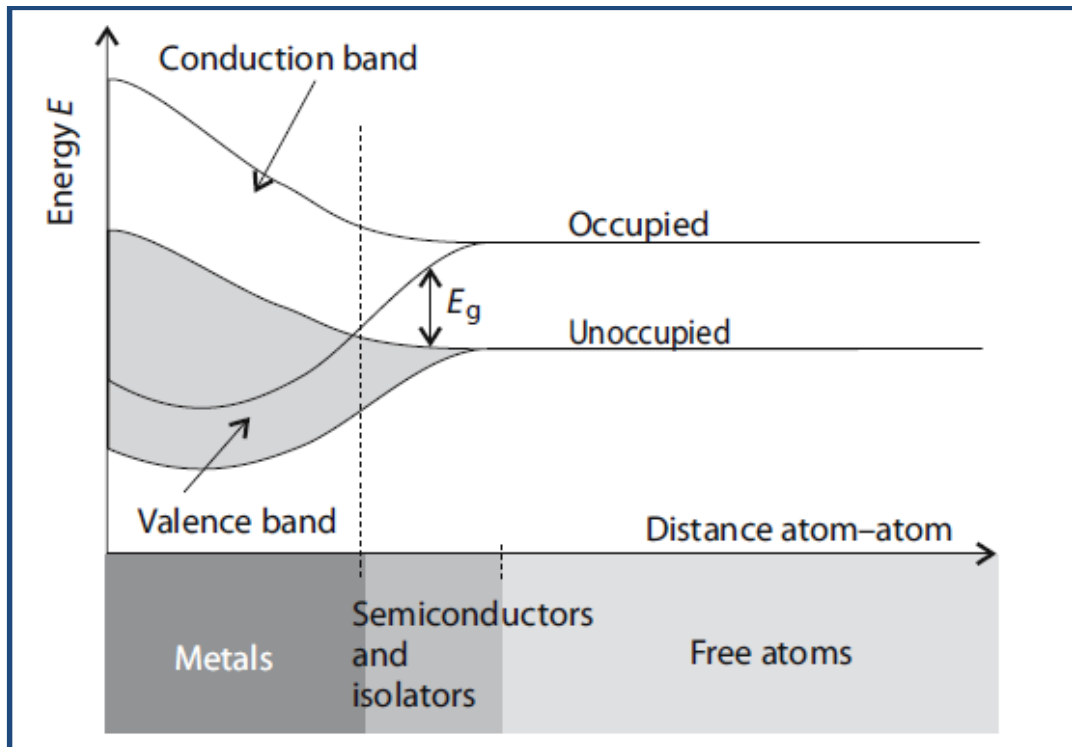


Figure 2-9: Origin of energy bands by combination of atomic orbitals ([Gründler 2007](#)).

The **valence band** is the highest range of electron energies in which electrons are normally present at absolute zero temperature. It is the filled states (with lower energy), and the energy at the top of the valence band is usually zero energy and is called **valence band edge**. The **conduction band** is the range of electron energies enough to release an electron from binding with its atom to move freely within the atomic lattice of the material as a 'delocalised electron'. It is the empty states (with higher energy) above the gap. The lowest point in the conduction band is called the **conduction band edge**. The **band gap**, defined as the energy difference between the valence and conduction bands, represents the energy required to transfer electrons from the valence band to the conduction band. The amount of energy, E_g , results from the energy difference between the lower edge of the conduction band, E_C , and the upper edge of the valence band, E_V , i.e., $E_g = E_C - E_V$.

The band structure over the entire Brillouin zone can be extrapolated from the zone centre energy gaps and optical matrix elements using the wave factor - electron momentum operator (k,p) method ([Yu and Cardona 2005](#)). It can also be used to obtain analytic

expressions for band dispersion and effective masses around high-symmetry points. Details of calculating the band dispersion by the $k\cdot p$ method is presented by [Yu and Cardona \(2005\)](#) and [Kassier \(2006\)](#).

The valence band of SnO₂ is mainly composed of O_{2p} orbitals and the conduction band consists of Sn_{5s} and Sn_{5p} orbitals. The bottom of the conduction band is more than 90% s type while the bottom of the conduction band and the top of the valence band are located at the Γ point $k = 0$ ([Tsuda et al. 2000](#)). Thus, the SnO₂ is a direct gap semiconductor in which the electrons can be excited to the conduction band without the help of photons to conserve the crystal momentum. The intrinsic energy gap, E_g , is as large as 3.6 eV and the stoichiometric SnO₂ is an insulator; therefore the high conductivity is due to deviation from stoichiometry.

Both SnO₂ and ZnO are direct gap semiconductors; i.e., valence band maximum and conduction band minimum occur at the same position in k -space, usually the so-called Γ point where $k = 0$. SnO₂ has a relatively large direct band gap of 3.6 eV at 300 K, and higher theoretical anode capacities of approximately, 790 mA h/g ([Kuchibhatla et al. 2007](#)). Their band structure predicts a direct optical band-gap at the Γ point, where the conduction band minimum (CBM) and the valence band maximum (VBM) occur. The conduction band has its minimum at the Γ point in the Brillouin zone and is a 90% tin s -like state ([Reichel 2005](#); [Schmid 2004](#)). The valence band consists of a set of three bands (2^+ , 3^+ and 5^+), with Γ_3^+ state as its maximum valence band.

[Falabretti and Robertson \(2007\)](#) studied the band structure and density of states (DOS) of SnO₂ by first principle calculations using the generalised gradient approximation (GGA) and Perdew-Burke-Ernzerhof (PBE) ultrasoft pseudopotentials (see Figure 2-10).

However, from the local-density approximation within the density functional theoretical framework, there is a low estimated 1.08 eV optical band-gap than the commonly observed experimental value near 3.9 eV ([Kykyneshi et al. 2011](#)).

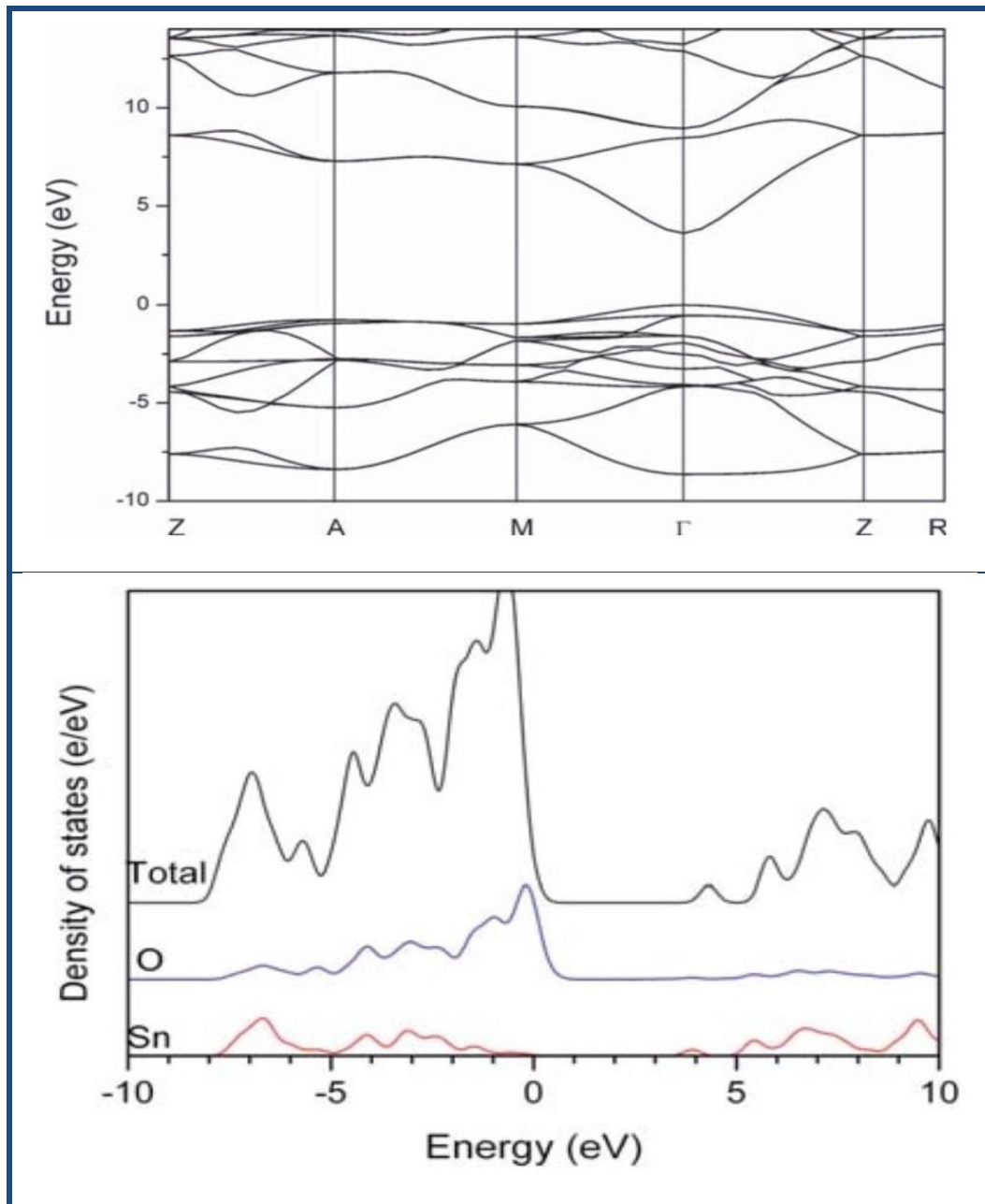


Figure 2-10: The electronic band structure of SnO₂ calculated using the GGA-PBE approximation (Falabretti and Robertson 2007).

There is a high dispersion of the density of states near the CBM; as an indication of a low conduction electron effective mass or a high electron mobility. [Kykyneshi et al. \(2011\)](#) reported calculated electron effective masses of 0.26 and 0.20 m_0 along the Γ - X and Γ - Z crystallographic directions, attributed to the anisotropy in the tetragonal crystal structure. The valence band of SnO₂ is composed mainly of O 2p states and some Sn 5d, indicating the ionic character of this oxide. Consequently, the dispersion of the density of

states near the VBM is low, and the hole effective mass in p -type SnO₂ is much higher than that of electrons, suggesting a hole effective mass of $\sim 1.0 m_0$ ([Kykyneshi et al. 2011](#)).

The NL-EPM band structure of wurtzite ZnO (Figure 2-11) is presented by [Bertazzi et al. \(2007\)](#). ZnO has direct band gap semiconductor (3.37 eV) and large excitation binding energy (60 meV). It has electron effective mass of $0.24m_0$, and the hole effective mass of $0.59m_0$, and its corresponding electron Hall mobility, μ , at 300K for low n -type conductivity is $200 \text{ cm}^2 \text{ V}^{-1} \text{ s}^{-1}$, and for low p -type conductivity is $5\text{--}50 \text{ cm}^2 \text{ V}^{-1} \text{ s}^{-1}$ ([Coleman and Jagadish 2006](#)).

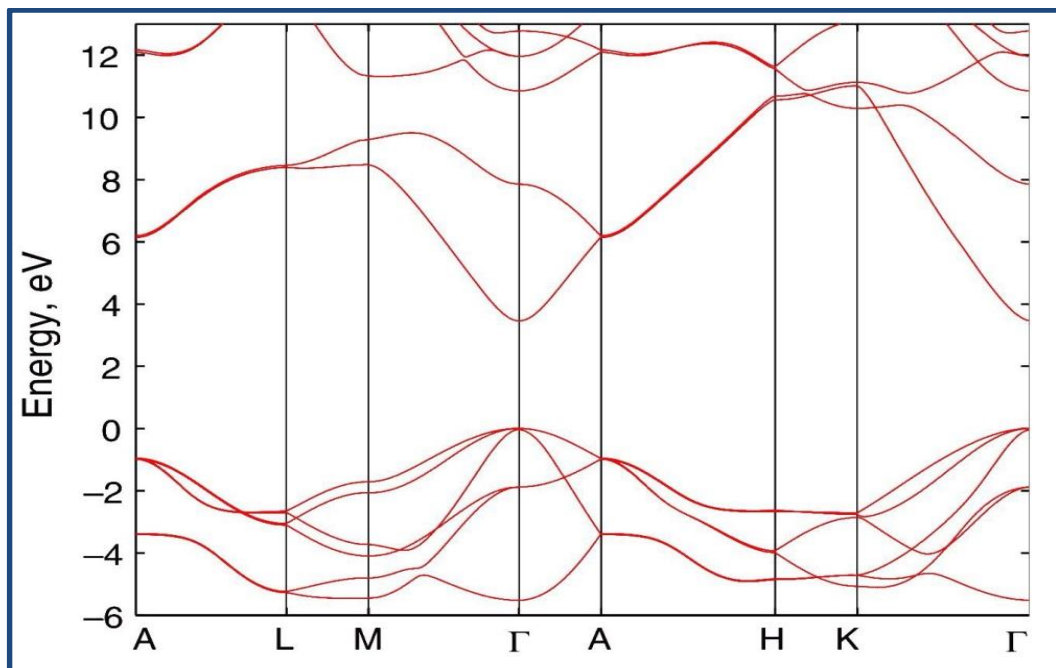


Figure 2-11: NL-EPM band structure of wurtzite ZnO ([Bertazzi et al. 2007](#)).

It has valence band maximum and conduction band minimum occurring at the Γ point. The conduction band is s -like from Zn at Γ and is spin-degenerate. The top three valence bands are p -like in character, and they are split by the spin-orbit interaction in both the zinc blende and wurtzite symmetry, while wurtzite symmetry also has a crystal field splitting ([Litton et al. 2011](#)). Karachanov and co-workers ([2006a](#); [2006b](#)) presented the electronic band dispersion and density of state for wurtzite-type and zinc blende-type ZnO

with the Fermi level set at zero energy, and calculated from LDA and LDA+ U, respectively.

[Goano et al. \(2007\)](#) applied the nonlocal empirical pseudopotential method (NL-EPM) in band structure calculation for detailed understanding of ZnO transport properties and breakdown characteristics for both electrons and holes, and effective design and optimisation of wurtzite ZnO-based devices ZnO (Figure 2-12).

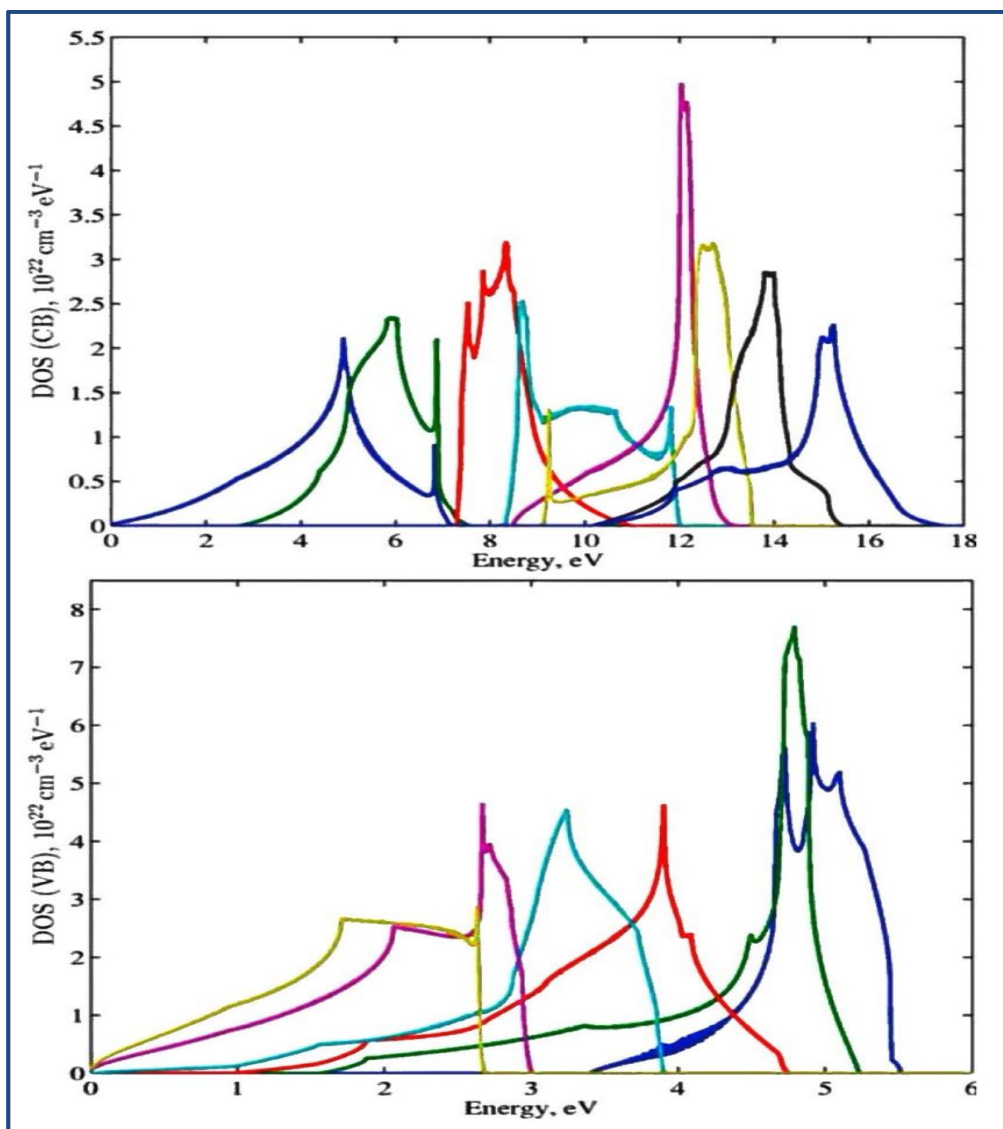


Figure 2-12: Density of states of the first eight conduction bands (top) and of the first six valence bands (bottom) of wurtzite ZnO corresponding to the proposed NL-EPM band structure ([Goano et al. 2007](#)).

They observed that their band structure closely matches the essential details of the valence and conduction bands in the entire first Brillouin zone (BZ), derived from experiments and earlier DFT computations.

Total density of states figures indicates the dominance of the lower part of the valence band by the O-2s orbital and the dominance of the upper part by the O-2p orbital in ZnO, and the dominance of the lower part of the conduction band by the Zn-2s orbital ([Mohammadi et al. 2011](#)). Comparing with a modified approach, [Mohammadi et al. \(2011\)](#) calculated the total densities of states and band structure using LDA, GGA and Engel-Vosko (EV)-GGA schemes for rocksalt, zinc-blende and wurtzite phases of ZnO to denote the nature of the bond character. They observed a large difference of the electronegativity between Zn and O that causes charge transfer from Zn to O atoms. The calculated electron density showed that charge density lines are almost spherical in rocksalt structure; a sign of existence ionic bond between Zn and O atoms. In zincblende and wurtzite structures Zn and O atoms shared electron more than rocksalt structure that causes the strong covalent interaction of the Zn-O bonds in ZnO ([Mohammadi et al. 2011](#)).

2.8.4 Work Function, Surface Coverage and Ionisation Potential

Work function ϕ is the minimum thermodynamic work or energy (in electron volts) required to transfer an electron at the chemical potential from the crystal into the vacuum immediately outside the solid surface; i.e., energy required to move an electron from the Fermi level into vacuum. There are no states at the chemical potential in pure semiconductors and in insulators ([Zumbühl 2007](#)). The work function is a characteristic property for any solid face of a substance with a conduction band (whether empty or partly filled) affected by two independent quantities: (i) the Fermi level position with respect to the band edges, and (ii) the surface dipole. Thus, the work function is defined as the energy difference between the Fermi energy E_F and the vacuum level energy E_{vac} (i.e., $\phi = E_{vac} - E_F$).

The **surface coverage**, θ , with adatoms is described as weakly dependence of the ratio of surface (i.e., adsorption-induced change in) conductivity, ΔG , to the adsorption-induced change in the work function, $\Delta\phi$ ([An'chkov et al. 2007](#)). Analysis of the dependence of $\Delta\phi$ and ΔG on the adsorption coverage has been described by Schrieffer model ([An'chkov et al. 2007](#)) and Anderson–Newns model ([An'chkov et al. 2008](#)).

The SnO₂ surfaces exhibit work functions between 4.4 and 5.7 eV, while work function of ZnO varies between 3.5 and 5.2 eV ([Klein et al. 2009](#)). The ionisation potential and work function of ZnO are strongly affected by surface orientation; while SnO₂-based materials show pronounced changes of ionisation potential and work function induced by surface oxidation. Further details of work function and surface coverage in MOX semiconductors are discussed in Chapter 3 (see Section 3.5.1).

The **ionisation potential**, I_P , (and electron affinity, χ_e) is the energy difference from the bottom of the valence band (and conduction band) to the vacuum energy level, respectively. The ionisation potential is given as $I_P = E_{vac} - E_{VB}$, and equivalently, the electron affinity is given as $\chi_e = E_{vac} - E_{CB}$. The ionisation potential is related to the electron affinity as $\chi_e = I_P - E_g$. The surface potential is given as $I_S = E_F - E_{VB}$. The ionisation potential and electron affinity are modified by surface dipoles depending on the details of the surface termination ([Klein 2013](#)). The ionisation potential of ZnO varies between 6.9 and 7.7 eV ([Klein 2013](#)), while SnO₂ films exhibit ionisation potentials of 7.54–8.11 eV ([Rachut et al. 2014](#)). Both the electron affinity and the work function are dependent on the bulk crystal/material properties of the metal oxide.

2.8.5 Bulk Properties

Bulk, surface and interface properties play vital roles in the applications of metal oxide semiconductors. The bulk properties of materials (density, modulus, yield strength, thermal and electrical conductivity, internal volumes, surface areas, diffusion, viscosity) are intrinsic; a small piece of the material has the same values for these properties as a large one ([Ashby et al. 2009](#)). It is a basic assumption of continuum mechanics that materials behave in this way; i.e., their mechanical properties are scale-independent. It

has been a useful, and for the most part, adequately accurate assumption, greatly simplifying the analysis of structures.

For nanoparticles, bulk properties are a function of physical, mechanical and chemical properties of the material, the geometry, size and surface characteristics of the individual particles, as well as the process history of the system as a whole. The understanding of thin film properties naturally relies on our understanding of bulk properties of materials ([Sree Harsha 2006](#)). In principle, all the bulk properties of metal oxide could be determined by the number and type of atoms they contain and by the manner of their arrangement with respect to each other. It impacts significantly on nanostructure defects. In addition to the usual defects that are found in bulk specimens (point defects, dislocations, stacking faults, grain and twin boundaries, impurity atoms), thin films can also have voids because of the discontinuous structure of many deposited films ([Sree Harsha 2006](#)).

Electronic signal transduction can often be attributed to bulk properties ([Raymo 2010](#)). The bulk conductivity, σ_{tot} , of a semiconductor crystal can be described as the sum of electronic (electron conductivity, σ_e , and proton conductivity, σ_p) and ionic conductivity, σ_{ion} , if the conduction processes are considered independent ([Schmid 2004](#)). For SnO₂ and ZnO gas sensors, optimal operation is between 200 and 400 °C; thus, the ionic contribution can be neglected, giving bulk conductivity as below:

$$\sigma = \sigma_e + \sigma_p + \sum \sigma_{ion,i} \approx \sigma_e + \sigma_p \quad (2.6)$$

However, the unintentional conductivity for ZnO and SnO₂ is not due to oxygen vacancies or cation interstitials, but rather to the incorporation of donor impurities, with hydrogen being a likely candidate ([Janotti et al. 2012](#)). The most successful explanation of the bulk properties of solids due to the mutual interaction of atoms with one another is in terms of the energy band theory of solids.

[Körber et al. \(2009\)](#) correlated the electronic surface and bulk properties of sputter deposited polycrystalline intrinsic and Sb-doped SnO₂ thin films using a combination of *in situ* photoelectron spectroscopy, electrical four-point conductivity, and optical

transmission measurements. Surface potentials such as work function and ionisation potential can be directly determined with the PES technique. However, in contrast to the highly surface sensitive PES, electrical and optical measurements provide information about the electronic bulk properties of materials. [Körber et al. \(2009\)](#) combined surface sensitive photoelectron spectroscopy (PES) with bulk sensitive electrical and optical measurements in order to determine surface potentials and reveal the defect structure (doping mechanism) of sputter deposited polycrystalline SnO₂ and SnO₂:Sb thin films, depending on the deposition conditions. They showed that the Fermi level position and surface dipole, i.e., work function and ionisation potential, of SnO₂ and SnO₂:Sb can be systematically controlled by changing the oxygen content in the sputter atmosphere. They suggested that different defect mechanisms for undoped and Sb-doped SnO₂ are attributed to bulk sensitive electrical conductivity and optical transmission measurements, and observed a depletion layer at the surface of oxidised SnO₂:Sb in contrast to flat band conditions in the case of undoped SnO₂ and reduced SnO₂:Sb.

[Erhart et al. \(2006\)](#) derived a model analytic bond-order potential to describe the bulk properties for ZnO to include cohesive energies, lattice parameters, and elastic constants, and compared it with the density functional theory (DFT). Their model described ZnO as a predominantly covalently bonded system. They complemented the Zn-O parameterisation by parameter sets for the elemental phases of zinc and oxygen. Their zinc potential yielded a good description of the coordination dependence of the bond lengths and cohesive energies although the elastic constant is not entirely satisfactorily described. The oxygen potential is capable of describing oxygen molecules as well as several hypothetical bulk phases. Thus, their potential is applicable in simulations which require a thermodynamic model for the entire Zn-O system, particularly for simulations of ZnO under oxygen or zinc-rich conditions.

2.8.6 Surface Properties

Gas sensitivity is strongly related to surface reactions; the sensitivity of the metal oxide based materials, will change with the factors influencing the surface reactions, such as chemical components, surface-modification and microstructures of sensing layers,

temperature and humidity ([Wang et al. 2010](#)). Nanostructures usually have very high surface reactivities; thus, the system strives to lower the surface energy by changing the geometric environment to a bulk environment for each surface atom (e.g., by undergoing surface reconstructions, chemisorption of gas-phase species, etc.) ([Korotcenkov 2012](#)). The substantial change in conductivity occurs on the film surface when a small concentration of detecting gas is present in a large presence of oxygen.

This phenomenon cannot be explained by the mechanism of bulk conductivity change however, because the partial pressure of oxygen could not be changed in this circumstance. The assumption is that surface processes, which are not in equilibrium with the bulk, control the conductance of the material ([Min 2003](#)). The influence of adsorbed molecules (atoms) of gases on the surface properties of semiconductor substrates is of very special importance. The effect of surface properties on other functions, such as bandgap of semiconducting materials, work function, transport mechanism and conductivity could be explained by the chemical processes on the thin film. Further details of surface interaction of SnO₂ and ZnO in chemical processes as it relate with surface chemistry, adsorption mechanism and work function are discussed in Chapter 3. The schematic band diagram of SnO₂ bulk is shown in Figure 2-13.

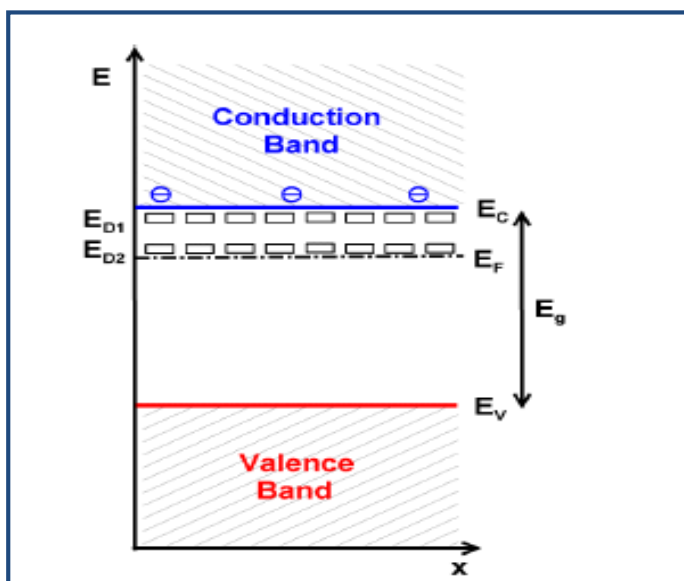


Figure 2-13: Schematic band diagram of SnO₂ bulk. Two vacancy donor level E_{D1} and E_{D2} are located 0.03 and 0.15 eV below the conduction band (E_c = 0eV). The bandgap (E_g) is 3.6 eV ([Schmid et al. 2004](#)).

2.8.7 Transport Properties

A good understanding of carrier transport is essential for the fabrication and characterisation of semiconductors. In nanostructured semiconductors, electron transport shows key differences with respect to their bulk counterparts, as narrowly linked to the presence of disorder in the material. [Anta \(2012\)](#) attributed the main consequence of disorder (i.e., structural inhomogeneity) in the electronic structure of the material to the appearance of localised states. The fact is that the breaking of the crystalline symmetry brings forward the appearance of defects in the lattice, either at grain boundaries or at interfaces, where dangling bonds and interactions with chemical species present in an embedding electrolyte or another semiconductor are produced. Defects in a lattice imply localised states for electrons and holes. The classical picture of band theory with a conduction band and a valence band should then be reformulated in a disordered semiconductor. Localised states can act as “traps” for electrons and holes that influence transport, and/or recombination centres that reduce the efficient collection of charges. Defect states can also act as dopants, with either a donor or an acceptor character, and convert an intrinsic semiconductor in an n -type or a p -type semiconductor ([Anta 2012](#)).

Thus, the critical dependence of electronic transport on structural inhomogeneities is characterised by the geometrical shapes, spatial arrangement and relative amount of microstructural components such as grains, grain boundaries, pores, second phase particles and various interfacial boundaries ([Wang et al. 2000](#)). Also, the interior of the grains contribute to the electrical transport in the nanostructure, because the space-charge region occupies the entire grain, and the potential barrier at the interface between adjacent grains is rather low ([Rickerby and Serventi 2010](#)).

Transport, or motion of charge carriers in a material, is described by Boltzmann’s transport equation, which relates changes in the carrier distribution (occupied energy states) to forces that drive the carriers to a non-equilibrium state ([Young et al. 1999](#)). The Boltzmann transport equation can be solved to give analytical solutions to the resistivity, Hall, Seebeck, and Nernst coefficients. These solutions may be solved

simultaneously to give the density-of-states (DOS) effective mass (md^*), the Fermi energy relative to the conduction or valence band, and a scattering parameter that is related to a relaxation time and the Fermi energy. The Nernst coefficient is essential for determining the scattering parameter and, thereby, the effective scattering mechanism(s). Details of scattering mechanisms are presented ([Bhargavi and Kubakaddi 2013](#); [Zhang and Ma 1996](#)).

For n -type materials, [Young et al. \(1999\)](#) described the carriers (electrons) in a degenerate material in equilibrium by the Fermi-Dirac distribution function $f_0(\vec{k}, \vec{r})$. When external driving forces from temperature gradients or electric and magnetic fields are imposed on a material, the carriers are driven to higher energy (excited) states. The redistribution of occupied energy levels from the equilibrium configuration may be described by a non-equilibrium distribution function $f(\vec{k}, \vec{r})$. After collision, carriers in excited states will return to their equilibrium distribution, scattering events between other charge carriers or imperfections in the material ([Young et al. 1999](#)).

Electron transport in vacuum and testing gas, could be designed and prepared using two kinds testing structures: field emission property and gas sensitivity properties for the vacuum and testing gas, respectively ([Liu et al. 2012](#)). In order to analyse the field emission property, when the surface electric field of the composite is higher than threshold, the electrons overflow from the composite surface to vacuum cavity and get to the anode to build the emission current. When the size of metal oxide nanostructure is comparable to the space-charge layer (L_d), the electron transport properties of the nanoparticles can be strongly modulated by absorption and desorption phenomena, and in this case they will exhibit very high gas sensitivity to ambient gases ([Chen et al. 2006a](#)). For the gas sensing property to be understood, the current difference is measured in resistance of the composite before and after adsorbing gas. Thus, transport of charge in metal oxide nanostructure is limited by trapping-detraping processes in which both energy and morphological disorder play a role ([Anta 2012](#)). While the electron transport is strongly coupled with charge transfer to external electron acceptors (recombination), the coupling determines the collection efficiency of the

device, which is the parameter to optimise for efficient production of energy, either electrical (in a solar cell) or chemical (in a photocatalytic device).

Applying an integrated computational approach, [Wang et al. \(2000\)](#) presented a phenomenological constitutive relation between quantitative microstructural features (such as the average grain size and porosity) and the electrical conductivity using an effective media theory of electrical conduction in porous granular ceramic materials. Using the particle-flow model and the continuum-phase-field⁵ approach ([Kazaryan et al. 1999](#)), they identified variables that characterise the relative contribution of the surface-diffusion, grain-boundary diffusion, and bulk-diffusion mechanisms to the transport. In regard to electrical transport, they observed that grains are good conductors, grain boundaries are poor conductors, and pores are insulators. Effectively, electrical conductivity of the sample is dependent on the volume fractions and spatial arrangement of these structural components, which can be obtained directly from the phase-field modelling.

The *s* and *p* electrons of SnO₂ (and ZnO) propagate with a large mobility ([Tsuda et al. 2000](#)). Electrical transport of SnO₂ occurs via the band conduction and the free carrier concentration changes with oxygen deficiency ([Madelung et al. 1998](#)). [White et al. \(2009\)](#) attributed the *n*-type electrical behaviour of as-grown SnO₂ to unintentionally doped (UID) materials such as oxygen and hydrogen. Generally, thin films with larger grain sizes possess higher electron mobility, depending on thin film growth conditions and doping ([Kykyneshi et al. 2011](#)). Thin films of SnO₂ have additional scattering mechanisms such as line defects and interfaces. A negative surface charge build up near the grain boundary due to electron trapping, and conduction electrons predominantly tunnel through the space-charge region. The grain boundary potential can be reduced by annealing in N₂ gas or vacuum, resulting in the recovery of mobility up to approximately 60 cm²/V s. An increase in the film thickness also helps to obtain

⁵ In the continuum phase field approach, in contrast to the boundary tracking methods, an arbitrarily complex microstructure is described by a set of spatially continuous and time-dependent field variables, such as local density, concentration, and crystallographic orientation or symmetry of the crystal structure ([Kazaryan et al. 1999](#); [Wang et al. 2000](#)).

higher carrier concentration, mobility, and thus conductivity. [White et al. \(2009\)](#) reported electron mobility of $260 \text{ cm}^2 / \text{V s}$ at a carrier concentration of $8 \times 10^{15} \text{ cm}^{-3}$ for early bulk SnO_2 at room temperature, and the transport properties of poly- and single crystalline SnO_2 thin films for a range of UID electron concentrations, mobilities, and resistivities, as $10^{19}\text{--}10^{20} \text{ cm}^{-3}$, $<30 \text{ cm}^2 / \text{V s}$, and $10^{-2}\text{--}10^{-3} \Omega \text{ cm}$, respectively.

The current transport is governed by the intergranular regions, which consist of depletion regions between ZnO grains, constituting electronic barriers for the current transport ([Ellmer 2011](#)). The carrier's transport is due to preferential channel path formed by the direct overlap among the neighbouring n -like metal orbitals; thus, the Zn structure ($3d^{10}4s^2$) gives rise to $\text{Zn}^{2+} + \text{O}^{2-}$ in ZnO films ([Martins et al. 2008](#)).

A surface conducting layer with sheet conductivity on the order of $10^{-4} \Omega^{-1}$, exhibit by ZnO, is created by heating it above 500 K in vacuum or inert gas or by exposure to above band gap UV without heating ([Swartz 2012](#)). This conducting layer is quenched on exposure to oxygen, particularly in the presence of humidity. The adsorbed oxygen atoms act as acceptors, creating a negative surface charge layer of trapped electrons, inducing a depletion region near the surface of a typical n -type crystal and decreasing the conductivity. The size of the depletion region alone is not enough to account for this drop in conductivity, which is measurable even when the thickness of the sample is much greater than that of any depletion region. Rather, some highly conducting surface layer is eliminated or masked by the oxygen ([Swartz 2012](#)).

[Heo et al. \(2004\)](#) measured the current–voltage characteristics of single ZnO nanorods as a function of both temperature and gas ambient. They observed that the conductivity of the nanorods can be increased by a post-growth anneal in hydrogen and these rods show a thermally activated current which is insensitive to measurement ambient. Without the hydrogen annealing treatment, the nanorods are sensitive to the measurement ambient and may be useful in gas sensing applications. For ZnO nanowire, [Weimann et al. \(2008\)](#) observed that the current–voltage characteristics

show a strong rectifying behaviour, indicating Schottky contacts of different barrier heights.

The effect of adsorption on the carrier mobility in the near-surface region of a semiconductor substrate has been investigated within the framework of the Schrieffer model by ([An'chkov et al. 2008](#)). Schrieffer model considers the effect produced by a surface field induced by adatoms on the effective surface mobility of carriers. It associates adsorption with the variation of the work function, $\Delta\phi$, of the adsorption system and the surface conductivity, ΔG , of the semiconductor substrate ([An'chkov et al. 2007](#)).

2.9 Sensor Performance Characteristics

The vital key in the operation of a chemical sensor is the interactions between an analyte molecule and the surface of receptor. The major determinants in the characterisation of nanostructures are morphology, crystal structure, chemistry and electronic structure of the sensing materials. From these determinants, the performance of a chemical sensor is characterised by parameters such as sensitivity, selectivity, stability, detection limit, dynamic range, resolution, response time and recovery time. Generally, an ideal chemical sensor should possess high sensitivity, selectivity and stability, low detection limit, wide dynamic range and fast response time and short recovery time ([Ma et al. 2013b](#)).

2.9.1 Calibration Curve

Sensor signal is obtained in forms of conductance, G , or resistance, R . A calibration curve, $G = f(C)$ and $R = f(C)$, is the relationship between the signal response and the stimulus or concentration of the target gas. This could be related as a log-log plot of (R_a/R_g) or (G_g/G_a) versus C ([Neri et al. 2008](#)).

2.9.2 Base Line

A baseline may be defined as the stabilisation of sensor signals when it achieves equilibrium with its environment ([Ravi 2006](#)). Normally, there may be large

fluctuations of sensor signals before stabilisation at the base line; it is essential that this base line be reached before commencement of tests or measurements.

2.9.3 Response and Sensitivity

Sensor **response** or **sensitivity** is represented in various forms. Sensor sensitivity, S , is defined as the ratio of change of resistance in test gas $\Delta R = R_a - R_g$, to the value of resistance in air R_a where R_g is the sensor resistance in the presence of the test gas:

$$S (\%) = \left(\frac{R_a - R_g}{R_a} \right) \times 100 \quad (2.7)$$

or

$$S = \frac{R_a}{R_g} = \frac{G_g}{G_a} \geq 1 \quad (2.8)$$

Sensitivity of oxidising gas by an n -type semiconductor or sensitivity of a reducing gas by a p -type semiconductor can be represented as:

$$S = \frac{R_g}{R_a} = \frac{G_a}{G_g} \geq 1 \quad (2.9)$$

In this study, sensitivity of a reducing gas by an n -type SnO₂ and ZnO is represented as ([Ahlers et al. 2005](#)):

$$S (\%) = \left(\frac{R_a - R_g}{R_g} \right) \times 100 = \left(\frac{G_g - G_a}{G_g} \right) \times 100 \quad (2.10)$$

(Partial) sensitivity, m , ([Gurlo et al. 2005](#)) is the slope of the analytical calibration curve; i.e., the change in the output signal (e.g., the change in the electrical resistance R (ohm) or the change in the electrical conductance (mho)) for a given change in concentration C (ppm) of the target gas. It is the quantitative ability of the sensor to change with the concentration of the target gas.

For reducing gas, m_{red} , is given as:

$$m_{red}(C) = - \frac{\partial R}{\partial C} = \frac{\partial G}{\partial C} \quad (2.11)$$

For oxidising gas, m_{ox} , is given as:

$$m_{ox}(C) = \frac{\partial R}{\partial C} = -\frac{\partial G}{\partial C} \quad (2.12)$$

(Partial) sensitivity of a reducing gas by an n -type semiconductor can be represented as percentage change in signal per unit gas concentration ([Panchapakesan 2001](#)):

$$S (\%) = \left(\frac{G_g - G_a}{G_a} \right) \times 100 \times \left(\frac{1}{C} \right) \quad (2.13)$$

or

$$S (\%) = \left(\frac{R_a - R_g}{R_g} \right) \times 100 \times \left(\frac{1}{C} \right) = \left(\frac{G_g - G_a}{G_g} \right) \times 100 \times \left(\frac{1}{C} \right) \quad (2.14)$$

The (partial) sensitivity m describes the change in the sensor signal (R or G) due to a specified change in the stimulus (gas concentration). The higher the value of the sensor's sensitivity, the more significant is the change in sensor signal (R or G) initiated by a small change in the gas concentration. Since MOX sensors are nonlinear sensors ([Gurlo et al. 2005](#)), the partial sensitivity varies with the aging of the sensor due to drifts or contamination effects ([Capone et al. 2003](#)).

Analytical sensitivity, γ , is a meaningful way to include the precision in the definition of the sensitivity. It is defined as the ratio of the slope, m , of the calibration curve to the standard deviation, σ_s , of the signals (i.e., resistance or conductance) at that sensitivity or concentration ([Bársan et al. 1999](#)):

$$\gamma = \frac{m}{\sigma_s} \quad (2.15)$$

where the slope of the calibration curve, m , is taken as the best interpolation of the experimental results, at the target gas concentration (or partial pressure) of interest:

$$m = \left(\frac{\partial S}{\partial C} \right)_{X_i} \quad (2.16)$$

Where S is the change induced by the presence of the analyte in the measured parameter or specifically: $S = S_g - S_0$ is represented as $\Delta G = G_g - G_0$ or $\Delta R = R_0 - R_g$, X_i denotes the parameters kept constant during the experiment, such as partial pressures of O_2 and humidity.

The standard deviation, σ_S , of the signals in terms of resistance, σ_R , is given as:

$$\sigma_R = \left(\frac{\partial R}{\partial C}\right)\sigma_C \text{ and } dR = \left(\frac{\partial R}{\partial C}\right)dC$$

The standard deviation of the sensor response represents the uncertainty with which the sensor response can be measured, while σ_C is the standard deviation of the stimulus represents the precision with which the gas concentration can be determined. Therefore, the analytical sensitivity can be written as:

$$\gamma = \frac{1}{\sigma_C} \quad (2.17)$$

2.9.4 Selectivity/Specificity

Selectivity is the ability of a sensor to respond to particular gas in the presence of other gases. Selectivity or cross-sensitivity of a sensor, m_{ij} of a sensor compares sensor signal or sensitivity to be monitored (S_i or m_i) to the sensor signal or sensitivity of the interfering stimulus (S_j or m_j) ([Gurlo et al. 2005](#)). It is its ability to concurrently discriminate and uniquely detect a specific target gas in the presence of interfering gas(es) ([Franke et al. 2006](#)). It is represented as the ratio of sensitivity of the target gas, S_i to the sensitivity of the competing gas, S_j ([Gurlo et al. 2005](#)):

$$\text{Selectivity, } m_{ij}(C_i, C_j) = \frac{S_i}{S_j} = \frac{m_i}{m_j} \quad (2.18)$$

But, this can be represented in terms of percentage as ([Jain et al. 2007](#)):

$$\% \text{Selectivity, } m_{ij}(C_i, C_j) = \frac{S_j}{S_i} \times 100 = \frac{m_j}{m_i} \times 100 \quad (2.19)$$

2.9.5 Detection Time

The detection time, τ_{det} , is the time taken for the sensor output signal to rise 10% ($\Delta t_{10\%}$) above its initial value after applying the target gas in a step function (Figure 2-14).

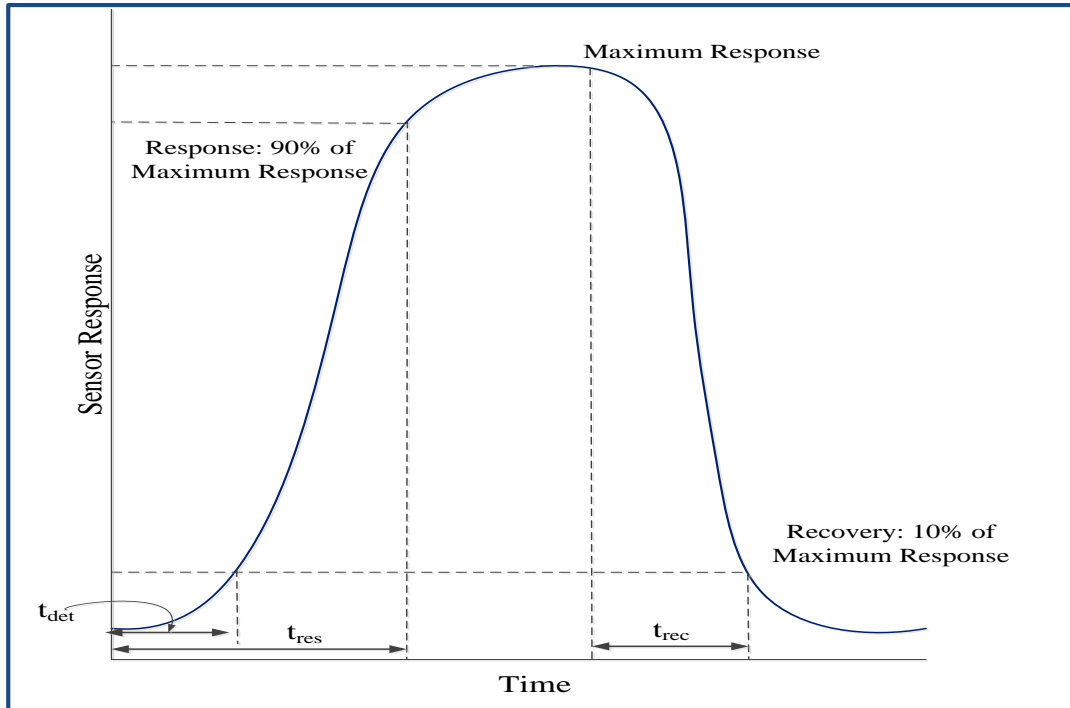


Figure 2-14: Response and recovery time.

2.9.6 Response Time

The response time, τ_{res} , (Figure 2-14) describes the time taken for the sensor output signal to reach 90% ($\Delta t_{90\%}$) of its saturation value after applying the target gas in a step function ([Franke et al. 2006](#); [Liewhiran and Phanichphant 2007](#)).

2.9.7 Recovery or Decay Time

The recovery or decay time, τ_{rec} , (Figure 2-14) is the time taken for the sensor output signal to drop to 90% ($\Delta t_{90\%}$) of its saturation value after switching off the target gas in a step function (i.e., time taken for the sensor response to recover to within 10 % above its initial value).

2.9.8 Reversibility

Reversibility is a key requirement of a successful chemical sensor. Ideally, thermodynamic reversibility is a measure of gas sensor measurand to relate to a thermodynamic state function. That is the ability for a certain sensor response

unequivocally corresponds to a certain analyte concentration at a certain temperature, without memory effects or hysteresis ([Hierlemann and Baltes 2006](#)).

2.9.9 Stability and Long-Term Effect

Stability is the ability of the sensor to maintain its sensitivity and response behaviour over a period of time. Depending on the application, the period could be between hours to years. Stability could be expressed in terms of drift in sensor response (see 2.9.11). The environmental variables and measurement conditions must be comparable for good stability values.

Also, it could be defined as the percentage change in conductance in synthetic air over the given time interval ([Panchapakesan et al. 2001](#)):

$$D = \left| \frac{G(t_1) - G(t_0)}{G(t_0)} \right| \times \frac{1}{t_1 - t_0} \quad (2.20)$$

Sensor stability can be distinguished in terms of active or passive stability. Active stability or reproducibility refers to sensor characteristics during a certain period of time at working conditions, which may include high temperature and the presence of a known analyte ([Bochenkov and Sergeev 2010](#)). Passive stability is connected with retaining the sensitivity and selectivity during a period of time after some normal storage conditions, such as room temperature and ambient humidity.

2.9.10 Reproducibility

Reproducibility is a measure of sensor similarity behaviour. In order to compare the reproducibility of two sensor batches one can either calculate the mean value and the standard deviation of a sensor property for both batches and compare them or calculate the reproducibility Q for each batch. It can be calculated as ([Gurlo et al. 2005](#)):

$$Q_{x'}(C_i) (\%) = \left(\frac{\left(\frac{1}{n} \right) \sum_{k=1}^n R_k \Big|^{C_{ij}}}{R_{max}} \right) \cdot 100 \quad (2.21)$$

where n is the number of characterised sensors, R_k the sensor response of the sensor k . The reproducibility values range from 0 (completely irreproducible sensor) to 100 (perfectly reproducible sensor).

2.9.11 Drift

Sensor drift represents the random temporal variations in the signal behaviour when it is exposed to the same analytes under identical conditions ([Padilla et al. 2010](#)). This effect is attributed to the fluctuations of the environmental variables and measurement conditions, such as gas concentration (C_i), relative humidity and operation temperature of the surrounding atmosphere and measurement time (Δt), system sampling non-specific adsorption, variations on flow rate, thermo-mechanical degradation and poisoning. All of these factors can modify both the baseline and the sensitivity of the sensors, and produce different responses and alters over time for the same target gas concentration, resulting in poor sensor repeatability, especially during the commencement and concluding phases of the experiment.

Mathematically, drift is represented as ([Gurlo et al. 2005](#)):

$$D(C_i, \Delta t) = \frac{\partial R}{\partial t} \Big|_{\Delta t}^{C_i} \quad (2.22)$$

In terms of percentage, it can be represented as:

$$\zeta(C_i, \Delta t) (\%) = \left(\frac{\left(\frac{1}{n} \right) \sum_{i=1}^n R_i}{R_{max}} \Big|_{\Delta t}^{C_i} \right) \cdot 100 \quad (2.23)$$

where n is the number of measurements, R_{max} the maximum sensor response value of the determined sensor response values R_i . To be able to compare drift values of different sensors, the environmental variables and measurement conditions must be comparable.

Drifts compensation methods are presented by ([Hosseini-Babaei and Ghafarinia 2010](#); [Romain and Nicolas 2010](#)). An application of signal pre-processing (response variable

including the base line signal), univariate sensor correction and multivariate array correction towards drift compensation is proposed by [Romain and Nicolas \(2010\)](#) .

2.9.12 Detection Limit

The detection limit (DL) is defined as the minimum detectable gas concentration, C_{min} . That is ([Gurlo et al. 2005](#)),

$$DL = C_{min} = f^{-1}(R_{min}), R_{min} = \bar{R}_0 + 3\sigma_0 \quad (2.24)$$

where $f^{-1}(R)$ is the inverse function of the calibration function, $f(c)$. The minimum sensor response R_{min} which is certainly detected is usually chosen as three times the standard deviation of the zero response σ_0 ; which is considered to be the noise of the measurement. Values above the DL indicate the presence of the target gas; values below the DL indicate absence of the target gas. The determination limit is a qualitative parameter; i.e., it is the signal value attributed to a specific target analyte. The limit of determination is always higher than the detection limit.

2.10 Parameters for Characterisation of Sensor Behaviour

2.10.1 Reception Function

The overall conduction in a sensor element is determined by the surface reactions, the resulting charge transfer processes with the underlying semiconducting material, and the transport mechanism within the sensing layer. The metal oxide active sensing element of semiconductor nanostructures possesses receptor and transducer functions. The sensor response is a convolution of the receptor and transducer functions ([Kim et al. 2013](#)). Ideally, the receptor function is associated with the recognition of specific interaction of the semiconductor surface with the target gas (analyte) via gas adsorption and surface reactions (see Figure 2-15a). For example, the interaction of SnO_2 with oxygen (in the air) results in a decrease in the work function. Details of reception function as it relates to the surface chemistry are described in Section 3.1 (see Chapter 3: Section 3.2, 3.3 and 3.6).

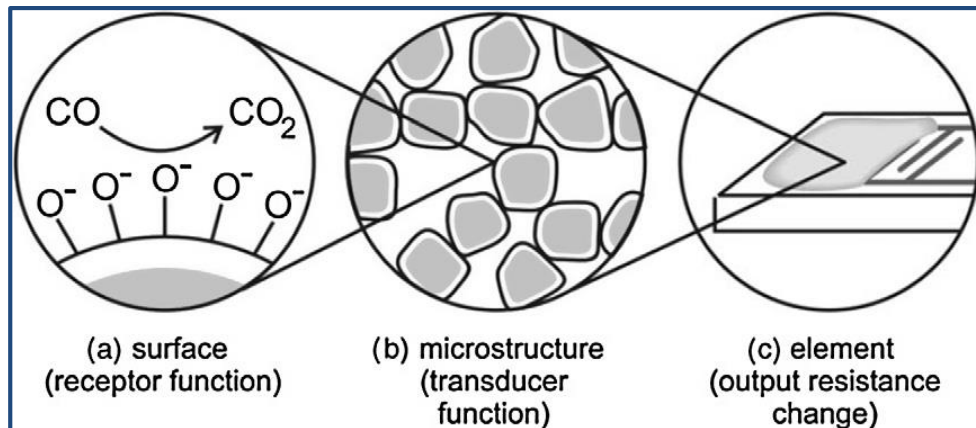


Figure 2-15: Receptor and transducer functions of semiconductor metal oxide gas sensors (Kim et al. 2013): (a) reception function by chemisorption and reaction between reducing gases (CO) and oxygen adions (O⁻) at the surface; (b) transducer function by electronic charge transport through the grains and across grain boundaries; and (c) the sensor element comprises of the sensing layer, electrodes for electrical measurements, substrate and integrated microheater.

2.10.2 Transducer Function

The transducer function refers to an effective transformation of the gas recognition into a gas concentration dependent signal output, i.e., the transformation of biochemical energy to electrical signals (i.e., conductance or resistance) (see Figure 2-15b). Transducer function depends on the band structure of the semiconducting oxide and the microstructure of the coagulating nanoparticles e.g. on the grain size and pore size. Depending on the morphology of the sensing layer, the sensing can take place at different sites of the nanostructure and play different roles in triggering characteristic changes in sensor properties (Barsan and Weimar 2001; Gurlo et al. 2005).

2.10.3 Geometrical Aspect

The complexity of electronic conductivity can be affected by electronic, catalytic and geometric properties of metal oxide polycrystalline semiconductors, such as grain-boundary potential, activated conductivity, field effect at the grain-grain junctions, porosity, overlap between the surface and grain-boundary potentials, two-dimensional geometry, etc. Usually, these features are neglected in the majority of theoretical work dealing with electronic and adsorptive phenomena on semiconductor surfaces

([Geistlinger 1993](#)). The surface geometric interaction with gas molecules can be characterised as: (a) electronic transfer of delocalised conduction-band electrons to localised surface states and vice versa; (b) changing of grain-boundary potentials and/or (c) contact potentials; (d) changing of surface-defect or bulk-defect concentration in the high-temperature region. A simple geometric model of a single, average cubic grain (Petritz model) can adequately accounts for the free carrier and mobility response of the SnO₂ and ZnO films ([Geistlinger 1993](#)).

However, under the same transport phenomena or kinetic reaction, the target gas does not interact with the entire surface of the sensing element. This could be attributed to the competing reaction-diffusion processes on the irregular geometry of the surface. With heterogeneous pore sizes, when the target gas is consumed at the outer sites during detection, if the reaction rate is higher than the diffusion rate, the gas molecules may not reach the inner sites ([Park 2010](#)). Therefore, due to the geometry of the nanostructure surface, gas may only be detected on the outer sites, leaving the inner sites. Depending on the geometric and electronic structure of the thin-film gas sensor, relationships can be derived in a consistent manner between the catalytic surface properties and the electronic bulk properties ([Geistlinger 1993](#)). Also, the geometrical aspect of the sensing mechanism can explain the spectra of sensor response fluctuations after it is exposed to the target gas ([Smulko et al. 2005](#)). In metal oxide semiconductors, the geometrical aspect can be modelled by the Knudsen diffusion model ([Park 2010](#); [Sakai et al. 2001](#)).

2.10.4 Film thickness

Thin films have been classified as super-thin, thin and thick films with thicknesses of 0.01 µm or less, 0.01-10 µm and 10 µm, respectively ([Abouzar et al. 2009](#)). That is less than 10 nm, 10-10,000 nm and greater than 10,000 nm, respectively.

2.10.5 Grain Size

The grain size and geometry of the sensing matrix depends on the method and temperature of synthesis, and deposition and sintering conditions ([Korotcenkov et al.](#)

[2009](#)). The resulting grain size and morphology have significant influence on the sensitivity of the sensor. As sensitivity is related to the amount of active sites on the surface of materials, the nanoporous structure is expected to provide an enhancement in both active surface area and analyte diffusion throughout the film. Effectively, high gas sensitivity and selectivity for SnO₂-based gas sensors is maintained by optimisation of sensor materials to achieve small grain size and large surface area ([Huang et al. 2006](#)).

Generally, the grain size is related to gas sensor conductivity, G , as stated in the following relation ([Korotcenkov et al. 2009](#)):

$$G \approx \varrho - \Gamma_S L_D \quad (2.25)$$

where ϱ = grain size, Γ_S = integral of surface conductivity. The integral of surface conductivity determines the part of grain scaled in units of Debye length (L_D).

As a rule, the surface in metal oxide is non-conductive due to depletion effect. Γ_S is defined by surface charging and electronic properties of bulk. Usually the determination of Γ_S requires the Poisson equation to estimate the potentials at boundaries.

However, metal oxide conductivity can be described using a modified grain model according to which the conductivity of 3-D networks of grains is controlled by the resistance of intergrain contacts ([Korotcenkov et al. 2009](#)):

$$R \approx \exp\left(\frac{eV_S}{kT}\right) \quad (2.26)$$

where V_S is a height of Schottky barrier at the inter-grain boundary, which is formed due to the oxygen adsorption and the trapping of electrons from the conduction band.

Generally, the framework of the grain model states that if the decrease of the grain size (ϱ) in metal oxides is sufficiently large, it should be accompanied by the growth of sensitivity of sensors, designed on their base. Therefore, an especially strong increase of sensor response is expected at the grain sizes, comparable with Debye length (L_D):

$$L_S = L_D \sqrt{\frac{eV_S}{kT}} \quad (2.27)$$

where the depletion layer, $L_D = \sqrt{\frac{\epsilon kT}{2\pi e^2 N}}$, and

the Schottky barrier (potential), $V_S = \frac{2\pi q^2 N_S^2}{\epsilon N}$

k is the Boltzmann constant, T is absolute temperature, ϵ is the dielectric constant of the material, and N is the concentration of charge carries.

If $\rho < 2L_S$, where L_S is the width of surface space charge region, every grain is fully involved in the space charge layer, and the electron transport is affected by the charge at adsorbed species; thus, allowing maximum sensor response ([Korotcenkov et al. 2009](#)). Further details are presented by [Barsan and Weimar \(2001\)](#), and application to SnO₂ by [Zhang and Liu \(2000\)](#).

The C₂H₅OH sensitivity of SnO₂ gas sensors was observed to decrease with increase in grain size ([Maekawa et al. 2001](#)); the maximum sensitivity decreased with the grain size between 26.2 and 64.6 nm (or sintering between 600 and 1000 °C for 2 h), but increased above 64.6 nm.

2.11 Conclusion

The fundamentals and operating principles of chemical sensors are presented in this chapter, providing the basis for understanding the dynamics of the problem relating the factors affecting sensors and their sensitivity behaviour; these are the primary research questions described in the thesis. The discussion includes classes of sensor, solid state and nanostructured sensors, dimensionalities of nanostructures, properties of metal oxide devices, sensor performance characteristics, parameters and characteristics of sensor behaviour; all of which are consistent components of the chemical sensor system under investigation.

Chapter Three

Sensing Mechanism, Surface Chemistry and Transport Phenomena

3.1 Sensing Mechanism

The overall sensing mechanism of metal oxide semiconductors is based on the surface reactions, the resulting charge transfer processes, and the transport phenomena within the sensing layer. Generally, the sensing mechanism occurs as a reversible process in the following steps: diffusion of target gas to the active sensing surface, adsorption of target gas to the active sensing surface, surface reaction on the metal oxide film, desorption of products from the active sensing surface, diffusion of products away from the active sensing surface. Thus, the sensor response mechanism is influenced by gas-surface adsorption-desorption process, surface diffusion-reaction (gas diffusion above surface, gas diffusion inside sensing film, and/or gas inter-crystallite diffusion), and redox reaction between reacting species on the sensor surface ([Vander Wal et al. 2009](#)); and these processes are better described by surface chemistry. [In the absence of a catalyst that promotes a surface reaction, gas diffusion should be considered to be a primary factor that determines the rate of response ([Xu et al. 2014](#))]. The **surface chemistry** involves the interaction of the reacting gaseous molecules in the air at the surface layer of the metal oxide and the associated charge transfer. This relates to the specific adsorbed oxygen species and the way in which the oxidation of reducing gases (such as alcohols, CO, hydrocarbons) or adsorption of oxidising gases (such as NO₂, O₃) will take place (see Section 3.2). As a consequence of this surface interaction (i.e., adsorption, reaction and desorption process), charge transfer takes place between the adsorbed gas species and the semiconducting sensitive material, and changes the electric potential on metal oxide crystal resulting in a change of the sensor resistance (or conductance).

This **charge transfer** can take place either with the **conduction band** or in a **localised manner**, and is observed by the physical changes in surface conductance (or resistance) depending on factors such as, specific material reactivity, grain size, microstructure, free charge concentration, sensitive layer morphology, geometry, etc. On the energy (conduction) band, the concentration of the free charge carriers will be influenced, and will determine the appearance of a depletion layer at the surface of the semiconductor material, due to the equilibrium between the trapping of electrons in the surface states (associated with the adsorbed species) and their release due to desorption and the reaction with target gas (see Section 3.3). Reducing molecules react with surface-adsorbed oxygen, leaving behind electron(s) and a higher conductivity. Whereas, upon oxidation, via adsorption of oxidising molecules at vacancy sites that accept electrons, electrons are withdrawn and effectively depleted from the conduction band, leading to a reduction of conductivity. While insights into the localised charge transfer is important, it will have no direct impact on the conduction ([Gurlo et al. 2005](#)).

3.2 Surface Chemistry: Adsorption Mechanism

Adsorption is a spontaneous process between the adsorbate (target gas) and the adsorbent (metal oxide semiconductor film surface). Thermodynamically, the change in free energy of the system is negative, because the translational freedom of the adsorbate is reduced when it is adsorbed. Adsorption proceeds from (a) physisorption – weak adsorption associated with dipole interactions and van der Waals forces – to (b) chemisorption – strong bonding, charge transfer between gas particle (adsorbate) and the film surface (adsorbent), since less energy E_a is required to provide the total energy of dissociating the molecule E_d ([Comini et al. 2009b](#)).

Generally, the thermodynamic relationship is given as ([Lyashkov and Tonkoshkur 2013](#)):

$$\Delta G = \Delta H - T\Delta S \quad (3.1)$$

where, all values are specific to adsorption, ΔG is change in Gibbs free energy, ΔH is change in enthalpy, T is temperature, and ΔS is change in entropy. The adsorption of

gases on solids is an exothermic process; thus, enthalpy of adsorption, ΔH_{ads} , must be negative (i.e. $\Delta G = -\Delta H + T\Delta S$). When $\Delta G < 0$, there is adsorption, and at $\Delta G > 0$, desorption occurs. The extent of gas adsorption (under equilibrium conditions), therefore, increases with decreasing temperature (provided ΔH and ΔS do not change considerably). Exceptions may occur, if the adsorbate dissociates and has high translational mobility on the surface ([Puzzovio 2009](#)).

Also, the dependence of sensitivity on entropy can be interpreted, with its static definition ([Lyashkov and Tonkoshkur 2013](#)):

$$S = k \cdot \ln[W(E, N)] \quad (3.2)$$

where k is the Boltzmann constant, $W(E, N)$ is the number of quantum-mechanical levels in the short interval of energies near the energy E of the system consisting of N particles.

3.2.1 Physisorption

Physisorption is the physical adsorption of the gas onto the surface of the metal oxide, without a chemical change in the nature, geometrical structure or charge change in the electronic structure of the gas particle and the film surface. This occurs at the initial interaction of the gas with surface (see Figure 3-1). The weak electrostatic interaction between adsorbate and surface can be described by van-der-Waals forces or dipole-dipole interaction. Equilibrium condition is attained rapidly, since there is no activation energy involved and the process is readily reversible.

Usually, at low temperatures (below 100 °C) physisorption is characterised by a high surface coverage θ with gaseous molecules, and a low surface coverage at high temperatures. For physisorption adsorption of up to one monolayer, the fractional surface coverage θ is defined as the ratio of number of molecules adsorbed per surface unit, N , to the total number of surface adsorption sites, N_t ([Reichel 2005](#)):

$$\theta = \frac{N}{N_t} \quad (3.3)$$

The rate of surface coverage or rate of adsorption is determined by the change in fractional coverage with time, $d\theta/dt$.

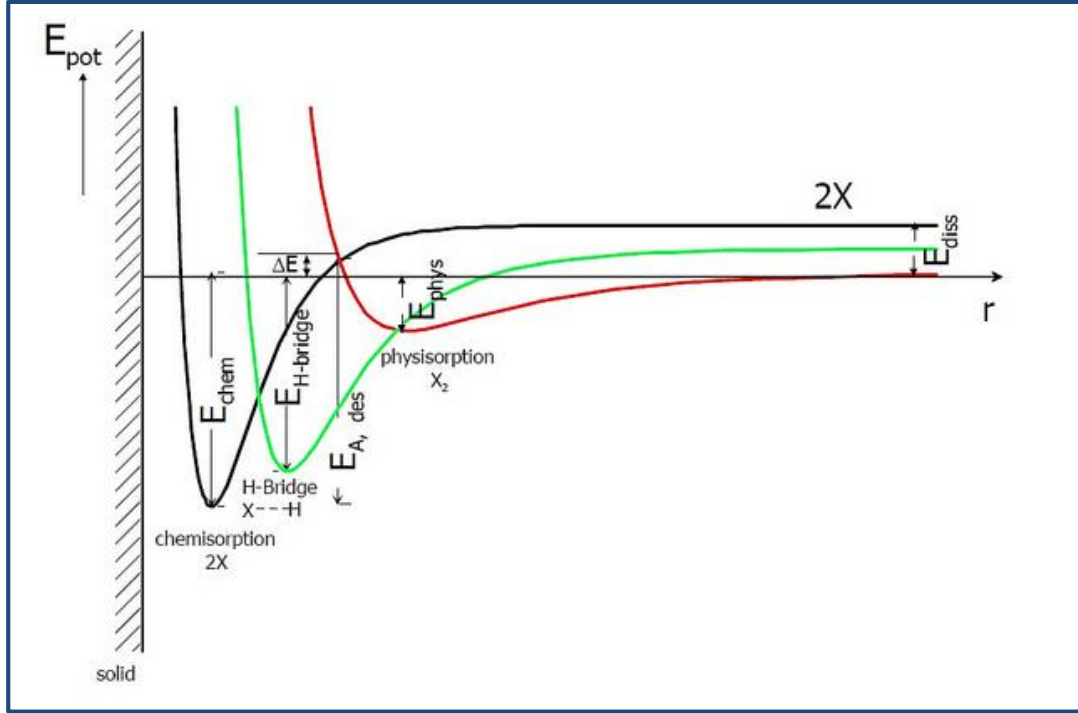


Figure 3-1: Lennards-Jones potential energy diagram for chemisorption, hydrogen bonding and physisorption on the surface (Harbeck 2005).

The Lennard-Jones Potential (i.e., a mathematical model that approximates the interaction between a pair of neutral atoms or molecules) can be used to describe the potential of the interacting particles (Harbeck 2005). The Lennard-Jones model assumes an equilibrium between adsorbed molecules and molecules in the gas phase (Batzill 2006). By the Lennard-Jones potential (Figure 3-1), the rate of chemisorption is determined by an activation barrier between a physisorbed state and the chemisorbed state and an activation barrier of desorption (Mazloom and Ghodsi 2012). This potential is approximated by a two-particle potential, which includes an attractive term and a repulsive term:

$$E_{pot} = E_{attr} + E_{rep} \propto 4\epsilon_{pot} \left[-\left(\frac{d}{r}\right)^6 + \left(\frac{d}{r}\right)^{12} \right] \quad (3.4)$$

where, E_{pot} = potential energy

E_{attr} = attraction energy

E_{rep} = repulsive energy

d = distance between the interacting particles

ϵ_{pot} = depth of potential

r = distance between two atoms in a molecule

The potential energies of physisorption (E_{phys}) and chemisorption (E_{chem}) can be described as a function of the distance r from the surface (Figure 3-1).

The physisorption of the adsorbate onto the surface results in a gain of ΔE (equal to E_{phys}). The interaction energy gas and surface bond is given as $\Delta E = 0-30\text{kJ/mol}$ with $\Delta E \sim r^6$ (Reichel 2005). Chemisorption and ionosorption adsorptions have stronger bonding between the gas and the surface.

3.2.2 Hydrogen Bonding

Hydrogen bonding is another electrostatic interaction whose magnitude of bond is between physisorption and chemisorption ($\sim 0.1\text{ eV}$) (Harbeck 2005). It takes the form of A-H...B, where A is an atom with electronegativity greater than that of hydrogen (e.g., O), and B is any σ or π electron donor site (Lewis base). Its intermolecular force is composed of a van-der-Waals and a covalent part. The bond could be symmetrical or asymmetrical; in the symmetrical bond, the proton can tunnel between the two equilibrium positions while in the asymmetrical the proton is more strongly bound to one atom than to another. Using the Lennard-Jones potential, the potential energy of this bond can be described as in Figure 3-1. The potential energy is described in Equation (3.5) (Harbeck 2005).

$$E_{pot} = E_{attr} + E_{rep} \propto 4\epsilon \left[-\left(\frac{d}{r}\right)^6 + \left(\frac{d}{r}\right)^9 \right] \quad (3.5)$$

3.2.3 Chemisorption

Chemisorption is a chemical reaction between the surface and the adsorbate resulting in a charge transfer. The charge transfer model assumes that adsorbed particles induce extrinsic two-dimensional surface states due to localised chemisorption and delocalised chemisorption. Localised chemisorption is due to a charge transfer between an adsorbent (e.g., surface site = surface atom or group of atoms) and an adsorbate. It is important to state that the changes induced by localised chemisorption processes are not easy to read out because they are not influencing the resistance (conductance) of the sensing layer ; and thus have no direct impact on the conduction mechanism ([Gurlo et al. 2005](#)).

Using a simple Lennard-Jones model for adsorption, the net rate of chemisorption $d\theta/dt$ is expressed as the difference in adsorption and desorption rates ([Batzill 2006](#); [Mazloom and Ghodsi 2012](#)):

$$\frac{d\theta}{dt} = k_{\text{ads}} \exp\left(-\frac{\Delta E_A}{kT}\right) - k_{\text{des}} \theta \exp\left(-\frac{\Delta E_A + \Delta H_{\text{chem}}}{kT}\right) \quad (3.6)$$

where ΔE_A is the activation barrier for chemisorption and ΔH_{chem} is the heat of chemisorption. The heat of chemisorption is equivalent to the different binding energies ($\Delta H \equiv E_{\text{binding}}$) ([Sahm et al. 2006](#)):

$$\frac{d\theta}{dt} = k_{\text{ads}} \exp\left(-\frac{E_A}{kT}\right) - k_{\text{des}} \theta \exp\left(-\frac{E_A + E_{\text{binding}}}{kT}\right)$$

The activation energy ΔE_A is the least energy that must be supplied to a molecule before it can be chemisorbed ([Bubphamala 2006](#)). Under steady state conditions, $d\theta/dt=0$ (or $dH/dt=0$), i.e. the rate of adsorption is equal to the rate of desorption, the coverage θ is dependent on the heat of chemisorptions ΔH_{chem} ; then, the coverage is given by:

$$\theta = \frac{k_{\text{ads}}}{k_{\text{des}}} \exp\left(\frac{\Delta H_{\text{chem}}}{kT}\right) \quad (3.7)$$

Thus, surface coverage θ decreases rapidly with increase in temperature. But experimentally, heat of chemisorption decreases with surface coverage due to the surface heterogeneity – high energy sites will be occupied first and low-energy ones later; while activation energy E_a can be regarded as the difference in the

electrochemical potential between the metal oxide semiconductor surface and the adsorbed oxygen, and therefore increases with coverage, due to the reduction of available surface electrons n_s ([Comini et al. 2009b](#)).

During chemisorption, the formation of new chemical bonds by the adsorbate results in stronger interaction with the surface due to a higher energy gain ΔE (equal to E_{chem}) than during physisorption (Figure 3-1). This occurs at temperature above 100 °C with activation energy above 50kJ/mol. The intersection point of the two curves represents the transition from physisorption to chemisorption, where the energy is the activation energy of chemisorption, ΔE_{ads} (Figure 3-1).

Molecularly or atomically, as a chemical bond is created during the reaction, chemisorption changes the electronic structure of the adsorbate and the surface, as electrons are captured in the adsorption complex or they are transferred from the adsorption complexes into the conduction band of the semiconductors. The corresponding concentration changes of the free charges (or reactivity) can be measured via changes in conductivity. The adsorbate, (e.g., X_2) dissociates (to $2X$), and the dissociation energy (of X_2), ΔE_{dis} , is represented at large distances. Potential curves of chemisorption, hydrogen bond and physisorption are characterised by the presence of a minimum, which corresponds to the heat of the process (ΔH_{ads}) ([Puzzovio 2009](#)). The heat of chemisorption is at a shorter distance from the solid surface than the heat of physisorption.

The chemisorption energy gain, ΔE_{chem} , depends strongly on the individual surface sites available and their reactivity. The most reactive sites will therefore be occupied with gaseous molecules during thermodynamic equilibration ([Reichel 2005](#)). However, the chemisorption energy not only depends on the number of reactive sites (high potential gain in ΔE_{chem}) but also on the ambient gas concentration, p_{gas} , and temperature T (probability of molecules overcoming the energy barrier, E_A).

Desorption also requires the molecule to overcome an energy barrier $E_{\text{des}} = E_{\text{chem}} + E_a$. Therefore chemisorption and desorption are both activated processes requiring an

activation energy supplied either thermally or by photoexcitation, contrary to physisorption which is a slightly exothermic process ([Reichel 2005](#)).

From chemisorption kinetics, the adsorption rate of gaseous molecules is proportional to the gas pressure (or concentration) and to the number of unoccupied adsorption sites according to

$$\frac{d\theta}{dt} = k_{ads}(1 - \theta)p_{gas} \quad (3.8)$$

where, the adsorption rate constant, k_{ads} , is given via the Arrhenius equation as

$$k_{ads} = A_{ads} \exp\left(-\frac{E_A}{kT}\right) \quad (3.9)$$

and A_{ads} is the pre-exponential factor, E_A is the activation energy for adsorption, k is the Boltzmann constant and T is the temperature.

The desorption rate is proportional to the number of occupied sites according to:

$$\frac{d\theta}{dt} = k_{des}\theta \quad (3.10)$$

where, the desorption rate constant, k_{des} , is given as

$$k_{des} = A_{des} \exp\left(-\frac{E_D}{kT}\right) \quad (3.11)$$

and A_{des} is the pre-exponential factor, E_D is the activation energy for desorption.

The net adsorption rate can therefore be described through Equations (3.8) and (3.10) by

$$\frac{d\theta}{dt} = k_{ads}(1 - \theta)p_{gas} - k_{des}\theta \quad (3.9)$$

Therefore, the resulting equilibrium coverage θ for $d\theta/dt = 0$ is

$$\theta = \frac{p_{gas}}{P_{gas} + \frac{k_{des}}{k_{ads}}}; \theta = f(p_{gas}, T) \quad (3.12)$$

The Langmuir isotherm is represented in Equation (3.12). It shows that all adsorption and desorption processes not only depend on the nature of the adsorbate and adsorbent but also on the availability of adsorbates (partial pressure) and on the temperature. The

above observations are correct only for adsorption and desorption of gaseous monolayers on surfaces of solids ([Reichel 2005](#)).

3.2.4 Ionosorption

Ionosorption is a (delocalised) chemisorption process in which the atoms or molecules are ionised through capturing of an electron from the bulk (conduction band) during the adsorption process (Figure 3-2).

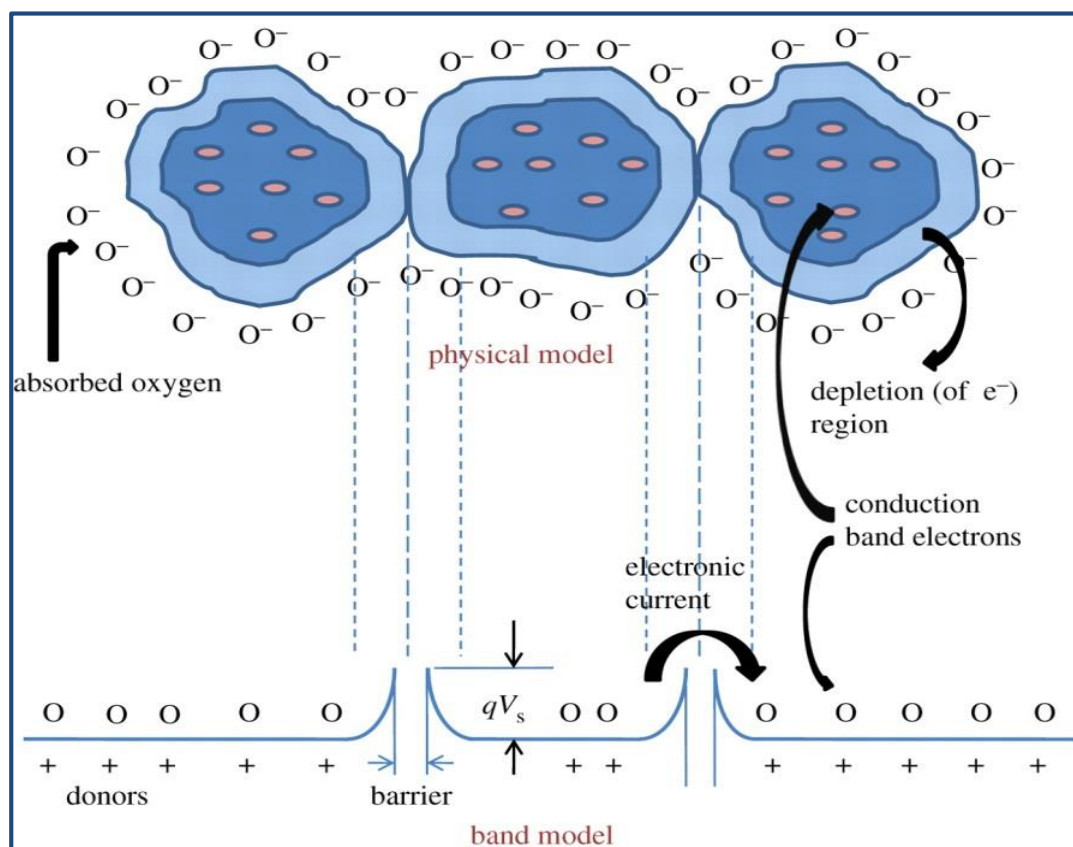


Figure 3-2: Model of intergranular grains contact/boundary of a thin film *n*-type semiconductor metal oxide gas sensor surface and oxygen ionosorption ([Ding et al. 2001](#)).

As a consequence of the charge transfers between molecules and surface, the chemical reactivity of the molecules, as well as their electronic and geometrical structures, are strongly influenced ([Harbeck 2005](#)). The process is predominantly the ionosorption of oxygen onto the surface of the metal oxide (see Section 3.2.5 for details of oxygen adsorption by metal oxides and Section 3.3 for energy band interpretation).

3.2.5 Adsorption of Oxygen

The sensing mechanism on the surface of the metal oxide commences with the ambient air. Oxygen, being the dominant non-inert component of synthetic (ambient) air, is the reaction-determining gas for measurements intended to model the influence of gases on tested gas sensors in real-life application.

Oxygen is a powerful electron acceptor and can be reduced to undergo several transformations when it interacts with metal oxide thin films. When the gas-sensing materials are exposed to air, oxygen molecules are adsorbed and become negatively charged via obtaining electrons from the conduction band of *n*-type semiconductors. Electrons are usually extracted from the surface of the semiconductor by the adsorbed oxygen (being an oxidising gas), decreasing the conductance (i.e., increasing the resistance) of the surface. In the process, the oxygen molecule becomes singly or doubly charged particles in the gas-sensing environment. The surface of the metal oxide film becomes charged, and prepared to interplay in the sensing mechanism (Figure 3-3).

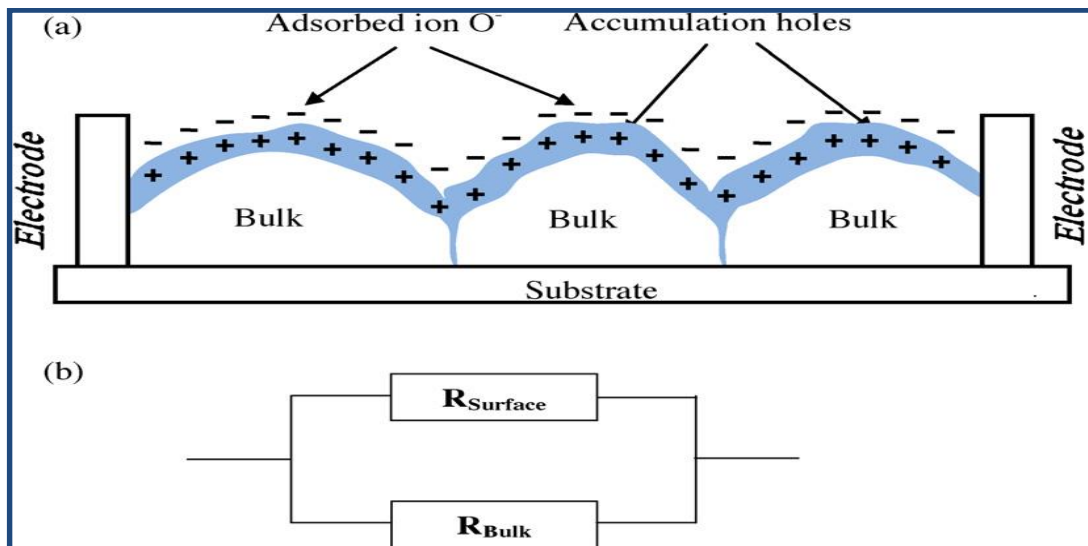
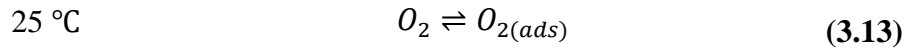


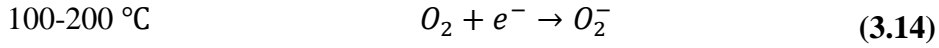
Figure 3-3: Sensor scheme (a) sensor structure, and (b) equivalent electrical circuit (Bejaoui et al. 2013).

Various species of oxygen can be formed depending on the substrate temperature, and the adsorption-desorption conditions. During chemisorption, oxygen is ionised and

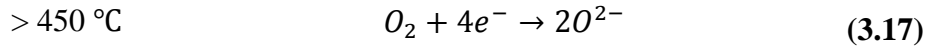
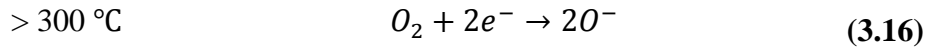
possibly dissociated and bound to the surface through an unoccupied chemisorption site for oxygen in various forms while extracting electrons from the semiconductor to ionise the chemisorbed oxygen. With SnO₂ and ZnO, oxygen react (or adsorb) and could form adsorbed neutral molecule, O₂, adsorbed neutral atomic molecule, O, superoxide ions, O₂⁻, charged atomic oxygen or ion radical, O⁻, and peroxide ions O₂²⁻ ([Gurlo 2006](#)). The reactions can be represented as ([Henrich and Cox 1993](#)):



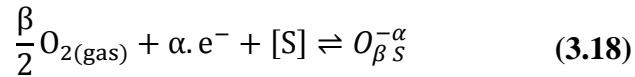
Room temperature ([Ding et al. 2001](#)):



Above 150 °C ([Ding et al. 2001](#)):

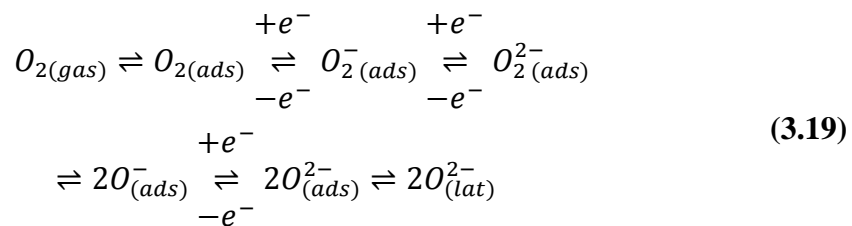


Equations (3.13) to (3.15) can be summarised as ([Reichel 2005](#)):



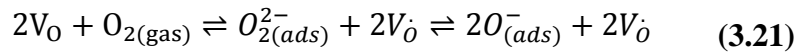
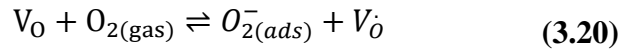
where O_{2(gas)} is an oxygen molecule in the ambient atmosphere and e⁻ is an electron which can reach the surface despite the electric field resulting from the surface double layer. The concentration of free charge carriers (electrons) is n_s, S is an unoccupied chemisorption site for oxygen, O_{βS}^{-α} is a chemisorbed oxygen species with: α = 1 for singly ionised forms, α = 2 for doubly ionised forms, β = 1 for atomic forms, β = 2 for molecular forms.

Alternatively, Equations (3.10) to (3.14) can be summarised as ([Rehrl 2011](#)):



where the subscripts (gas), (ads) and surface (lat) denote that the corresponding gas species as gas molecule unbounded in the atmosphere, adsorbed and bounded into the crystal lattice of the surface, respectively.

Using the Kröger–Vink⁶ notation ([Schmidt-Mende and MacManus-Driscoll 2007](#)), it can be represented as ([Chen et al. 2011](#)):



where V_O represents oxygen vacancy, and $V_{\dot{O}}$ single electropositive oxygen vacancy.

All these processes are equilibrium reactions, and the amount in which they occur depends very much on the temperature, the partial pressure of oxygen and on the characteristics of the adsorbent ([Sahm et al. 2006](#)). The superoxide ions, O_2^- , is classified as an ‘electrophilic’ agent while O^{2-} connected with the lattice at the surface as a ‘nucleophilic’ agent ([Cheong and Lee 2006](#)).

Figure 3-4 shows the temperature of ionosorption for SnO_2 . At low temperature, oxygen may adsorb as neutral molecular O_2 (physisorption) or atomic O (dissociative physisorption). At elevated temperatures, chemisorbed oxygen species act as surface electron acceptors, trapping electrons and reducing surface conductivity of the tin oxide. The dominant oxygen species on the SnO_2 surface is chemisorbed molecular oxygen (i.e., either neutral $O_{2(ads)}$ or charged $O_{2(ads)}^-$) between the temperatures of 100 and 200 °C ([Sahm et al. 2006](#)). At higher temperatures (>150 °C), this non-dissociative molecular oxygen may acquire another electron and dissociate into adsorbed atomic form ($O_{(ads)}^-$ and $O_{(ads)}^{2-}$). While the singly ionised form ($O_{(ads)}^-$) dominates the temperature range below 450 °C; above 450 °C, O^{2-} is predominant

⁶ There are a number of intrinsic defects with different ionisation energies, as indicated by the Kröger Vink notation: i = interstitial site, Zn = zinc, O = oxygen and V = vacancy. The terms indicate the atomic sites, and superscripted terms indicate charges, where a dot indicates positive charge, a prime indicates negative charge, and a cross indicates zero charge, with the charges in proportion to the number of symbols ([Schmidt-Mende and MacManus-Driscoll 2007](#)).

([Barsan and Weimar 2001](#)). This species could be directly incorporated as bridging oxygen into the SnO₂ and ZnO lattice in the form of $O_{(lat)}^{2-}$ above 600 °C.

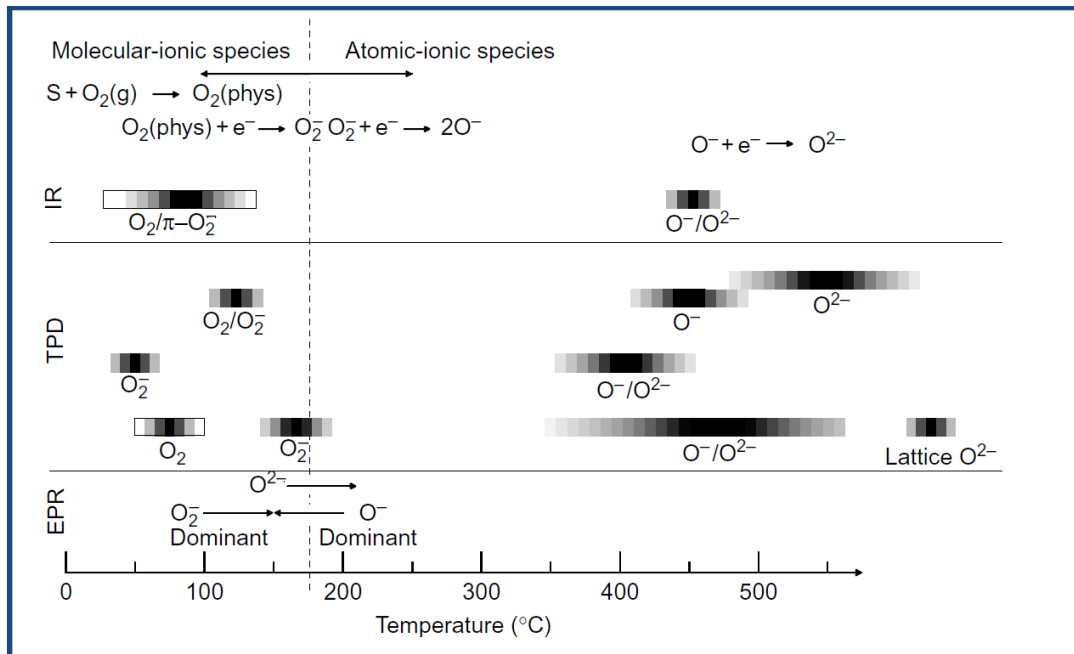


Figure 3-4: Oxygen species detected at different temperatures at surfaces with IR (infrared analysis), TPD (temperature programmed desorption), EPR (electron paramagnetic resonance) ([Gurlo et al. 2005](#)).

On the energy band, the adsorbed charged species create additional surface states (with either acceptor or donor character) within the band gap of the *n*-type semiconductor because of the electron-depleted space-charge layer in the surface region. The adsorbed analyte molecules are ionised by a transfer of valence electrons to empty electron states inside the adsorbent solid ([Oberhüttinger et al. 2011](#)). The fewer electrons present in the conduction band lead to a higher surface potential barrier, and therefore, result in a higher resistance. The adsorbed oxygen molecules act as a trap for the conduction band electrons of semiconductor due to the strong electronegativity⁷ ([IUPAC 1997](#)) of SnO₂ and ZnO, causing a depletion layer and band bending (i.e., a surface potential, Φ_s) on the surface ([Sahner and Tuller 2010](#); [Zeng et al. 2012](#)). This space-charge depletion layer consequently increases the energy barrier,

⁷ Electronegativity is a chemical property of an atom (or a functional group) to attract electrons to itself ([IUPAC 1997](#)).

and in turn, creates an electrically resistive surface region, which can be readily detected experimentally as increasing surface resistance. The height of the surface potential Φ_s , as well as the width d_s of the depletion layer are dependent upon the quantity of charged adsorbates determines. From Poisson's equation, they are represented as ([Sahner and Tuller 2010](#)):

$$\Phi_s = \frac{\theta^2}{8e_0\varepsilon_0\varepsilon_r n_{\text{bulk}}} \quad (3.22)$$

$$d_s = \sqrt{\frac{2\varepsilon_0\varepsilon_r\Phi_s}{e_0 n_{\text{bulk}}}} = \frac{\theta}{e_0 n_{\text{bulk}}} \quad (3.23)$$

where e_0 is electron unit charge, ε_0 is permittivity of free space, ε_r is relative permittivity of the semiconductor, and n_{bulk} is bulk electron concentration (but more precisely, n_{bulk} could be replaced by the effective bulk concentration of ionised donors, D_{eff}). Since the width, d_s , of the depletion layer depends strongly on the amount of charged adsorbates, any process interaction of the sensor in the presence of a reactive gas, will directly affect the near-surface conductivity of the semiconductor.

3.2.6 Adsorption of Water Vapour

Various studies of water adsorption on SnO_2 have applied by conductivity measurements ([Yamazoe et al. 1979](#)), transmission infrared spectroscopy (IR) ([Thornton and Harrison 1975a](#); [Thornton and Harrison 1975b](#)), and temperature programmed desorption (TPD) in He carrier gas ([Yamazoe et al. 1979](#)). Figure 3-5 shows the temperature of water vapour adsorption on SnO_2 . At room temperature, water can be adsorbed on metal oxide surfaces as physisorbed neutral molecules. At elevated temperatures, between 100 and 500 °C, the interaction of a metal oxide surface with water vapour leads to hydrogen-bonded molecules, chemisorbed reactive molecular water and hydroxyl group adsorption. At lower temperatures, there is coexistence of molecular water and hydroxyl groups on the metal oxide surface up to 47 °C ([Santarossa et al. 2013](#)). Above 200 °C no more molecular water can be found on a SnO_2 surface, as desorption peaks were assumed to originate from desorption,

recombination, or disproportionation of hydroxyl groups; while hydroxyl groups may still be detected above 400 °C. The types of hydroxyl groups generated on adsorption of water vapour on the metal oxide surfaces are classified as chemisorbed terminal hydroxyl groups (M-OH), chemisorbed rooted hydroxyl groups which include the lattice oxygen (O_{lat}-H), and hydrogen bridged hydroxyl groups (associated hydroxyl groups) ([Harbeck 2005](#)).

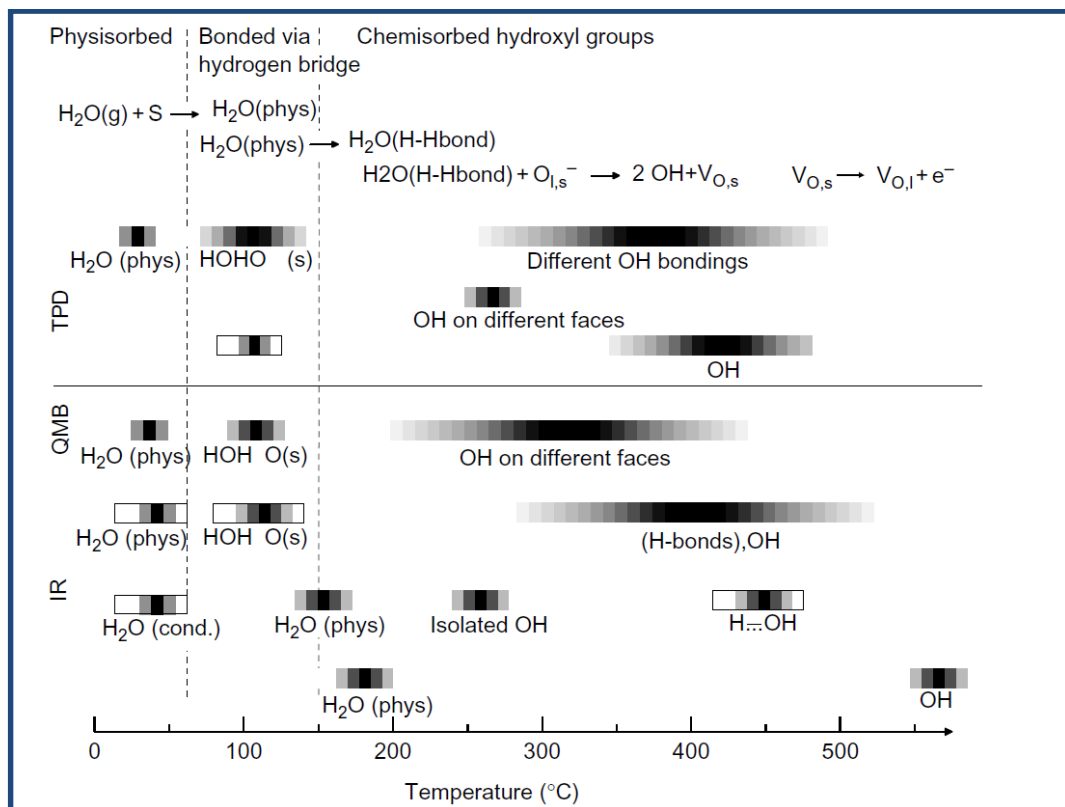
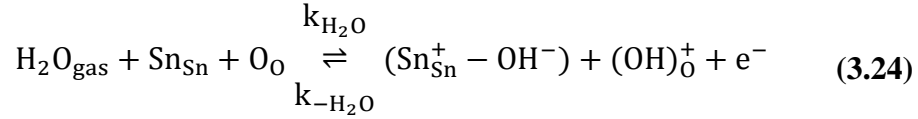


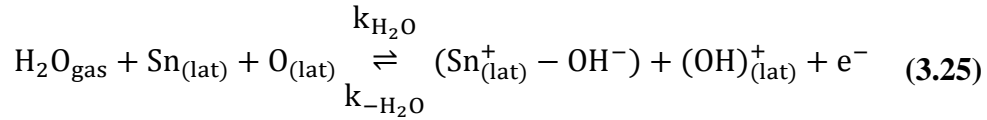
Figure 3-5: Water-related species formed at different temperatures at SnO₂ surfaces with IR, TPD, EPR ([Gurlo et al. 2005](#)).

Generally, a reversible increase in surface conductance by metal oxide semiconductor is attributed to the presence of water vapour ([Bârsan and Weimar 2003](#)). The increase of the conductance is observed as the disappearance of hydroxyl groups from the reaction. **Three mechanisms** of water vapour adsorption on SnO₂ were proposed for explaining the experimentally proven increase of surface conductivity in the presence of water vapour ([Barsan and Weimar 2001](#); [Bârsan and Weimar 2003](#)). The **first mechanism** attributed to the simple H₂O dissociation

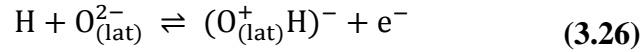
resulting in electron donation to the ‘rooted’ OH group, the one including lattice oxygen. The proposed equation is ([Barsan and Weimar 2001](#); [Bârsan and Weimar 2003](#)):



This equation can be represented as ([Rehrl 2011](#)):



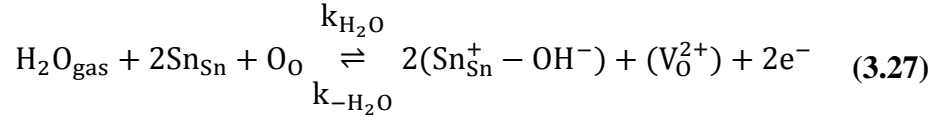
where $(\text{Sn}_{\text{Sn}}^+ - \text{OH}^-)$ is referred to as an isolated hydroxyl group (dipole), and OH_{O}^+ is the rooted one, the built-up rooted hydroxyl group, the latter is already ionised. The reaction implies the homolytic dissociation of water and the reaction of the neutral H atom with the lattice oxygen ([Reichel 2005](#)):



The rooted hydroxyl group is normally in the lattice fixing two electrons consequently being in the 2-state ([Gurlo et al. 2005](#)). The OH_{O}^+ , having a lower electron affinity⁸ ([IUPAC 1997](#)), (lose electron) gets ionised to become a donor, and subsequently injected an electron into the conduction band ([Gurlo 2006](#)).

The **second mechanism** takes into account the possibility of the reaction between the hydrogen atom and the lattice oxygen and the binding of the resulting hydroxyl group to the Sn atom ([Barsan and Weimar 2001](#); [Bârsan and Weimar 2003](#)). The resulting oxygen vacancy will produce, by ionisation, the additional electrons, as proposed in the equation:

⁸ Electron affinity is the energy required to detach an electron from the singly charged negative ion (energy for the process: $X^- \rightarrow X + e^-$) ([IUPAC 1997](#)). In solid state semiconductors, electron affinity, χ , is energy obtained by moving an electron from the vacuum just outside the semiconductor to the bottom of the conduction band just inside the semiconductor: $\chi = E_{\text{C,S}} - E_{\text{C,B}}$ ([Gurlo 2006](#)).



A **third mechanism** could be the interaction of the hydroxyl group or the hydrogen atom originating from the water molecule with an acid or basic group, which are also acceptor surface states ([Barsan and Weimar 2001](#); [Bârsan and Weimar 2003](#)). The co-adsorption of water with another adsorbate, which could be an electron acceptor, may change the electron affinity after the interaction; or the pre-adsorbed oxygen could be displaced by water adsorption.

The differences in the three mechanisms involve the process of electron delivery through the metal oxide. In the **first (i.e., water dissociation) mechanism**, the ionisation of the rooted OH is sufficient to induce an electron donation to the conduction band ([Santarossa et al. 2013](#)). But in further analysis, the effect of water could be included by considering the potential of an increased background of free charge carriers on the adsorption of oxygen. According to the **second (i.e., oxygen vacancy) mechanism**, the rooted group, $\text{OH}_{(\text{lat})}^+$, evolves binding to a neighbouring Sn atom, producing an oxygen vacancy. This vacancy donates two electrons to the conduction band of the semiconductor through an ionisation process. Further examination could include the influence of water adsorption as an electron injection combined with the appearance of new sites for oxygen chemisorption; this is valid if one considers oxygen vacancies as good candidates for oxygen adsorption ([Gurlo et al. 2005](#)). In this case, by applying the mass action law to Equation (3.26), one has to introduce the change in the total concentration of adsorption sites $[S_t]$:

$$[S_t] = [S_{t0}] + k_0 p_{\text{H}_2\text{O}} \quad (3.28)$$

$[S_{t0}]$ is the intrinsic concentration of adsorption sites and k_0 is the adsorption constant for water vapour.

The **third mechanism** implies an indirect process where pre-adsorbed species are changing the electron affinity of the surface. For instance, the terminal and rooted hydroxyl groups could react with acidic or basic groups present on the surface

([Santarossa et al. 2013](#)). However, the predominant mechanism is predominantly still debated and requires further theoretical and experimental studies ([Santarossa et al. 2013](#)). However, in any of these mechanisms, the particular state of the surface has a major role, because it is considered that steps and surface defects will increase the dissociative adsorption ([Gurlo et al. 2005](#)).

3.3 Types of Adsorption-Desorption Models

The relationship between the equilibrium amount of gas adsorbed and the pressure of the gas at a given temperature is termed as **adsorption isotherm** ([Puzzovio 2009](#)). It determines the thermodynamic functions attributed to the adsorption complex and the isosteric⁹ heats of adsorption ([Gopel 1985](#)). Various isotherms, modified into various models, have been developed to describe the adsorption process. Typical models apply Langmuir, Brunauer-Emmett-Teller (BET), Freundlich, Wolkenstein, and Kolmogorov equations. These models are formulated based on the adsorption-desorption kinetics. Initial fundamentals of the adsorption-desorption kinetics was presented in Section 3.2.

3.3.1 Langmuir Model

The classical thermodynamic adsorption model is based on the Langmuir theory; that is the rate of sorption process is proportional to the actual concentration in the bulk and to the number of unoccupied adsorption sites, whereas that of desorption is proportional only to the number of sites occupied by solute molecules. Therefore the adsorption and desorption processes not only depend on the nature of the adsorbate and adsorbent but also on the availability of adsorbates (partial pressure) and on the temperature.

The Langmuir isotherm is derived based on the following assumptions:

- (a) surface homogeneity with equivalent (size and shape of) adsorption sites;

⁹ Isosteric represents a condition where two different molecules have the same number of atoms and the same number and configuration of valency electrons, as carbon dioxide and nitrous oxide ([Gopel 1985](#)).

- (b) monolayer coverage (i.e., adsorption of a single layer);
- (c) only a single adsorbate per site; no further adsorption when all sites are occupied;
- (d) each site-molecule interaction process releases a constant amount of adsorption heat energy, and the bonding energy between the adsorbent and the adsorbate is independent of the covering rate; and
- (e) adsorption and desorption rate and energy are independent of neighbouring sites or population of neighbouring adsorbed molecules (e.g., adsorption heat is independent of coverage).

Assume that θ , a unit-less quantity, is the fraction of surface coverage (i.e., the number of surface sites covered) with the target gas molecules (or the density of adsorbed target gas molecules); the fraction of surface site unoccupied by target gas molecules is $(1 - \theta)$; C is the concentration of target gas. At dynamic equilibrium, the rate of adsorption and rate of desorption are equal (see Section 3.2.3). Therefore, the net adsorption-desorption rate can therefore be described by the Langmuir theory as Equation (3.29) ([Reichel 2005](#))

$$\frac{d\theta}{dt} = k_{ads}(1 - \theta)p_{gas} - k_{des}\theta \quad (3.29)$$

Since gas pressure p depends on molar concentration C , it can be used instead of pressure ([Asar et al. 2012](#)). Therefore, Equation (3.29) can be represented as:

$$\frac{d\theta}{dt} = k_{ads}(1 - \theta)C - k_{des}\theta \quad (3.30)$$

At dynamic equilibrium, $d\theta/dt = 0$:

$$k_{ads}(1 - \theta)C = k_{des}\theta \quad (3.31)$$

where C is the concentration of target gas; k_{ads} and k_{des} are the rate constants for adsorption and desorption processes, respectively.

Therefore, the resulting equilibrium coverage θ is independent of time, and thus results in the Langmuir isotherm:

$$\theta = \frac{k_{ads}p_{gas}}{k_{des} + k_{ads}p_{gas}}$$

Dividing both numerator and denominator on RHS by k_{des} :

$$\theta = \frac{\frac{k_{ads}}{k_{des}}p_{gas}}{\frac{k_{des}}{k_{des}} + \frac{k_{ads}}{k_{des}}p_{gas}} \quad (3.32)$$

Therefore, denoting the ratio of the adsorption rate to desorption rate as $K = \frac{k_{ads}}{k_{des}}$, the Langmuir isotherm (or Langmuir adsorption equation) for a net adsorption process at equilibrium is given as:

$$\theta = \frac{N(t)}{N} = \frac{Kp_{gas}}{1 + Kp_{gas}} \quad (3.33)$$

This can be written in terms of concentration as:

$$\theta = \frac{N(t)}{N} = \frac{KC}{1 + KC} \quad (3.34)$$

The behaviour of different values of K is shown in Figure 3-6.

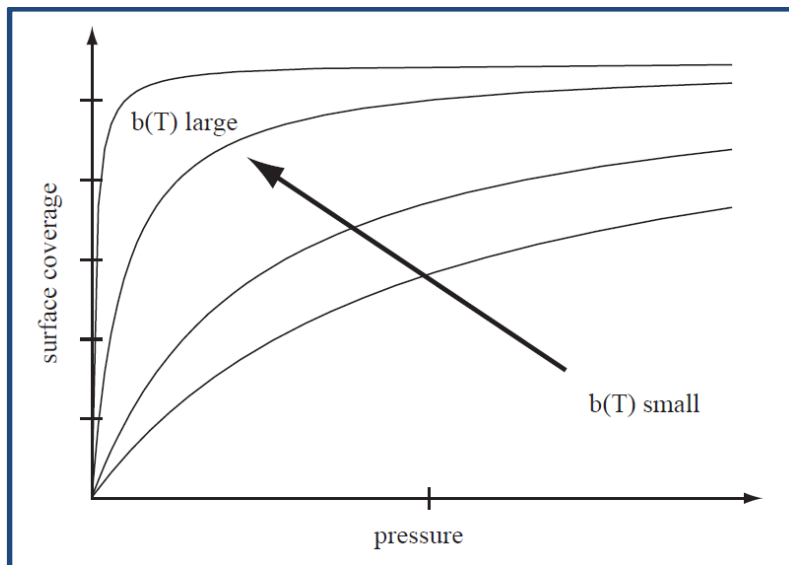


Figure 3-6: Characteristics of several Langmuir isotherms for different K [$K = b(T)$] values (Hildenbrand 2003).

The Langmuir isotherms indicates that the fractional coverage θ increases with increasing pressure and approaches one only at very high pressure, when the gas is forced on to every available site ([Puzzovio 2009](#)).

The fractal coverage, $\theta(t)$, is obtained from the integration of ([Baleanu et al. 2011](#); [Sedlak et al. 2012](#)):

$$\frac{d\theta}{dt} = k_{ads}(1 - \theta)C - k_{des}\theta \quad (3.35)$$

The kinetic parameters, association constant K' and the inverse of relaxation time k_{obs} , can be given, respectively, as ([Asar et al. 2012](#); [Sedlak et al. 2012](#)):

$$K' = \frac{C}{C + \frac{k_{des}}{k_{ads}}} \quad (3.36)$$

and

$$k_{obs} = k_{ads}C + k_{des} \quad (3.37)$$

Therefore, the fractal coverage can be determined as a function of time as ([Asar et al. 2012](#)):

$$\theta(t) = K'(e - e^{(-k_{obs}t)})$$

In this study, the measure of the surface coverage is sensitivity, S , during the adsorption and desorption processes. S_{max} is the maximum sensitivity on the surface of the thin film. Thus, this equation can take the form:

$$S(t) = S_{max}K'(1 - e^{-k_{obs}t}) \quad (3.38)$$

From a plot of sensitivity versus time, K' and k_{obs} , k_{ads} , k_{des} and equilibrium constant K ($K = k_{ads}/k_{des}$) values were calculated. The Gibbs free energy, ΔG , of adsorption/desorption process in terms of K at a constant temperature is defined as:

$$\Delta G = -RT \ln K$$

where R = the universal gas constant (8.314 J/mol K), and T = the temperature (K).

3.3.2 Brunauer, Emmet and Teller (BET) Model

The Brunauer-Emmett-Teller (BET) theory is an extension of the Langmuir model to thermodynamic adsorption in multilayers. The derivation of the BET model ([Brunauer et al. 1938](#)) is based on the following assumptions:

- (a) each surface homogeneity with equivalent (size and shape of) adsorption sites;
- (b) gas molecules physically adsorb on each solid layers;
- (c) there is no interaction between each adsorption layer;
- (d) the second and all following layers are less strongly adsorbed than the first layer; and
- (e) the Langmuir theory can be applied to each layer.

In a multi-point linear form, the BET-equation is written as:

$$\frac{p}{(p_0 - p)V} = \frac{1}{aV_m} + \frac{a - 1}{aV_m} \frac{p}{p_0} \quad (3.39)$$

where

p = partial pressure of adsorbate gas at given temperature, in pascals;

p_0 = saturation pressure at given temperature;

V = volume of gas adsorbed at standard temperature and pressure (STP) [273.15 K and atmospheric pressure (1.013×10^5 Pa)], in millilitres;

V_m = volume of gas adsorbed at STP to produce an apparent monolayer on the sample surface, in millilitres;

α = dimensionless constant related to the adsorption enthalpy of the adsorbed gas.

The above equation is for multilayer adsorption. With $\frac{1}{aV_m} = 0$, single point BET equation can be applied to shorten the measurement time. The major application of BET adsorption is for the analysis of the surface area and morphology of thin films ([Korotcenkov 2008](#)).

3.3.3 Freundlich Model

The Freundlich isotherm is an empirical modification of Langmuir isotherm to describe the multisite adsorption behaviour and consequences of surface heterogeneity of semiconductor films ([Gautam and Jayatissa 2012](#); [Hu et al. 2002](#)). The Freundlich isotherm considered the inhomogeneous surface to consist of different areas characterised by various adsorption heats Q_i or by various inverse adsorption coefficients b_i . The surface occupation degree can be written as ([Gautam and Jayatissa 2012](#)):

$$\theta = \int_{Q_{min}}^{Q_{max}} \frac{P}{P + b(Q)} f(Q) dQ = \int_{b_{min}}^{b_{max}} \frac{P}{P + b} f(b) db \quad (3.40)$$

where $\frac{P}{P+b(Q)}$ is the probability occupying an area with a given value of $b(Q)$; $f(Q)$ and $f(b)$ are the distribution density of adsorption heats and inverse adsorption coefficients. The adsorption behaviour is described by the Freundlich isotherm as ([Gautam and Jayatissa 2012](#)):

$$\theta = \frac{N(t)}{N} = \frac{\alpha C^\beta}{1 + \alpha C^\beta} \left(1 - \exp\left(-\frac{t}{t_A}\right) \right) \quad (3.41)$$

where α is proportionality factor, and β is the exponent. Depending on the characteristics (i.e., α and β) of the semiconducting material, the amplitude approaches αC^β at low gas concentrations and approaches 1 when the concentration of gas tends to infinity. But, in simplified form, the Freundlich isotherm can be represented as ([Hu et al. 2002](#)):

$$\theta = \frac{N(t)}{N} = \alpha C^\beta \quad (3.42)$$

for $0 < \beta < 1$.

The relative response of the sensor can be related to concentration by a Freundlich isotherm of the form ([Johnson et al. 2011](#)):

$$S = \frac{\Delta R}{R} \propto \frac{\alpha C^\beta}{1 + \alpha C^\beta} \quad (3.43)$$

where S is the sensitivity, C is the analyte concentration. The time-dependence of sensitivity $S(t)$ during response $S_{res}(t)$ and recovery $S_{rec}(t)$ can be modelled by exponential terms as follows ([Gautam and Jayatissa 2012](#); [Johnson et al. 2011](#)):

$$S_{res}(t) = A_{res} \left[1 - \exp\left(-\frac{t}{\tau_{res}}\right) \right]$$

and

$$S_{rec}(t) = A_{rec} \exp\left(-\frac{t}{\tau_{rec}}\right)$$

where A is the amplitude, and τ_{res} and τ_{rec} are time constants for response and recovery, respectively. Nevertheless, [Arnold et al. \(2009\)](#) observed that the Freundlich models failed to model the experiment at higher concentration.

3.3.4 Wolkenstein Model

The Wolkenstein adsorption model incorporates the electronic interactions and their effect on the adsorptivity of semiconductor substrate into the description of chemisorption on semiconductors. In this process, localised electronic states, created by chemisorbed species, serve as traps for electrons or holes (acceptor-like or donor-like states, respectively), depending on their nature ([Geistlinger 1993](#); [Rothschild and Komem 2003](#)). The model considers both chemical equilibrium between the surface and the gas phase, and electronic equilibrium at the semiconductor surface.

The basic assumptions of the Wolkenstein adsorption isotherm are that (i) there is only one gas species (for adsorption) and (ii) chemisorption is the only source of surface charging. Simply, in two successive steps, the Wolkenstein adsorption process occurs by transforming adsorbed particles from the neutral (i.e., weak chemisorbed species) state to the ionised (i.e., strong chemisorbed species) state, and vice versa. During the first step (weak or neutral chemisorption), the bond between the adsorbate and the substrate is weak and does not involve electronic transfer from the bulk to the surface (or vice versa); the electrons of the atom or the molecule remain located in the vicinity of the adsorbate involving a simple deformation of the orbitals ([Guérin et al. 2006](#); [Šetkus 2012](#)). The binding energy of the adsorbate, E_{ads} , corresponds to the loss of free energy of the system during the adsorption process. The electrical properties of the

material do not change during this neutral chemisorption, but the perturbation created by the adsorbate induces surface state, E_{ss} , in the band gap. Thus, the surface state acts as a trap for the electrons.

The second step (i.e., strong chemisorption) occurs when an electron of the conduction band, with conduction energy E_c , is transferred from the semiconductor to the adsorbed species. The binding energy of the adsorbate is increased by $E_s = E_c - E_{ss}$, that is the loss of free energy of the system during the ionisation process. This process involves the creation of a negative superficial charge and a chemisorption-induced surface potential barrier V_s ($V_s < 0$), defined by Poisson's equation.

Considering these two steps, the evolution of the surface coverage with chemisorbed gas θ is defined by the rate equation of non-dissociative chemisorption as ([Guérin et al. 2006](#); [Rothschild and Komem 2003](#); [Šetkus 2012](#)):

$$S_0(1 - \theta) \frac{p}{\sqrt{2\pi mkT}} = N^* \theta^0 \nu^0 \exp\left(-\frac{E_{ads}}{kT}\right) + N^* \theta^- \nu^- \exp\left(-\frac{E_{ads} + E_c^b - E_{ss}}{kT}\right) \quad (3.44)$$

where S_0 is the adsorption probability (i.e., condensation coefficient or oscillation frequencies), p is the ambient gas partial pressure, m is the molecular mass of the target gas, k is the Boltzmann constant, T is the thermodynamic temperature (in K), $\theta = (N^0 + N^-)/N^*$ is the total coverage of both neutral and charged adsorbates (N^* is the number of adsorption sites per unit surface area), $\theta^0 = N^0/N^*$ is the partial coverage of neutral adsorbates (N^0 is the number of neutral adsorbates per unit surface area), and $\theta^- = N^-/N^*$ is the partial coverage of charged adsorbates, (N^- is the number of chemisorbed adions¹⁰ per unit surface area), E_c^b is the conduction-band edge in the bulk of the sensor, ν^0 and ν^- are the desorption probabilities (i.e., typical phonon frequency of the lattice or oscillation frequencies of the corresponding adsorbates) for neutral and ionised chemisorbed species, respectively. Typically, $\nu^0 = \nu^- = 10^{13}$ Hz ([Rothschild and Komem 2003](#)). The flux rate of the arrival of gas molecules at the sensor surface R_f (molecules/cm²s), is proportional to their average velocity v and their concentration n ; represented as ([Jakšić et al. 2014](#)):

¹⁰ Adion is an adsorbed ion.

$$R_f = \frac{nv}{4} = \frac{p}{\sqrt{2\pi mkT}} \quad (3.45)$$

At equilibrium, $d\theta/dt = 0$, the rate equation includes both the weak and strong chemisorption states characterised by the neutral θ^0 and ionised θ^- coverage of the surface. These two parameters are related to the total coverage θ by the Fermi-Dirac statistics ([Šetkus 2012](#)).

The occupation probability of the chemisorption-induced surface state in thermal equilibrium is given by the Fermi-Dirac distribution function:

$$\frac{N^-}{N^0 + N^-} = f_{FD}(E_F - E_{SS}) = \left[1 + \left(-\frac{E_F - E_{SS}}{kT} \right) \right]^{-1} \quad (3.46)$$

and

$$\frac{N^0}{N^0 + N^-} = 1 - f_{FD} \quad (3.47)$$

where E_F is the Fermi energy.

Further simplification with $\theta^- = f_{ED}\theta$; and $\theta^0 = (1-f_{ED})\theta$, yields the Wolkenstein adsorption isotherm for non-dissociative chemisorption on semiconductors as:

$$\theta = \frac{\beta p}{1 + \beta p} \quad (3.48)$$

with

$$\beta = \frac{\beta_0 \left[1 + \exp\left(\frac{E_F - E_{SS}}{kT}\right) \right]}{\left[1 + \frac{v^-}{v^0} \exp\left(-\frac{E_C^S - E_F}{kT}\right) \right]} \quad (3.49)$$

and

$$\beta_0 = \frac{S_0}{N^* v^0 \sqrt{2\pi mkT}} \exp\left(\frac{E_{ads}}{kT}\right) \quad (3.50)$$

Formally, the Wolkenstein adsorption isotherm resembles the Langmuir isotherm [$\theta = \beta_0 p / (1 + \beta_0 p)$]. The major difference is that the coefficient β_0 in Langmuir's isotherm is independent of the coverage θ , whereas in Wolkenstein's isotherm β

is a function of θ ([Rothschild and Komem 2003](#)). The difference is because the chemisorption-induced surface potential barrier eV is dependent on the surface charge density. However, by the Wolkenstein adsorption equation, a strongly chemisorbed species must return its trapped electron to the bulk and return to the neutral state before desorbing and a neutral chemisorbed species must release its bonding energy, E_{ads} , before desorbing ([Guérin et al. 2006](#)).

Applications of Wolkenstein model include numerical computation of the SnO_2 ([Rothschild and Komem 2003](#)), simulation of the dynamic response of sensors to gas ([Guérin et al. 2006](#)), and modelling of noise in sensor signal ([Gomri et al. 2006](#)).

3.3.5 Kolmogorov Model

The Kolmogorov adsorption-desorption model is based on the interaction between two reservoirs; the target gas molecules and the sensor surface ([Sedlak et al. 2012](#)):

- (i) analysed gas with concentration n , temperature T and partial pressure p ,
- (ii) sensor sorbent surface with total surface density of sites for the adsorption of analysed gas N_0 , with surface density of sites occupied by analysed gas molecules N_t .

For the transition probability intensities, the system is assumed to be ([Sedlak et al. 2012](#); [Sikula et al. 2005](#)): (i) Markovian¹¹, (ii) near equilibrium, and (iii) generation–recombination processes may take place between these two reservoirs. The random process of adsorption on the surface site is assumed to have two states and to be stationary with a constant transition probability density μ_{ij} defined by:

$$\mu_{ij} = \lim_{t \rightarrow s} \frac{p_{ij}(s, t)}{t - s} \quad (3.51)$$

where p_{ij} represents the transition probability at time s from the i -state to the j -state at time t . The process is similar to generation–recombination in semiconductors; the

¹¹ A Markovian (stochastic) process has the Markov property if the conditional probability distribution of future states of the process (conditional on both past and present values) depends only upon the present state; that is, given the present, the future does not depend on the past.

adsorption process corresponds to recombination, while desorption corresponds to molecule generation (i.e., emission of free particle) from sorbent. The transition probability density for molecule capture (response) and molecule emission or release (recovery) is denoted by μ_{10} and μ_{01} , respectively. There are two physical measurable quantities: [the pulse duration in the lower and the upper states ([Sikula et al. 2005](#))] the characteristic time τ_{res} for a molecule to be captured on the surface site (and respond to the gas sensing) is inversely proportional to the transition probability density μ_{10} :

$$\mu_{10} = \frac{1}{\tau_{res}} \quad (3.52)$$

and the characteristic time τ_{rec} for molecule emission or release from the surface site is inversely proportional to the transition probability density μ_{01} :

$$\mu_{01} = \frac{1}{\tau_{rec}} \quad (3.53)$$

The probabilities $p_{ij}(t)$ of the transition from the state i into the state j are found by solving the Kolmogorov differential equations ([Sedlak et al. 2012](#); [Sikula et al. 2005](#)):

$$\frac{dp_{ij}(t)}{dt} = \sum_{k \in \{1\}} \mu_{ik} p_{kj}(t) \quad (3.54)$$

for $i, j = 0, 1$, with the conditions $p_{ii}(0) = 1, p_{ij}(0) = 0$, for $i \neq j$.

In thermodynamic equilibrium the statistics that the surface site is free or occupied by molecule is described by the absolute probability distributions Π_0 and Π_1 . At stationary state, the absolute probability distribution Π_i is solved by Kolmogorov equation in the form:

$$\sum_{k \in \{1\}} \Pi_i \mu_{ik} = 0 \quad (3.55)$$

where

$$\Pi_0 = \left[1 + \frac{\mu_{01}}{\mu_{10}} \right]^{-1}$$

$$\Pi_1 = \left[1 + \frac{\mu_{10}}{\mu_{01}} \right]^{-1}$$

The absolute probability distributions Π_0 and Π_1 are similar to the Fermi-Dirac statistics for the trap to be free and occupied by an electron, respectively ([Sikula et al. 2005](#)).

Thus, kinetic equation describing surface density of adsorbed molecules follows from Equation (3.55) in the form:

$$\frac{dp_{10}}{dt} = \mu_{10}\Pi_0 + \mu_{11}\Pi_1 \quad (3.56)$$

$$\frac{dp_{01}}{dt} = \mu_{00}\Pi_0 + \mu_{01}\Pi_1 \quad (3.57)$$

where μ_{00}, μ_{11} are densities that the system is persisting in the state 0 or 1, respectively.

With $\mu_{10} = C_N n$ for adsorption, $\mu_{01} = C_N n_1$ for desorption and C_N as coefficient of adsorption,

$$\frac{dN}{dt} = \text{adsorption (N)} - \text{desorption (N)} = C_N n(N_0 - N) - C_N n_1 N \quad (3.58)$$

The surface density of adsorbed molecules is proportional to the coefficient of adsorption C_N , concentration of adsorbed molecules n , sensor surface density of sites N_0 and the effective concentration of occupied sites n_1 .

A comparison of the Langmuir and Wolkenstein models is presented by ([Baleanu et al. 2011](#); [Sedlak et al. 2012](#))

3.4 Electronic Conduction and Surface States

The electronic structure of metal oxide semiconductor surfaces and adsorption processes of different gases can be characterised by the electronic band model. This can be described by the use of the surface state of the semiconductor. The surface is an imperfection in the sense that it is a region where the normal periodicity of the electrical field of the crystal is disrupted ([Ding et al. 2001](#)). From quantum analysis, the localised energy levels (called **surface states**) in the forbidden gap will arise at the

surface, and can exchange electrons with the bulk atoms. The **intrinsic surface states** refer to localised energy levels at the surface created by the semiconductor itself, while the **extrinsic surface states** are localised energy levels created by adsorbed gas molecules (like oxygen) at the surface of the metal oxide ([Ding et al. 2001](#)). The gas adsorption and desorption kinetics at the sensor surface affect density of surface states, N_s , which determines the maximum amount of charge that can be trapped ([Tang 2004](#)). The change in the density of current carriers representing injection or withdrawal of charge to or from the bands of the semiconductor, results in the formation of a double layer. Generally, in both surface states the exchange of electrons between the conduction band of the metal oxide and a surface state leads to an occupied and consequently charged surface state. Intrinsic surface states can also include the surface energy levels created by impurities, dopings, oxygen vacancies in metal oxide semiconductors, and dislocation of atoms at the surface, without possible reaction between surface and gas analyte. Decisive extrinsic surface states materials include adsorbed oxygen ions. Adsorbed oxygen ions have a decisive influence on the surface conductivity; they act as surface acceptors binding electrons from the conduction band of the solid and decreasing the surface conductivity, whereas oxygen vacancies act as donors increasing the surface conductivity. Ionosorption of adsorbed oxygen into several forms was described in Sections 3.2.4 and 3.2.5.

3.5 Transport Phenomena

Transport phenomena involve the motion of charge carriers under the action of applied electric internal or external fields. For semiconducting metal oxides, the conduction mechanism in the sensing layer has a very large impact on the magnitude and even on the direction of the sensor signal ([Bârsan 2011](#)). Even in very similar surface reactivity (reception function), the translation of the surface charge transfer processes into sensor resistance changes (transduction function) can be very different. Generally, the transport phenomenon (or transduction function) is described based on the nature of the sensing layer: compact or porous layers as shown in Figure 3-7 ([Barsan and Weimar 2001](#); [Gurlo et al. 2005](#)).

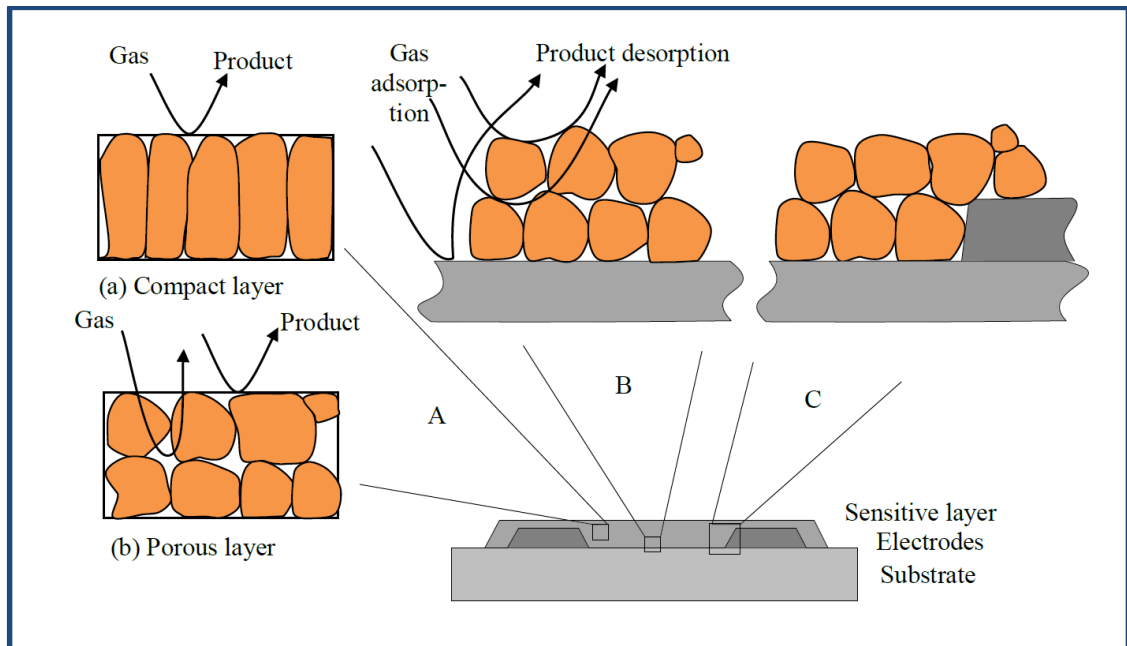


Figure 3-7: Schematic layout of a typical resistive gas sensor. The sensitive metal oxide layer is deposited over the metal electrodes onto the substrate (Barsan and Weimar 2001).

In the **compact layers**, the penetration and interaction of the target gas into the sensitive layer occurs only at the geometric surface. In the case of **porous layers** the gas penetrates into the sensitive layer down to the substrate. There are at least two possibilities in the **compact layers** scheme: **completely or partly depleted layers**, depending on the ratio between layer thickness and Debye length λ_D . For **partly depleted layers** (Figure 3-8), when surface reactions do not influence the conduction in the entire layer ($z_g < z_0$), the conduction process takes place in the bulk region (of thickness $z_0 - z_g$, much more conductive than the surface depleted layer) (Gurlo et al. 2005). The resistance is influenced by surface reactions, and the conduction is parallel to the surface. This explains the limited sensitivity in conductive layer with a reaction-dependent thickness.

For **completely depleted layers** in the absence of reducing gases (e.g., sensing on a SnO_2 nanowire), exposure to reducing gases could act as a switch to the partly depleted layer case (due to the injection of additional free charge carriers). Exposure to oxidising gases could act as a switch between partly depleted and completely depleted layer cases (Barsan and Weimar 2001; Gurlo et al. 2005).

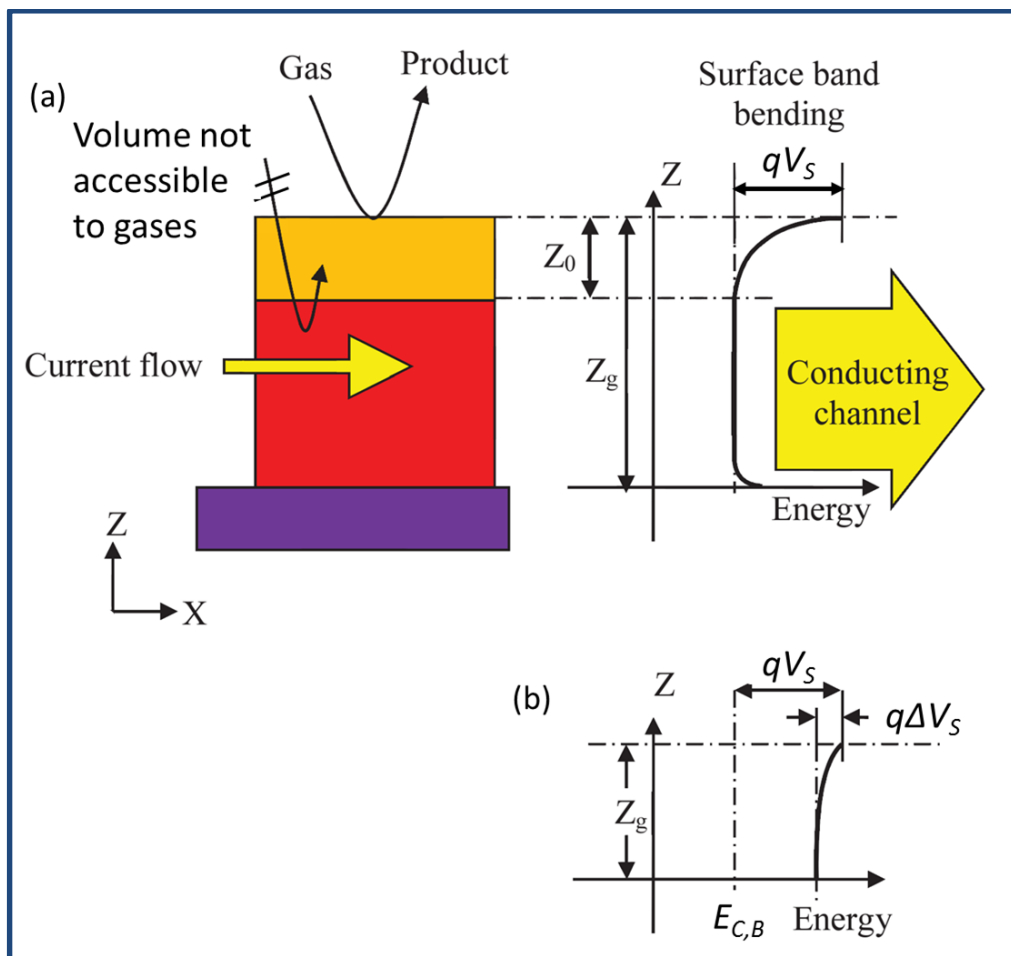


Figure 3-8: Schematic representation of a compact sensing layer with geometry and energy band representations; z_0 is the thickness of the depleted surface layer; z_g is the layer thickness and qV_s the band bending. (a) represents a partly depleted compact layer (“thicker”), and (b) represents a completely depleted layer (“thinner”) [Modified from [Barsan and Weimar 2001](#); [Min 2003](#)].

For **porous layers**, the presence of necks between grains may complicate the transport phenomena (Figure 3-9). It may be possible to have all three types of contribution presented in a porous layer (Figure 3-10): surface/bulk (for large enough necks $z_n > z_0$), grain boundary (for large grains not sintered together), and flat bands (for small grains and small necks) ([Barsan and Weimar 2001](#)). Also, the possibility of switching role of reducing gases is valid for porous layers. For small grains and narrow necks, when the mean free path of free charge carriers becomes comparable with the dimension of the grains, a surface influence on mobility should be taken into consideration.

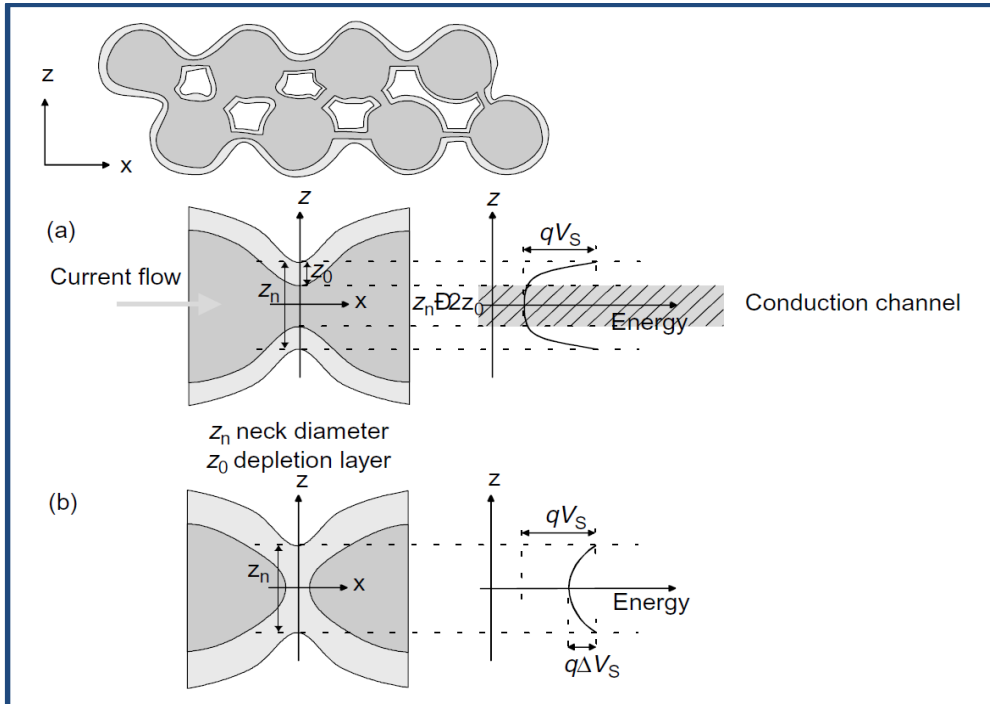


Figure 3-9: Schematic representation of a porous sensing layer with geometry and surface energy band-case with necks between grains (z_n is the neck diameter; z_0 is the thickness of the depletion layer): (a) represents the case of only partly depleted necks whereas (b) represents large grains where the neck contact is completely depleted (Gurlo et al. 2005).

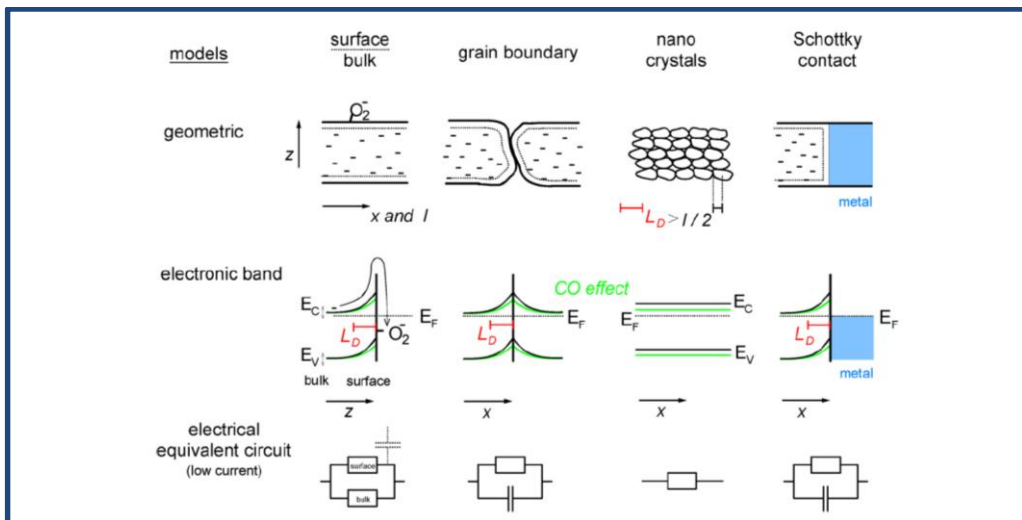


Figure 3-10: Different conduction mechanisms and changes upon O_2 and CO exposure to a sensing layer in overview. This survey shows geometries, electronic band pictures and equivalent circuits. E_C minimum of the conduction band; E_V maximum of the valence band; E_F Fermi level; L_D Debye length (Barsan et al. 2007).

This happens because the number of collisions experienced by the free charge carriers in the bulk of the grain becomes comparable with the number of surface collisions; the latter may be influenced by adsorbed species acting as additional scattering centres ([Gurlo et al. 2005](#)).

A further detail of the conduction mechanism based on the sensing layers has been reported by Barsan and his co-workers ([Bârsan 2011](#); [Barsan et al. 1999](#); [Barsan and Weimar 2001](#)). Applications of different conduction models were presented for SnO₂ ([Fort et al. 2006](#)) and ZnO ([Yang et al. 2013](#)).

3.5.1 Charge Transfer Model and Space Charge Region

The Charge Transfer Model (CTM) consists of a process of extraction and injection of electrons by extrinsic surface acceptors or donors, connecting the sensing mechanism with a variation in the Space Charge Region (SCR) and, consequently, with variations in the layer conductivity ([Velasco-Vélez 2012](#)). The *n*-type behaviour of SnO₂ and ZnO is associated with the native non-stoichiometry caused by oxygen vacancies (or deficiencies) in the bulk of the metal oxide due to ionosorption and chemisorption (Figure 3-11).

Adsorbed oxygen (and other oxidizing gases such as NO₂ and O₃) usually traps electrons at the surface of *n*-type semiconductors, and form a space charge region near the solid–gas interface, as a consequence of charge transfer between the solid and the adsorbate (electron injection or extraction). This makes the surface charge (conductivity) of the semiconductor lower than the bulk conductivity, giving rise to energy band bending ($q\Delta V_s > 0$) and work function ($\Delta\Phi > 0$) at the region near the surface of the oxide grains. A detail of ionosorption for an electron acceptor interaction and an *n*-type semiconductor is illustrated in the right side of Figure 3-11. An electron acceptor molecule X_{gas} (such as O₂) is physisorbed at the surface of the metal oxide to create an unoccupied surface level. Consequently, an electron transfer from the sensing material will occur and a partial charge (X^{ad})^{δ-} will be trapped at the surface

and a depletion layer will result illustrated by a band bending. This band bending will increase with the concentration of chemisorbed ions at the surface until a steady state is achieved. The width of the depletion layer depends on the surface charge and therefore on the gas concentration of the gas X (i.e., O₂) ([Gurlo et al. 2005](#)).

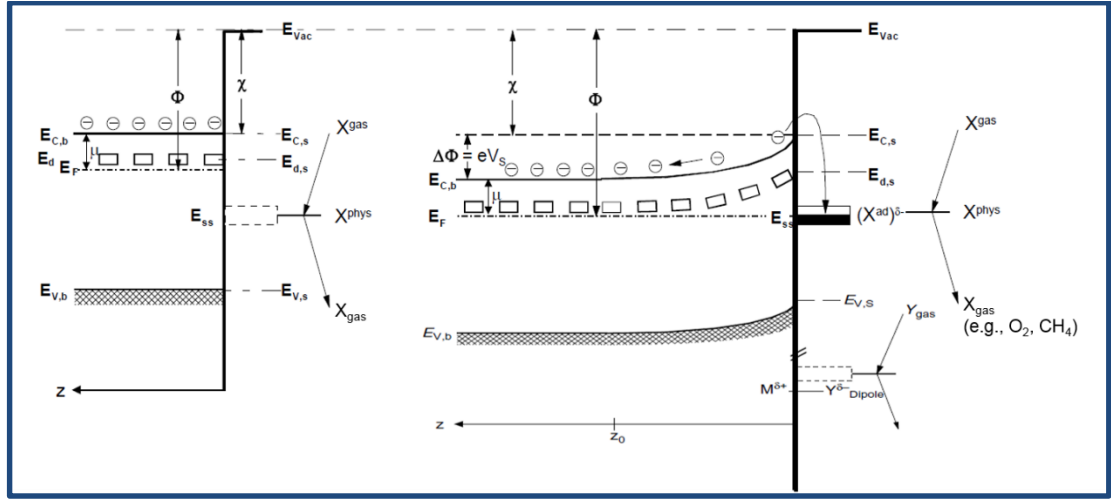


Figure 3-11: Band bending on *n*-type semiconductor during ionosorption of oxygen [modified from ([Gurlo 2006](#); [Schmid et al. 2004](#))].

The work function of semiconductors contain three contributions: the energy difference between the Fermi level and conduction band in the bulk ($E_C - E_F$)_b, band bending qV_S (q denotes elementary charge), and electron affinity χ (due to the definition, $qV_S = E_{C,S} - E_{C,B}$) ([Gurlo et al. 2005](#); [Sahm et al. 2006](#)):

$$\Phi = (E_C - E_F)_b + qV_S + \chi \quad (3.59)$$

Upon gas exposure, the three contributions may change:

$$\Delta\Phi = \Delta(E_C - E_F)_b + q\Delta V_S + \nabla\chi \quad (3.60)$$

Assuming that the difference between Fermi level and conduction band in the bulk is unaffected by gas adsorption at the surface, the change in the bulk can be neglected. Then, the work function changes induced by gas exposure can be modelled by the change in band bending and/or electron affinity:

$$\Delta\Phi = q\Delta V_S + \nabla\chi \quad (3.61)$$

From experiments, changes in the contact potential difference (CPD) due to changes in the ambient atmosphere are directly linked with changes in the work function of the sensing material ([Sahm et al. 2006](#)):

$$\Delta\text{CPD} = \frac{\Delta\Phi}{q} \quad (3.62)$$

where q is the elementary electron charge.

The corresponding conductance G may formally be described by the following equation ([Gurlo et al. 2005](#)):

$$G = G_0 \exp\left\{\frac{(E_F - E_C)_b - qV_s}{kT}\right\} = G_0 \exp\left\{\frac{\chi - \Phi}{kT}\right\} \quad (3.63)$$

Within a polycrystalline porous layer (Figure 3-2), the conduction mechanism can be described by the building of surface barriers due to the interaction between the surface of SnO_2 grains and adsorbed gas molecules, i.e. the bending of the bands. As the concentration of the free charge carriers at the surface depends on the height of the intergranular barriers, changes in the resistance of the sensing layer are correlated with changes in band bending ([Sahm et al. 2006](#)):

$$\begin{aligned} \frac{R_a}{R_g} &= \exp\left(q \frac{\Delta V_s}{kT}\right) \\ R_a &= R_g \exp\left(q \frac{\Delta V_s}{kT}\right) \end{aligned} \quad (3.64)$$

where R_a denotes the resistance in absence, R_g denotes the resistance in the presence of the investigated gas, and $q\Delta V_s$ represents the change in band bending due to the interaction with the analyte, V_s is the grain boundary potential, k is the Boltzmann constant. The Boltzmann constant is given as $k = 8.62 \times 10^{-5}$ eV/K ([Bai et al. 2013](#)).

$$\ln R_a = \ln R_g + \left(q \frac{\Delta V_s}{kT}\right) \quad (3.65)$$

$$\begin{aligned} \ln \frac{R_a}{R_g} &= \ln \frac{G_g}{G_a} = q \frac{\Delta V_s}{kT} \\ \ln(S + 1) &= q \frac{\Delta V_s}{kT} \end{aligned} \quad (3.66)$$

Therefore, the change in band bending, $q\Delta V_s$, can be determined from the slope ($q\Delta V_s/k$) of a plot of $\ln(S+1)$ versus $1/T$.

Assuming that changes of the electrical resistance due to gas interaction can be attributed mainly to the intergranular barriers: while the contribution of the contact resistance between sensing layer and metal electrodes to the overall resistance and, its changes due to gas interaction with the oxide grains are negligible. Thus, combining Equations (3.61) to (3.64), the change in electron affinity ($\Delta\chi$) is given as:

$$\Delta\chi = \Delta\Phi - kT \ln \frac{R_a}{R_g} \quad (3.67)$$

Therefore,

$$kT \ln \frac{R_a}{R_g} = kT \ln \frac{G_g}{G_a} = \chi - \Phi \quad (3.68)$$

According to [Gurlo et al. \(2005\)](#), the appearance of a dipole ($M^{\delta+} - Y^{\delta-}$) through the direct charge transfer from/to the metal atom (“localised chemisorption”) changes *only electron affinity* χ , the appearance of the depletion/accumulation layer (“ionosorption”) changes *only band bending* $q\Delta V_s$. In more complex cases, such as ethanol interaction in humid air, both types of changes could be expected; thus separating the contributions from these two effects can be made by performing simultaneous conductance and work function change measurements.

3.6 Surface Reaction Processes by Metal Oxide Semiconductors

Generally, gas sensing by metal oxide semiconductors is due to the charge transfer processes taking place between the semiconductor and the reacting gases adsorbed at the oxide’s surface. The actual manner in which the surface reactions are linked to the final sensor effect is observed as the change of the sensor’s resistance or conductance. This change depends on many factors such as specific material reactivity, microstructure, free charge concentration, sensitive layer morphology, etc ([Weimar and Barsan 2009](#)). In the energy band, electrons driven by the energy difference

between the conduction band and surface states can be trapped by surface states, resulting in a distinctive sensing mechanism. This sensing behaviour is dependent on the classification of the semiconductor: whether n -type semiconductors (in which electrons are the majority carriers) or a p -type (in which the holes are the majority carriers) semiconductors (Figure 3-12). The influence of the conduction type on n -type materials (e.g. SnO₂, WO₃, etc) and p -type materials (such as Cr₂O₃, Cr_{2-x}Ti_yO_{3+z}, NiO, etc) is presented in Figure 3-12.

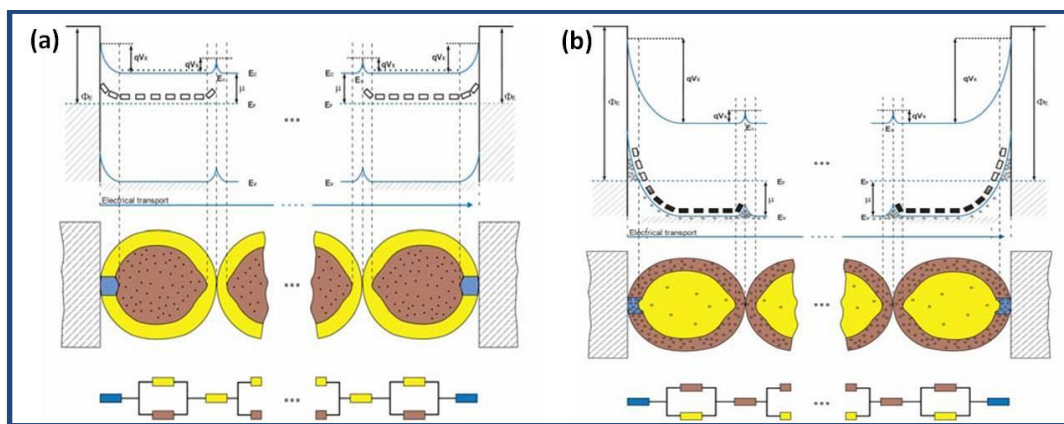


Figure 3-12: Schematic representation of the sensitive layer for semiconductor; brown colour indicates low resistance while yellow indicates high resistance elements: (a) n -type materials, and (b) p -type materials ([Weimar and Barsan 2009](#)).

The conduction processes exhibited by metal oxides are presented in details by ([Bârsan 2011](#); [Barsan et al. 1999](#); [Barsan and Weimar 2001](#)). Our interest in this research will be the sensing reaction of n -type metal oxide semiconductors with reducing gases (see Section 3.6.1).

3.6.1 Surface Reactions with Reducing Gases

The n -conducting properties of SnO₂ and ZnO are attributed to the electron donor effect of the oxygen surface defects (e.g., oxygen vacancies) in the crystal lattice, which can be singly and doubly ionised and play a significant role in the process of gas sensing. This can be explained in terms of a surface ionisation process, in which ionosorbed oxygen is removed from the metal oxide surface and in which electrons, initially trapped on surface oxygen ions, are re-emitted into the metal oxide

semiconductor conduction band, thus generating a sensor signal, as observed increase in the conductivity of the metal oxide ([Hackner et al. 2010](#)).

The sensor sensitivity is controlled by grain size and connectivity between grains. The presence of thin grain boundaries within the material promotes sensor resistance in large grains. As the grain size decreases to values near that of the thickness of the space-charge region (Debye thickness), ca. 10-100 nm for SnO₂, the so-called “all surface”, sensitivities are maximised ([Scott et al. 2001](#)). Properties of nanostructure, such as internal surface area, surface roughness, state of agglomeration, and tortuosity affect reaction-diffusion, and thus, control the sensitivity of thin films. [Scott et al. \(2001\)](#) reported three distinct effects of microstructure on the response of gas-sensitive resistors: the dimension of critical elements of the microstructure (“grains” and “necks”) in relation to the characteristic space charge dimension for the material; the effect of concentration gradients through the porous sensor structure of the gas to be detected, caused by the catalytic decomposition of the target gas on the heated surface of the sensor material; and the change in effective electrical connectivity through the random resistor network that constitutes the porous microstructure as some elements of the network are gas-sensitive and others are not.

The reaction of reducing gases (such as CO, H₂, alcohol) with *n*-type semiconductor (such as SnO₂ and ZnO) involve interaction with the adsorbed surface oxygen ions, and freeing electrons that can return to the bands. The interaction of target gas molecule with a solid metal oxide surface can be described by a number of consecutive steps including adsorption, chemical reaction and desorption of reaction products ([Krivetskiy et al. 2013](#)). The sensing mechanisms have been presented for major reducing gases, such as CO ([Fort et al. 2006](#)) and H₂ ([Gu et al. 2012](#)). Our discussion will focus on ethanol and methanol sensing on SnO₂ and ZnO, and their nanocomposites.

A typical representation of oxygen chemisorption in the presence of a reducing gas (CO₂) is shown in Figure 3-13.

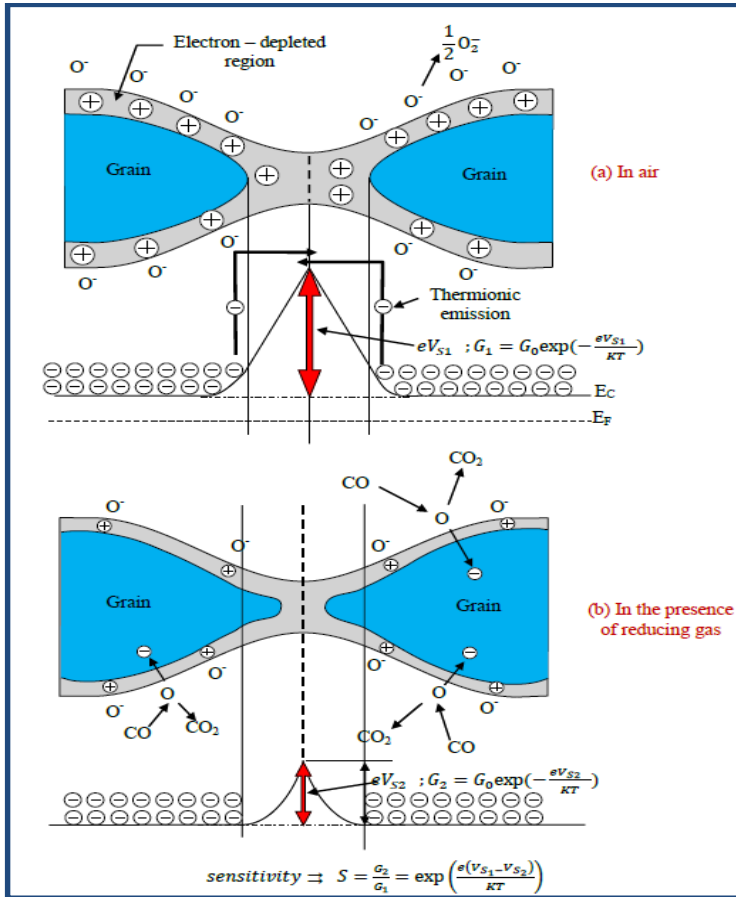
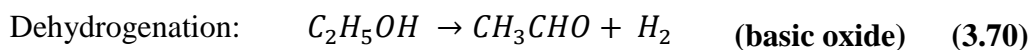
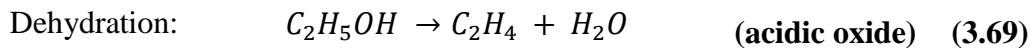


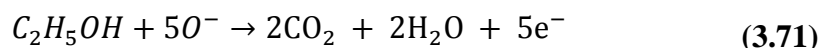
Figure 3-13: Microstructure and energy band model of a gas sensitive SnO₂ film (Licznarski 2004).

Initially, the adsorbed oxygen ions extract electrons from the metal oxide sensor and create a space charge region near the film surface (see Section 3.2.5). Then, depending on the acid–base properties of the oxide, adsorbed alcohol molecules react with ionic oxygen species and produce electrons at elevated operating temperature, via the following two reactions (Hemmati et al. 2011; Jinkawa et al. 2000; Ko et al. 2013; Yamazoe et al. 2003):



The formation of active sites on the sample surface and the reaction of alcohol molecules are shown schematically in Figure 3-14 (Mishra et al. 2013). For devices

made from coupled nanocomposites of SnO₂ and ZnO, dehydrogenation is the favoured reaction path since ZnO is a basic oxide (Lorenz et al. 2013). After dehydrogenation, the aldehyde, CH₃CHO, is subsequently oxidised by the chemisorbed oxygen ions as in the following equation (Ko et al. 2013):



Thus, the surface oxidation reaction of ethanol with SnO₂ and ZnO could be represented as (Yang et al. 2009):

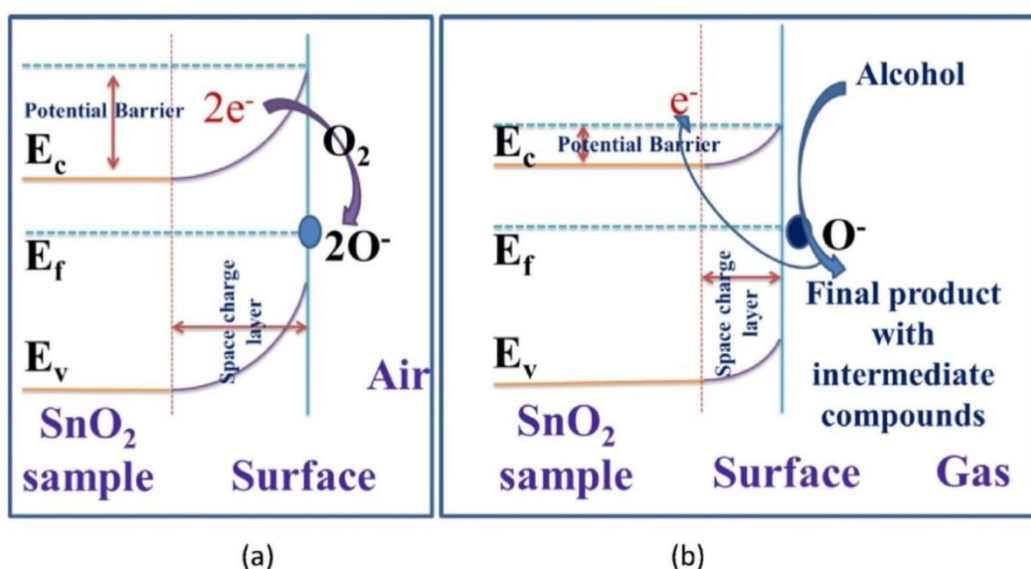
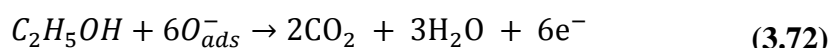
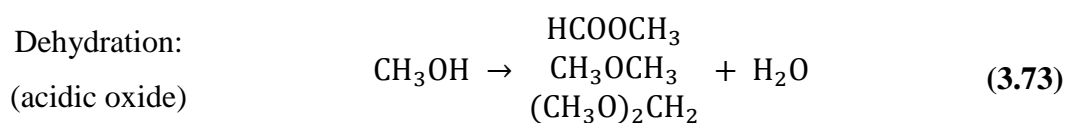


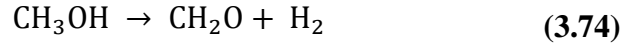
Figure 3-14: Schematic representation of (a) adsorption of atmospheric oxygen on the sample surface, and (b) reaction of alcohol molecules with the adsorbed oxygen species (active sites) (Mishra et al. 2013).

For methanol, the main products include dimethylether (CH₃OCH₃), methylformate (HCOOCH₃) and dimethoxymethane or methylal ((CH₃O)₂CH₂) formed by an dehydration under acidic condition, whereas formaldehyde (CH₂O) are formed by oxidative dehydrogenation path (Neri et al. 2006):



Dehydrogenation:

(basic oxide)



As the electronegativity of the metal cation added increased, the primary product from ethanol changed to C_2H_4 , while methanol changed to CH_4 . Depending on the operating conditions, the products of the dissociation could subsequently oxidise, partially or completely, to CO_2 , CO and H_2O . Dehydration usually takes place at lower temperatures compared with dehydrogenation ([Cheong and Lee 2006](#)). Nevertheless, both the dehydration and dehydrogenation reactions cannot affect the electrical resistance of the sensor element unless those are followed by consecutive reactions which consume the adsorbed oxygen ([Jinkawa et al. 2000](#)). Thus, the variation in surface resistance is dependent on the species and amount of chemisorbed oxygen on surface. The adsorption reaction process is described in Section 3.2.5.

After the reaction of a reducing gas with the surface oxygen ions, electrons are freed and may return to the bands. The resulting effect is the decrease in the band bending ($q\Delta V_S < 0$ and $\Delta\Phi < 0$) and, for the metal oxide, the increase of the surface conductance ([Gurlo et al. 2005](#)). In the development of a model for the dependence of the resistance on the reducing gas concentration, the following assumptions can be made: (i) the reaction of a reducing gas takes place with the previously adsorbed oxygen ions; and (ii) the adsorption of reducing gas is proportional with the gas concentration in the gas phase (quite reasonable but never really experimentally proved). Thus, one can combine quasi-chemical reactions formalism with semiconductor physics calculations to obtain power-law dependencies (of target gas partial pressure p_g or concentration C_g) of the form ([Gurlo et al. 2005](#)):

$$G \sim p_g^n \sim C_g^n \quad (3.75)$$

where the value of n depends on the morphology of the sensing layer and on the actual bulk properties of the sensing materials. In terms of sensitivity, this can be represented as ([Arnold et al. 2009](#)):

$$S = kC^n \quad (3.76)$$

where S is the sensitivity, C is the analyte concentration, and k and n are empirically determined constants that depend on the nature of the analytes being detected.

3.7 Surface Reaction Process and Conduction Model of Coupled SnO₂ and ZnO Nanocomposite

Applications of coupled metal oxides are expected to produce interesting array of nanocomposites¹² for wide applications. Very little is known about the reaction behaviour of SnO₂ with ZnO; most of the knowledge coming from the field of ZnO based varistors ([Peiteado et al. 2006](#)). It is expected that SnO₂ will act as double ionised donor impurity in ZnO lattice, or vice versa, so contributing to increase the semiconductor behaviour of this oxide. The properties of nanocomposite nanostructures, such as morphology and the interfacial characteristics, along with the combined synergetic or complementary behaviours of the materials possess unique physical, chemical, optical, mechanical, magnetic and electrical properties unavailable from that of the component materials and have attracted much attention for a wide range of device applications such as gas sensors ([Yang 2011](#)).

Pure SnO₂ has a higher conductivity than pure ZnO ([Hemmati et al. 2011](#)). Coupled metal oxide nanostructures (e.g., SnO₂–ZnO) have high specific surface area; as such, they exhibit very good potential for applications in gas sensors, photo-catalysis, photoelectrochemical cells and nanoscale optoelectronic devices ([Sun et al. 2007](#); [Vaezi 2011](#)). Various synthetic and characterisation methods of have been reported coupled metal oxide nanostructures, such as nanofibers ([Asokan et al. 2010](#)), nanowires ([Choi et al. 2013](#); [Thanh Le et al. 2013](#)), nanobelts ([Sun et al. 2007](#)). The applications of SnO₂–ZnO for gas sensing have been reported ([Yoon et al. 2010](#); [Zhang and Zhang 2008](#)).

But presently, there is no confirmed gas sensing mechanism for coupled metal oxide nanocomposites, with detailed activity of the constituent metal oxide with the target gas. Therefore we will attempt to present a detailed possibility of the sensing mechanism of SnO₂–ZnO nanocomposite.

¹² Nanocomposites are nanostructures formed by mixing two or more dissimilar materials having nano-dimensional phase(s) in order to control and develop new and improved structures and properties ([Yang 2011](#)).

Based on surface-conductance change mechanism, [Tianshu et al. \(1999\)](#) observed that the gas sensing mechanism of SnO₂ and ZnO is similar to their principles of catalytic process. A strong photoconducting response of SnO₂ can achieve a favourable adsorption–desorption behaviour at room temperature by illuminating the devices with ultraviolet (UV) light of energy near the SnO₂ band gap ([Comini et al. 2009a](#)). Photocatalytic analysis of SnO₂–ZnO binary systems is reported by ([Liu et al. 2010](#); [Zhang et al. 2004b](#); [Zheng et al. 2014](#)). The photocatalysis of ZnO–SnO₂ nanocomposite has higher activity than individual SnO₂ and ZnO separately ([Cun et al. 2002a](#)). [Krivetskiy et al. \(2013\)](#) reported a great similarity between sensor materials and catalysts of metal oxide heterogeneous reactions. The major difference between the sensor materials and catalysts is that the interaction of the former with components of the gas phase to ensure maximum changes in the intrinsic fundamental properties (electrical, optical and magnetic ones) of the metal oxide, while catalysts promotes the yield of the reaction products. Therefore, the sensing mechanism of coupled metal oxide nanocomposite can be studied using the principles

A mechanistic scheme of the charge separation and photocatalytic reaction for SnO₂–ZnO photocatalyst is shown in Figure 3-15. From photocatalysis, the conduction band position of SnO₂ is lower than that of ZnO; therefore, SnO₂ act as a sink for the photogenerated electrons in the coupled oxides ([Zhang et al. 2004b](#)). Since the holes move in the opposite direction from the electrons, the photogenerated holes in SnO₂ might be trapped within the ZnO particle, making charge separation more efficient; then the recombination of electrons and holes in SnO₂–ZnO is greatly suppressed by catalysis.

This is another reason that the nanometer coupled oxide ZnO–SnO₂ possessed both higher photocatalytic oxidation and reduction activities than those of single ZnO or SnO₂. A modification in a photocatalytic system is presented in Figure 3-15 ([Liu et al. 2010](#); [Zheng et al. 2012](#)).

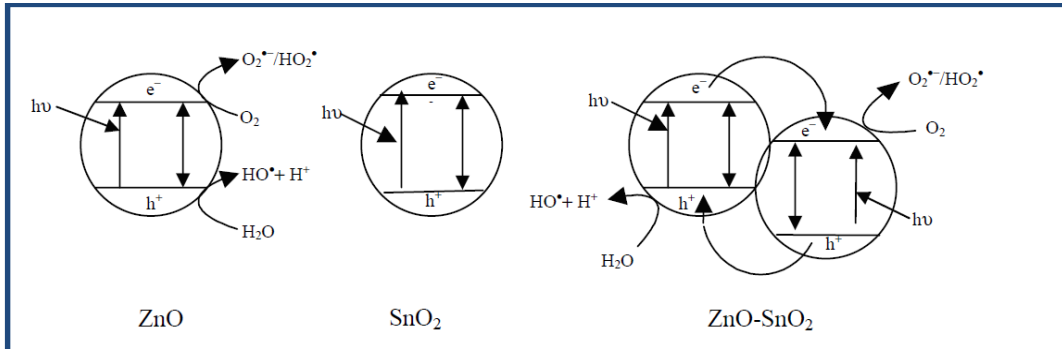


Figure 3-15: A schematic diagram illustrating the principle of charge separation and photocatalytic activity for the couple oxides ([Zhang et al. 2004b](#)). A similar mechanism is presented by ([Zheng et al. 2012](#)).

The photocatalytic activities of coupled metal oxides can provide further insight into the synergistic effects of metal ion doping and semiconductor/semiconductor heterostructure on the activity of nanocatalysts and sensing applications ([Zheng et al. 2014](#)). The electron transfer and the energy level are illustrated in Figure 3-16.

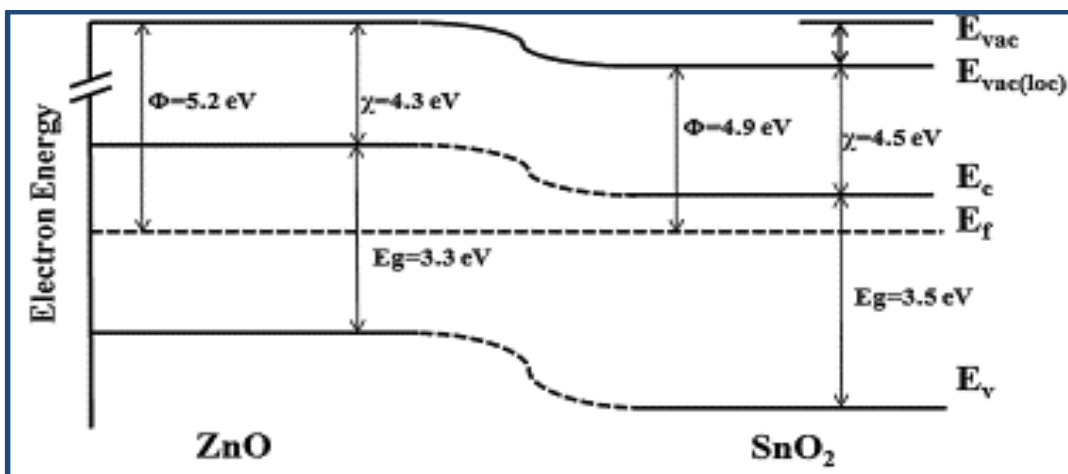
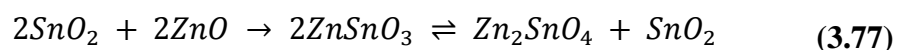


Figure 3-16: Schematic of the band energy level of ZnO-SnO₂ hetero-junction used for gas sensing ([Mondal et al. 2014](#)).

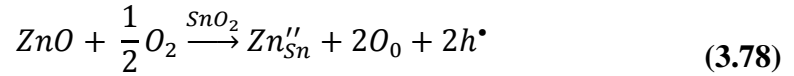
The solid reaction between SnO₂ and ZnO results in zinc stannate, with two possible forms expressed as:



The two different oxides (i.e., ZnSnO₃ or Zn₂SnO₄) are non-toxic, but they have differing crystallographic structures and Zn:Sn ratios. The ZnSnO₃ has orthorhombic

phase, while Zn_2SnO_4 has a cubic spinel crystal structure; but both have a large band gap of 3.6 eV ([Young et al. 2002](#)). Zn_2SnO_4 is more stable than $ZnSnO_3$; decomposition of $ZnSnO_3$ occurs at 700 °C, while Zn_2SnO_4 is reported to be thermally stable even at 1300 °C ([Cun et al. 2002b](#)). By analysis of morphology, the addition of SnO_2 to ZnO causes a reduction in the mean crystallite size of ZnO and SnO_2 . [Liu et al. \(2010\)](#) reported a band gap of 3.14 eV for SnO_2 - ZnO (at 500 °C); this is between that of pure ZnO and SnO_2 . The band gap energy of SnO_2 - ZnO is attributed to band gap energy contributions of the corresponding ZnO , SnO_2 and/or Zn_2SnO_4 crystallite phases in the composite nanostructure ([Liu et al. 2010](#)).

The addition of Zn^{2+} reduces the conductivity of SnO_2 without any change in its microstructure ([Hemmati et al. 2011](#); [Yu and Choi 1998](#)). The Zn^{2+} cations substitutes the Sn^{4+} cations in the n -type SnO_2 lattice, and increases the concentration of oxygen ion vacancy (i.e. hole carriers) by the following reaction:



where in the Kröger–Vink notation, Zn''_{Sn} is a zinc ion sitting on a tin lattice site with two negative charges, and O_0^X is an oxygen ion sitting on an oxygen lattice site with a neutral charge while, $V_0^{\bullet\bullet}$ is an oxygen ion vacancy, with double positive charges. The increased hole concentration due to the acceptor reduces the electron concentration and thus the conductivity values of n -type SnO_2 .

Individually, SnO_2 and ZnO have contributed to a significant range of sensor devices. However, the photocatalytic incorporation of SnO_2 was reported to have no effect on the conduction mechanism in ZnO , because the non-linearity of the Sn-added $Zn_{1-x}Sn_xO$ is quite similar to that of the Sn-free ZnO ([Park et al. 2008](#); [Peiteado et al. 2006](#)).

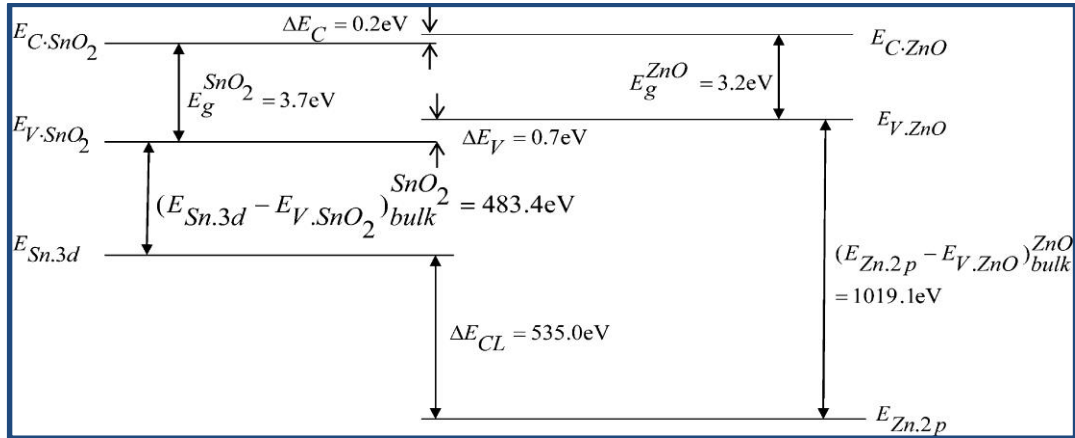
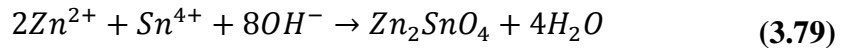
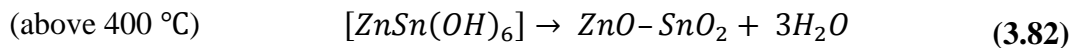
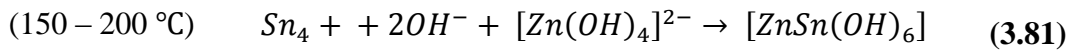
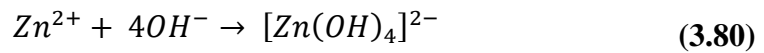


Figure 3-17: Band alignment diagram of the SnO₂-ZnO photocatalyst (Uddin et al. 2012).

From the reaction of ZnO and SnO₂, the nanocomposites (SnO₂-ZnO, ZnSnO₃, Zn₂SnO₄) formed could be initiated by the reaction between Zn²⁺, Sn⁴⁺ and OH⁻ ions (Mondal et al. 2014):



The proposal is that a meta-stable cubic [ZnSn(OH)₆] phase is first produced by the reaction between above three ions at 150–200°C. But at higher temperature, [ZnSn(OH)₆] decomposes and re-crystallises to form ZnO-SnO₂ nanocomposite (Hemmati et al. 2011). Therefore it can be confirmed that the whole ZnO-SnO₂ formation process is expressed by the following chemical equations (Mondal et al. 2014):



Mondal et al. (2014) compared nanostructures annealed at the different temperatures (Figure 3-18).

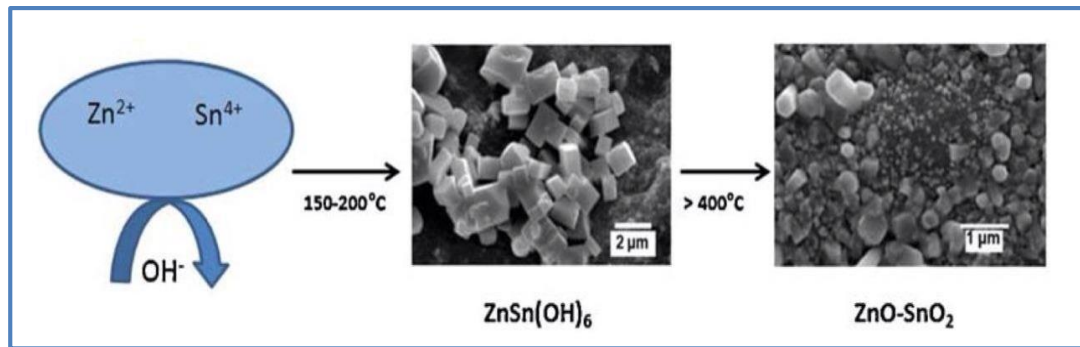


Figure 3-18: Schematic of the formation process of ZnO–SnO₂ composite. (a) SEM image of the meta-stable [ZnSn(OH)₆] intermediate and (b) morphology of ZnO–SnO₂ composite ([Mondal et al. 2014](#)).

Thus, in our research, the nanostructures were annealed at 600 °C to confirm that the SnO₂–ZnO thin films were formed. However, this study will seek to analyse further details on the sensing behaviour of SnO₂–ZnO, and its possible products across its spectrum of combination.

3.8 Conclusion

Sensing mechanism, surface chemistry and transport phenomena of metal oxide semiconductors are discussed in this chapter. Sensing and transport mechanism includes charge transfer in either the conduction band or the localised manner. Types of layers considered include compact, porous, compact, completely or partly depleted layers. The surface chemistry includes adsorption mechanisms such as physisorption, chemisorption, ionosorption, hydrogen bonding, oxygen and water vapour adsorption processes. Adsorption-desorption kinetic models presented are Langmuir, BET, Freundlich and Kolmogorov models. Surface reaction processes by metal oxide semiconductors, and particularly, conduction models of SnO₂ and ZnO sensors are discussed.

Chapter Four

Materials Design, Fabrication and Characterisation of Metal Oxide Gas Sensors

4.1 Introduction

This chapter presents a detailed description of the design, development and fabrication of the different types of thin film sensors prepared based on the combination of SnO₂ and ZnO powder targets. The flow-diagram of gas sensor fabrication, characterisation and sensing process is presented in the following procedures (Figure 4-1). The gas sensor fabrication, characterisation and sensing processes were undertaken at the National Nanofabrication Centre, Centre for Nano Science and Engineering (CeNSE), Indian Institute of Science (IISc).

4.2 Experimental Procedures

- 1) Standard wafer/substrate cleaning
- 2) Thermal oxidation of the wafer
- 3) Preparation of metal oxide target
- 4) Deposition (sputtering) of gas sensitive thin film on the substrate
- 5) Deposition of heater on the rear side of the substrate by sputtering through a precision mechanical shadow mask
- 6) Deposition of electrodes on the sensitive film and attachment of leads for electrical measurement.
- 7) Characterisation of thin film nanostructure
- 8) Gas sensing process

The flow chart in Figure 4-1 describes the sensor design, fabrication and characterisation procedures.

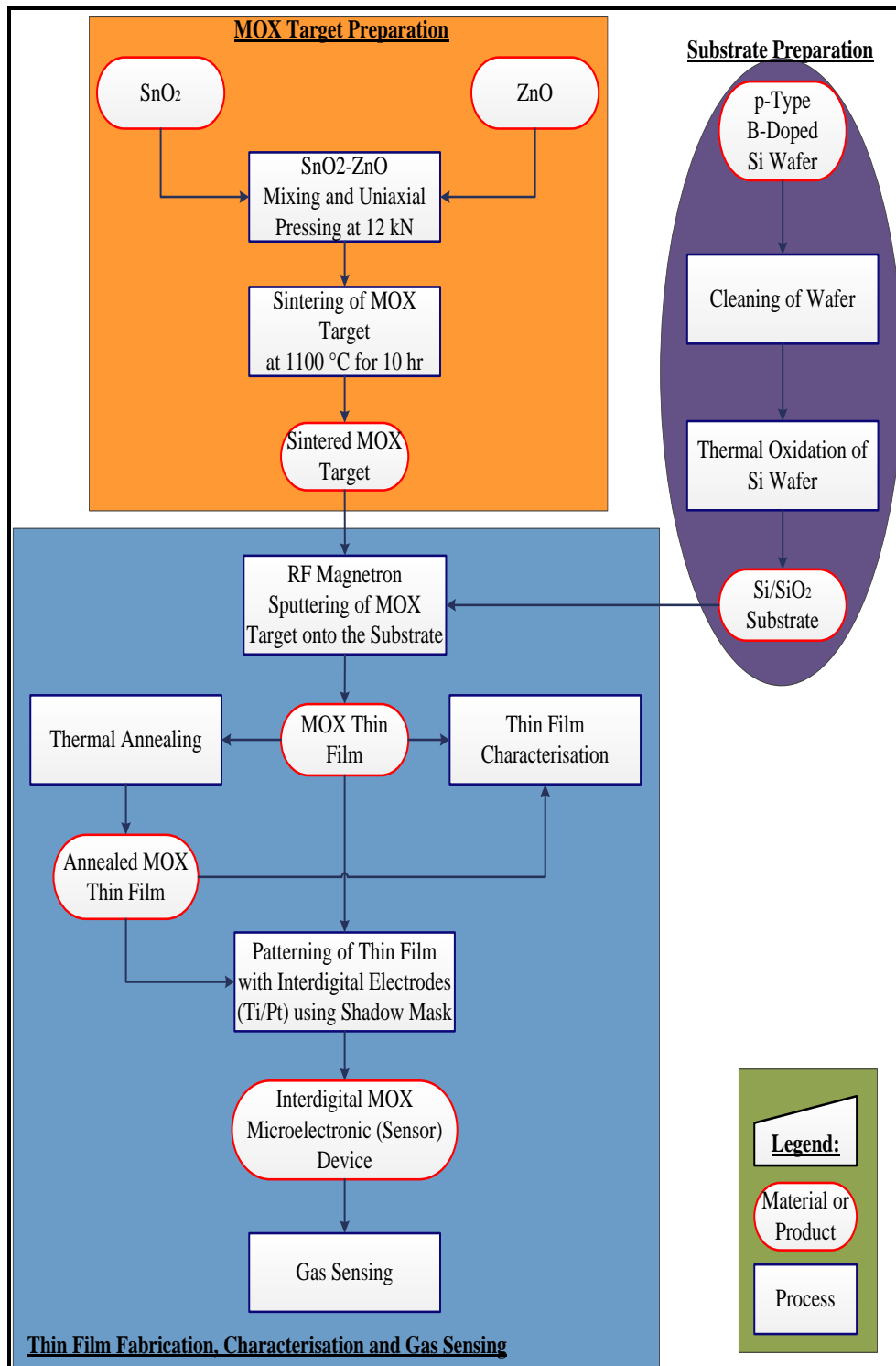


Figure 4-1: Flow-diagram of gas fabrication, characterisation and sensing.

4.3 Preparation/Cleaning of the Wafer/Substrate

The substrates used the experiments were *p*-type boron-doped Si (100) wafers (from www.semiwafer.com). They were one-sided polished, with diameter of 7.62 cm, and thickness of 375 ± 25 μm . Measured by four point probe technique, they have sheet resistance of 1.0 – 15.0 Ω/sq . In order to achieve high performance of devices fabricated, the silicon wafers were cleaned using standard cleaning procedure to remove organic, inorganic and metal particulate contaminants, as described below.

4.3.1 Piranha Cleaning

Before thermal oxidation, the silica wafers were cleaned with a freshly prepared piranha solution to remove any dirt or organic matter from the wafer substrates. **The piranha solution** is a strong oxidising solution composed of sulphuric acid and 30% hydrogen peroxide (i.e., in a 1:3 ratio mixture) ([Nakamura et al. 2001](#)). Usually, it is prepared in a fume hood. The resulting mixture reacted exothermic with vigorous bubbling, as it was continuously (but slowly) stirred with the temperature heated up to about 110 °C. The solution was allowed to cool slightly to a stabilised condition before use.

Piranha Cleaning Process: To avoid a potential violent boiling or explosion, or thermal shock that could crack the wafer, the cleaning process involved turning on the heat and gentle immersion of the wafer into the piranha solution. The wafer was cleaned in the solution for 20-30 min at temperature of 100-110 °C. Then, the wafer was gently removed from the solution, trying to avoid dripping. The wafer was immersed in rinse beaker with running deionised water for 5-10 min. The wafers were air dried, ready for oxidation. To dispose the used piranha solution, it was allowed to cool to room temperature, aspirated and then carefully poured into the waste acid sink while running copious amounts of water over the sink.

The standard cleaning process of the Si wafers was concluded by a sequence of acetone, methanol, deionised water, and blow dry process, before thermal oxidation.

4.3.2 Thermal Oxidation

Thermal oxidation of the Si wafers involved a three-step process: a **wet-dry-wet oxidation** process. The **wet-dry-wet oxidation** process was undertaken at a temperature of 1150 °C for 90 minutes using a Horizontal Production Furnace, manufactured by Tempress® Systems, The Netherlands. The advantage is to produce an electrically cleaner oxide interface for effective film reactivity.

4.4 Preparation of Metal Oxide Target

4.4.1 Preparation of Molar Concentrations

The analytical grade SnO₂ powder (product number 244651) was 325-mesh, 99.99% trace metal basis. The analytical grade ZnO powder (product number 205532) was <5 μm particle sizes, 99.99% based on trace metal analysis. Both metal oxides were purchased from Sigma Aldrich.

The 25 Tons Manual Lab Press (Table-Top) from Kimaya Engineers, India, was used for this research (Figure 4-2). The die of the manual press compartment has an internal diameter of 3.0 in (i.e., 7.62 cm) and the required thickness of the pellet, *h*, was 4 mm (i.e., 0.4 cm).

The preparation of the target pellets involved mixing, compacting and sintering of the metal oxide powders. Using the theoretical density of the compound and expected thickness of the target pellet, the mass of the powder in the compartment, *m*, was calculated as follows:

$$m = \rho * v \tag{4.1}$$

where ρ = density of metal oxide powder

v = volume of metal oxide powder in the manual press compartment

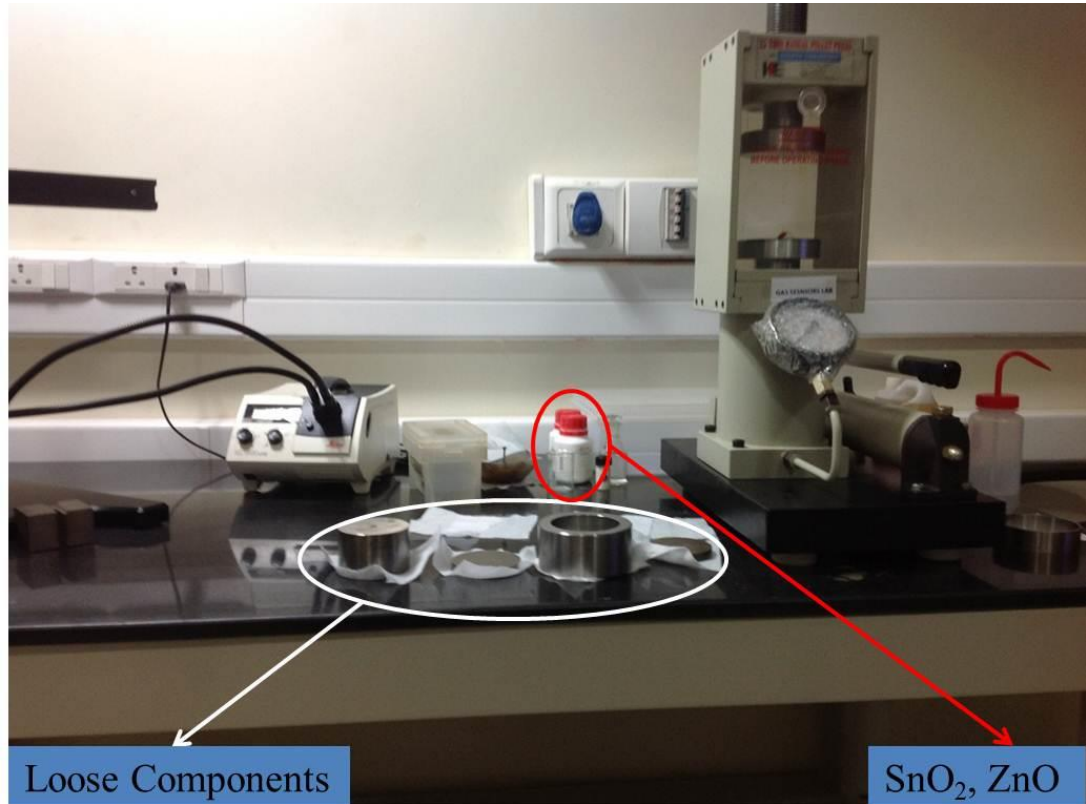


Figure 4-2: 25-Ton Manual Laboratory Press (Table-Top).

The basic properties of SnO₂ and ZnO are given in Table 4-1.

Table 4-1: Basic properties of SnO₂ and ZnO

| Property | SnO ₂ | ZnO |
|------------------------------|------------------|--------|
| Molar Mass (g) | 150.709 | 81.408 |
| Density (g/cm ³) | 6.95 | 5.606 |
| Melting Point (°C) | 1630 | 1975 |

The pore-free density of the mixed powder is calculated as ([Höganäs 2012](#)):

$$\rho_{Mix} = \frac{1}{\left(\frac{w_{SnO_2}}{\rho_{SnO_2}} + \frac{w_{ZnO}}{\rho_{ZnO}}\right)} = \frac{\rho_{SnO_2} * \rho_{ZnO}}{(\rho_{ZnO} * w_{SnO_2}) + (\rho_{SnO_2} * w_{ZnO})} \quad (4.2)$$

where ρ_{Mix} = density of the powder mix (g/cm³)

w_{SnO_2} = weight fraction of SnO₂ (g)

ρ_{SnO_2} = density of SnO₂ (g/cm³)

w_{ZnO} = weight fraction of ZnO (g)

ρ_{ZnO} = density of ZnO (g/cm³)

Therefore, five metal oxide (MOX) sensors were prepared based on the mole compositions of the SnO₂ and ZnO mixtures (Table 4-2). The production of metal oxide (MOX) pellets involved combination of the SnO₂ and ZnO powders in their mole fractions, and thorough mixing. The MOX powder (or mixture) was then compacted using the nanoparticle Table-Top 25 Tons Manual Lab Press (Figure 4-2).

Table 4-2: Molar fraction compositions of the metal oxide mixtures

| Sensor Type | Mole Percent | |
|-------------------------------|------------------|-----|
| | SnO ₂ | ZnO |
| S | 100 | 0 |
| S ₃ Z ₁ | 75 | 25 |
| SZ | 50 | 50 |
| S ₁ Z ₃ | 25 | 75 |
| Z | 0 | 100 |

Initially, the loose components of the press were washed with isopropanol and acetone, and then lubricated with stearic acid. The metal oxide (SnO₂ and ZnO) powder was weighed (as described in Table 4-2), and mixed thoroughly at different mole ratios, with the mole fractions in the range 25–100%, and poured into the manual press compartment. The components of the press were coupled, the metal oxide mixtures were compacted into a target using a hydraulic press with a pressure typically of a uniaxial force of 12 kN applied to the nanoparticles for 20 min to obtain the target pellet. The target pellets were stored in a pellet box, ready for sintering.

4.4.2 Sintering

Sintering is process of compaction of loose agglomerate of nanoparticles into a coherent nanostructured solid at temperatures below their melting point. This process involves external control limited to macroscopic parameters like temperature and pressure, resulting in significant structural self-organisation on the particle scale to create a nanocrystalline solid of macroscopic dimension ([Wolf et al. 2012](#)).

During this research, sintering was undertaken in a tube furnace under a heated flowing oxygen atmosphere with constant heating rate 10 °C/min to a maximum of

1100 °C for SnO₂, ZnO and mixed samples. Generally, the sintering temperature can be correlated with the material's melting point; a powder is converted into a solid at temperatures below the melting point. To improve the optimisation process, the heating was sustained at the maximum temperature for 5 hours to reduce cost.

During the sintering process of SnO₂–ZnO nanoparticle mixtures, there is a probable formation of a Zn₂SnO₄ (or ZnSnO₃) phase at the grain boundaries as the predominant densification mechanism occurs ([Liu and Ning 2009](#)). The cross-sections of the sintered pellets were mechanically polished into discs of 18 mm in diameter and 3 mm in thickness before thin film deposition.

4.5 Thin Film Deposition: Radio Frequency (RF) Magnetron Sputtering

Thin film deposition was undertaken by RF magnetron sputtering using the Tecport Sputter Coater (Figure 4-3). The sputtering process is a plasma phenomenon where energetic gas ions bombard the surface of a solid (target material) and eject plasma, which are then deposited onto the surface of a substrate.

The Tecport Sputter Coater can be used for the deposition of metals, metal oxides, dielectrics and alloys. Operating gases are argon and oxygen (and nitrogen for venting). It has four circular substrate holders of 6-in diameter, and capable of a coating uniformity up to 4-in substrate size using target of dimensions 3-in diameter and equal to or less than 6 mm thickness. Its substrate heating could be up to 350 °C using radiant heaters, and could operate at substrate planetary rotation.

In this research, the MOX thin film was deposited over the surface of Si/SiO₂ substrate using RF sputtering technique. The as-prepared MOX target, 18 mm in diameter and 3 mm in thickness, was placed in the ceramic disc, while the substrates were attached onto the substrate holder with heating block (Figure 4-4).



Figure 4-3: Tecport Sputter Coater.

The operating conditions are as stated in Table 4-3.

Table 4-3: Process parameters for Tecport RF magnetron sputtering of MOX thin films

| | |
|-----------------------------------|---|
| Target Material | MOX (SnO ₂ , ZnO, or SnO ₂ -ZnO Mixtures) |
| Target and Substrate Temperature | Room temperature |
| Target to Substrate Distance (cm) | 5 |
| Power (W) | 60 W |
| Base Pressure (mbar) | 5×10^{-6} |
| Working Pressure (mbar) | 3×10^{-3} |
| Pre-Deposition Time (sec) | 600 |
| Deposition Time (min) | 5, 10, 15, 20, 30, 45 |
| Hidden Ar | On |
| Ar Gas (sccm) | On |
| O ₂ (sccm) | No |

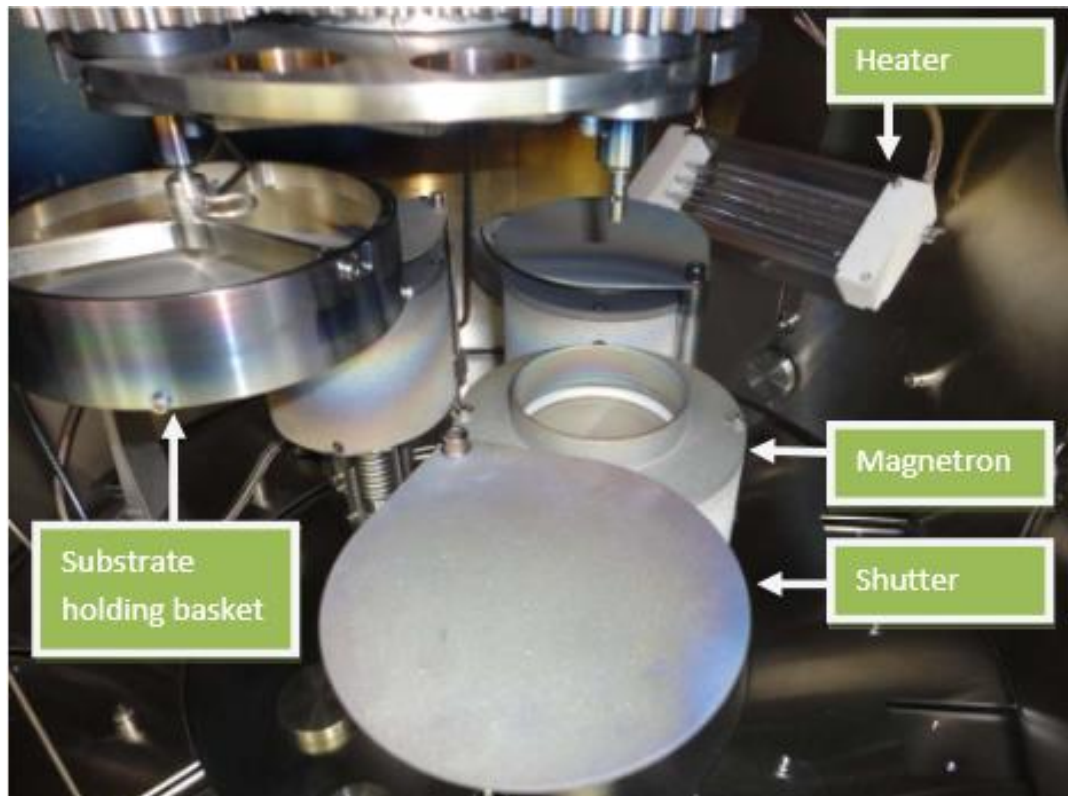


Figure 4-4: Tecport sputter coater open chamber.

The distance between the target and substrate could affect the quality of MOX film; when it is too close there may be contamination of the film by impurity, and when it is too long, the quality of plasma deposition may be poor. Aluminium foil was used to cover the edges of each substrate to provide a sharp edge on the film for metric thickness measurements with a Dektak profilometer after thin film deposition.

The RF power applied to the plasma was tuned to regulate the sputtering yield rate. This power was supplied by RF generator at a frequency of 13.56 MHz. At this frequency, it experienced non-interference with radio transmitter signals ([Youssef et al. 2008](#)). Initially, the chamber was evacuated by setting the pressures lower than 5.0×10^{-6} mbar, using the diffusion and rotary pump. The operating pressure determines both the glow discharge and rate of film deposition. The discharge was sustained by ionising collisions of electrons in the gas. The rate of ionising collisions decreased with decreasing gas density (and hence gas pressure), so that the discharge current will also decrease. Alternatively, as electrons undergo collision, sputtered plasma from the

target may collide with gas atoms on their way to the substrate, at a rate which will increase with increasing pressure.

Sputtering was done in an atmosphere of a mixture of argon (99.99%) and oxygen (99.99%). Oxygen serves as the reactive gas while argon acts as the sputtering enhancing gas ([Ozgur et al. 2005](#)). The oxygen partial pressure percentage maintained at 15%, and nitrogen gas was vented through the mass-flow-controlled gas inlets. The MOX target was powered to strike the plasma, and set to pre-deposit for 10 minutes. Pre-deposition helps to clean any dirt from the surface of the target, and deposits a fine layer of MOX on the chamber walls thus preventing further contamination due to outgassing from the surface. Also, it stabilises the plasma sputtering rates from the target, particularly if the target is a nanocomposite. All the thin films were deposited at room temperature (no intentional heating of the substrate).

The above deposition parameters, such as the O₂/Ar gas pressure, target-substrate distance, RF power, and gas flow rate were arrived at after as optimal conditions. With expected film thickness of 50 nm to 1µm, all sputtering conditions (except the deposition time) were maintained the same during the films deposition in order to avoid changes in the stoichiometry of MOX films, or influence in their structural and optical properties.

4.6 Post-Deposition Treatment: Annealing

Thermal annealing is the heat treatment of nanostructures in order to alter its material and mechanical properties. The process involves heating the material above its critical temperature, sustaining heating at that temperature for some time, and then slowly cooling. Usually, heating is at approximately 900–1100 °C in nitrogen or hydrogen gas atmosphere. The effects of thermal annealing include activation of defect centres in the nanostructures, and minimisation of long-term drifts in later operation ([Fahrner 2006](#)).

In this study, after deposition, some of the MOX thin films were thermally annealed in N₂/H₂ atmosphere at an annealing temperature of 600 °C. The annealing process involved heating (5 min), annealing (90 min) and cooling (15 min). From a base pressure of 4×10^{-2} Pa, the working pressure was 5×10^{-2} Pa in the vacuum.

The furnace atmosphere during the annealing process is a reducing environment, with the MOX reduced by H₂ ([Jin et al. 2010](#)). At this annealing condition, oxygen escaped from the MOX ([Tu et al. 2012](#)), and resulted in a lower concentration ratio of O to Sn, and O to Zn. Therefore, from optimal processes, annealing was undertaken at this condition to reduce cost and increase the Sn and or Zn interstitial concentration, and this result in the presence of more O vacancies in the sensing device. With the sputtering conditions, this supports the oxygen deficiency in the MOX thin films, and confirms the production of oxygen-deficient or *n*-type metal oxide semiconductors.

4.7 Interdigital Patterning

Prior to deposition of platinum (Pt), titanium (Ti) was deposited onto the thin film. This process is to ensure a good adhesion of Pt onto the substrates.

4.7.1 Optimisation of Interdigital Patterning Process

The substrates were rinsed with acetone and dried at 245 °C for 90 s. The printing of interdigital electrodes on the substrates was undertaken by lithographic lift-off method, using the EVG 620 Double Sided Aligner. Then the interdigital electrodes were sputtered with Ti/Pt (Figure 4-5a); subsequently, a lift-off of the photoresist was carried out using acetone.

Another attempt involved the application of a double photoresist, and spin coating of dual photoresist. The process began with application of photoresist LOR 10A and baking at 135 °C for 60 s; allowed to cool; then application of photoresist S183, and baking at 135 °C for 60 s. During the lift-off process, everything (including the pattern) etched out again. Another set of patterns were made using A25216E photoresist. The

results were the same: complete lift-off of the pattern; unsuccessful lithographic process.

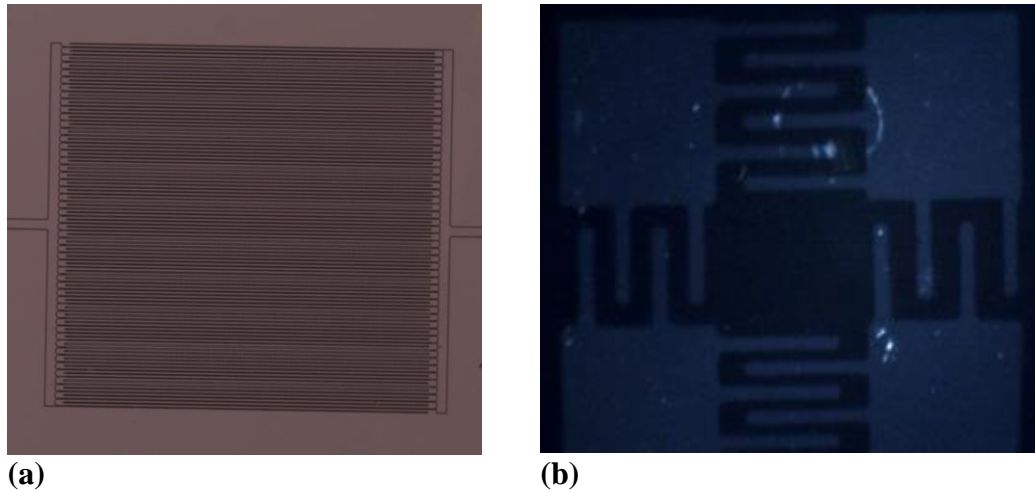


Figure 4-5: Interdigital patterned structure (a) photolithography, and (b) shadow mask.

4.7.2 Shadow Mask Patterning

Shadow mask patterning was adapted for interdigital patterning using a predesigned shadow mask (Figure 4-5b). The operating conditions are as stated in Table 4-4. The deposition of Ti prior to Pt ensured an excellent adhesion of Pt onto the thin film, for effective gas sensing.

Table 4-4: Process parameters for Tecport magnetron sputtering of Ti/Pt pattern

| Target Material | Platinum (Pt) | Titanium (Ti) |
|-----------------------------------|---------------|---------------|
| Target to Substrate Distance (cm) | 5 | 5 |
| Power (W) | 60 | 150 |
| Voltage (V) | 340 | 342 |
| Current (A) | 0.19 | 0.19 |
| Pre-Deposition Time (sec) | 120 | 300 |
| Deposition Time (sec) | 20 | 95 |
| Thickness Required (sec) | 10 | 100 |
| Hidden Ar | On | On |
| Ar Gas (sccm) | 50 | 50 |
| O ₂ (sccm) | No | No |

4.8 Thin Film Characterisation

4.8.1 Film Thickness

Film thickness of the MOX semiconductors was measured using a Dektak Surface Profiler and FE- SEM. The Dektak Surface Profiler process involves the sliding of a diamond tipped stylus over the thin film surface to determine the change in depth from the surface of the thin film to the substrate. The film thickness data obtained from Dektak Surface Profiler were compared with those from FE-SEM (see Section 5.2 for results).

4.8.2 Field Emission - Scanning Electron Microscope (FE-SEM)

Field Emission - Scanning Electron Microscope (FE-SEM) provides secondary electron images of organic and inorganic materials at nanoscale resolution ([Kalantar-zadeh and Fry 2008](#)). By scanning the electron probe of the FE-SEM across the surface of the sensor and monitoring the secondary electrons emitted, the surface morphology and topography of the thin film of the gas sensor can be determined. FE-SEM can be used to monitor the formation and growth of thin films and nanostructures, or improve the understanding of the interaction between the sensing layer/media and the analyte.

In this study, film thickness, grain size and surface morphology of the MOX thin film sensor were analysed by the use of a FE-SEM (Carl Zeiss Ultra-55 from GEMINI® Technology) represented in Figure 4-6.

Samples of the thin film were mechanically split using a diamond blade before mounting onto the aluminium stubs for the specimen chamber. For optimum resolution, the Carl Zeiss Ultra-55 was operated at an accelerating voltage of 5 kV, beam current of 5 (μ A) and a high vacuum of 10^{-6} Pa for gun chamber and 10^{-6} Pa for specimen chamber.

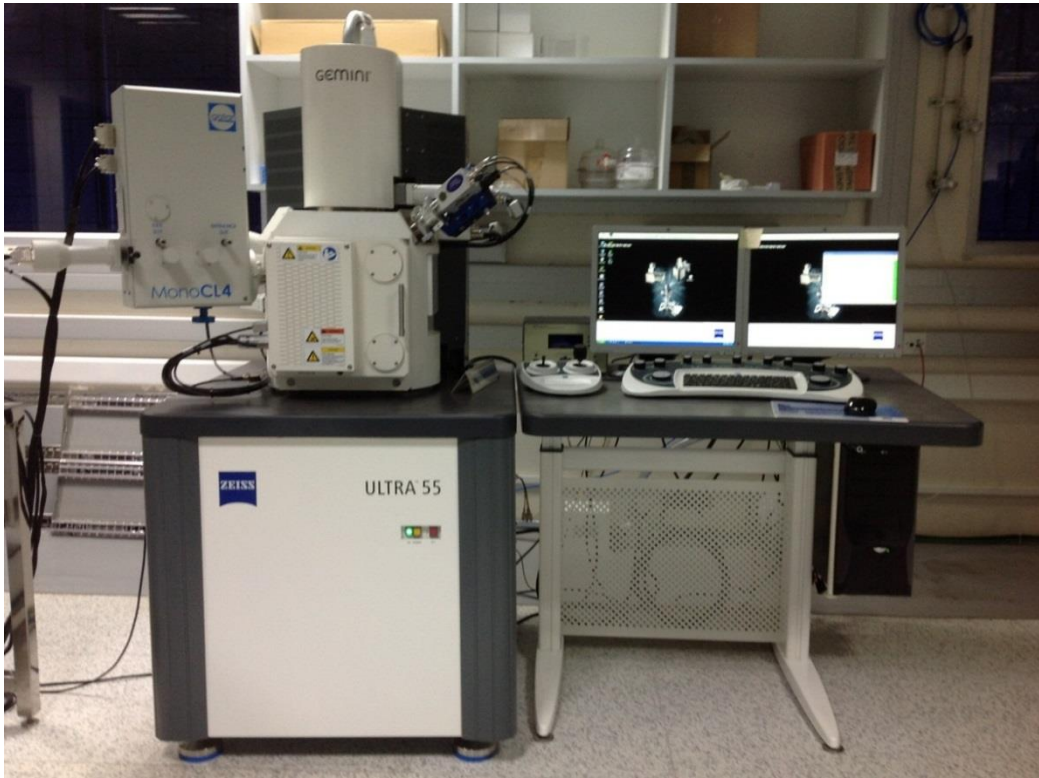


Figure 4-6: Carl Zeiss ULTRA 55.



Figure 4-7: Q150R Rotary-Pumped Sputter Coater/SEM Carbon Coater.

To avoid charging by the electron beam with high energy and improve surface conductivity, a thin layer of gold (Au) was sputtered onto the sample using a compact rotary-pumped combined sputter coater and SEM carbon coater (Q150R ES), from Quorum Technologies (Figure 4-7). It was operated at a pressure of 50 mTorr, and Au coating of 20% was applied on the sample. This enabled precise imaging and effective measurement of boundaries, particles, and features of the sample at different magnifications.

4.8.3 Energy Dispersive Spectroscopy (EDS)

Energy dispersive X-ray spectroscopy (EDS or EDX), also referred to as energy dispersive X-ray analysis (EDAX), is an analytical technique used for the chemical characterisation or elemental analysis of thin films. Usually used in conjunction with SEM, the process involves bombarding the sample surface area with electrons, from an electron beam instrument, and measurement of characteristic X-ray energies using an energy dispersive spectrometer.

In this research, EDS was carried out with FE-SEM using a Carl-Zeiss ULTRA 55 (with a fully integrated Energy and angle selective Backscattered electron (EsB) detector) for chemical characterisation and elemental analysis (Figure 4-6). Results of the films characteristics are presented in Section 5.3.

4.8.4 Atomic Force Microscope (AFM)

The surface structures of the thin films was analysed by AFM using Bruker Dimension Icon with ScanAsyst (Figure 4-8). AFM functions as a current, chemical, physical and biological sensor, and can sense (or characterise) virtually any surface, measuring van der Waals, electrostatic, magnetic, capillary, Casimir, and solvation forces. The AFM is used to determine the nanoparticle size, real topographical and 3D surface image of the thin film sensor.

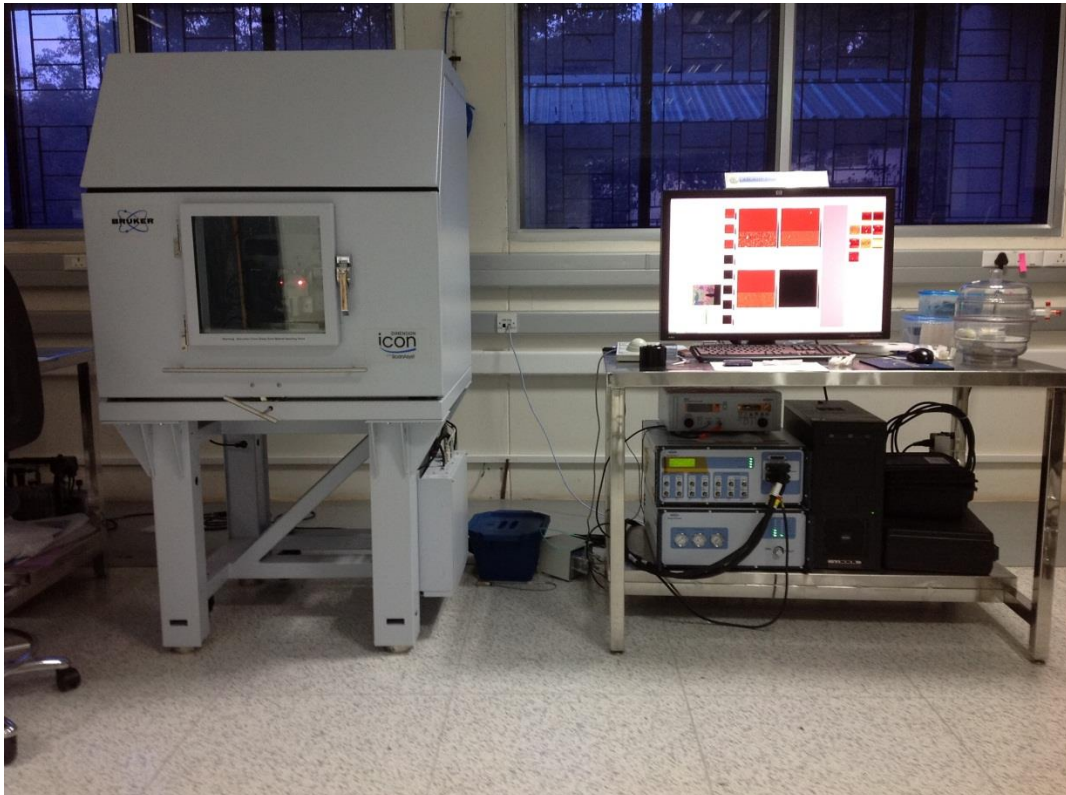


Figure 4-8: AFM (Bruker Dimension Icon with ScanAsyst).

Using the tapping mode, details of the surface roughness and grain size distribution of the nanostructures of the thin films were studied against deposition duration and sensor composition. Results are presented in Section 5.4.

4.9 Gas Sensing

4.9.1 Gas Sensing System

The gas sensing behaviour of the MOX thin film sensors was studied using a purpose built gas sensing rig constructed at the CeNSE, IISc, India. The system is designed to test different sensors under different gas atmospheres at different temperatures/pressure conditions. The gas sensing system provides an environment for management of controlled conditions for sensing reproducibility and versatility (Figure 4-9).

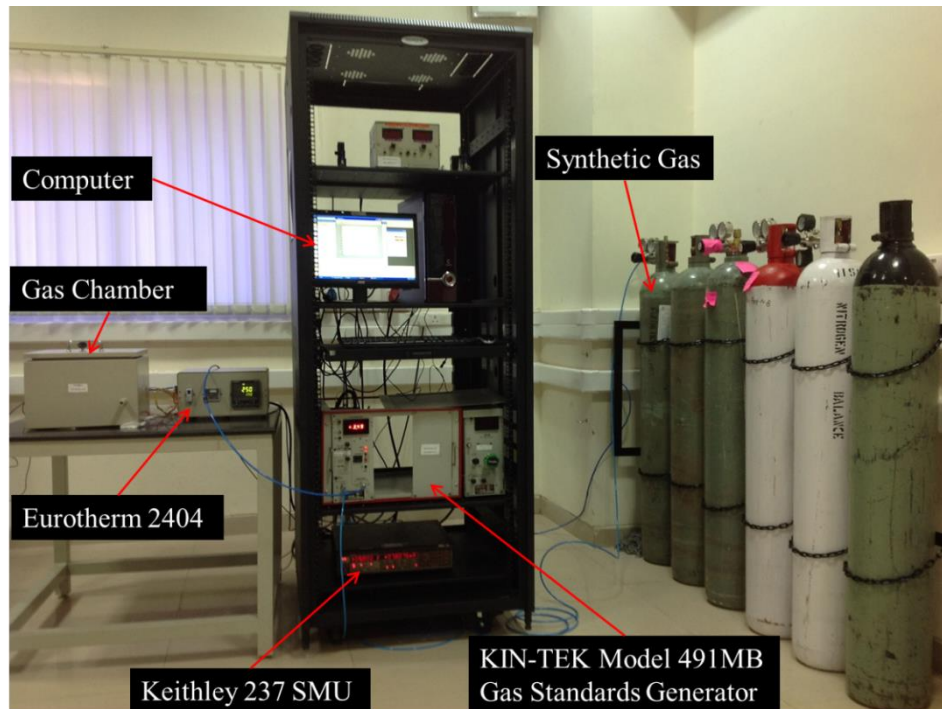


Figure 4-9: Gas sensing system.

The gas sensing system consists of a gas chamber, KIN-TEK Model 491MB Gas Standards Generator (in conjunction with Gas Feed System, Trace Source™ Gas permeation tube, and the KIN-TEK 491M Base Module), temperature controller (Eurotherm 2404), source meter unit (Keithley 237 High Voltage Source Measure Unit), and a computer.

The gas chamber is of dimension 34 cm by 18 cm by 17 cm. There is a feed-through that ensures that internal of the gas chamber is isolated from the external environment. Inside the chamber (Figure 4-10), there is a graphite block which was used to heat the sensing device using a tungsten heater element. The graphite block has a temperature range of 25 - 300 °C; this was controlled through a thermo couple (Eurotherm® 2404). The pads on the sample are probed using the micromanipulators. Each of the micromanipulators has an electrical connection each with a positive terminal and negative terminal. The positive terminal of one of the probe connects to the measure terminal of the SMU, while the positive terminal of the other probe connects to the drive in terminal of the SMU. The negative terminals of both the probes go to the earth terminal.

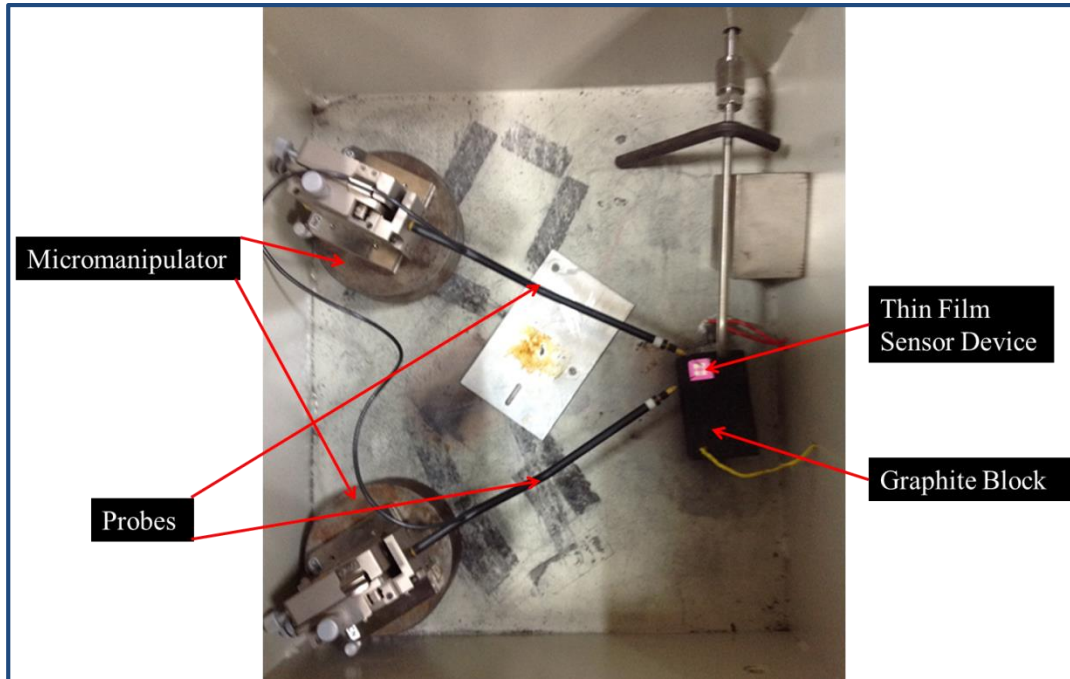


Figure 4-10: Gas Chamber (Internal).

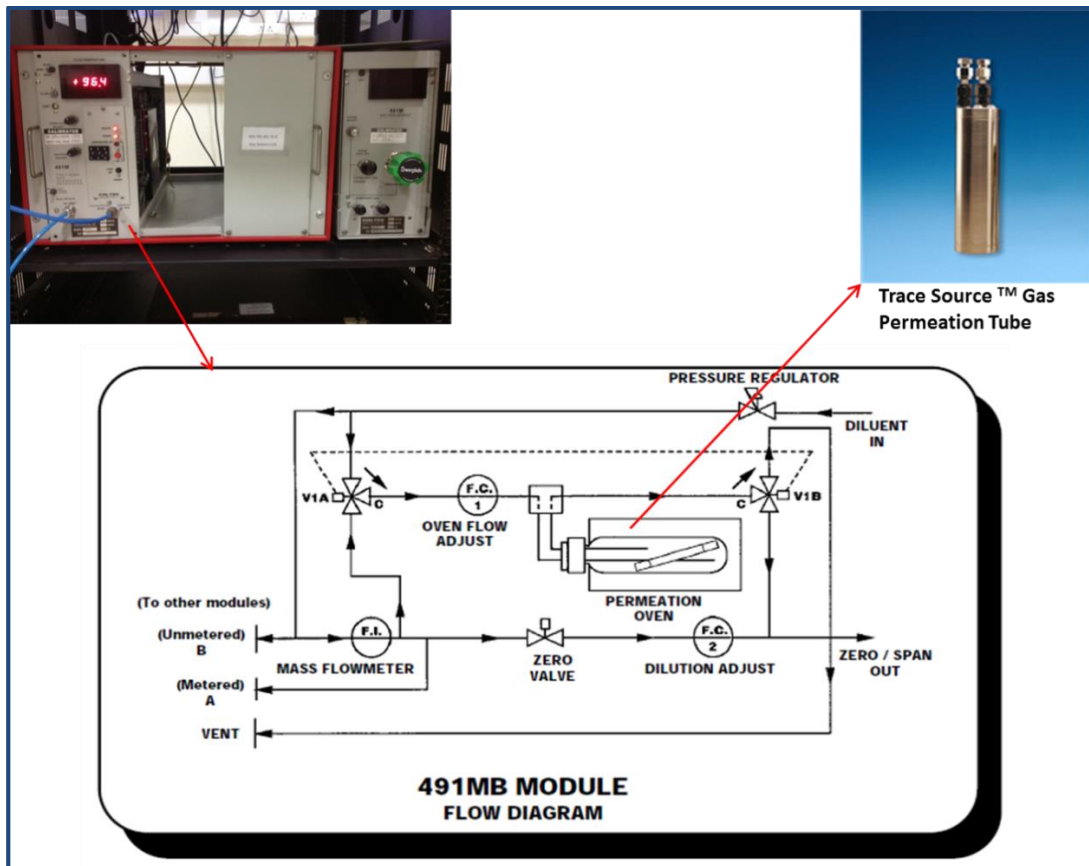


Figure 4-11: KIN-TEK Model 491 MB Module.

The internal configuration of the KIN-TEK Model 491MB Gas Standards Generator is described in Figure 4-11. The Trace SourceTM gas permeation tube contains the target gas (i.e., methanol or ethanol gas) required for the sensing process.

4.9.2 Gas Sensing Measurement Procedure

The gas sensing measurement involved the following protocol:

- 1) Apply a constant voltage from the SMU through one probe while measuring the current through the other probe in the SMU.
- 2) Place interdigital electrode (sensing MOX thin film) device on the graphite heater in the gas chamber and close the gas chamber.
- 3) Place the permeation tube containing the target gas in the permeation oven of the Model 491MB Gas Standards Generator, and connect the inlet and outlet lines (Figure 4-11).
- 4) Set the temperature of the KIN-TEK Model 491M Gas Standards Generator to 100 °C.
- 5) Allow the temperature to reach 100 °C.
- 6) Probe the sensing device to complete the electrical circuit.
- 7) Turn on the synthetic gas valve; allow it to flow until the signal response stabilises. The synthetic gas is made of N₂ and O₂ at 79.5% and 20.5% composition, respectively.
- 8) Commence recording of the signals by turning on the target gas flow to the required flow rate (corresponding to the required concentration). Allow target gas flow for 5 min.
- 9) Then turn off target gas, and continue recording sensor signal response for 5 min.
- 10) After the signals has stabilised for synthetic gas, stop the sensing process.

The flow rate of synthetic gas was set 1.54 sccm using the dilution adjustment of the KIN-TEK 491 MB Module. The optimum operating temperatures of SnO₂ and ZnO nanostructures is between 250 and 350 °C ([Tang et al. 2014](#)). Above 350 °C, sensitivity of the metal oxides usually decreases with increase in temperature ([Hafaiedh et al. 2008](#)).

Therefore, we focused our study within the optimum operating temperature range of the materials. Consequently, the gas sensing experiments were undertaken on the fabricated thin film gas sensors at operating temperatures of 150, 250 and 350 °C by monitoring changes in the sensor conductance as the gas flow gas was changed from synthetic air to the target (test) gas. Target gases (ethanol and methanol) were flown at 100, 150, and 200 ppm. Resistance was calculated from the current recorded under a DC bias voltage of 5 V using the Keithley 237 SMU.

For real-time visualisation of the gas sensing behaviour, a current versus time graph was plotted using MATLAB code incorporated into the readout-signal process. The typical raw digital signal of the sensor response is represented in Figure 4-12. Further processing and analyses of the typical sensor response is discussed in Chapter 6.

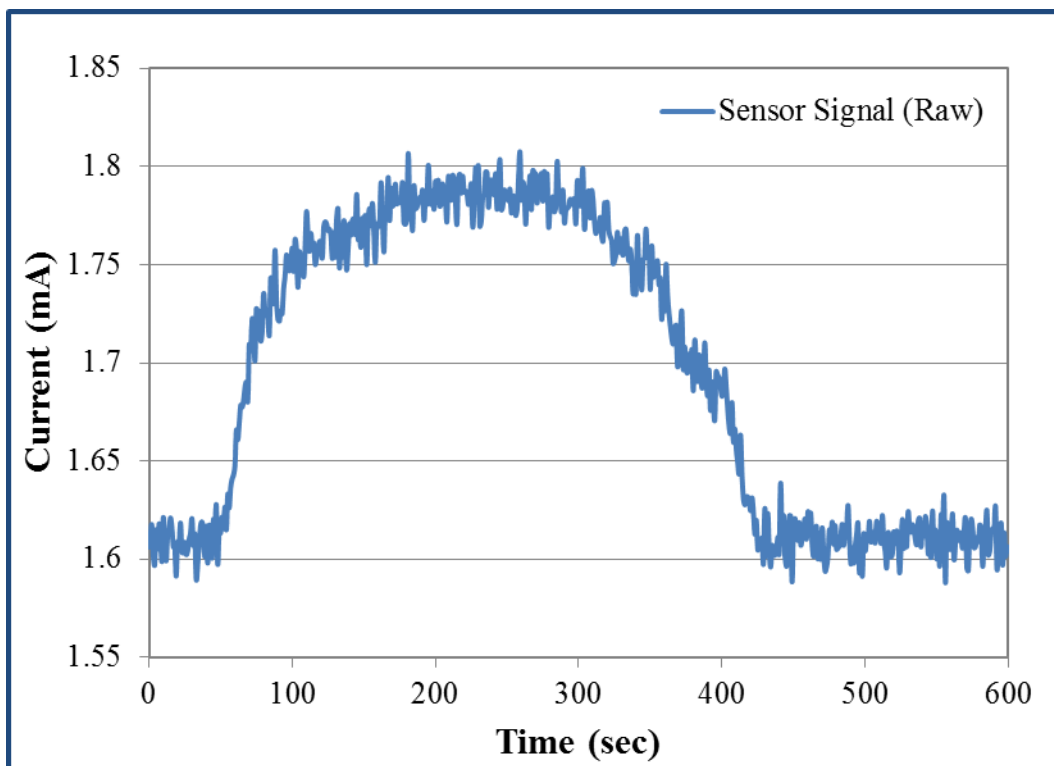


Figure 4-12: Typical sensor digital signal.

4.10 Conclusion

In this chapter, the details of the sensor device fabrication and thin film characterisation have been discussed. Substrate and MOX target preparation were presented, and the conditions of film deposition (by RF magnetron sputtering) process have been discussed. The optimisation of the patterning process is described. The design of the gas sensing system, along with component instruments, is described. The gas sensing procedures are also presented, with an example of a typical raw digital signal of a sensor. An easily reproducible, cost-effective and novel procedure for gas sensor fabrication, characterisation and sensing process is presented, with results versatility.

Chapter Five

Metal Oxide Thin Film Characterisation

5.1 Introduction

Films and coatings are often classified as unique materials with differing properties in the same materials, depending on the method of preparation. These unique characteristics are very important in the choice of material preparation, and the objective of application. Therefore, thin film characterisation involves the application of diagnostic methods and models to determine the composition, structure, morphology, and mechanical, optical and electrical properties of the films. Effectively, thin film characterisation uses property measurements to optimise the film preparation method and ascertain the final nature of the film. In this chapter, the results of film characterisation are presented as they relate to the nature of the as-fabricated metal oxide sensors. The effect of the molar composition of the each metal oxide in the nanocomposite on the film morphology is investigated, and analysed for possible relationship to sensor sensitivity.

5.2 Film Thickness

Applications in nanoelectronic require the maintenance of precise and reproducible film metrology, i.e., knowledge of the film thickness as well as lateral dimensions. A film thickness may be defined in three ways ([Mattox 2010](#)): (i) geometrical thickness – separation between surfaces; (ii) mass thickness; and (ii) property thickness.

The geometrical thickness is the separation between surfaces, and does not take into account the composition, density, microstructure, etc.; it is measured in mm, nm, Å, or μ . Mass thickness is measured in mg/cm^2 ; with knowledge of material density, it can be converted to a geometrical thickness ([Mattox 2010](#)). Property thickness

measures some property such as electrical conductivity, beta (electron) backscatter, ion backscattering, X-ray absorption, or optical adsorption; these properties may be sensitive to film density, microstructure, composition or crystallographic orientation. Measurements of property thickness require calibration standards. Generally, film thickness is measured using optical techniques (such as multiple beam interferometry, ellipsometry, spectral reflectometry and spectrophotometry) or mechanical techniques (such as profilometry and quartz crystal microbalance).

In this study, a Dektak surface profilometer was used to measure the film thickness using a diamond tipped stylus by sliding over the thin film surface. The values of thickness collaborated with those obtained from the FE-SEM. A complete comparison of the film thickness based on deposition time showed slight variations in annealed and unannealed samples as illustrated in Figure 5-1.

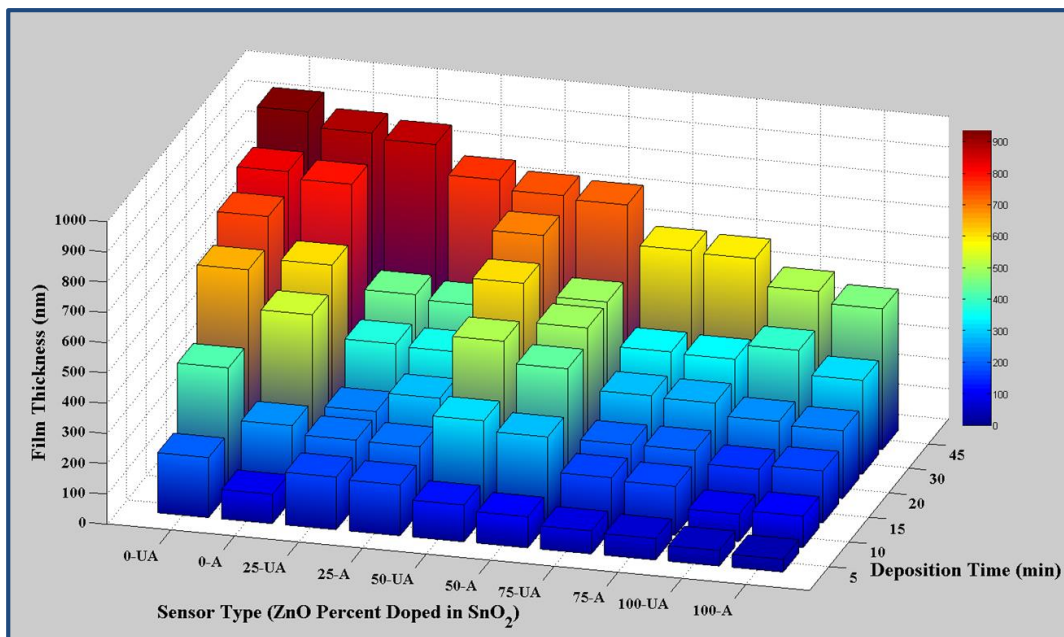


Figure 5-1: Film thickness plot (UA: Unannealed; A: Annealed).

Generally, film thickness of annealed samples was thinner than unannealed samples. This is attributed to the increased thermal oxidation of the film, and improvement in the crystallinity, morphological changes, changes of atomic distances and grain size ([Yıldırım et al. 2012](#)). For both annealed and unannealed samples, the thickness

variation decreased with increasing ZnO molar concentration in the sensor device; with pure SnO₂ sensor sample having the highest thickness, and pure ZnO device having the lowest thickness. The decreasing thickness could be attributed to the fact that the density of SnO₂ is greater than the density of ZnO, and the density of the nanocomposite tends to decrease as the molar mass of ZnO increases in the sample. Generally, the thicknesses of individual MOX devices increased with increasing deposition time.

However, for the mixed nanocomposites, at deposition times of 10, 20, 30 and 45 min, the thickness of SZ was higher than S₃Z₁ and S₁Z₃. These variations could be attributed to increasing structural heterogeneities in the samples from the pure metal oxides toward the mixed nanocomposites, SZ.

Deposition and post-deposition (annealing) conditions have strong influences on the properties of metal oxide thin films ([Pan et al. 2001](#)). The decrease in thickness with annealing is confirmed by [Kim et al. \(2008\)](#) for a SnO₂ films fabricated by photochemical metal-organic deposition using photosensitive starting precursors. The SnO₂ film crystallinity was observed to be enhanced with an increase in anneal temperature, and the film thickness decreased with annealing ([Kim et al. 2008](#); [Park et al. 2006](#)). At the same conditions, the resistivity of SnO₂ films decreased with increasing annealed temperature ([Park et al. 2006](#)).

Using a filtered vacuum arc deposition procedure, [Çetinörgü et al. \(2007a\)](#) reported film thickness in the range 100–363 nm for SnO₂ and ZnO samples deposited for 90 s. For SnO₂ semicrystalline film, sputtered with RF power of 100, 150 and 250 W, and O₂ concentration of 0% to 15%, on some substrates at room temperature and some heated to 150 °C, thicknesses were reported by [Tosun et al. \(2012\)](#) as 200±20 nm, 300±20 nm and 500±20 nm thick.

In ZnO–SnO₂ films fabricated using 2:1 molar ratio by RF magnetron sputtering at substrate temperature varied from 27 to 300 °C, [Cha et al. \(2012\)](#) reported film thicknesses of between 250 and 300 nm. There is no reported film thickness for

nanocomposite (or similar) sensors fabricated by RF magnetron sputtering using SnO₂ and ZnO in 3:1, 1:1 or 1:3 molar ratio in the literature. But in a similar set of S, S₃Z₁, SZ, Z, S₁Z₃ thick paste sensors, prepared by [de Lacy Costello et al. \(2002\)](#), the average dry film thickness was 50 μm, while the screen-printed SZ was 3 mm. A SZ nanostructure, prepared by combinatorial solution deposition of SnO₂-ZnO thin films showed cross-sectional film thicknesses of the films 5–6 μm ([Kim et al. 2007](#)).

The effects of the thickness variation, substrate type and annealing on the crystallinity parameters and optical properties of the ZnO thin films are reported by [Kapustianyk et al. \(2007\)](#). Deposited by magnetron sputtering on glass substrate between 0.5 and 60 min, they observed thickness of 10 – 600 nm. For ZnO deposited on a quartz substrate and annealed in air at 850 °C, they reported thickness of 600 nm. A ZnO sensor prepared using spray pyrolysis technique showed thickness of 250–350 nm ([Sahay and Nath 2008](#)).

In order to obtain films of similar thicknesses, [Alvarez et al. \(2013\)](#) selected discharge power of 150 W and 300 W, and pressure of 5×10^{-4} mbar and 8×10^{-4} mbar, for SnO₂ and ZnO, respectively. With resulting yield power densities of 6.5 W/cm² for ZnO and 3.3 W/cm² for SnO₂, quite similar to those used in industry by the manufacturing processes of low emissivity coating where the dielectric layers are deposited at the maximum possible power, they set the residual vacuum pressure to 5×10^{-6} mbar to obtain SnO₂ and ZnO film thicknesses ranging from 20 to 800 nm. That is [Alvarez et al. \(2013\)](#) applied higher discharge power and pressure for ZnO than SnO₂ films in order to obtain the same thickness. But in our research, we applied the same depositional conditions for all fabricated thin films. The implication is that different substrate and deposition/post-deposition conditions affect the film thickness formed.

5.3 FE-SEM and Energy Dispersive Spectroscopy (EDS)

The FE-SEM was used to analyse the film thickness, elemental composition, cross-section, grain size and surface morphology. Other useful information from FE-SEM could include surface textures, evidence of film voids, hillocks, and micro-cracks on

the film. All samples were confirmed for elemental composition. The EDS spectrum, representing the elemental compositions for SnO₂, SnO₂-ZnO and ZnO samples deposited for 30 min, are shown in Figure 5-2.

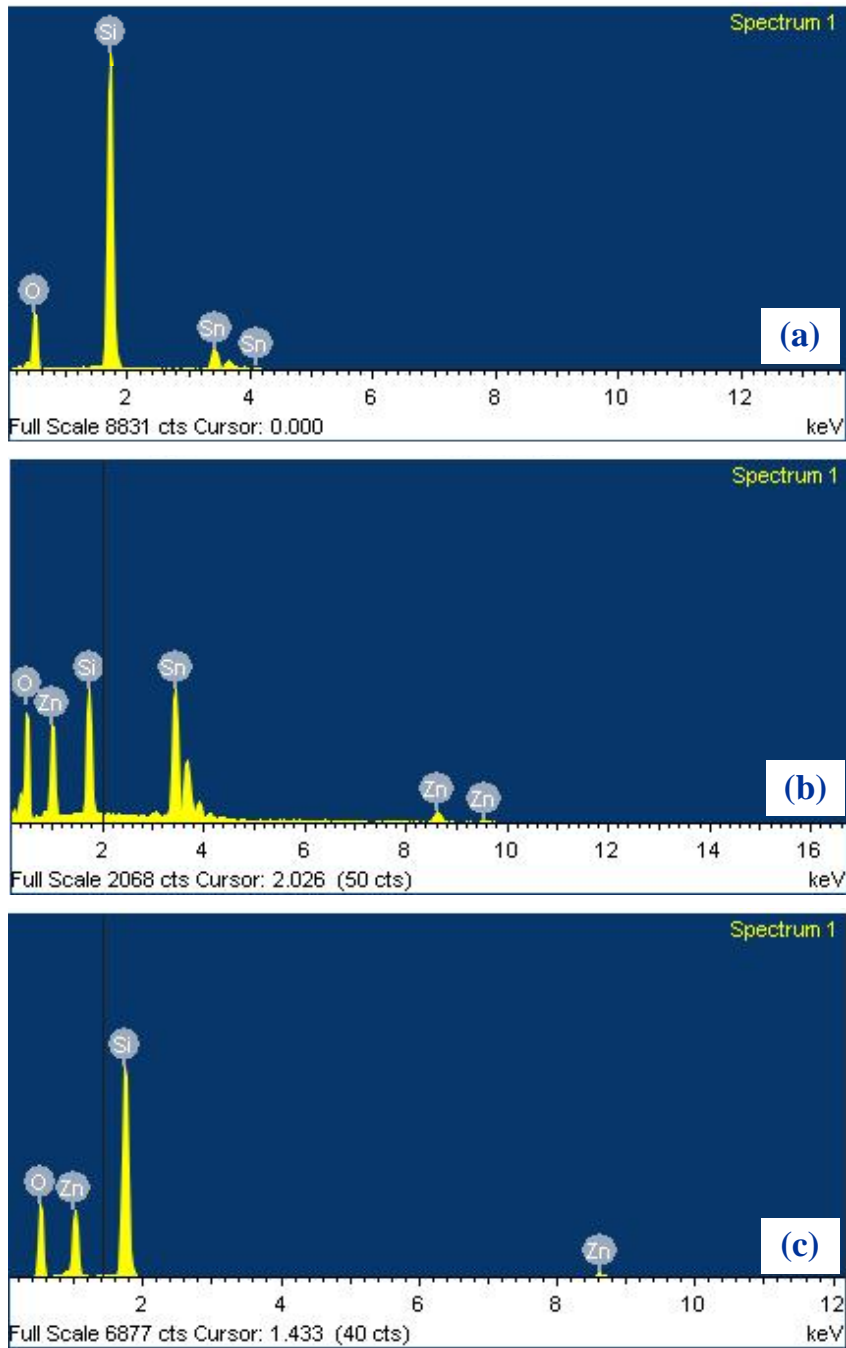


Figure 5-2: Elemental composition of samples (a) SnO₂, (b) SZ, and (c) ZnO.

Using films deposited for 15 min, our typical set of thin film cross-sections from FE-SEM is represented in Figure 5-3.

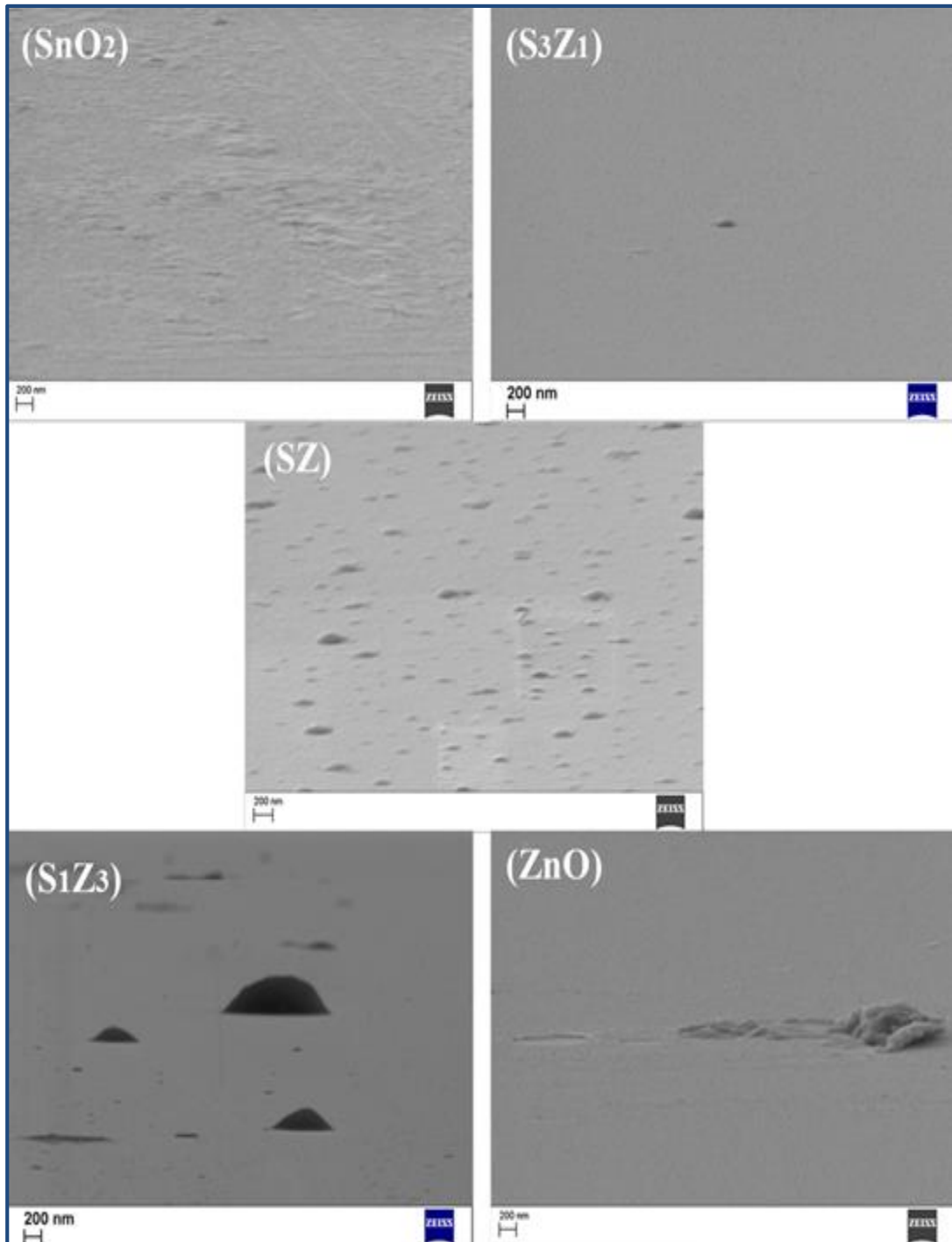


Figure 5-3: Film surface cross-section.

Thin film surface images (deposited for 30 min) from FE-SEM is represented in Figure 5-4.

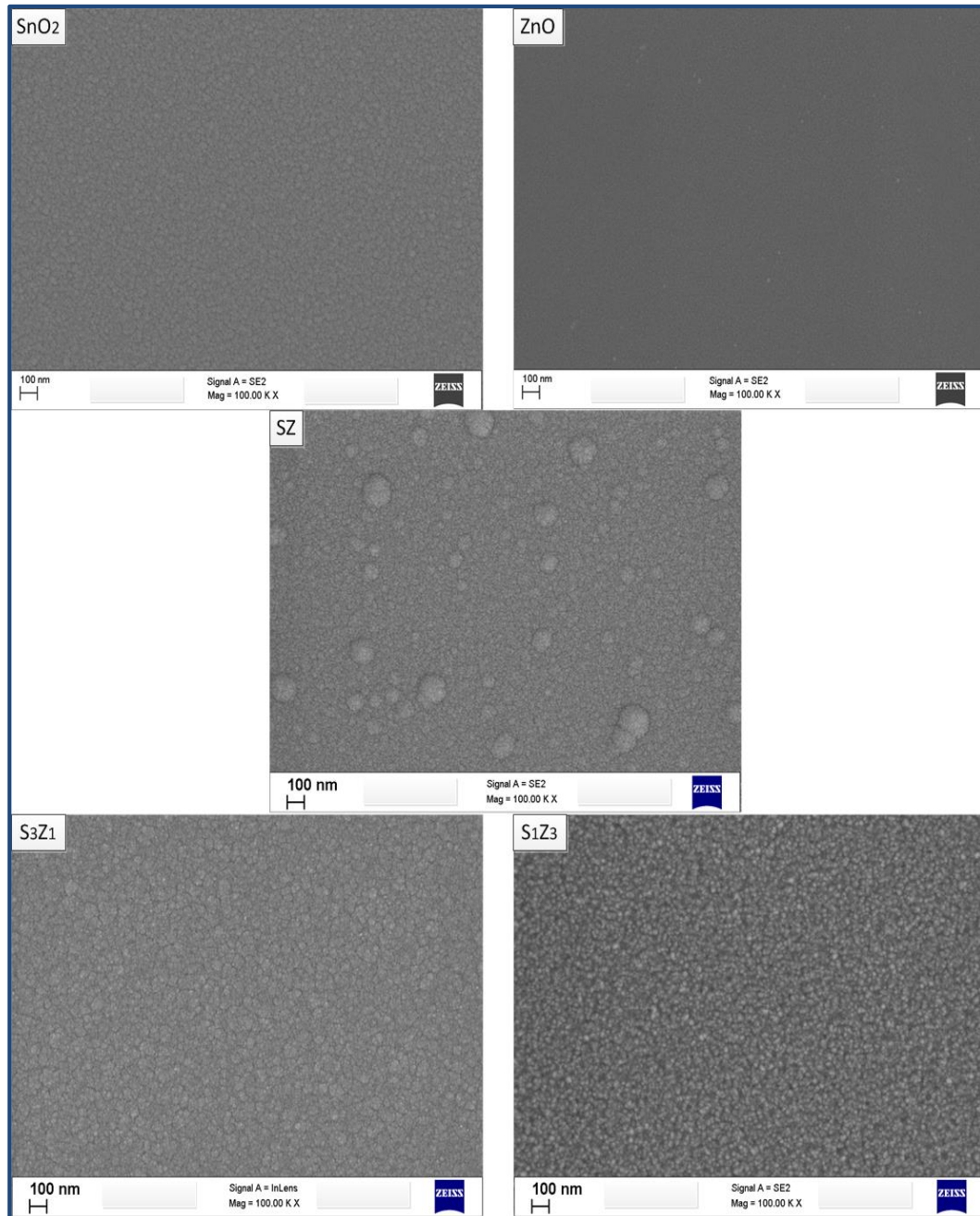


Figure 5-4: FE-SEM images films deposited for 30 min.

From the surface and cross-section images, the morphology revealed a more homogeneous structure with the pure (SnO_2 and ZnO) samples, while the S_3Z_1 , SZ and S_1Z_3 revealed some heterogeneity on their crystallinity.

Detailed particle size profile of the as-fabricated nanostructures based on deposition times is represented in Figure 5-5.

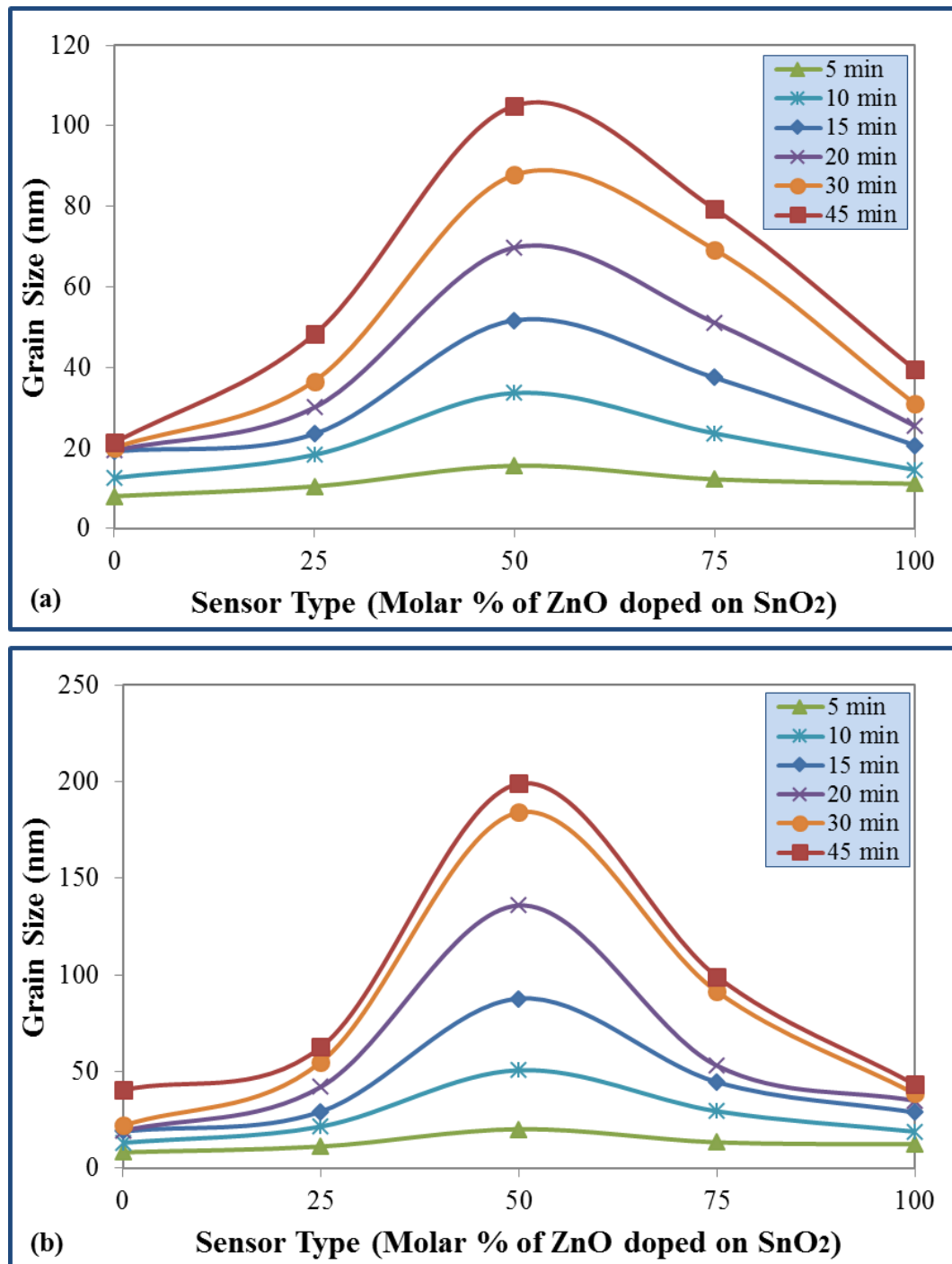


Figure 5-5: Particle size of (a) as-fabricated, (b) annealed nanostructures.

The particle (or grain) size of the samples was observed to increase with change from the pure SnO₂ and pure ZnO. For any deposition time, the lowest was the SnO₂ sample, followed by the ZnO sample. The highest particle size, with large conglomerates, was exhibited by the SnO₂-ZnO sample. The grain sizes of samples increased as the concentration of the mixture increases from the pure metal oxides. S₃Z₁ samples have higher grain sizes than S₃Z₁ samples. Across the sensors, the gran size variations as a function of deposition time is most obvious with those deposited for 45 min, and least obvious with those deposited for 5 min.

The largest agglomerates were by SnO₂-ZnO sample deposited for 45 min. As large conglomerates are not assumed to be taking part in the light-trapping process ([Shah et al. 2004](#)), we infer that this could be the reason for the poor sensitivity recorded by the SnO₂-ZnO sensor devices (see Chapter 6 for detailed sensitivity behaviour).

A complete distribution of both the unannealed and annealed samples is shown in Figure 5-6. The greater grain size of the annealed samples could be attributed to the increased crystallisation of the particle agglomerates.

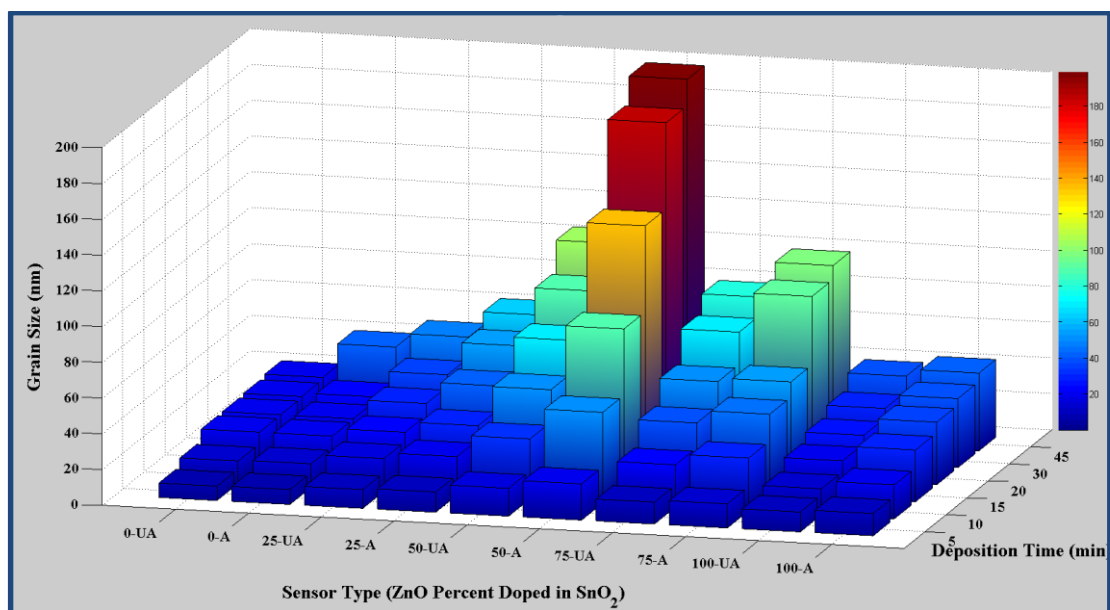


Figure 5-6: Grain size plot (UA: Unannealed; A: Annealed).

Grain size is a strong function of the film thickness suggesting that metal oxide crystals nucleate and grow during deposition ([Tosun et al. 2012](#)). For SnO₂, film formation starts out as amorphous structure, and then the crystallites nucleate and grow as the deposition proceeds. As confirmed by our research, the particle size of ZnO is known to be larger than SnO₂ ([Wagh et al. 2004](#)), and crystal growth of polycrystalline SnO₂ is affected by zinc doping ([Tian et al. 2012](#)).

Mostly, small concentrations of ZnO occupy the surface sites of SnO₂ nanoparticles and prohibit the formation of contact necks between particles and the coalescence of tiny SnO₂ particles to larger size. In analysis of SnO₂-ZnO samples, [Nikan et al. \(2013\)](#) observed that the average particle size of the samples increases with the weight percentage of ZnO in the range of 1–5 wt%. This may be attributed to the formation of ZnO amorphous phase, when concentrations beyond its solid substitutional solution are doped. Also, the formation of ZnO amorphous phase, when doped concentrations are beyond its solid substitution solution could cause this increment ([Nikan et al. 2013](#); [Tian et al. 2012](#)). The same effect could occur by addition of SnO₂ to ZnO. But, there must be an optimum level of increase. Therefore, that is the reason for increased particle size of SZ than S₁Z₃ and S₃Z₁ and the pure metal oxide samples.

Deposition durations showed some variations on the surface homogeneity and film thickness. The most significant differences were most obvious with the SZ samples (Figure 5-7). There was increase in agglomeration as the deposition duration increased. This behaviour could have significant effect of gas sensitivity.

Also, annealing has a large effect on the crystallinity of the films in terms of grain size, residual strain, and the defect density ([Wu et al. 2011](#)). Based on substrate temperature, films deposited at 150 °C substrate temperature were observed to be greater than those deposited at room temperature ([Tosun et al. 2012](#)). We observed that the grain size of some annealed sample films were greater than the unannealed samples (e.g. ZnO samples deposited for 20 min: Figure 5-8).

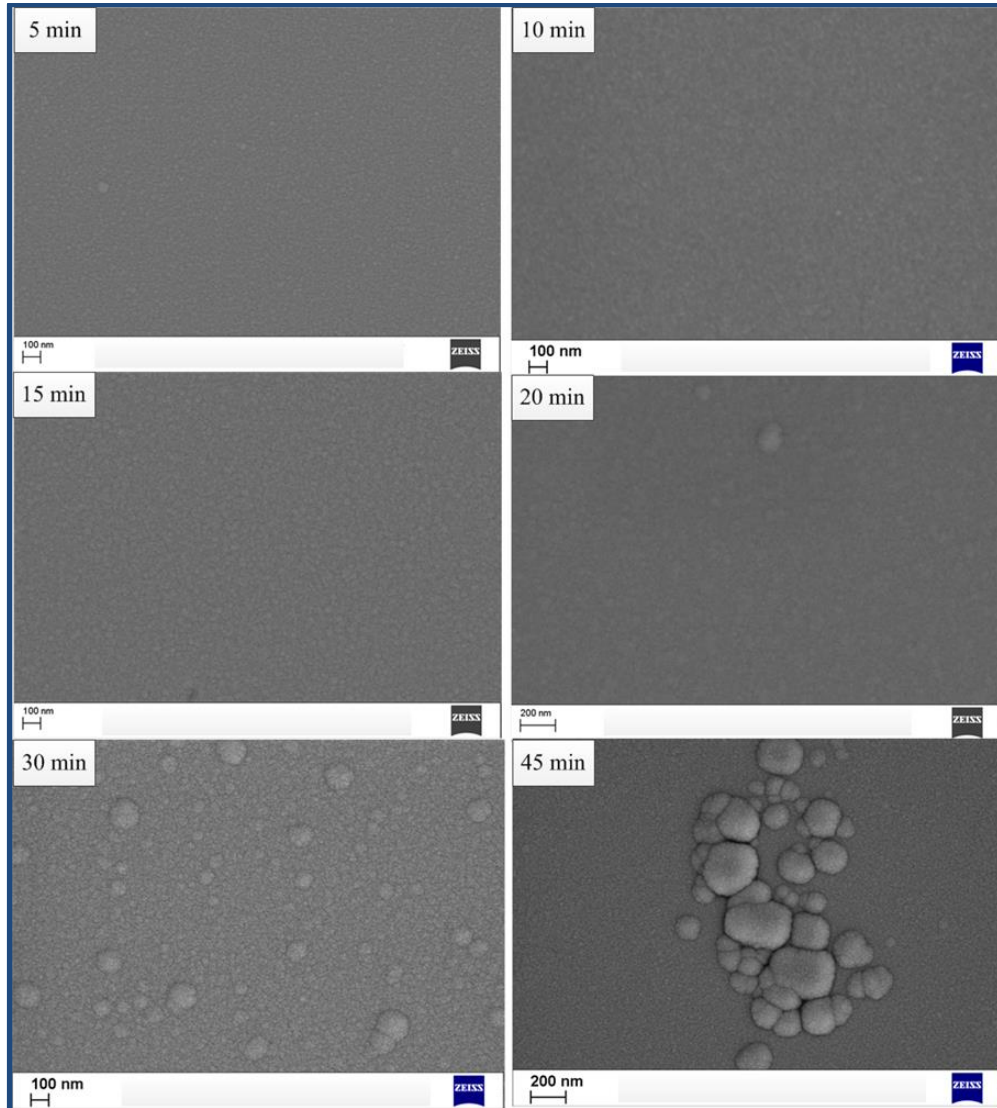


Figure 5-7: SnO₂-ZnO as-fabricated samples.

[Di Giulio et al. \(1993\)](#) observed increase in grain size from 12 nm to 92 nm with annealing reactive sputtered SnO₂ films at 450 °C for 1 h. Our results are consistent with their observations. [Çetinörgü et al. \(2007b\)](#) observed an increase in the film surface average grain size from 15 nm to 46 nm as function of the annealing on samples of SnO₂ thin films fabricated by filtered vacuum arc deposition. This behaviour is attributed to desorption of negative charged oxygen species and passivation of surface and defects at grain boundaries ([Chang et al. 2011](#)). Also, as observed by increased crystallisation, the enhanced characteristics of the annealed samples could be attributed to significant agglomeration of the particles on annealing.

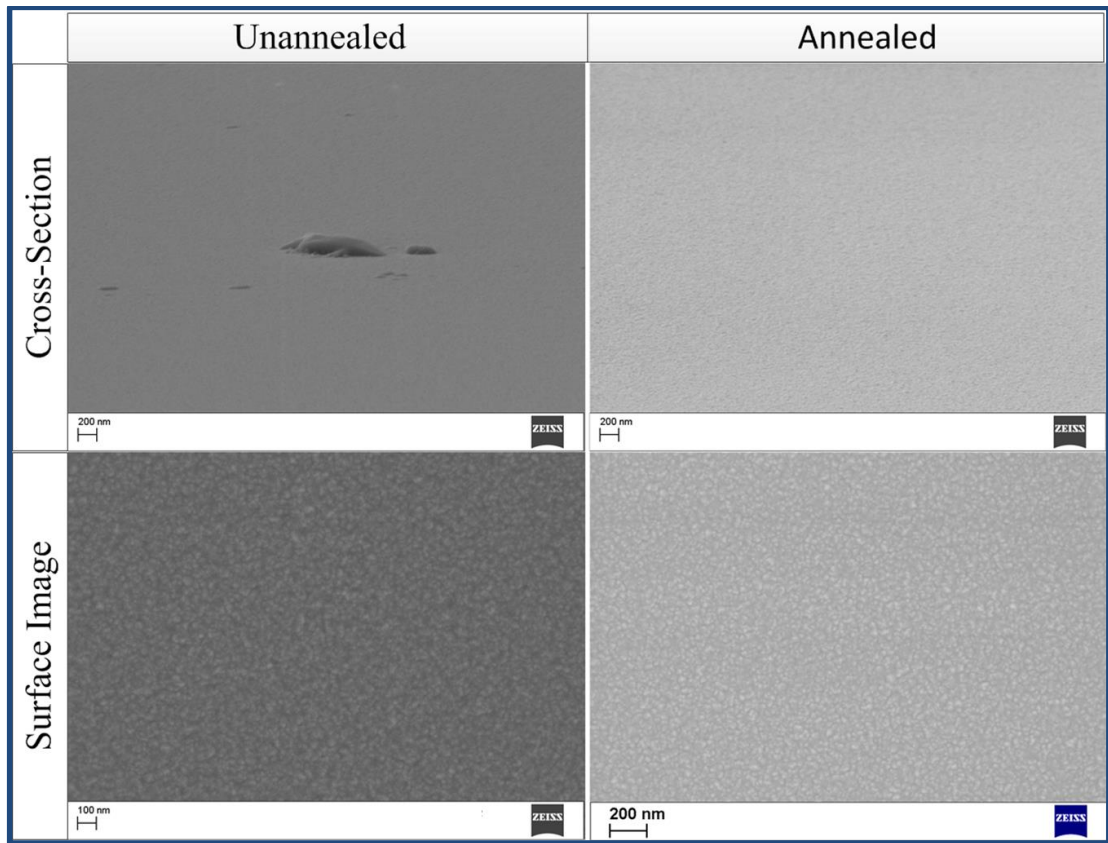


Figure 5-8: ZnO samples deposited for 20 min.

5.4 Atomic Force Microscope (AFM)

Using Bruker Dimension Icon with ScanAsyst, detailed observation was carried out for morphology over a $5.0 \times 5.0 \mu\text{m}$ film surface area of the samples. Analysis by atomic force microscope (AFM) images was undertaken using NanoScope Analysis software to determine the surface roughness. This could be characterised by the root mean square (RMS) parameter and average grain height. The RMS roughness is the standard deviation of the surface from the mean plane within the sampling area, while average roughness is the arithmetic average of the absolute distances of the surface points from the mean plane. Another parameter could be the maximum roughness; i.e., the maximum vertical distance between the highest and lowest data points in the image following the planefit.

A comprehensive characterisation of the surface morphology parameters for all the samples is presented in Figure 5-9. The RMS roughness, average roughness and grain

height are 1.2 - 5.18, 0.538 - 3.68 and 12.37 – 127 nm for unannealed samples, and 0.329 – 3.59, 0.55 – 3.62 and 7.33 – 118.69 nm for annealed samples, respectively. The RMS roughness was observed to be higher than the average roughness for both as-fabricated and annealed samples. But for the grain height, the as-fabricated samples were higher than the annealed samples. Compared to other samples, the S₂Z samples were observed to reflect the lowest surface roughness parameters, while the highest values are the S₁Z₃ samples. For the pure samples, ZnO samples are observed to be higher than the SnO₂ samples. This could attribute the reason S₃Z₁ samples exhibited lower roughness than the S₁Z₃ samples.

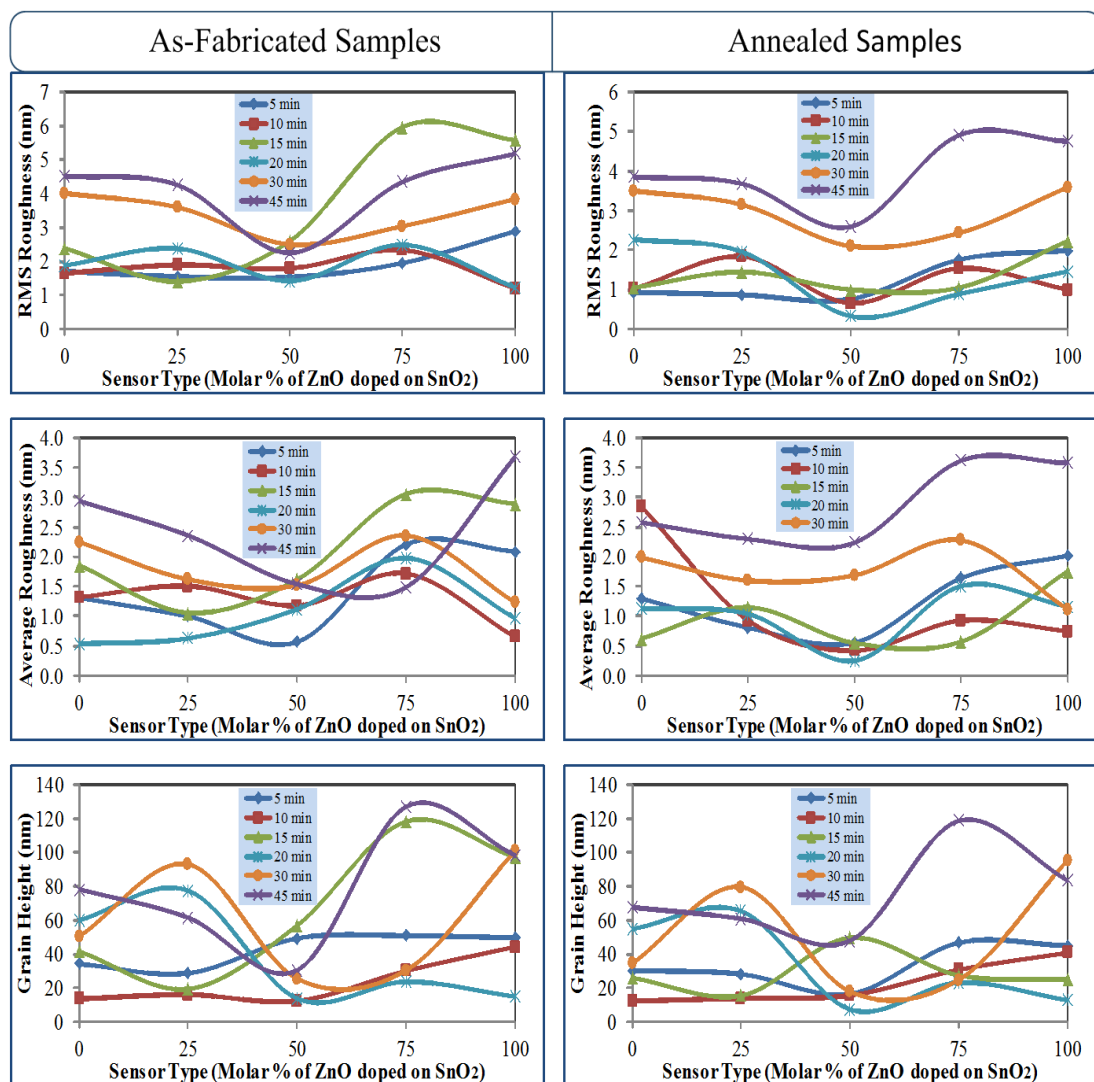


Figure 5-9: Surface roughness characterisation.

In this study, surface roughness values for SnO₂ thin films are higher than those fabricated by laser chemical vapour deposition method; the surface roughness was determined to be about 0.5 nm, and the maximum grain height estimated to be about 2 nm, while the maximum grain width (i.e., nominal thickness) was about 20 nm ([Kwoka et al. 2007](#)). But with a similar process, [Alterkop et al. \(2003\)](#) fabricated a SnO₂ film with 100–800 nm thickness and 6–8 mΩ cm resistivity. They remarked that the surface roughness depended on film thickness and only weakly depended on the annealing time. As a function of film thickness, they observed that the surface roughness decreased from 4.4 nm for a film thickness of 150 nm to 2.6 nm for 780 nm films. [Çetinörgü et al. \(2007b\)](#) reported an increase in the film surface roughness from 0.2 to 1.8 nm for SnO₂ with annealing.

Generally, the AFM images indicated minor hillocks on a relatively dense film surface. But, as a function of the annealing, the unannealed samples had more rounded protrusions than the annealed samples. Our values revealed a general reduction in surface roughness as a result of annealing. A representative morphology of the films deposited for 30 min is shown in Figure 5-10.

The SZ were observed to be smoother than others for both as-fabricated and annealed samples. With nanocomposites, the closest comparison of sensor compositions to this research is by [Chen et al. \(2009\)](#) for SnO₂ nanoparticle - ZnO nanotetrapods composites prepared in weight ratios of 2:1, 1:1, and 1:2 (denoted by them as S2Z1, S1Z1, S1Z2). Between 1 and 10 μm thickness, the roughness factor were found to lie between those of the pure SnO₂ nanoparticle and pure ZnO nanotetrapods in the following decreasing order: S2Z1, S1Z1 and S1Z2.

For ZnO–SnO₂ films fabricated by the filtered vacuum arc, the average surface roughness and the grain size observed by [Çetinörgü \(2007\)](#) were in the range 0.3–1.5 nm and 19–24 nm, respectively. For a chemical vapour deposited diamond thin films, the surface roughness was found to be 4.5 and 4.0 nm with and without SnO₂ overlayer, respectively ([Koinkar et al. 2005](#)). For ZnO and SnO₂ layers deposited by reactive magnetron on silver films, roughness parameters were 7.5, 27.5 and 19.9 nm

for ZnO, and 2.9, 1.8 and 5.3nm for SnO₂, while nominal thicknesses of the films were 200, 400 and 800 nm, respectively ([Alvarez et al. 2013](#)).

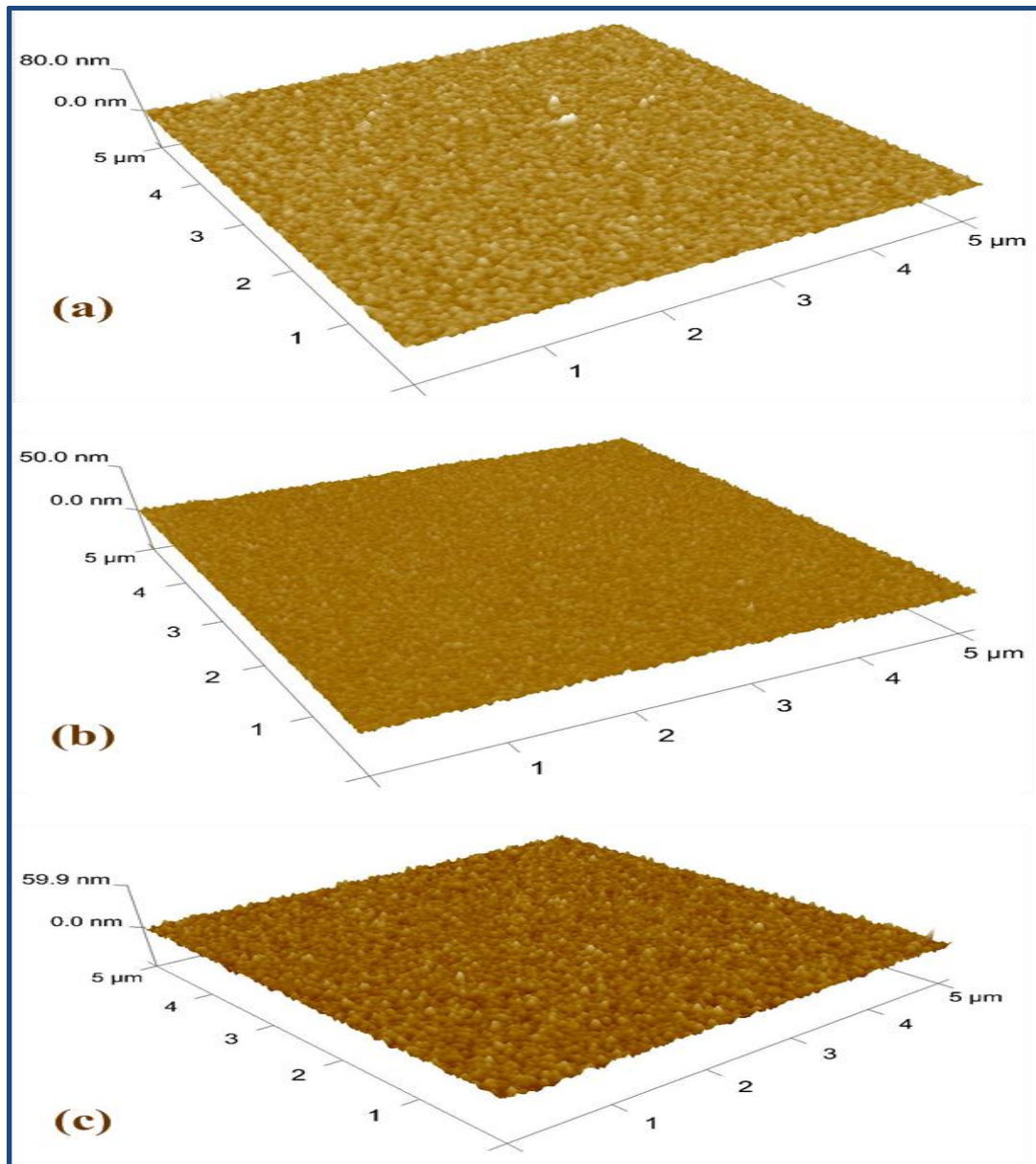


Figure 5-10: Representation of AFM images of films as-deposited samples (a) SnO₂, (b) SZ, and (c) ZnO.

This could be due to the effect of temperature on the film surface. In a (2:1 molar ratio) ZnO–SnO₂ films reported by [Cha et al. \(2012\)](#), the RMS roughness of the films obtained at 27 °C in pure Ar was 1.17 nm. Addition of O₂ to Ar (O₂: Ar = 10%) was observed to decrease the roughness of the films to 0.90 nm. By increasing the substrate

temperature during sputtering, the surfaces of the films were smoothed; therefore, the roughness of the films grown at substrate temperatures of 200 and 300 °C was observed to decrease to 0.74 nm and 0.85 nm, respectively.

Figure 5-11 shows the annealed samples of SnO₂ and ZnO deposited for 20 min.

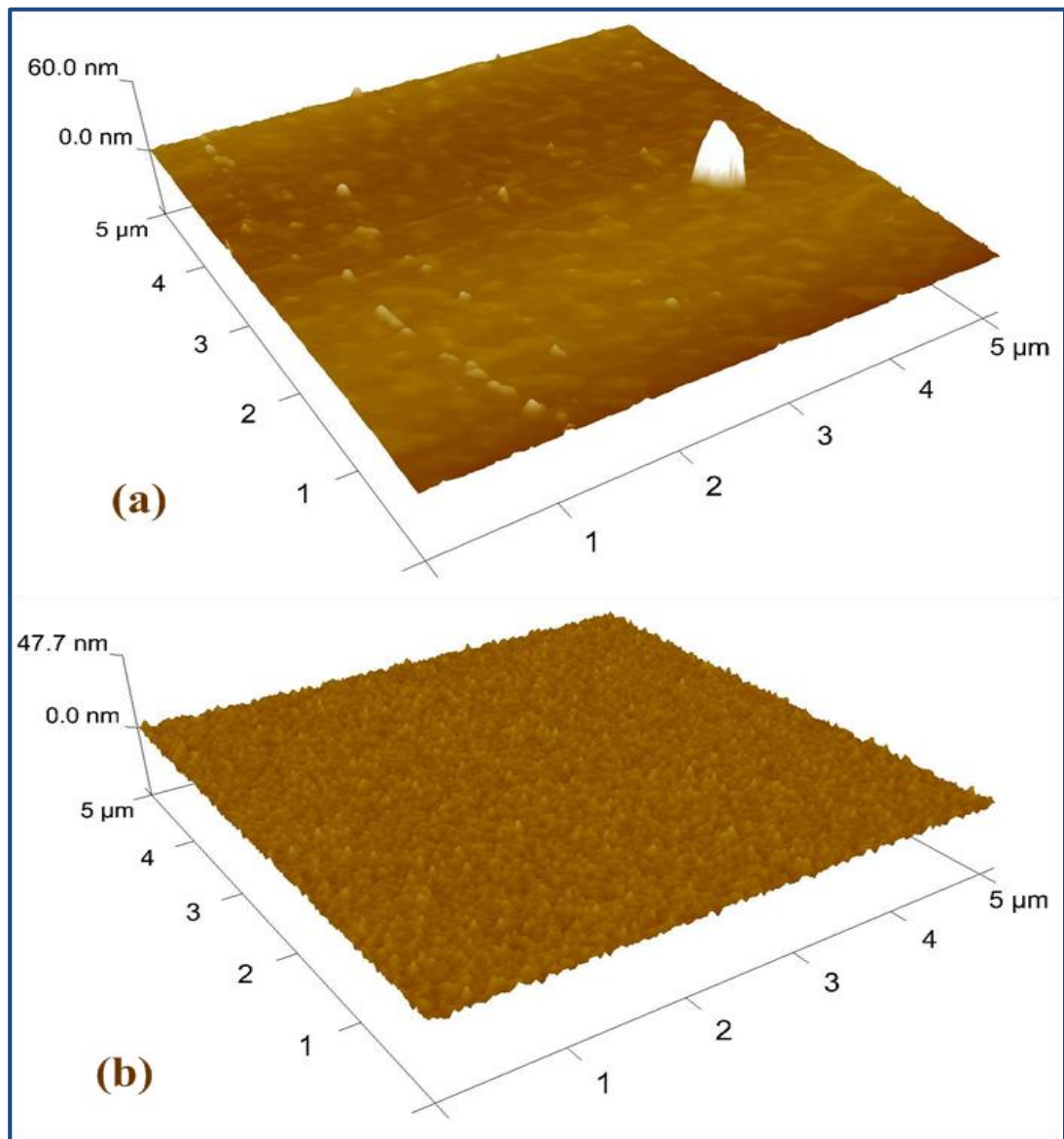


Figure 5-11: Annealed SnO₂ and ZnO deposited for 20 min (a) SnO₂, and (b) ZnO.

In our analysis, roughness values for some ZnO films were observed to be higher than for SnO₂ films of similar deposition condition. For example, for samples deposited for

45 min, SnO₂ sample had RMS roughness of 5.18 nm, while ZnO roughness was 4.52 nm. A similar behaviour was observed with samples deposited for 5 and 15 min, while the reverse was observed with samples deposited for 10, 20 and 30 min.

[Çetinörgü et al. \(2007a\)](#) reported that samples of SnO₂ and ZnO deposited at room temperature and at 400 °C varied in roughness; the RMS roughness of ZnO film was observed to increase from 1.3 nm at room temperature to 5 nm at 400 °C, whereas roughness of SnO₂ films decreased from 1.5 nm at room temperature to 0.5 nm at 400 °C, respectively. This is an indication of different film formation and film growing mechanism for the SnO₂ and ZnO samples ([Alvarez et al. 2013](#)).

On the effect of substrates on the roughness metal oxide films, [Kapustianyk et al. \(2007\)](#) reported surface roughness of 1.12 – 12.2 nm and grain size of 10 – 116 nm for ZnO thin films deposited by magnetron sputtering on glass substrate between 0.5 and 60 min. For ZnO deposited on a quartz substrate and annealed in air at 850 °C, they reported surface roughness and grain size of 22 and 170 nm, respectively. For similar sample annealed in Zn vapour, surface roughness and grain size was 25 and 300 nm, respectively. Thus, structural and optical properties of metal oxides are affected by the method of deposition and post-deposition.

With our results, it can be confirmed that film deposition and post-deposition conditions affect the film surface roughness. And the molar composition of doped ZnO plays vital role in the surface roughness. Also, the surface roughness affect film conductivity by influencing the surface chemisorption process ([Alvarez et al. 2013](#)). The electrical properties of metal oxide thin films depend on oxygen vacancies, doping concentration, film thickness, microstructure, deposition conditions such as deposition temperature, substrate temperature, precursor solutions ([Elangovan et al. 2004](#); [Yıldırım et al. 2012](#)). Therefore, film thickness, surface roughness and grain size effects have very significant influence on the sensitivity of the materials and their nanocomposites. And the combination effect of metal oxide in nanocomposites could also play a major role in the sensitivity of the sensor (see Chapters 6 and 7).

5.5 Proposed Binary Phase Structure and Solubility of Coupled SnO₂-ZnO Nanocomposites

As described in Section 2.8, SnO₂ has a tetragonal rutile crystal structure with lattice constants of $a = 0.4737$ nm and $c = 0.3186$ nm; while ZnO has a hexagonal wurtzite crystal structure with lattice constants of $a = 0.3296$ nm and $c = 0.52065$ nm. With such big differences in crystal structures and lattice constants, the phase structure of the SnO₂-ZnO nanocomposites could form a uniform phase, closely resembling the spinel-type structure of Zn₂SnO₄ ([Palmer and Poeppelmeier 2002](#); [Peiteado et al. 2006](#)). The unit cell of the nanocomposites could be face-centred cubic (space group Fd-3m) with lattice parameter, $a \approx 8.6574$ Å ([Palmer and Poeppelmeier 2002](#)). Structurally, all Sn⁴⁺ are octahedrally coordinated, while the Zn²⁺ are distributed half in tetrahedral coordination, and half in octahedral coordination. The coupled SnO₂-ZnO nanocomposites exhibit binary behaviour with one intermediate compound, Zn₂SnO₄, and two-phase regions between each end member and Zn₂SnO₄ ([Palmer and Poeppelmeier 2002](#)).

In the solid state reactions, SnO₂ and ZnO are assumed to be doped with small amount of ZnO and SnO₂, respectively; therefore, the composites in the intermediate composition range are considered to be composed of more resistive SnO₂-solid solution and more conductive ZnO-solid solution ([Yu and Choi 1998](#)). However, the solid solubility levels of metal oxides are still unclear ([Iglesias et al. 2007](#)). From the nominal value, [Palmer and Poeppelmeier \(2002\)](#) reported that the lattice parameters of Zn₂SnO₄ were unchanged in two-phase mixtures with ZnO or SnO₂, indicating minimal solubility of either oxide into the spinel. For polycrystalline materials, the solid solubility limit of SnO₂ into the ZnO lattice is below 0.1 mol% ([Iglesias et al. 2007](#)), while solubility of ZnO into SnO₂ has been estimated to be smaller than 2 mol% ([Yu and Choi 1998](#)). Therefore, both ZnO and SnO₂ have minimal solubility in each other, and are expected to form nanocomposites above 2 mol%. Also, this confirms the strong effect of geometrical arrangement of two phases in the nanocomposite system on electrical conductivity and gas sensing properties, based on the different molar compositions of the sensors (see Section 6.2).

5.6 Conclusion

This chapter has discussed the results of film characterisation. In morphology study, there is an observed transition in thickness, grain size, and surface roughness as the samples move from pure to mixed metal oxides. The S/Z samples indicated the highest grain size, but lowest surface roughness. The SnO₂ samples exhibited the highest thickness, while the ZnO samples were the lowest. The S₃Z₁, S/Z and S₁Z₃ samples showed gradual reduction in film thickness in that order. The structural analysis revealed the nanocrystalline images to have minor hillocks on a relatively dense film surface. The unannealed samples have more rounded protrusions than the annealed samples.

There is limited literature on film characteristics of nanocomposites of SnO₂ and ZnO, their binary phase and solubility behaviour. Therefore, our results will serve as the baseline. For the pure samples, comparisons with materials reported in the literature, deposition/post-deposition conditions have very significant effects on the resulting film thickness and morphologies. There could be some relevant effect on the behaviour of the sensors developed from these materials. The effects of these parameters as they affect sensitivity will be analysed in Chapter 7.

Chapter Six

Gas Sensor Signal Processing and Gas Sensitivity Behaviour

6.1 Sensor Response Data Normalisation

In this study, to extract relevant key features from the data in terms of the static change of the sensor parameter (e.g. resistance), a fractional difference model was used to normalise the sensor response, and determine the sensitivity of the target gas by the sensor ([Ahlers et al. 2005](#)):

$$S (\%) = \left(\frac{R_a - R_g}{R_g} \right) \times 100 \quad (6.1)$$

where R_a is the sensor resistance in synthetic air, and R_g is the sensor resistance in the presence of the test gas. The sensor behaviours were then characterised using this term.

6.2 Characterisation of Gas Response

Gas response analysis was undertaken with sensor devices deposited for 30 min. Before further analysis of the signal response, the raw data was smoothed using the Savitzky-Golay filter ([Savitzky and Golay 1964](#)). Applying the polynomial of 3 and span of 55, the Savitzky-Golay filter was preferred because it maintained the shape and resolution of the responses. Also, using the smoothed signal, the error calculated was between 5 and 10 % ([Basseby et al. 2014](#)). Details are as described in Appendix A.

The response of each sensing film to methanol gas was analysed at concentrations of 100, 150 and 200 ppm, while the sensor response of ethanol was analysed at only the concentration of 200 ppm. At each concentration, gas analyses were undertaken at operating temperatures of 150, 250, and 350 °C. The response behaviour of all the sensors was consistent with n -type semiconductor sensors; i.e., resistance decreases with increasing temperature because more electron-hole pairs are generated ([Barsan and Weimar 2001](#)). Values of the sensor response were normalised as gas sensor

sensitivity (%). The gas sensor sensitivity values were calculated for each of the sensor at each target gas concentration and for each operating temperature using Equation (6.1).

Presently, there is no reported research in the literature analysing the sensitivity behaviour of sensors fabricated using the entire (regularly spaced) spectrum of samples prepared using a molar mixture from 0 to 100% of SnO₂ and ZnO mixtures. The major thrust of this study is to analyse the sensitivity behaviour of different gases across the combined spectrum of SnO₂ and ZnO nanostructured sensor. The response profile were recorded and analysed. To analyse the viability of the sensor and their various compositions, the response and recovery time were also detected. The gas sensing results from different sensors are discussed, and then compared in terms of gas concentration, operating temperature and sensor composition. A typical sensor response plot is shown in Figure 6-1.

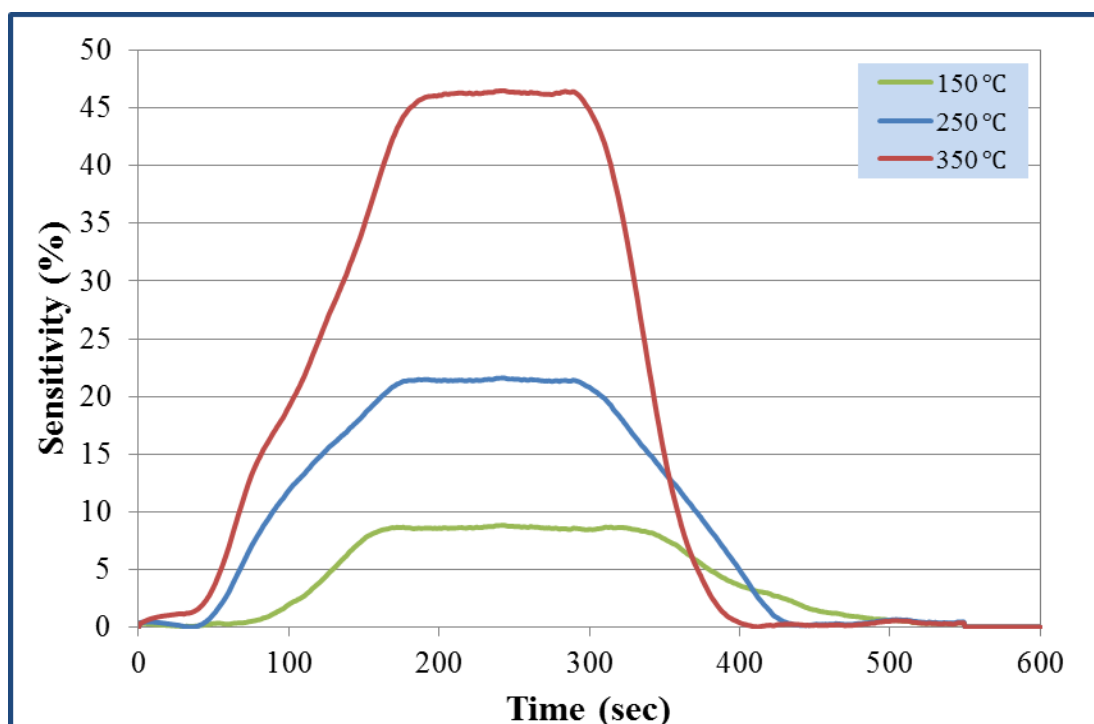


Figure 6-1: Typical sensor response (SnO₂ sensor response behaviour with 200 ppm methanol).

This plot shows that the sensitivity was zero before the introduction of the target gas. It gradually begins to increase with time once the target gas was introduced, reached a maximum value and stayed there as long as the target gas was flowing. Once the target gas was removed, the sensitivity gradually decrease and eventually reached zero. The sensitivity was observed to vary as a function of both the target gas concentration and measurement temperature.

Here, Figure 6-1 shows typical plots of sensitivity versus time for pure SnO₂ sensor at three different substrate temperatures of 150, 250 and 350 °C with 200 ppm methanol flow. However, a more interesting behaviour was evidenced with the plots of sensitivity versus sensor type (Figure 6-2).

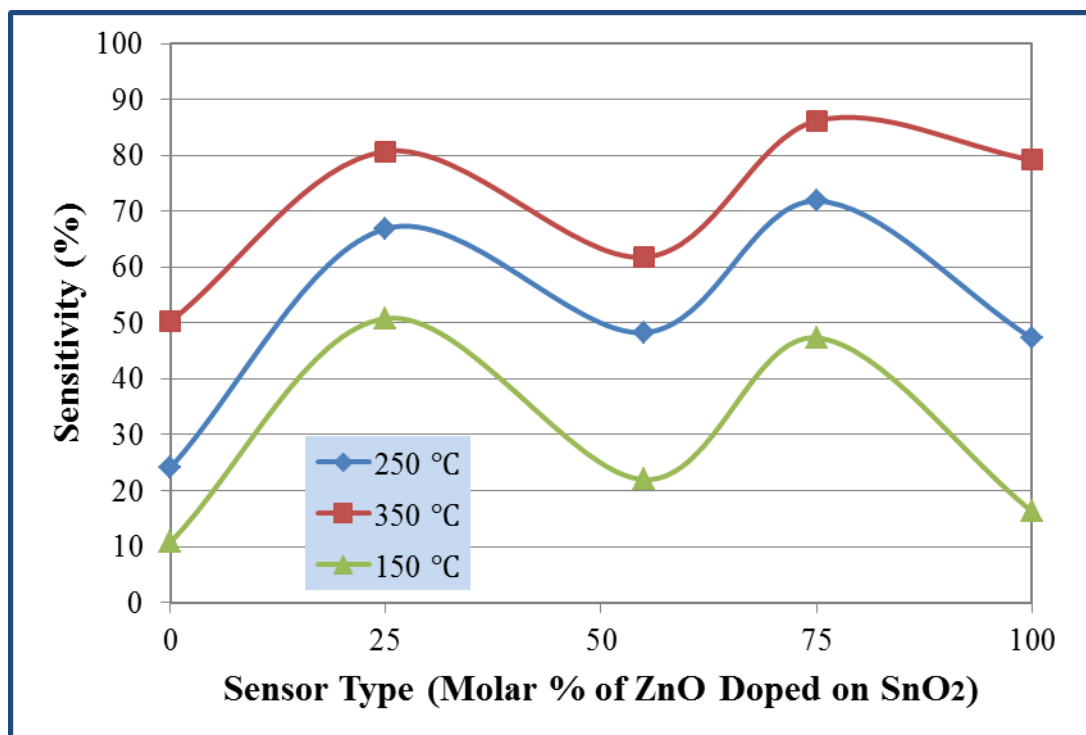


Figure 6-2: Typical sensitivity – sensor type plots (200 ppm ethanol).

Similar plots were obtained for all the sensors for different concentrations of gas and different substrate temperatures, but they are omitted for conciseness of expression and are included in the Appendix B.

Generally, gas sensitivity increases with increasing gas concentration and increasing temperature (Figure 6-2). The increase in sensitivity as the temperature was increased can be attributed to the energy activation by the external heat source to overcome the energy barrier of the reaction ([Ang et al. 2011](#)).

Detailed analysis is presented based on sensor composition, gas concentration and operating temperature. Using a linear regression analysis, the coefficient of determination for each sensor device at respective conditions is presented in Table 6-1.

Table 6-1: Coefficient of determination (R^2)

| Conditions/Parameters | | Sensor Types | | | | |
|-----------------------|------------|------------------|-------------------------------|--------|-------------------------------|--------|
| Plot | Legend * | SnO ₂ | S ₃ Z ₁ | SZ | S ₁ Z ₃ | ZnO |
| S v C | 150 °C | 0.9629 | 0.9901 | 0.8832 | 0.9489 | 0.9866 |
| | 250 °C | 0.8556 | 0.8550 | 0.9489 | 0.9457 | 0.9754 |
| | 350 °C | 0.8002 | 0.9574 | 0.9665 | 0.9850 | 0.9954 |
| S v T | M100 | 0.9011 | 0.9992 | 0.8775 | 0.9767 | 0.9798 |
| | M150 | 0.9364 | 0.9065 | 0.9777 | 0.9998 | 0.9941 |
| | M200 | 0.9666 | 0.9983 | 0.9460 | 0.9997 | 0.9818 |
| | E200 | 0.9663 | 0.9981 | 0.9665 | 0.9777 | 0.9999 |
| ΔS v C | 250-150 °C | 0.8026 | 0.7598 | 0.9832 | 0.9436 | 0.9180 |
| | 350-150 °C | 0.7797 | 0.9515 | 0.9989 | 0.9934 | 0.9893 |
| | 350-250 °C | 0.7714 | 0.5577 | 0.5196 | 0.9779 | 0.9996 |
| ΔS v T | M150-M100 | 0.9989 | 0.7564 | 0.5426 | 0.9326 | 1.0000 |
| | M200-M100 | 0.9333 | 0.9849 | 0.8019 | 0.6414 | 0.9959 |
| | M200-M150 | 0.9290 | 0.1321 | 0.9461 | 0.3179 | 0.9839 |
| | E200-M200 | 0.9606 | 0.9483 | 0.9971 | 0.8489 | 0.5105 |

* M = Methanol; E = Ethanol

Curve fitting was carried out to analyse the sensor behaviour at these conditions, and compared against each other. The coefficient of determination indicates the proportionate amount of variation in curve fit based on respective conditions.

6.2.1 Effects of Sensor Composition and Gas Concentration on Sensitivity

Generally, pure ZnO sensor device recorded a higher sensitivity than pure SnO₂ sensor device at all conditions. As parameters change, the trends vary according to sensor

composition, gas concentration and operating temperature (as discussed in the following sub-sections) for each sensor device.

6.2.1.1 SnO₂ Sensor Device (S)

The sensitivity-temperature behaviour of pure SnO₂, S, sensor device on methanol (MOH) is shown in Figure 6-3. The sensitivity to methanol was observed to increase with increasing gas concentration and operating temperature.

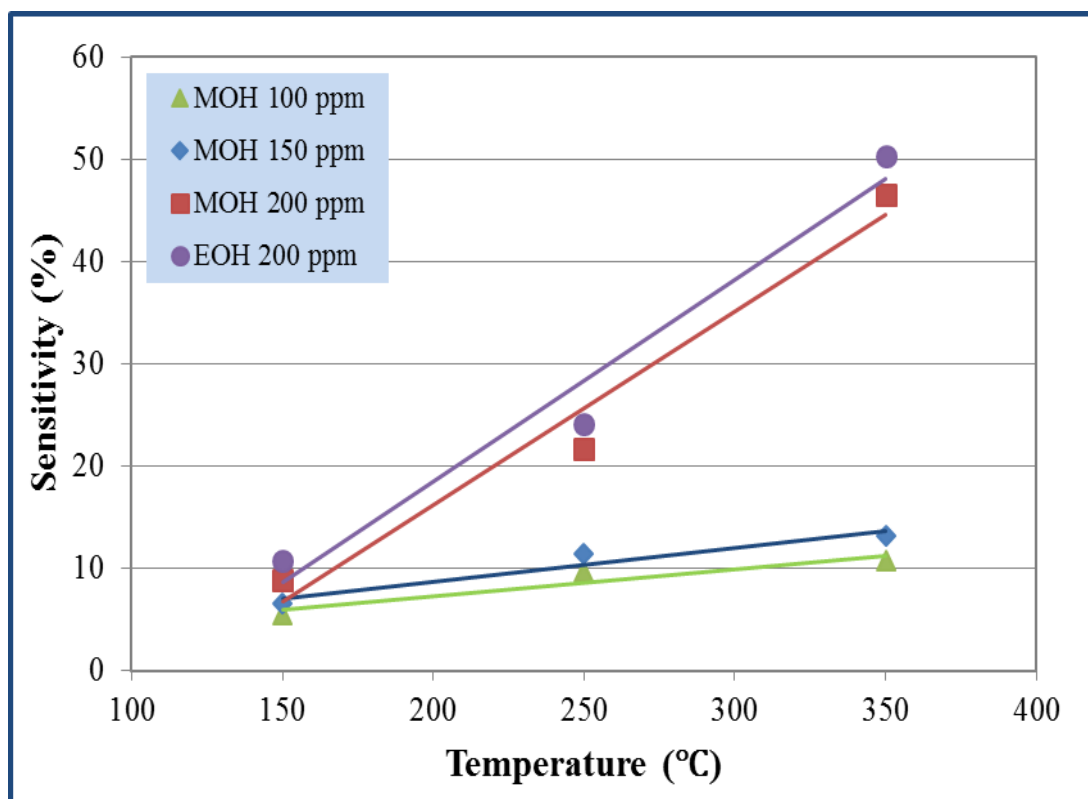


Figure 6-3: Sensitivity-temperature plots of SnO₂ with methanol and ethanol.

At 350 °C, the SnO₂ sensitivity of methanol with 200 ppm increased by 4.67 and 3.81 times from 100 and 150 ppm, respectively (Figure 6-4). Across the different concentrations, at 350 °C, the methanol sensitivity increased by 3 and 1.5 times from 150 and 250 °C, respectively. Compared with other sensor types, SnO₂ was more responsive than only the SZ sensor with 100 ppm methanol at 150 and 250 °C (Figure 6-5).

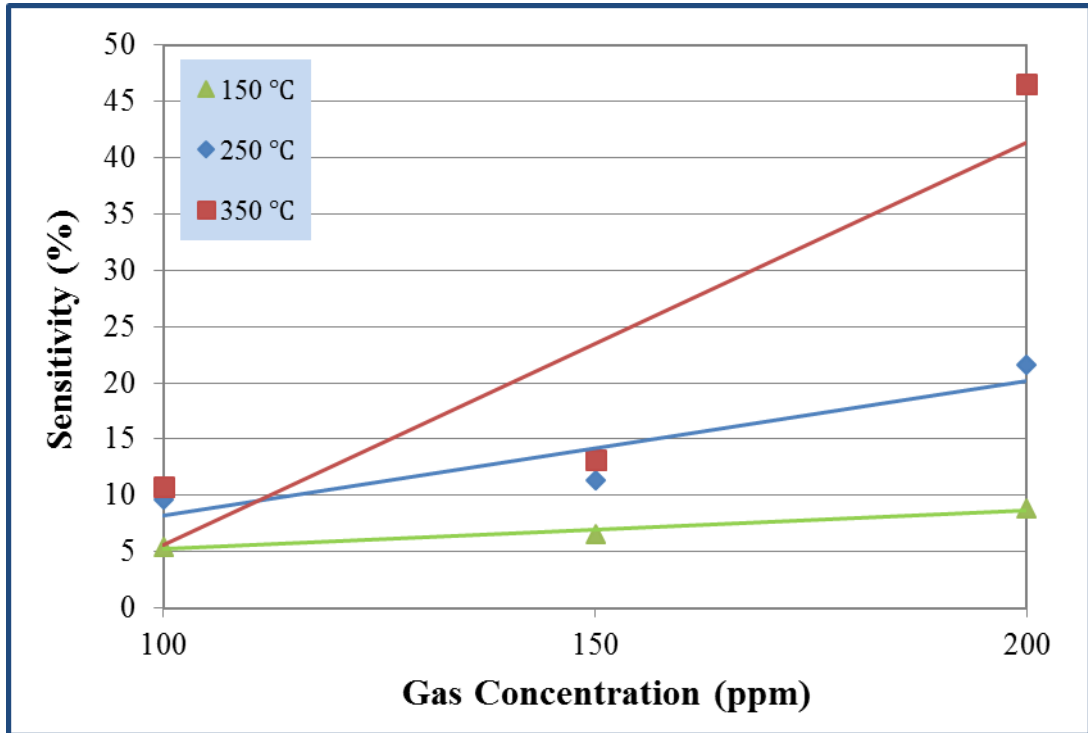


Figure 6-4: Sensitivity-concentration plots of SnO₂ with methanol.

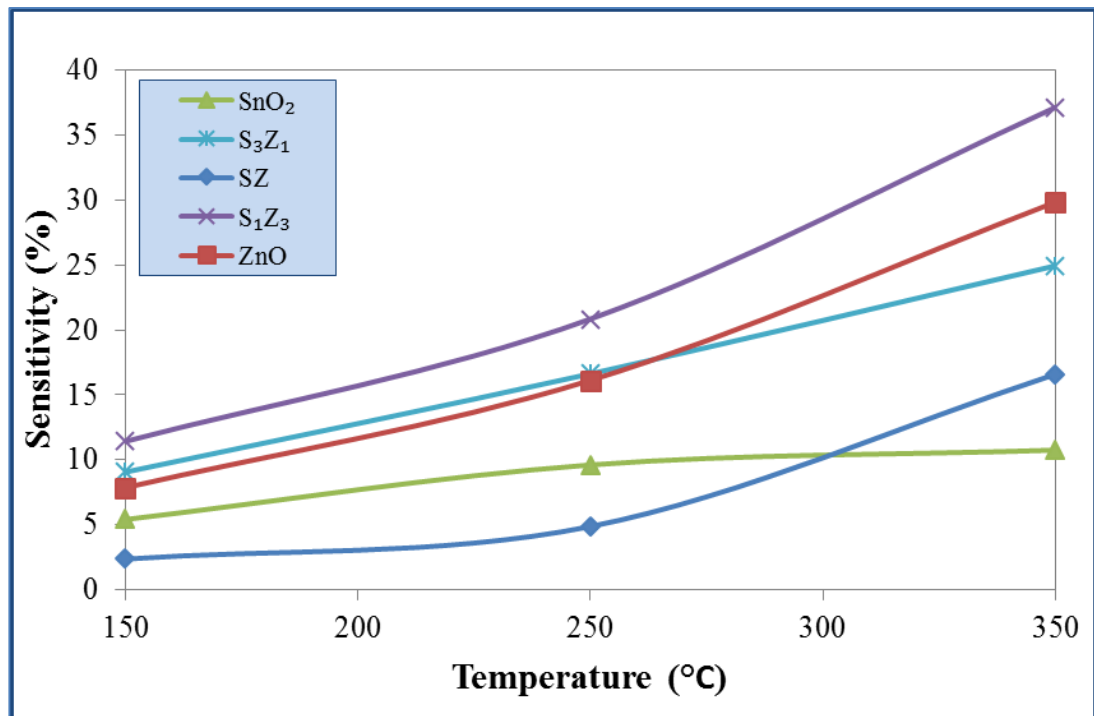


Figure 6-5: Sensitivity-temperature plots with 100 ppm methanol.

On other gas concentrations and operating temperature, SnO₂ sensor device was less sensitive than other sensors. As reported for hydrothermally generated nanocrystalline SnO₂ (Chiu and Yeh 2007) and ultrasonic spray pyrolysis prepared SnO₂ sensor (Patil et al. 2010), this investigation confirmed that sensitivity to ethanol is generally more than methanol on RF sputtered nanostructured SnO₂ thin film sensors.

The best linear fit on the sensitivity versus temperature plot was with 200 ppm methanol; while the best fit on the sensitivity-concentration relation was methanol at 150 °C.

Based on the sensitivity difference versus temperature plot, SnO₂ sensor indicated the best linear curve fit with $R^2 = 0.9989$ on the sensitivity values of methanol concentration from 100 to 150 ppm (Figure 6-6). This is a very significant improvement from the sensitivity versus temperature and sensitivity versus concentration plots, compared to it coefficient of determination values.

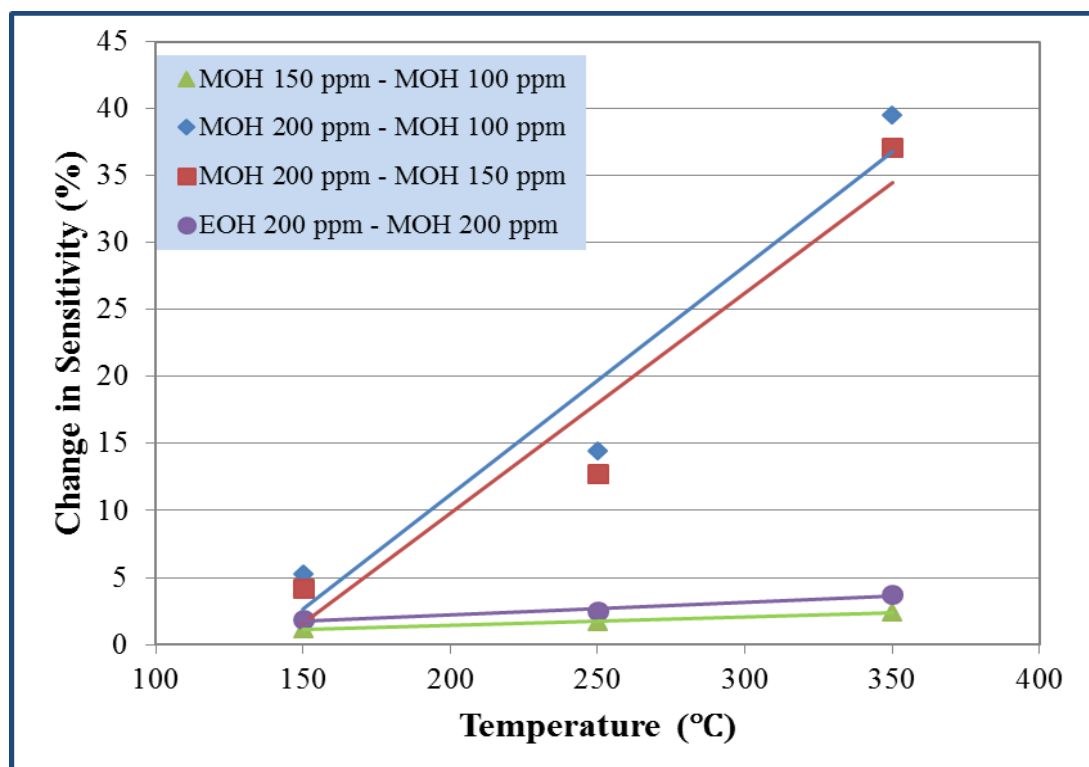


Figure 6-6: Sensitivity difference – temperature plots of SnO₂.

The coefficient of determination exhibited its worst fit ($R^2 = 0.77139$) with methanol on the sensitivity difference versus concentration plot of sensitivity change between 350 and 250 °C (see Table 6-1). Sensitivity of SnO₂ sensor to ethanol (EOH) had a very good fit ($R^2 = 0.96634$) on the linear plot of sensitivity versus temperature (Figure 6-3). On the sensitivity difference versus temperature plots, ethanol had a coefficient of determination of 0.9606 (Figure 6-6). The behaviour of pure SnO₂ sensor device, with 200 ppm ethanol was observed to be 1.14 times more than to methanol across the observed temperature range; but the best ethanol response was at 350 °C with sensitivity of 50.26 %. This result supports ethanol/methanol selectivity in the process.

In 3D SnO₂ microstructures assembled by nanosheets, prepared by hydrothermal synthesis, [Guo et al. \(2013\)](#) observed that the sensitivity of ethanol was higher than methanol at 50 ppm. [Chiu and Yeh \(2007\)](#) observed about 2-fold sensitivity increase of ethanol over methanol at 100, 200 and 500 ppm. Their results are consistent with by this research, as shown by our results.

In the sensitivity characterisation of pure and modified SnO₂ catalytic pellets, [Ang et al. \(2011\)](#) did not observe any significant discrimination between methanol and ethanol. Monitored at 300 °C, [Patil et al. \(2010\)](#) reported ethanol sensitivity enhancement of 2.57 fold over methanol and 10.75 fold over propanol (i.e., CH₃CHOHCH₃) at 500 ppm with pure SnO₂ nanocrystalline thin film sensor. At 250 and 350 °C, ethanol was 19 and 1 fold over methanol sensitivity. But [Hafaiedh et al. \(2008\)](#) reported ethanol to increase in sensitivity with concentration increment, but to decrease in sensitivity after 300 °C than 350 and 400 °C. They attributed the optimum behaviour of ethanol at 300 °C to change in the transformation phase, while the decrease in sensitivity beyond 350 °C was associated to a semiconductor-like behaviour. These serve as a further confirmation that results from this present investigation compared with pure SnO₂ nanocrystalline thin film sensor.

6.2.1.2 SnO₂ (75%) - ZnO (25%) Sensor Device (S₃Z₁)

The sensitivity of methanol to S₃Z₁ sensors was observed to increase with increasing gas concentration and operating temperature. At 350 °C, the S₃Z₁ sensor sensitivity was greater than 250 and 150 °C by 4.1 and 2.43 times, respectively (Figure 6-7).

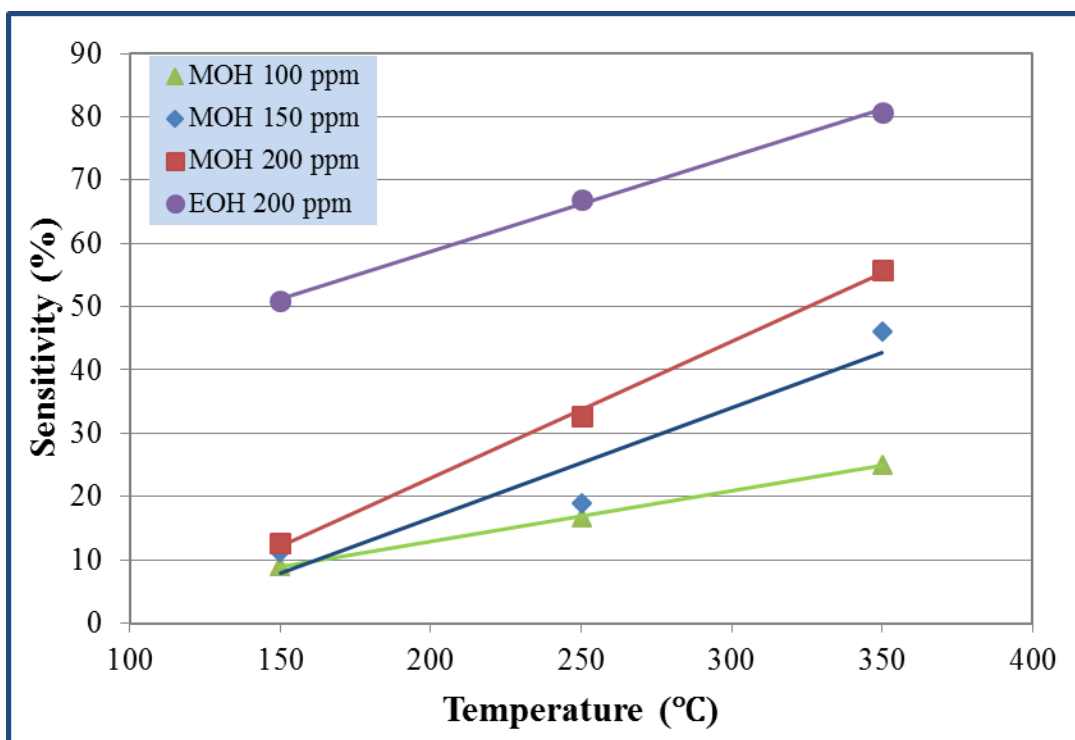


Figure 6-7: Sensitivity-temperature plots of S₃Z₁ with methanol and ethanol.

With 100 ppm methanol, the sensor was more sensitive at 350 °C than at 150 and 250 °C by 2.75 and 1.5 times, respectively. The behaviour of S₃Z₁ sensor device with the widest sensitivity magnitude was with methanol concentration of 150 ppm between operating temperatures of 250 and 350 °C. With 200 ppm methanol, the sensor was more sensitive at 350 °C than at 150 and 250 °C by 4.38 and 1.7 times, respectively. Despite the low sensitivity values with 100 ppm methanol and at 150 °C, they recorded the best curve fit on the sensitivity-temperature and the sensitivity-concentration plots.

S₃Z₁ sensors indicated their best linear curve fit ($R^2 = 0.9992$) on the sensitivity versus temperature plot with 100 ppm methanol. It exhibited its worst fit ($R^2 = 0.13208$) on

the sensitivity difference versus temperature plot of sensitivity change with methanol between 200 and 150 ppm (Figure 6-8 and Figure 6-22).

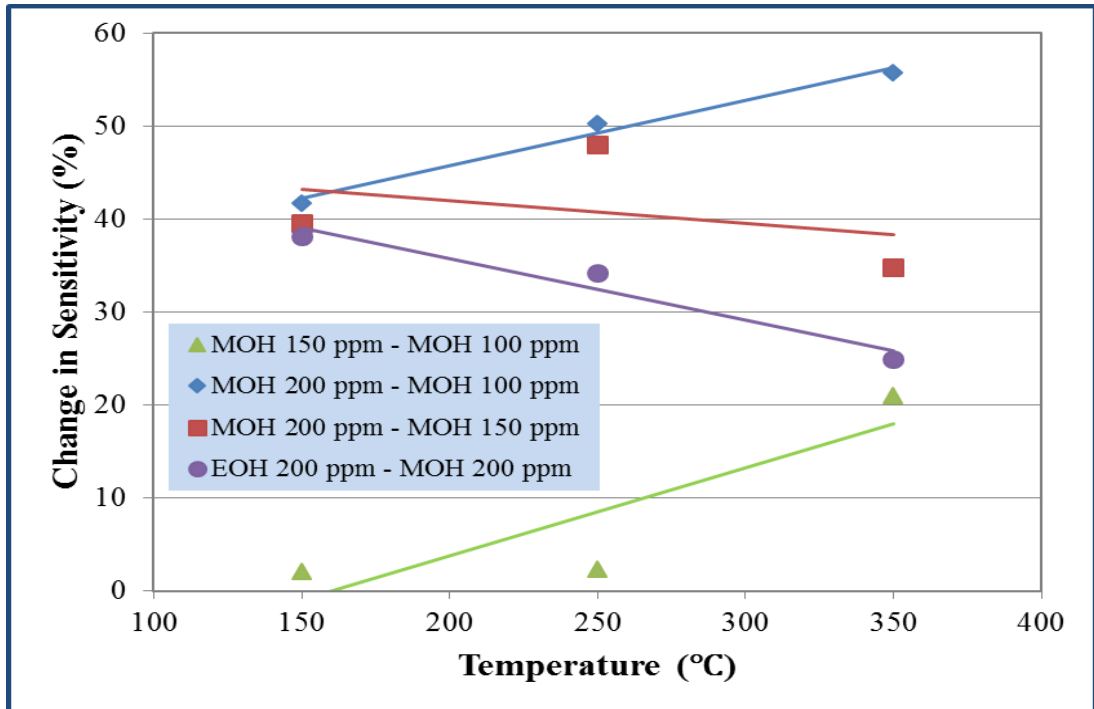


Figure 6-8: Sensitivity difference - temperature plots of S₃Z₁.

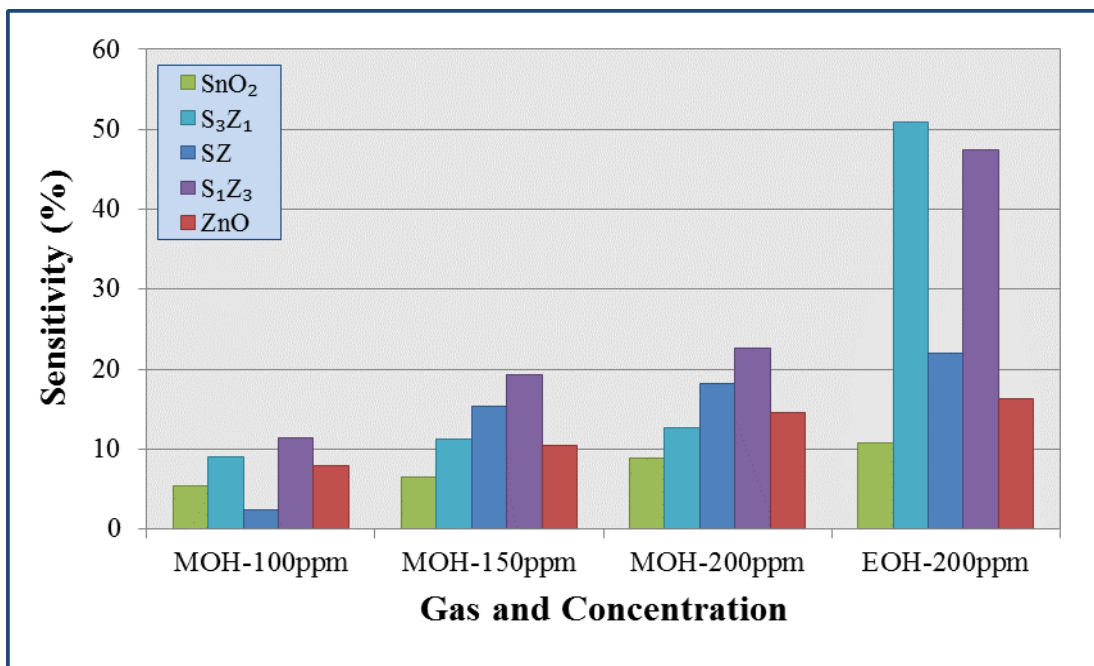


Figure 6-9: Sensor sensitivity to methanol and ethanol at 150 °C.

The sensitivity difference versus sensor type plots of 200 ppm ethanol indicated that the change in sensitivity between 350 and 150 °C was higher than the change in sensitivity between 250 and 150 °C, and between 350 and 250 °C. Most other plots exhibited very good linear fits.

Compared to other sensors, the S_3Z_1 sensor performed better than pure SnO_2 and SZ sensors (Figure 6-5). The sensor devices exhibited the best sensitivity with 200 ppm ethanol at 150 °C (Figure 6-9). With 200 ppm, ethanol was observed to be about 2.5 times more sensitive than methanol.

Consistent with our results, [de Lacy Costello et al. \(2002\)](#) observed an increase in sensitivity as concentration of molar percent of ZnO increased in the SnO_2 sensors. But, in a similar molar composition sensor device, fabricated by the combinatorial dropping of source SnO_2 and/or ZnO sols, [Kim et al. \(2007\)](#) observed that the S_3Z_1 sensor device was less sensitive to ethanol than SnO_2 sensor, but more sensitive than ZnO sensor. They reported that the addition of ZnO to SnO_2 decreased the response to ethanol, and attributed this to the fact that a decrease in surface area with increasing the ZnO content has a larger effect than the change in the acid–base properties.

However, our results serve as baseline results based on RF magnetron sputtering fabrication of nanocomposites of SnO_2 and ZnO thin film sensors.

6.2.1.3 SnO_2 (50%) - ZnO (50%) Sensor Device (SZ)

From analysis of SZ sensors, methanol with 200 ppm was more sensitive than with 100 ppm by 9.88 and 9.23 times at 250 and 150 °C, respectively (Figure 6-10).

At 250 °C, the 200 ppm methanol was more sensitive than 150 ppm by 1.59 fold. But its widest sensitivity magnitude, in terms of gas concentration, was with 100 ppm; at 350 °C, sensitivity was 6.96 and 3.39 times more than at 150 and 250 °C, respectively (Figure 6-11).

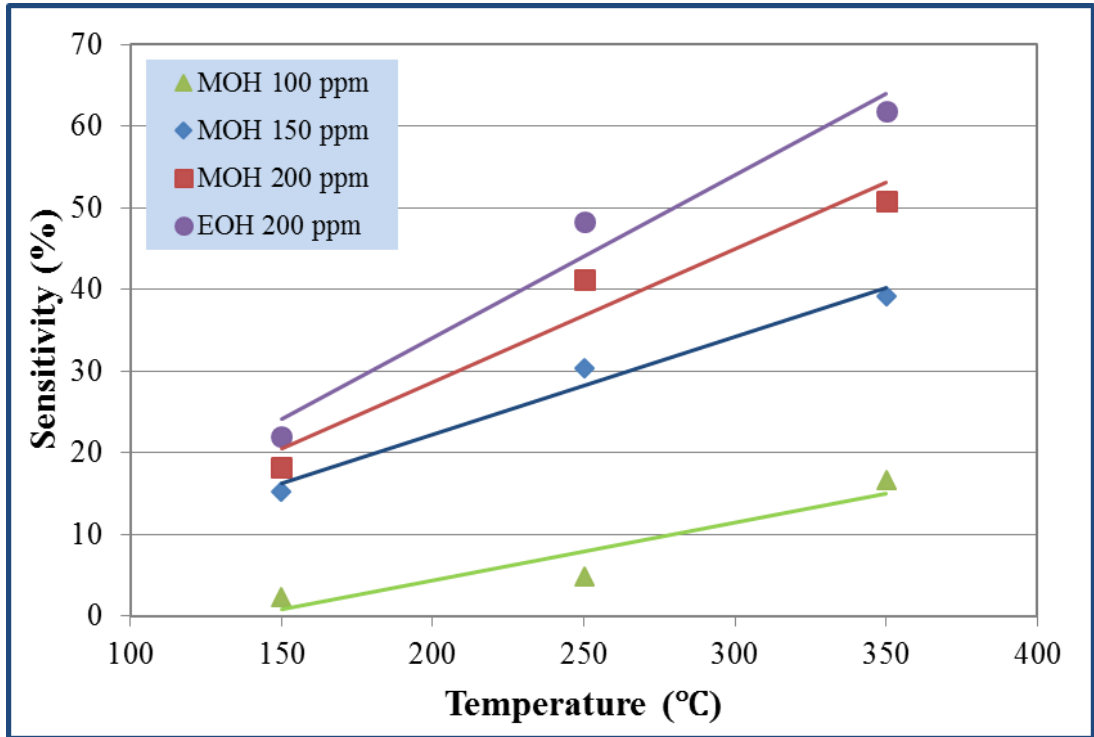


Figure 6-10: Sensitivity-temperature plots of SZ with methanol and ethanol.

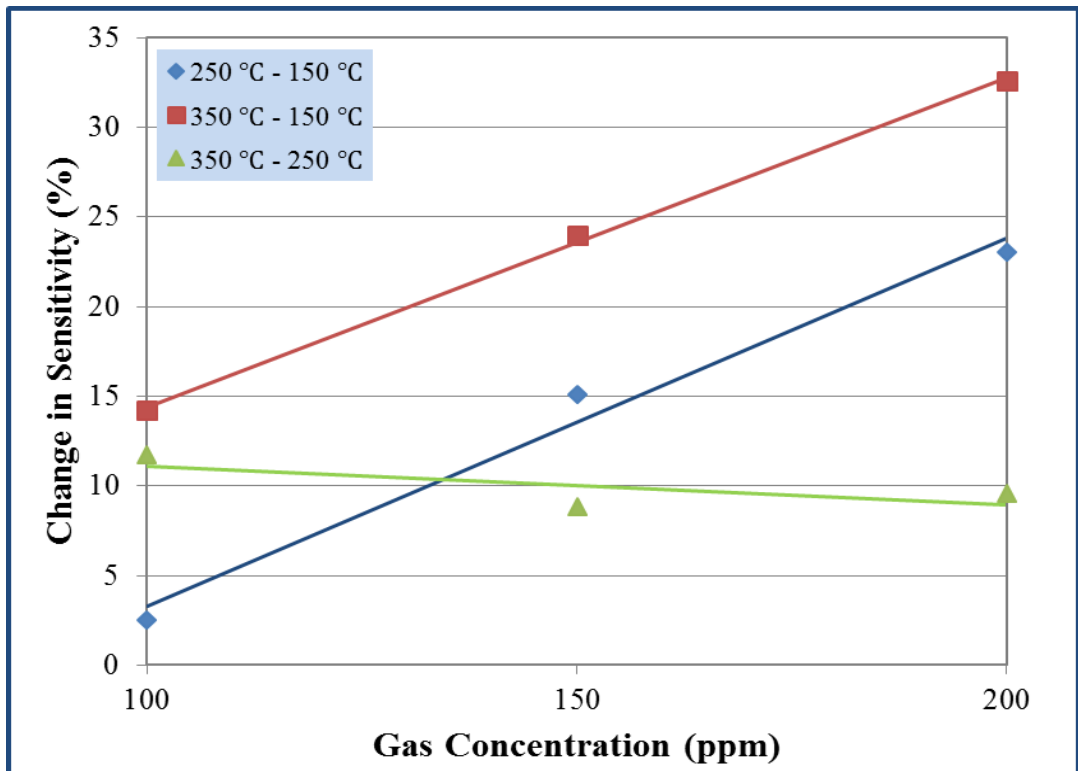


Figure 6-11: Sensitivity difference - concentration plots of SZ with methanol.

Except with 100 ppm methanol at 150 and 250 °C where it was less, the sensitivity of the SZ sensors was mostly greater than that of pure SnO₂ sensor, but less sensitive than that of pure ZnO sensor (Figure 6-9 and Figure 6-12).

This is contrary to the report by [Kohl et al. \(2000\)](#). They observed that mixed metal oxide produced higher sensitivity than both SnO₂ and ZnO sensors. Similarly, in SnO₂-ZnO composite nanofibres synthesised by electrospinning method, [Tang et al. \(2014\)](#) also observed that the SZ nanofibre was more sensitive than pure SnO₂ and ZnO nanofibres. These variations could be due to differences in method of preparation ([de Lacy Costello et al. 2002](#)).

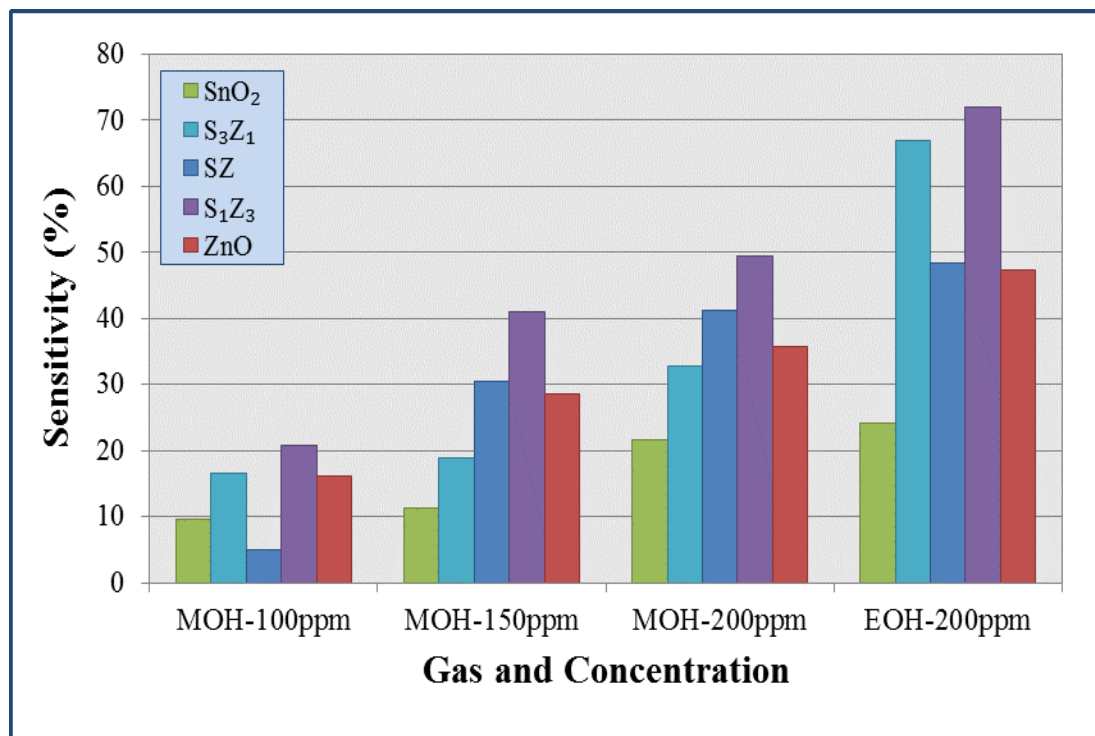


Figure 6-12: Sensor sensitivity to methanol and ethanol at 250 °C.

On the sensitivity difference versus concentration plots, the best linear fit ($R^2 = 0.9989$) by SZ sensor was with methanol at temperature between 350 and 150 °C; while the worst fit ($R^2 = 0.5196$) on the sensitivity difference versus concentration plots was with methanol at temperature between 350 and 250 °C. The sensitivity difference versus sensor type plots of 200 ppm ethanol indicated that the change in sensitivity

between 350 and 150 °C was higher than the change in sensitivity between 250 and 150 °C, and between 350 and 250 °C (Figure 6-22).

The sensitivity of S₁Z₃ sensor with methanol and ethanol was observed to increase with increasing gas concentration and operating temperature. Generally, ethanol was observed to be 1.2 times more sensitive than methanol. With 200 ppm, ethanol analysed at 350 °C was 2.8 and 1.23 times more sensitive than at 150 and 250 °C, respectively.

In a core-shell nanowire, [Thanh Le et al. \(2013\)](#) reported that a gas response of the SnO₂-ZnO core-shell nanowire was 12.5 times higher than that of SnO₂ nanowire in the detection of 100 ppm ethanol at 400 °C. Also, in a double-layer SnO₂-ZnO gas sensor, produced by sol-gel controlled-annealing of SnO₂ on the top layer and two-stage chemical precipitation from an aqueous zinc containing solution to produce the ZnO bottom coating, [Vaezi \(2008\)](#) obtained the same sensitivity as pure SnO₂ sensor for ethanol. This indicates that S₁Z₃ nanocomposites prepared by RF magnetron sputtering could produce the preferred sensitivity and selectivity.

6.2.1.4 SnO₂ (25%) - ZnO (75%) Sensor Device (S₁Z₃)

In analysis of S₁Z₃ sensors with methanol at 200 ppm, it was 3.43 and 1.58 times more sensitive at 350 °C than at 150 and 250 °C, respectively (Figure 6-13). At 150 °C, the 200 ppm methanol was more sensitive than 100 and 150 ppm by 4.14 and 2.45 times, respectively (Figure 6-14).

On regression analysis, the S₁Z₃ sensor with sensitivity difference – concentration plot exhibited its best fit ($R^2 = 0.9934$) with methanol at temperature between 150 and 350 °C. On the sensitivity versus temperature relation, the best fit ($R^2 = 0.9998$) was with 150 ppm methanol; while their worst fit ($R^2 = 0.3179$) was on the sensitivity difference – temperature relation was with methanol between concentrations of 150 and 200 ppm (Figure 6-14). Similar to other sensors, the sensitivity difference versus sensor type plots of 200 ppm ethanol indicates that the change in sensitivity between

350 and 150 °C is higher than the change in sensitivity between 250 and 150 °C, and between 350 and 250 °C (Figure 6-22).

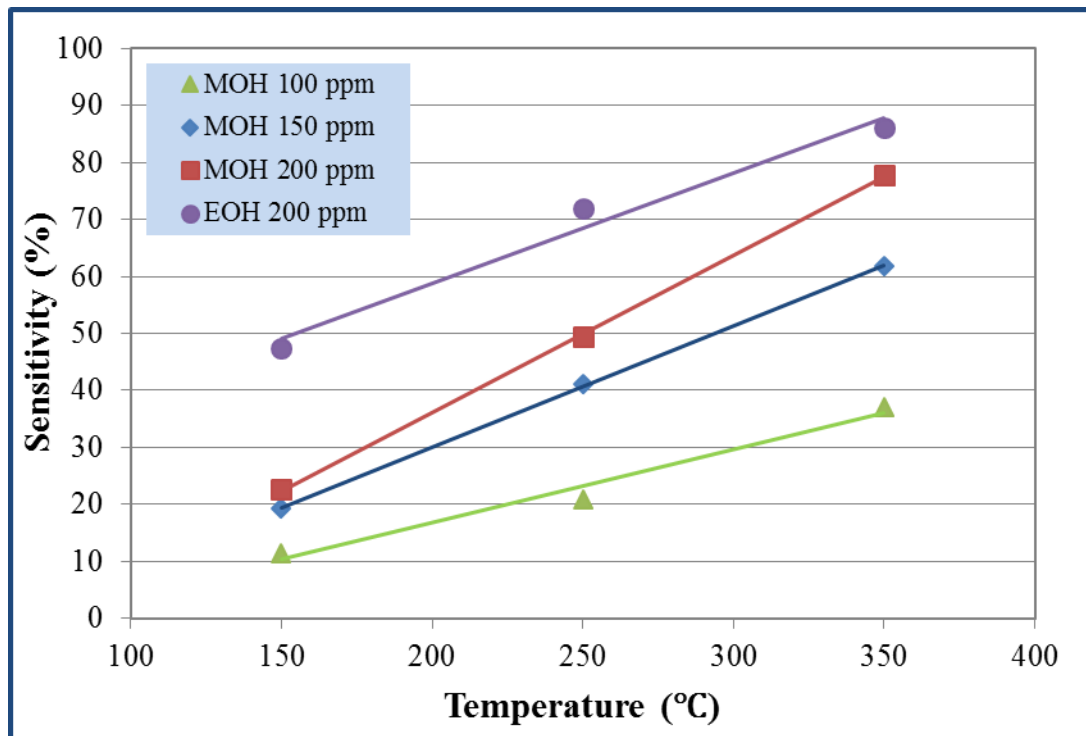


Figure 6-13: Sensitivity-temperature plots of S_1Z_3 methanol and ethanol.

Ethanol was observed to be about 1.55 times more sensitive than methanol. Compared to other prepared sensors at most conditions, the sensitivity behaviour of S_1Z_3 was the very best, followed by S_3Z_1 , SZ , Z and S , in decreasing order (Figure 6-9 and Figure 6-12). The consistent high sensitivity of S_1Z_3 could be attributed to the effect of molar composition of ZnO and SnO₂. This behaviour could be attributed to the corresponding higher catalytic activity of ZnO over SnO₂ (Cun et al. 2002a).

In a similar SnO₂–ZnO composite sensor, prepared by alternate deposition of droplets of SnO₂ and ZnO sols, Kim et al. (2007) observed that the sensitivity of ethanol with a sensor made by (similar) S_1Z_3 composition was higher than that made with pure ZnO, but less than sensor made with pure SnO₂.

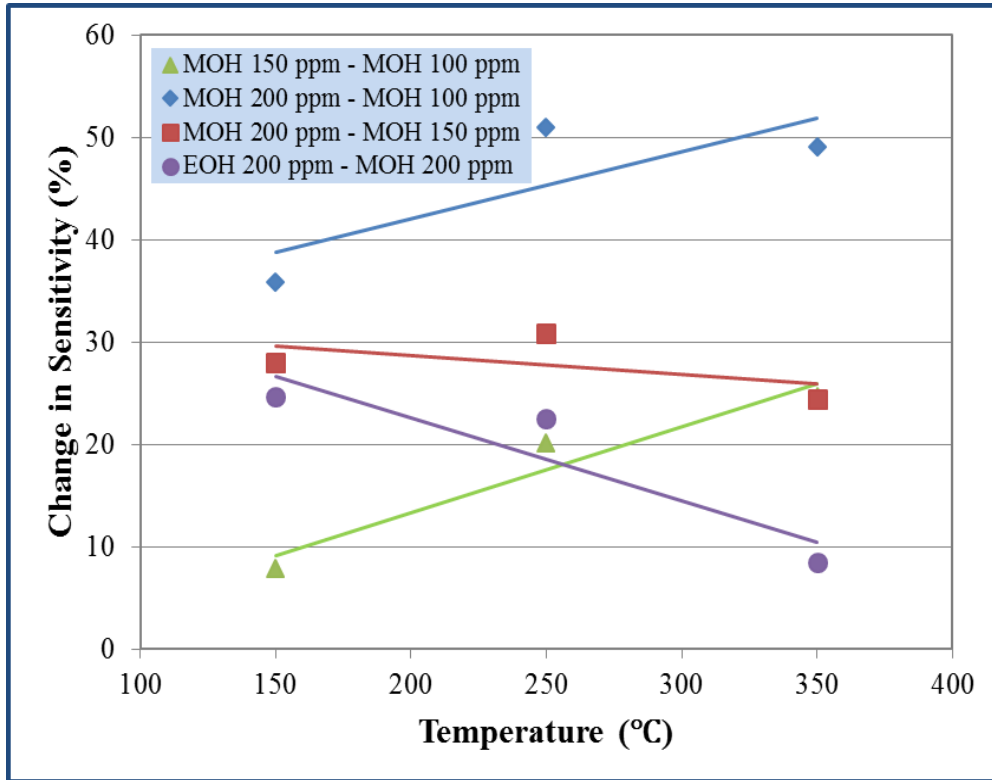


Figure 6-14: Sensitivity difference – temperature plots of S_{1Z3} .

6.2.1.5 ZnO Sensor Device (Z)

The response characteristics of the ZnO thin film sensors, Z, operated at 150 °C as a function of time for methanol and ethanol are represented in Figure 6-15. Methanol, with 200 ppm, was 4.84 and 1.96 times more sensitive at 350 °C than at 150 and 250 °C, respectively (Figure 6-16). At 100 ppm, methanol was 3.79 and 1.85 times more sensitive with 350 °C than 150 and 250 °C, respectively.

Compared with a ZnO sensor prepared using spray pyrolysis technique, [Sahay and Nath \(2008\)](#) tested the sensor with methanol concentration of 100 ppm at 350 °C operating temperature; they illustrated a change in sensitivity of about 15 and 9 % from 200 and 250 °C, respectively. These results indicate that our method produces a better gas response than sol or spray pyrolysis methods.

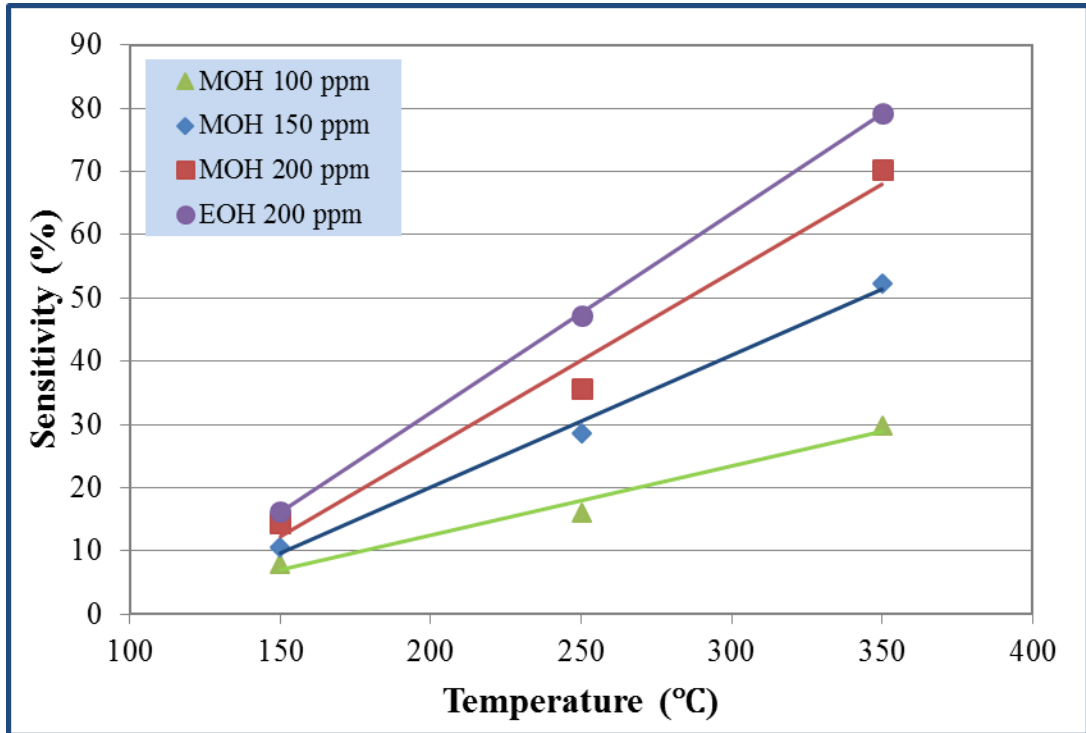


Figure 6-15: Sensitivity-temperature plots of ZnO methanol and ethanol.

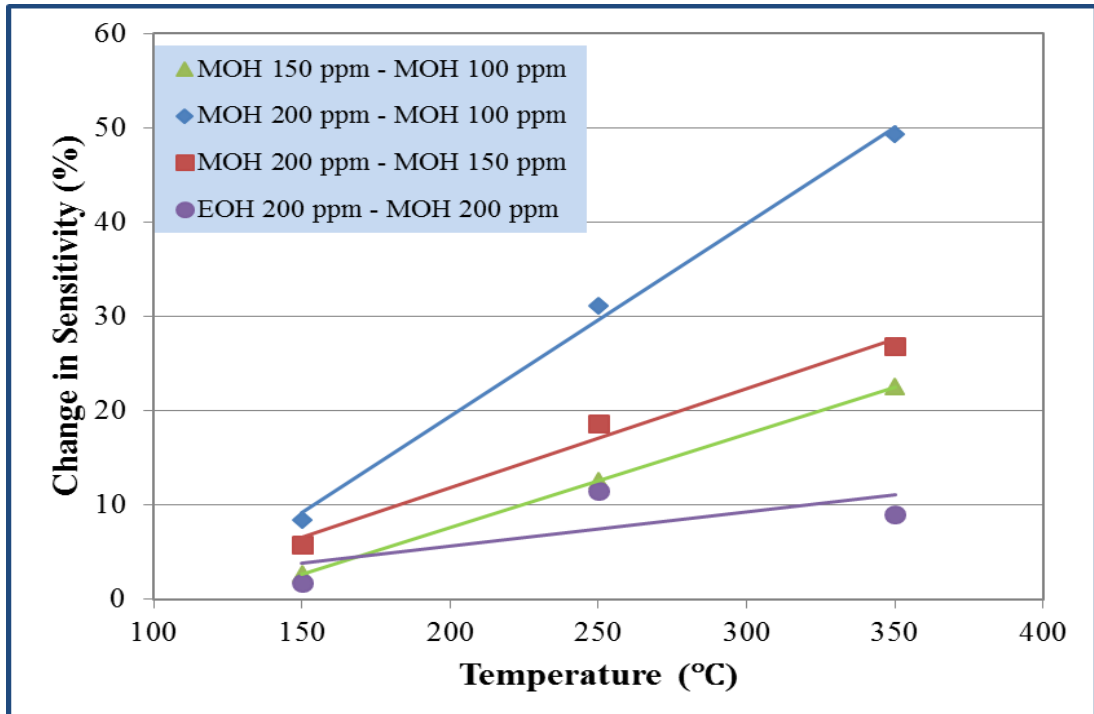


Figure 6-16: Sensitivity difference - temperature plots of ZnO.

The sensitivity of ethanol was 1.2 times more than methanol at 200 ppm. Ethanol was 4.86 and 1.68 times more sensitive at 350 °C than at 150 and 250 °C, respectively. The ZnO sensor exhibited overall best linear fit ($R^2 = 1$) on the sensitivity difference versus temperature plots with methanol concentration between 150 and 100 ppm (Figure 6-16), followed by the sensitivity versus temperature plot with 200 ppm ethanol ($R^2 = 0.9999$). Similar to other sensors, the sensitivity difference versus sensor type plots of 200 ppm ethanol indicated that the change in sensitivity between 350 and 150 °C is higher than the change in sensitivity between 250 and 150 °C, and between 350 and 250 °C (Figure 6-22). But, similar to pure SnO₂ sensor, the change in sensitivity between 350 and 250 °C was slightly higher than sensitivity difference between 250 and 150 °C. Other plots by the ZnO sensors gave very good fit.

In an analysis of thick film ZnO nanostructures prepared by thermal oxidation technique under normal atmosphere, [Wongrat et al. \(2009\)](#) observed a low sensitivity of about 7.5 for 1000 ppm ethanol at 300 °C. But, using flowerlike ZnO nanosheets synthesised by a facile chemical solution route to analyse 100 ppm ethanol and methanol, [Huang et al. \(2010\)](#) recorded a high sensitivity ($R_a/R_g = 24.1$ and 13.8) at a working temperature of 320 °C. This was attributed to small thickness of ZnO nanosheets and 3D structures of the flowerlike ZnO nanostructures. Therefore, method of sensor fabrication could be an important factor in the gas sensitivity.

6.2.2 Sensitivity Profile in Time Domain

The sensitivity trends vary according to changes in target gas concentration and operating temperature. With **100 ppm**, the behaviour of methanol is represented with sensitivity profile at 150 °C (Figure 6-17). Compared to other sensors, it was observed that the SZ sensor recorded a very slow response and recovery with 100 ppm methanol at 150 and 250 °C. With **150 ppm**, methanol sensitivity was observed to increase with increasing molar concentration of ZnO in SnO₂ and increasing operating temperature (Figure 6-18). This response and recovery behaviour was confirmed by the high response and recovery times (Figure 6-24 and Figure 6-26).

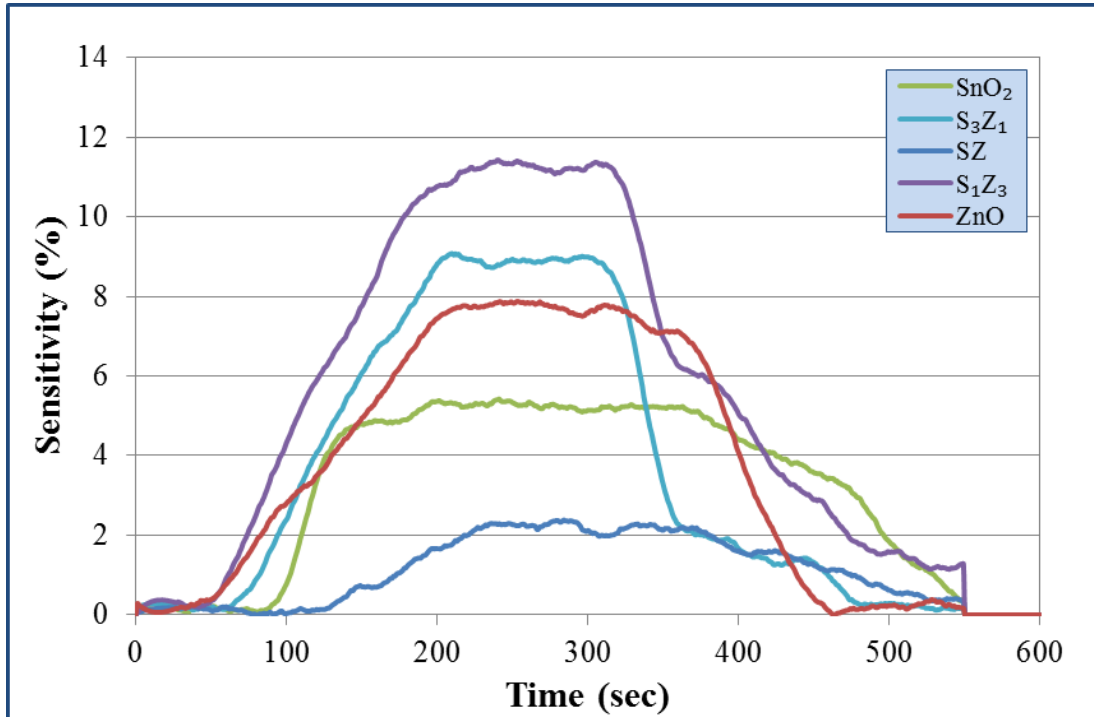


Figure 6-17: Sensitivity-time profile for 100ppm methanol at 150 °C.

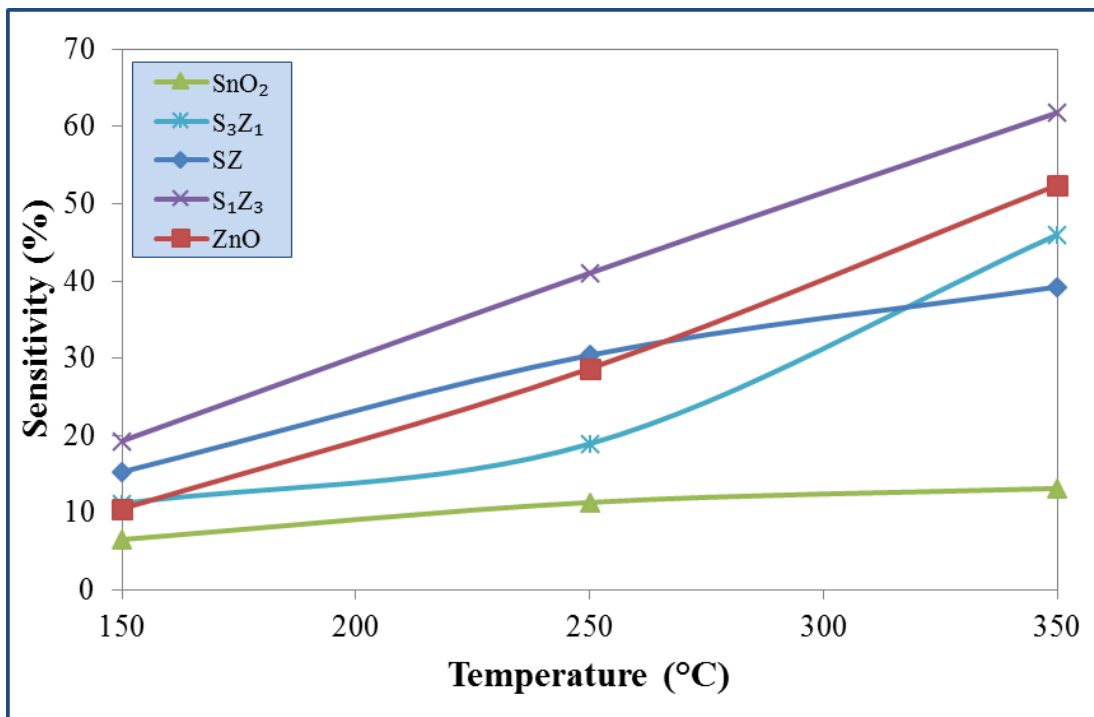


Figure 6-18: Sensitivity vs. temperature plots with 150 ppm methanol.

[Kim et al. \(2007\)](#) observed that the sensitivity of ethanol and acetone to pure SnO₂ and ZnO thin films were similar to each other. This was attributed to similarities in their chemical nature of ethanol and acetone ([Al-Hardan et al. 2010](#)). But, in contrast to our results, [Kim et al. \(2007\)](#) reported that the addition of ZnO to SnO₂ decreased the response to ethanol; i.e., their sensor, S₃Z₁, was less sensitive than S with ethanol. Alternatively, the doping of SnO₂ on to ZnO enhanced the sensitivity of their sensor; i.e., S₁Z₃ was more sensitive than Z in ethanol atmosphere.

In our research pure SnO₂ sensor device was observed to record the lowest sensitivity, while S₁Z₃ sensor profiled the best sensitivity at all conditions. Methanol sensitivity profile with 150 ppm at 250 °C is shown in Figure 6-19. Compared to pure ZnO and to coupled ZnO–SnO₂, the photocatalytic activity of pure SnO₂ is very low ([Cun et al. 2002a](#)). This behaviour could be attributed to the effect of ZnO as a doping agent on SnO₂ and other metal oxide sensor devices.

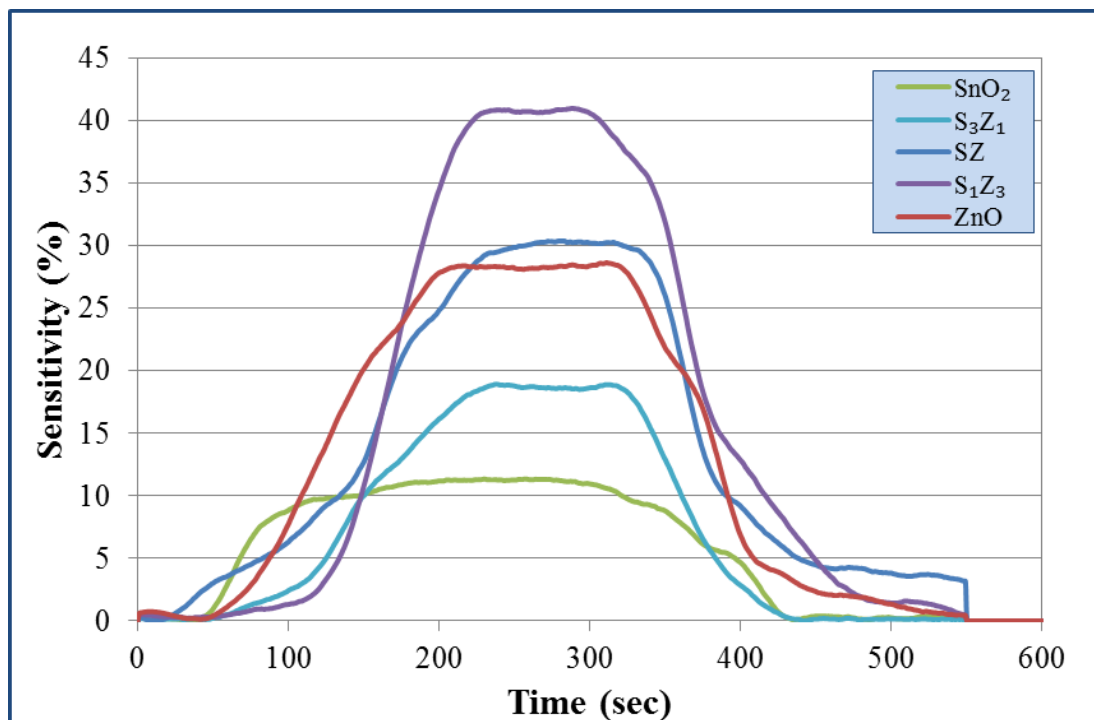


Figure 6-19: Sensitivity-time profile for 150 ppm methanol at 250 °C.

With 200 ppm, there was an interesting sensitivity increasing trend with change from methanol to ethanol, and increasing operating temperature (Figure 6-3). The response

profiles with 200 ppm methanol and ethanol at 350 °C are represented in Figure 6-20 and Figure 6-21, respectively. In most cases, SZ sensor device exhibited a lower sensitivity than S_3Z_1 and S_1Z_3 sensor devices for a particular gas and operating temperature; the only exceptions were at 150 and 250 °C (methanol) where SZ sensor exhibited higher sensitivity than S_3Z_1 device. This behaviour provides some insights towards the development of optimal sensor sensing parameters (discussed in Chapter 7).

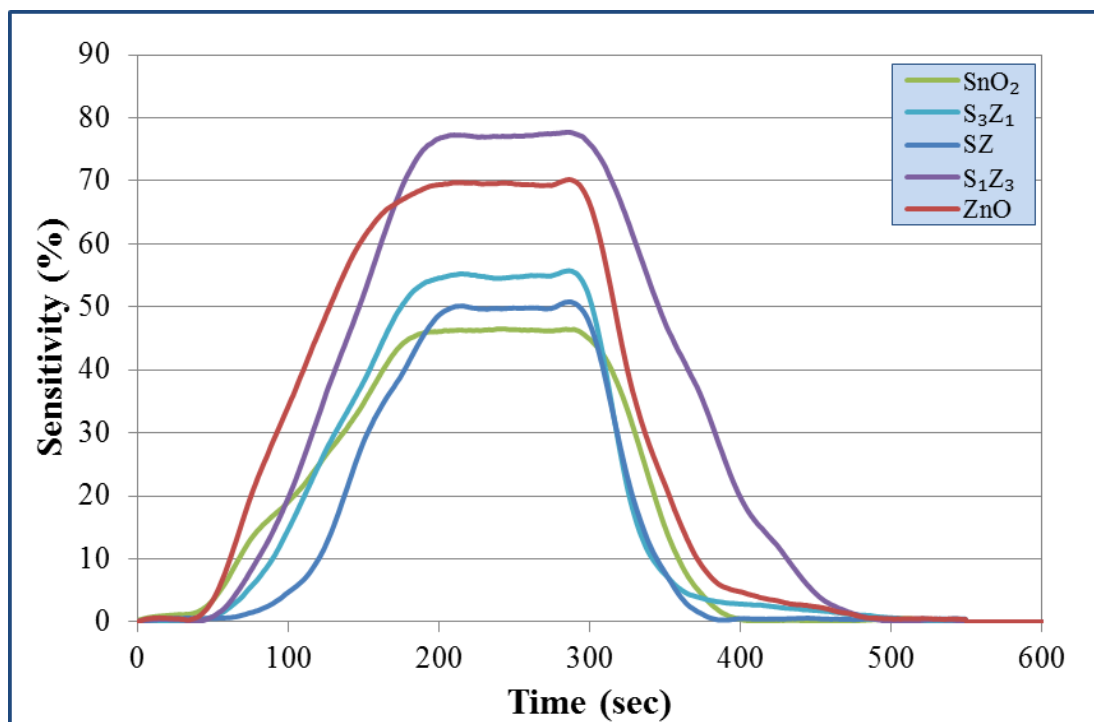


Figure 6-20: Sensitivity-time profile for 200 ppm methanol at 350 °C.

[Kohl et al. \(2000\)](#) prepared thick film mixed metal oxides sensors to demonstrate their sensitivity on decane, 1-decene, 1-decyne and 1,5,9-decatriene. Contrary to our research, they observed that mixed metal oxide sensors, such as SZ, gave higher relative conductance than pure ZnO sensor and SnO₂. We observed that the sensitivity of the SZ sensors was only higher than that of pure SnO₂ sensor, but less than pure ZnO sensor.

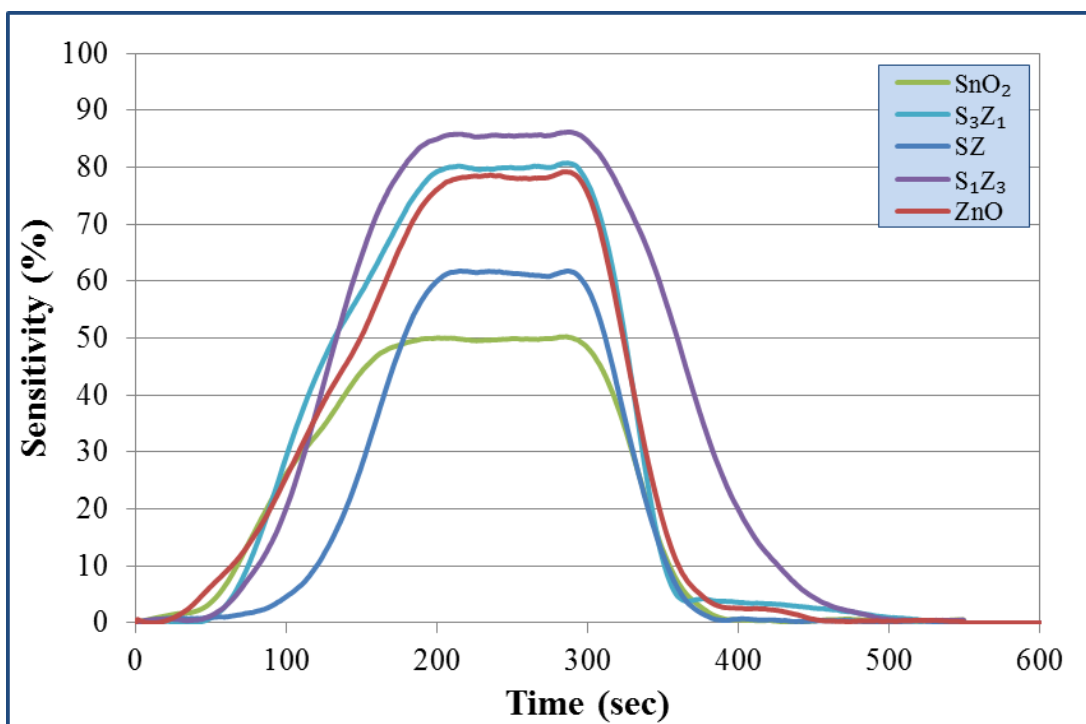


Figure 6-21: Sensitivity-time profile for 200 ppm ethanol at 350 °C.

[Hemmati et al. \(2011\)](#) reported that resistance in air of ZnO and 0.05 molar SnO₂ doped ZnO (i.e., Z-S(0.05)) sensors was dramatically higher than the other sensors. This is consistent with our observation; pure SnO₂ has a lower resistance than pure ZnO and other sensors. In their comparison of molar concentration mixed SnO₂-ZnO nanostructures prepared by precipitation method, [Hemmati et al. \(2011\)](#) observed that a similar SZ sensor device exhibited the lowest response to 300 ppm ethanol at 300 °C relative to pure SnO₂ and ZnO sensors. The response behaviour of Z sensor was higher than S sensor in their analysis; but their Z-S(0.05) nanostructure sensor gave sensitivity higher than S, Z and 0.05 molar ZnO doped SnO₂, S-Z(0.05), sensors at 300 °C with 300 ppm ethanol.

In a photocatalytic analysis, [Lu et al. \(2012\)](#) reported that when the molar ratio of ZnO to SnO₂ was varied as 10:1, 2:1, 1:1 and 1:10, the response of the sensor to 500 ppb NO₂ changed two orders of magnitude, and was remarkably higher than those of pure ZnO (1:0) and SnO₂ (0:1). They observed the maximum response to be achieved by the sensor with a device prepared from a 1:1 molar ratio of ZnO to SnO₂.

Similarly, during the photocatalytic activities of ZnO–SnO₂ nanocomposites, [Cun et al. \(2002a\)](#) observed that nano-sized coupled oxides ZnO–SnO₂ in a molar ratio of 2:1 showed stronger photocatalytic activity than 1:1 molar ratio samples, and pure ZnO, SnO₂ and Zn₂SnO₄ samples. Also, using a ZnO–SnO₂ (Zn:Sn = 2:1, 1:1, 1:2 compositions) nanofibers sensor array, at 300 °C, [Song and Liu \(2009\)](#) reported that ethanol sensitivity of nanofibre with 2:1 (molar ratio Zn:Sn) was highest, followed by 1:1 and 1:2, in respective order. This conclusion agrees with our results, although with a slightly different behaviour. Therefore, the higher sensitivity exhibited by S₁Z₃ sensor device could be attributed to the fact that the heterostructure formed improves the chemical interactions, adsorption of gases, and changes in electronic band energies in the nanocomposite.

In a set of thick film sensors consisting of mixtures of SnO₂ and ZnO powders in a range of proportions constructed by [de Lacy Costello et al. \(2002\)](#), they observed ethanol sensitivity increasing in the following order: S, S₃Z₁, SZ, Z, S₁Z₃. This behaviour is very close to the behaviour of our set of sensors.

In a series of sensors synthesised by electrospinning method at different tip-to-collector distances to prepare pure and (0.5 to 5.0 wt %) ZnO-doped SnO₂ fibres with nano-porous structure, [Nikan et al. \(2013\)](#) reported that the best response was recorded by the 1.0 wt % ZnO sensor, compared to others. They attributed this to the fact that high response of a sensor requires moderate catalytic activity ([Habibzadeh et al. 2010](#)).

This observation has collaborated with our set of sensors. The optimum sensor detection of ethanol and methanol from this work revealed that the S₁Z₃ sensor device was the most sensitive, followed by S₃Z₁, Z, SZ and S sensor devices. This behaviour has confirmed the morphological heterogeneity (particle size and roughness) reported in Chapter 5. With the excess of one metal oxide over the other on the S₁Z₃ and S₃Z₁ sensors, the increase in sensitivity is ascribed to the reduction in mutual inhibitory effect in the stage of grain growth ([Tang et al. 2014](#)).

6.2.3 Sensitivity Difference Behaviour

Relative to temperature, the sensitivity difference versus sensor type plots, as represented in Figure 6-22, presents an interesting and unique interpretation of the sensitivity behaviour of gas sensors relative to operating temperature differences.

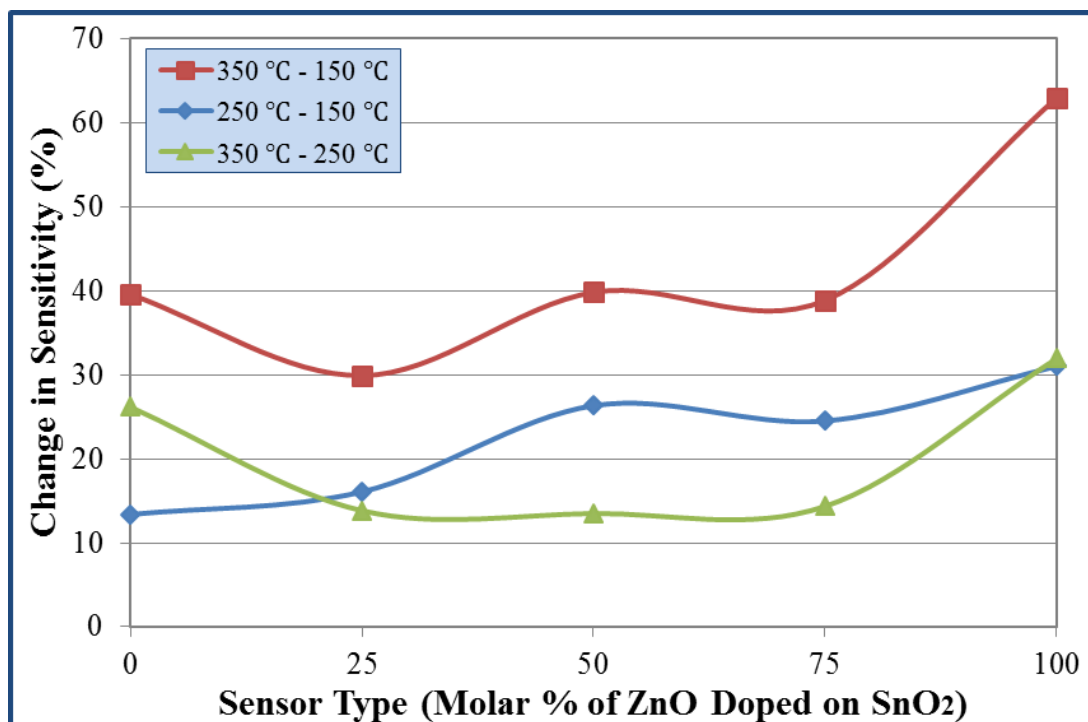


Figure 6-22: Sensitivity difference – sensor type plots of 200 ppm ethanol.

For 200 ppm ethanol (Figure 6-22), the change in sensitivity between 350 and 150 °C was higher than the change in sensitivity between 250 and 150 °C and between 350 and 250 °C. The high sensitivity difference exhibited between 350 and 150 °C is an indication that operating temperature has significant effect in the sensitivity behaviour of all the sensor devices studied.

Similar to 200 ppm methanol (Figure 6-23), the low sensitivity difference exhibited between 350 and 250 °C confirmed that fact that the magnitude of operating temperature may not have significant effect in the sensitivity behaviour. This interpretation is quite innovative.

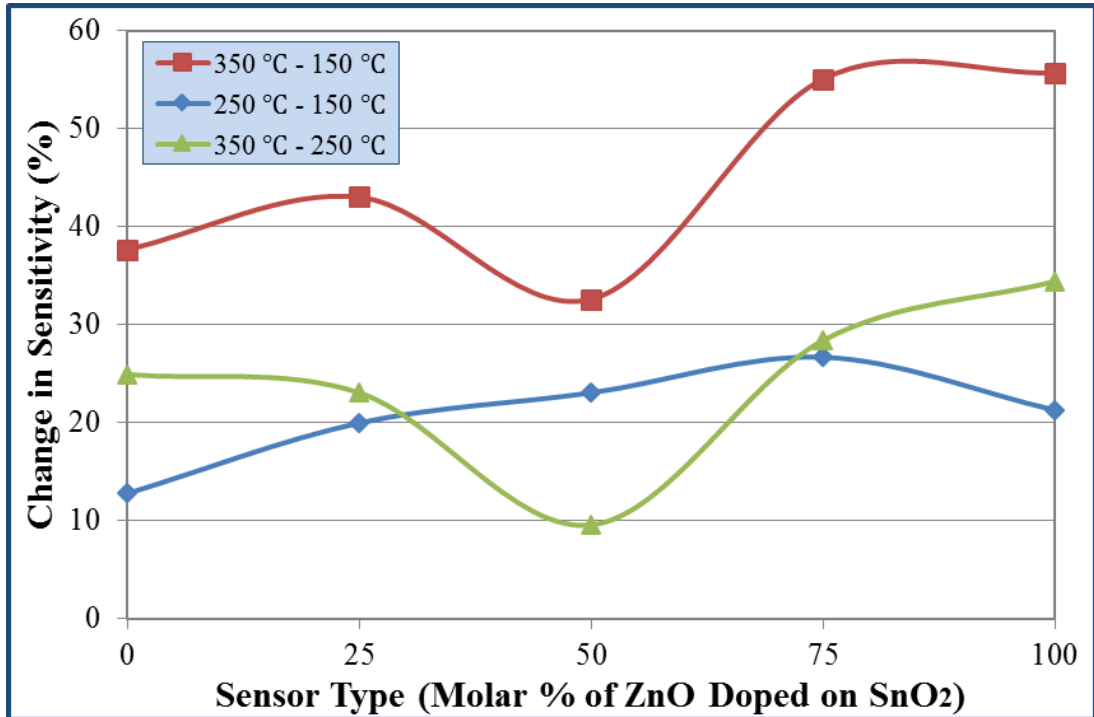


Figure 6-23: Sensitivity difference – sensor type plots of 200 ppm methanol.

From both Figure 6-22 and Figure 6-23, a major observation was with the sensor devices fabricated from pure MOXs. The ZnO sensor devices exhibited a higher sensitivity difference than SnO₂ sensor devices, confirming the higher sensitivity of ZnO over SnO₂ on both methanol and ethanol. With both gases, S₁Z₃ sensor devices exhibited higher sensitivity difference than S₃Z₁ sensor devices. However, SZ sensor devices had higher sensitivity difference with ethanol than with methanol. These sensitivity difference behaviour are in consistence with the sensitivity behaviour of the sensor devices.

6.2.4 Transient Response Curve Analysis

The sensitivity profiles (Figure 6-19 to Figure 6-21) illustrated the transient response behaviour of the sensors. They represent the adsorption-desorption reaction of the sensor-gas interaction process on the thin film surface.

The detection, response and recovery time of the target gases are vital indices of the adsorption-desorption kinetic process, and are very important parameters for

designing sensors for the desired application. The detection time, τ_{Det} , describes the time taken for the sensor output signal to indicate a 10% change from the initial value after applying the target gas. The response time, τ_{Res} , describes the time taken for the sensor output signal to reach 90% of its saturation value after applying the target gas. The recovery or decay time, τ_{Rec} , is the time taken for the sensor output signal to drop to 90% of its saturation value after switching off the target gas.

Visual representations of typical detection, response and recovery time for different sensors at different target gas concentrations and operating temperatures are depicted in Figure 6-24 to Figure 6-26. Generally, the lower the durations of detection, response and recovery, the better are the sensors.

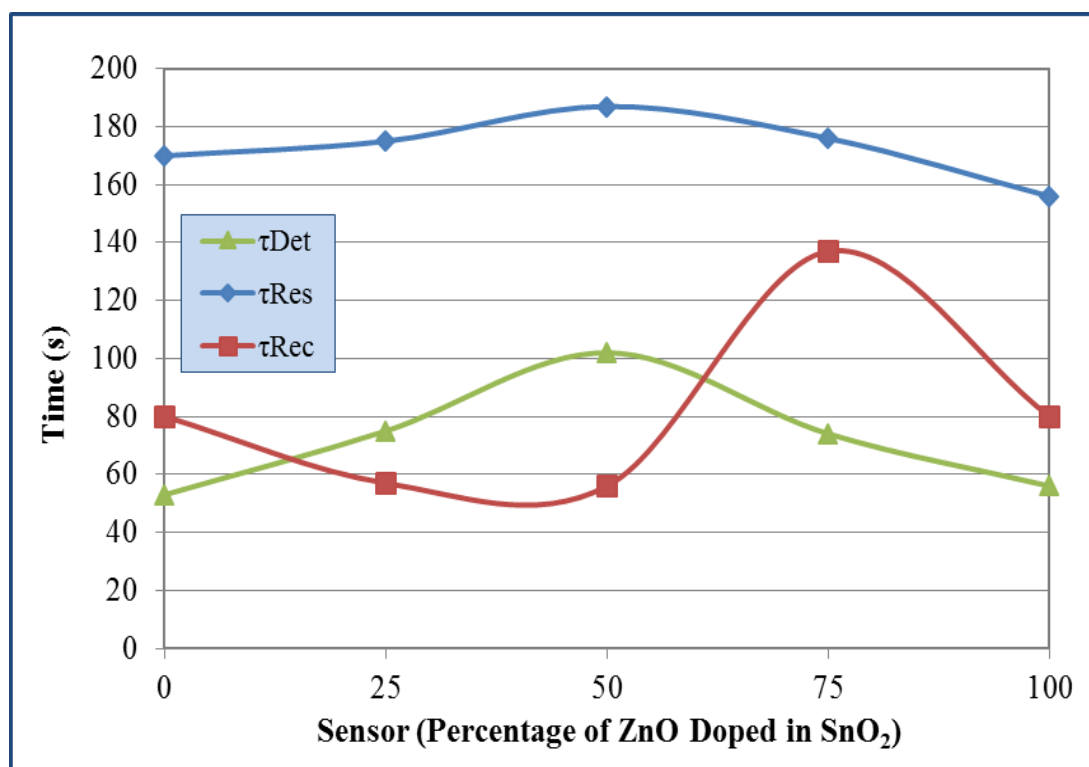


Figure 6-24: Response and recovery time plots of 200 ppm methanol at 350 °C.

The average detection time for the sensors was observed to decrease with increase in operating temperature, but increase slightly with increase in gas concentration. Detection times was in the range of $0.5 \leq t_{\text{Det}} < 2$ min; the best detection was 30 s for S sensor device with 150 ppm methanol at 350 °C, and the worst was 130 s for SZ

sensor device with 100 ppm methanol at 250 °C. The detection times for \mathbb{Z} sensor devices were slightly higher than for \mathbb{S} sensor devices, but higher values were observed in the combined mixtures as the heterogeneity increases.

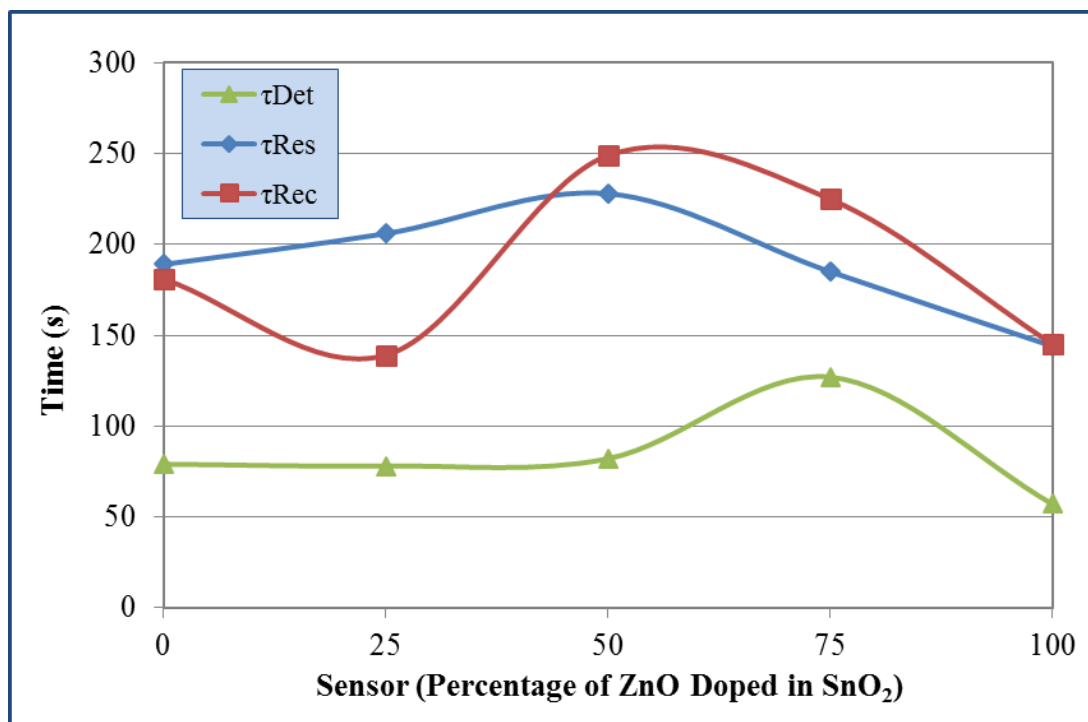


Figure 6-25: Response and recovery time plots of 150 ppm methanol at 150 °C.

The best response time was 118 s for ZnO sensor with 200 ppm methanol at 150 °C, while the best recovery time was 54 s for $\mathbb{S}_3\mathbb{Z}_1$ sensor with 200 ppm ethanol at 250 °C. $\mathbb{S}\mathbb{Z}$ exhibited the worst response and recovery times with methanol; the worst response time of 234 s was with 100 ppm at 250 °C, and the worst recovery time of 249 s was with 150 ppm (at 150 and 250 °C) and with 200 ppm (at 150 °C).

Ethanol with 200 ppm displayed the best detection time of 55 s with \mathbb{S} sensor at 350 °C, and the worst detection time of 112 s with $\mathbb{S}_1\mathbb{Z}_3$ sensor at 150 °C (Figure 6-26). This could be attributed to the increased in chemical activities as temperature increases, and increase in structural heterogeneity. There is no reported literature on detection times for characterisation of gas sensors. However, the detection, response and recovery profiles of 200 ppm methanol (Figure 6-24) and 200 ppm ethanol (Figure

6-26) at 350 °C were quite similar across the different sensor devices. Thus, these data serve as the baseline sensor behaviours.

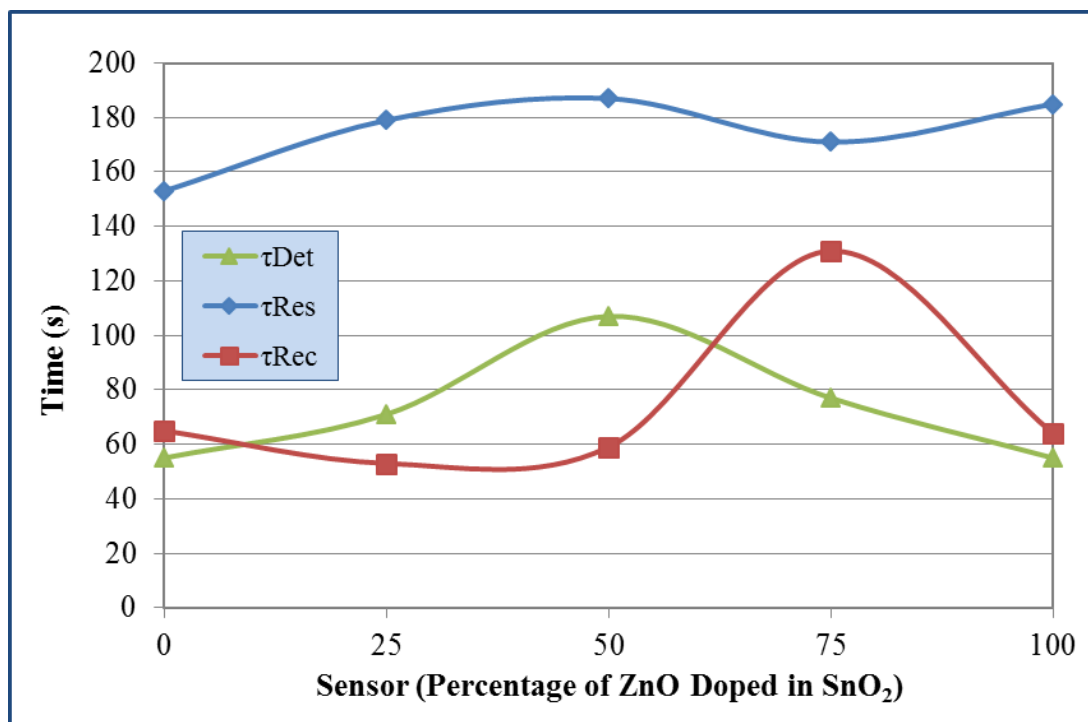


Figure 6-26: Response and recovery time plots of 200 ppm ethanol at 350 °C.

For pure SnO₂ sensor device, the response and recovery times were best values with 100 ppm methanol at 350 °C as 154 and 115 s, respectively. With 200 ppm, the best response time (153 s) was at 150 °C, while the best recovery time (80 s) was at 350 °C. The fast response and recovery by ZnO, SnO₂ and S₃Z₁ sensor were attributed to their relative homogeneous film surface (Chapter 5). The slow response and recovery by SZ could be attributed to its high heterogeneous surface.

Compared with SnO₂ sensor prepared by screen-printing technology, [Yadava et al. \(2010\)](#) reported response and recovery time of 90 s and 200 s, for 5000 ppm methanol at 200 °C. These values are considerably higher than our values despite their high gas concentration.

In our research, ethanol (with 200 ppm) indicated best response times of 153 s with S sensor at 350 °C and S₃Z₁ at 250 °C. The best recovery time, as exhibited by S₃Z₁ at 350 °C was 53 s. The worst response/recovery times were at 150 °C; response time of 242 s by S sensor, and recovery time of 183 s by SZ sensor. Therefore, the faster response–recovery behaviour by S₃Z₁ samples could be attributed to the addition of ZnO nuclei and the formation of SnO₂–ZnO hetero-junctions in the prepared nanostructure ([Ma et al. 2013a](#)).

[Ang et al. \(2011\)](#) reported the same response and recovery times of 13.3±3 s, for pure SnO₂ catalytic pellets analysed with 100 ppm ethanol at 300 °C. For pure SnO₂ fabricated by spray pyrolysis method, and analysed in 400-800 ppm ethanol at 50-350 °C, the response and recovery times reported by [Kumar et al. \(2014\)](#) was 4–6 s and 40–45 s, respectively. For hollow nanospheres nanostructures exposed to 100 ppm ethanol, [Ma et al. \(2013a\)](#) calculated response and recovery times of about 10 and 23 s for the ZnO-doped porous SnO₂ nanospheres based sensor, and about 110 and 140 s for pure porous SnO₂ nanosphere, both at 150 °C of sensor operating temperature of 150 °C ([Ma et al. 2013a](#)). Their hollow nanospheres nanostructures were synthesised by a controllable and scalable route.

Generally, the SZ sensor devices exhibited poor detection, response and recovery time. There is an absence of reported data on methanol and ethanol response and recovery times with these sensor devices. For a hollow hierarchical SnO₂–ZnO composite nanofibers synthesised by an electrospinning method, [Tang et al. \(2014\)](#) reported a response and recovery time of about 20 s and 40 s, respectively, for 10 ppm methanol at 350 °C. In a similar nanocomposite of an ZnO/Fe₂O₃ (of 40/60 mol %) screen-printed onto a glass substrate, [Arshak and Gaidan \(2005\)](#) reported that the response and recovery times of the sensor at room temperature for 4000 ppm methanol, ethanol and propanol, were 10 and 10, 15 and 20, and 40 and 70 s, respectively. [Tang et al. \(2014\)](#) described the sensing mechanism of SZ composite sensor devices as surface-controlled type. Therefore, the poor response and recovery times of SZ sensors could

be attributed to the high surface heterogeneity effect from the competing metal oxides, since the combined metal oxides are in equal molar concentrations.

In most cases, pure ZnO sensor device, Z, gave the best detection, response and recovery time. Comparing 100 ppm ethanol, [Huang et al. \(2010\)](#) reported a response and recovery time of 2 and 15 s, respectively, at 320 °C using ZnO 3D nanosheet sensor, while [Jing and Zhan \(2008\)](#) reported 32 and 17 s for response and recovery time from porous ZnO nanoplates at 380 °C.

For gas concentration of 200 ppm and operating temperature of 150 °C, detection time was better with methanol sensitivity than ethanol. But at 250 and 350 °C, both methanol and ethanol exhibited similar transient time behaviour across the sensors. For example, with 200 ppm methanol and ethanol, the detection, response and recovery times exhibited very similar profiles at 350 °C (Figure 6-24 and Figure 6-26). There was a rise in detection and response times from pure SnO₂ to SZ sensor devices, then drop towards pure ZnO sensor devices. On the contrary, there was a decrease in response times from pure SnO₂ towards the SZ sensor devices, then rise to S₁Z₃ sensor devices before dropping to pure ZnO sensor devices. The SZ sensor devices exhibited highest detection and response times, but lowest response time; while S₁Z₃ sensor devices exhibited highest response times.

Generally, the response and recovery times were observed to decrease with increasing temperature. In comparison, methanol has better response and recovery times than ethanol. This can be attributed to the fact that the lower the molecular weight and the higher the chemical reactivity, the shorter will be the response times. Surface area and morphology could affect the kinetics of the surface reaction. Apart from the chemical reactivity, the recovery time is affected by accompanying desorption of water vapour and carbon dioxide, after alcohols combustion ([Vrñata et al. 2000](#)).

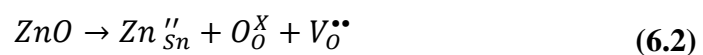
Therefore, for practical use of these sensor devices, the detection, response and recovery time could be further reduced with increase in temperature, decrease in

molecular structure of the target gases, and increase in surface area of the sensing elements.

6.3 Proposed Sensing Mechanism

Coupled metal oxide nanocomposites experience modification of their physical, electrical and optical properties, and may increase the catalytic activity by increasing the charge separation and extending the energy range of activation. A mixture of SnO₂ and ZnO was observed to generate hydrogen from water in the presence of a sensitizer (ruthenium bipyridyl complex) and a hole scavenger (i.e. ethanol) under visible light irradiation ([Tennakone and Bandara 2001](#)). Both SnO₂ and ZnO can be excited by photons, but ZnO shows higher photocatalytic activity than SnO₂. These results originated from the transfer of energetic electrons (hot electrons) injected to SnO₂ via dye-sensitisation to ZnO, whose conduction band position is above that of SnO₂, leading to a wide separation of the electron and the hole ([Cun et al. 2002a](#)). SnO₂ can act as a sink for the photogenerated electrons in the SnO₂–ZnO nanocomposite.

Pure SnO₂ has a higher conductance than pure ZnO, but the addition of Zn²⁺ reduces the conductance of SnO₂ without any change in its microstructure. The increase of the concentration of oxygen ion vacancy by the presence of Zn²⁺ cations in the *n*-type SnO₂ lattice is described by the following reaction ([Hemmati et al. 2011](#)):



where in the Kröger–Vink notation, Zn_{Sn}'' is a zinc ion sitting on a tin lattice site with two negative charges, and O_O[×] is an oxygen ion sitting on an oxygen lattice site with a neutral charge while, V_O^{••} is an oxygen ion vacancy, with double positive charges.

The catalytic activity of ZnO is higher than that of Zn₂SnO₄, and much higher than that of SnO₂. But SnO₂–ZnO coupled oxide shows even higher photocatalytic activity than that of ZnO. This may be due to the larger specific surface area of SnO₂–ZnO than ZnO, which is in favour of high catalytic activity. Also, the recombination of the generated electron/hole pairs is suppressed and, therefore, resulting in SnO₂–ZnO exhibits higher catalytic activity. But as holes move in the opposite direction from the

electrons, generated holes might be trapped within the ZnO particle, making charge separation more efficient in nanocomposites with greater molar composition of Zn^{2+} than in nanocomposites with lower molar composition of Zn^{2+} ([Cun et al. 2002a](#)).

Therefore, the sensing mechanism of the $\text{SnO}_2\text{-ZnO}$ nanocomposite is dependent on the energetic electrons and oxygen ion vacancy available for the gas-surface reaction. And, the superior sensitivity of S_1Z_3 and S_3Z_1 , compared to other sensors, is attributed to their stronger photocatalytic activity. Although, in our experiments, SZ sensors exhibited low sensitivities in the operational temperature and gas exposure conditions, the simulated model (in Chapter 7) shows that the SZ sensor may exhibit superior sensitivity at higher gas concentrations.

6.4 Summary and Conclusion

The response behaviour was observed to change with variations in the composition of the gas sensors, the gas concentration, and the operating temperatures. The relationship between sensitivity and gas concentration can be observed to be near linear at the operating temperature. This was because of the increasing gas-adsorbing vacancies on the surface of the sensor with increase in operating temperature. The increasing gas concentration corresponded to increasing electrons and corresponding increase in reactivity on the surface of the sensor.

The sensitivity profile illustrated the transient response behaviour of the sensors. Generally, the sensors performed best at 350 °C with gas concentration of 200 ppm. The best sensitivities were displayed by S_1Z_3 , followed by S_3Z_1 sensor devices. Pure ZnO sensors performed better than pure SnO_2 sensor devices. SnO_2 (50%) - ZnO (50%) sensor device exhibited poor detection, response and recovery time. The high sensitivity displayed by S_1Z_3 and S_3Z_1 sensor devices was attributed to excess of one metal oxide over the other, and the reduction in mutual inhibitory effect in the stage of grain growth on the formed surface structure. This behaviour could also be attributed to the fact that the photocatalytic activity of pure SnO_2 is very low, compared to pure ZnO and to coupled $\text{SnO}_2\text{-ZnO}$ nanocomposites ([Hamrouni et al.](#)

[2013](#)). Also, these results confirmed that varying the molar compositions of SnO₂ and ZnO in the prepared sensors can promote the charge transportation in the nanocomposites, and be used to fine-tune the sensitivity and selectivity to a desired gas. The sensitivity of the pure metal oxides could actually be reduced when the metal oxides are in 1:1 molar composition. The best sensitivity could be obtained with 25% dope composition.

These sensors have very good tendency for increased selectivity between ethanol and methanol. In average, ethanol was more sensitive than methanol by 1.14, 2.5, 1.2, 1.55 and 1.2 times for SnO₂, S₃Z₁, SZ, S₁Z₃ and ZnO sensors, respectively. Also, from the analysis of the change in sensitivity between ethanol and methanol at different temperatures and concentrations, the features exhibited by ethanol are distinctly clear from those by methanol. Therefore, these features indicate a possible application of the sensor to distinguish and discriminate between volatile hydrocarbons.

The response time is affected by the chemical reactivity of the target gas, while the recovery process is affected by the oxygen concentration and the completeness of the desorption process. Therefore, for a given sensor type, the sensor sensitivity can be modelled as:

$$S(ST) = f(GT, C, T) \quad (6.3)$$

where ST = sensor type, GT = gas type, C = gas concentration, and T = operating temperatures.

For each combination of gas type and concentration, we could extract a sensitivity profile describing the sensor response to the target gas, and prepare standard curves for each sensor at different temperatures. Such standard curves could be used for comparison of the sensor's response to an unknown analyte, and identification of the gas type and concentration ([Beckers et al. 2013](#)). Excellent linear relationships have been observed on the sensitivity-temperature and the sensitivity-concentration plots. In our analysis, the curve fit from sensitivity versus temperature relationship gave better fit than the sensitivity versus concentration plots. Also, the sensitivity difference versus temperature plots gave better fit than the sensitivity difference versus

concentration plots. With further analysis, these relationships will be compared with power law models, and applied in the simulation of sensor behaviours at various concentrations and operational temperatures in Chapter 7.

Chapter Seven

Analysis of Gas Sensitivity and Simulation of Sensor Behaviour

7.1 Introduction

The electrical response of metal oxide thin films depends on the doping proportion of sensor constituents, deposition conditions, film nanostructure, oxygen vacancies, target gas atmosphere and sensing environment ([Elangovan et al. 2004](#); [Yıldırım et al. 2012](#)). The rate of response of solid state gas sensors is controlled by various processes, such as water and oxygen adsorption/desorption, oxygen inter-crystallite diffusion, gas diffusion inside porous structure, and bulk oxygen diffusion ([Korotcenkov 2005](#)). A complete description of the gas-sensing mechanism for metal oxide based sensors starts with film surface – gas molecule interactions ([Gurlo et al. 2005](#)). The interaction utilises spectroscopic data, numerical quantum mechanics, thermodynamics, kinetics and semiconductor physics, to model charge transfer (adsorption, reaction, desorption, etc.). Surface spectroscopy obtains detailed information about adsorption complexes; while numerical quantum mechanics determines the associated energetic (electronic) levels of the surface, adsorption complex, precursor state, and free molecule. Statistical thermodynamics and kinetics link calculated energy levels with surface coverage of adsorbed species corresponding to real experimental conditions (dependent on temperature, pressure, etc.).

Therefore, different conduction and reaction models can be applied for gas sensitivity analysis of metal oxides semiconductors (see Chapter 3). Such models include the oxygen-vacancy model ([Gurlo and Riedel 2007](#); [Tricoli et al. 2010](#)), the ionosorption model ([Barsan and Weimar 2001](#); [Oprea et al. 2006](#)), the diffusion-reaction model ([Boeker et al. 2002](#); [Matsunaga et al. 2003](#); [Sakai et al. 2001](#)), and oxygen diffusion model ([Kamp et al. 2001](#)). Other reaction models have been described as sensitivity relates with conduction and gas surface reaction ([Chwieroth et al. 2001](#)), surface state

trapping for dynamic conductance response ([Ding et al. 2001](#)), Wolkenstein chemisorption theory ([Kissine et al. 2001](#)), non-dissociative and dissociative chemisorption ([Rothschild and Komem 2003](#)). As discussed in Chapter 3 in terms of nanostructures, models have been developed in relationship to film thickness dependence and structural inhomogeneties ([Hossein-Babaei and Orvatinia 2003](#)), grain size ([Rothschild and Komem 2004](#); [Yao et al. 2013](#)), space-charge ([Chen et al. 2006b](#)), surface-depletion ([Li et al. 2007a](#)), and contact-controlled structure ([Feng et al. 2005](#)). Data behaviour has been analysed as drift ([Velasco-Velez et al. 2008](#)), noise ([Gomri et al. 2006](#)), and hysteresis ([Elokhin et al. 2007](#)). These models apply the physical/chemical properties of sensors and gases to build relationships in the sensor responses.

In this chapter, sensitivity analysis was undertaken to analyse the interaction of each sensor type as a function of gas concentration and operating temperature, and their interactions. A modified chemisorption model was developed, and applied to the characterisation of the sensitivity behaviour of as-fabricated sensors.

7.2 Sensitivity Analysis

The gas sensitivity data were analysed using 3-way factorial design (ANOVA). The aim was to determine the effect of sensor type, gas concentration and temperature on sensor sensitivity, along with their relationship to sensor sensitivity itself. The factorial univariate is a form of experimental design in which every level of every fact is paired with every level of every other factor ([Ho 2013](#)). For this research, the factorial design is particularly appropriate, because it allowed the assessment of the effects of sensor type, gas concentration and operating temperature separately, as well as their joint effects (i.e., interaction of these variables), across their respective levels. Since the experiments involve multiple independent variables and one dependent variable, this analysis was undertaken using the general linear model (GLM) univariate analysis. The process involves a 3-way interaction, in which the sensor sensitivity across sensor type, gas concentration and operating temperature and their interactions were analysed.

7.2.1 Factorial Analysis of Sensitivity to Methanol Based on Sensor Type, Gas Concentration and Operating Temperature

The three-way interaction analysis was run on the methanol results using tests of simple main-effects; i.e., the effect of sensor type across the levels of gas concentration and temperature, the effect of gas concentration across the levels of sensor type and temperature, and effect of temperature across the levels of sensor type and gas concentration. The assumption of homogeneity of variance was tested by the Levene's test of equality of error variance. The Levene's test is a statistical inferential test often used to verify assumption of hypothesis.

Where the factor is significant, post hoc test was run to determine the unique combinations among the factors that have effect on sensitivity; i.e., the post hoc is the test for simple effect of one factor at one level of the other factor. In case of interactions among factors, the Sheffe post hoc comparison was undertaken to clarify (i.e., locate) differences between the levels of experimental conditions ([Ho 2013](#)). The Sheffe's method is a one-step multiple comparison method for analysis of variance of all possible contrasting levels among factors.

To determine statistical significance (p -value) among the factors or groups, we used the descriptive statistics; the p -value is an indication of the probability of the null hypothesis. The mean, M , and standard deviation, SD , are indices in the analysis of the significance of each factor. Also, the strong effect size, η , for a particular factor indicates its practical significance on the sensitivity.

7.2.1.1 Factorial Analysis of Gas Concentration and Operating Temperature

With a particular sensor type, the effects of gas concentration and operating temperature was analysed, individually and their interactions. The Levene's test of equality of error variances (across all levels of gas concentration and temperature) indicated significant level $p > 0.05$, with statistic of $F = 2.038$; therefore, the error of variance of sensitivity was equal across groups of the factors.

Examination of the significant level for the main effects indicated $p < 0.05$ for both concentration and temperature, individually. There was a significant main effect for concentration, $F(2, 36) = 17.569, p < 0.001 (\eta^2 = 0.494)$. The strong effect size, η , for concentration was an indication of its practical significance on the sensitivity. To analyse the differences (simple effects) between the three levels of concentration, the results from the Sheffe post hoc comparison and the boxplot analysis across all level of temperature (Figure 7-1) indicated that the 200 ppm affected sensitivity (by $M = 37.25, SD = 21.16$) more significantly than the 150 ppm ($M = 27.05, SD = 17.34$) and 100 ppm ($M = 14.91, SD = 9.81$). This confirmed the sensitivity behaviour discussed in Section 6.2 (Figure 6-8 and Figure 6-11).

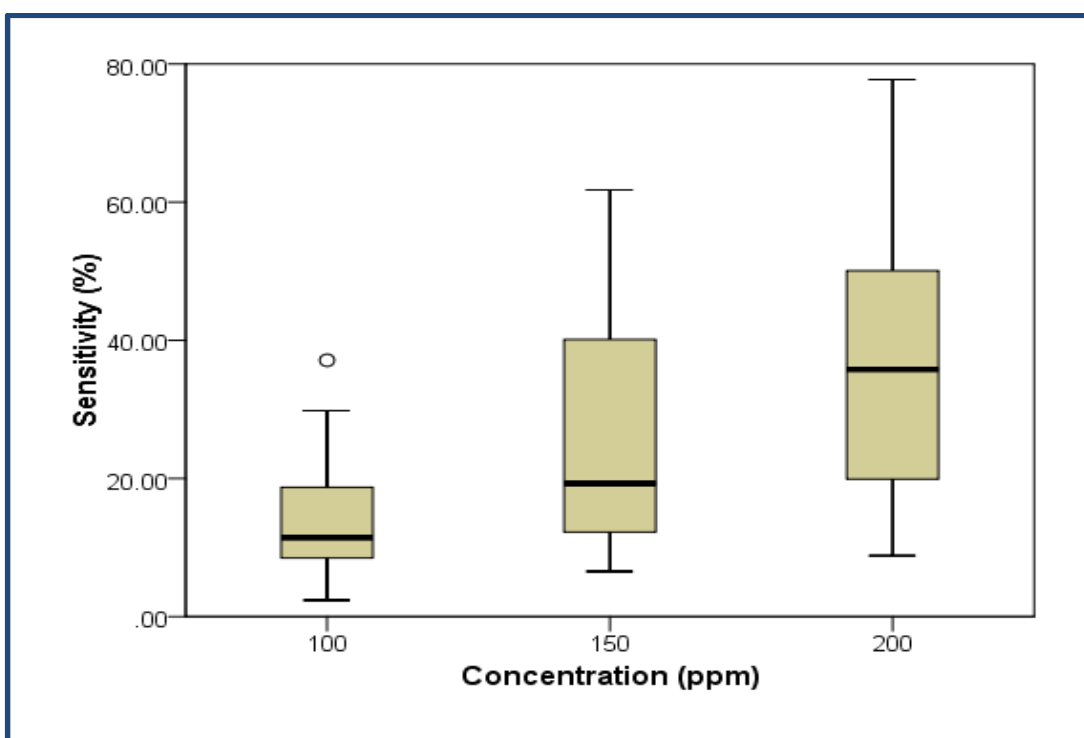


Figure 7-1: Boxplot of sensitivity versus methanol concentration (across all sensor types and operating temperatures).

For temperature, there was a significant main effect, $F(2, 36) = 32.689, p < 0.001 (\eta^2 = 0.694)$. Figure 7-2 represents the boxplot for sensitivity versus temperature across all levels of concentration. The temperature at 350 °C ($M = 42.19, SD = 20.35$) affected

sensitivity more than 250 °C ($M = 25.27$, $SD = 13.01$) and 150 °C ($M = 11.73$, $SD = 5.52$) with some variability within each group, as observed in Section 6.2.

The concentration by temperature interaction was marginally significant, $F(4, 36) = 2.332$, $p = 0.074$ ($\eta^2 = 0.206$). However, there was a strong effect size for interaction of concentration and temperature, indicating their possible practical significance on the sensitivity. Individually, as gas concentration and operating temperature increase the higher their effects on the sensitivity. This is a confirmation of the sensitivity characteristics as discussed in Section 6.2.

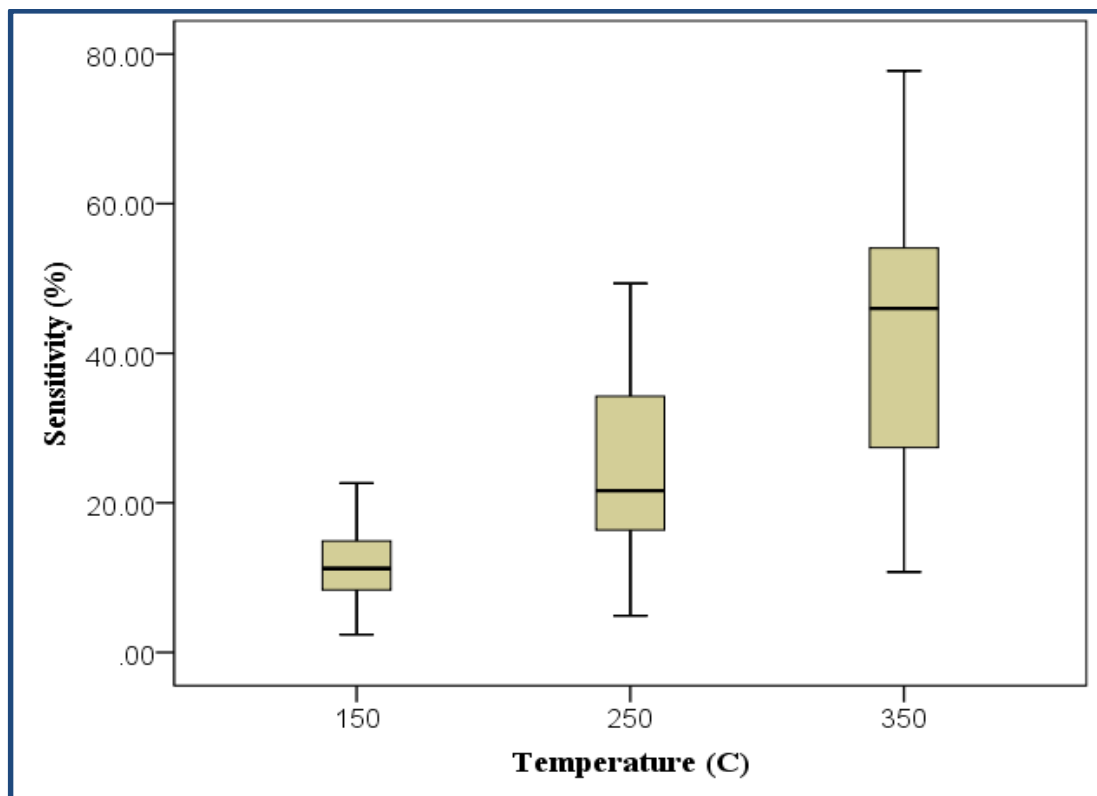


Figure 7-2: Boxplot of sensitivity versus temperature (across all sensor types and gas concentrations).

7.2.1.2 Factorial Analysis of Sensor Type and Operating Temperature

With constant gas concentration, the effects of individual and the joint interaction of sensor type and operating temperature was investigated. The Levene's test of equality of error variances (across the levels of sensor type and temperature) indicated $p = 0.042$; this demonstrated a violation of the assumption of homogeneity of sensitivity

across groups of the factors. Examination of the p -values for the main effects indicated $p < 0.05$ for both sensor type and temperature, individually. The main effect of sensor type was significant, with $F(4, 30) = 3.534, p < 0.05 (\eta^2 = 0.320)$. The moderate effect size for sensor type indicated that it has some practical significance on the sensitivity. Figure 7-3 show the boxplot for sensor type across all operating temperatures and concentrations. From Sheffe's post hoc comparison, the S₁Z₃ sensor was more sensitive (by $M = 37.91, SD = 21.99$) than the pure SnO₂ sensor ($M = 14.87, SD = 12.76$). Other sensor pairs were not significantly different.

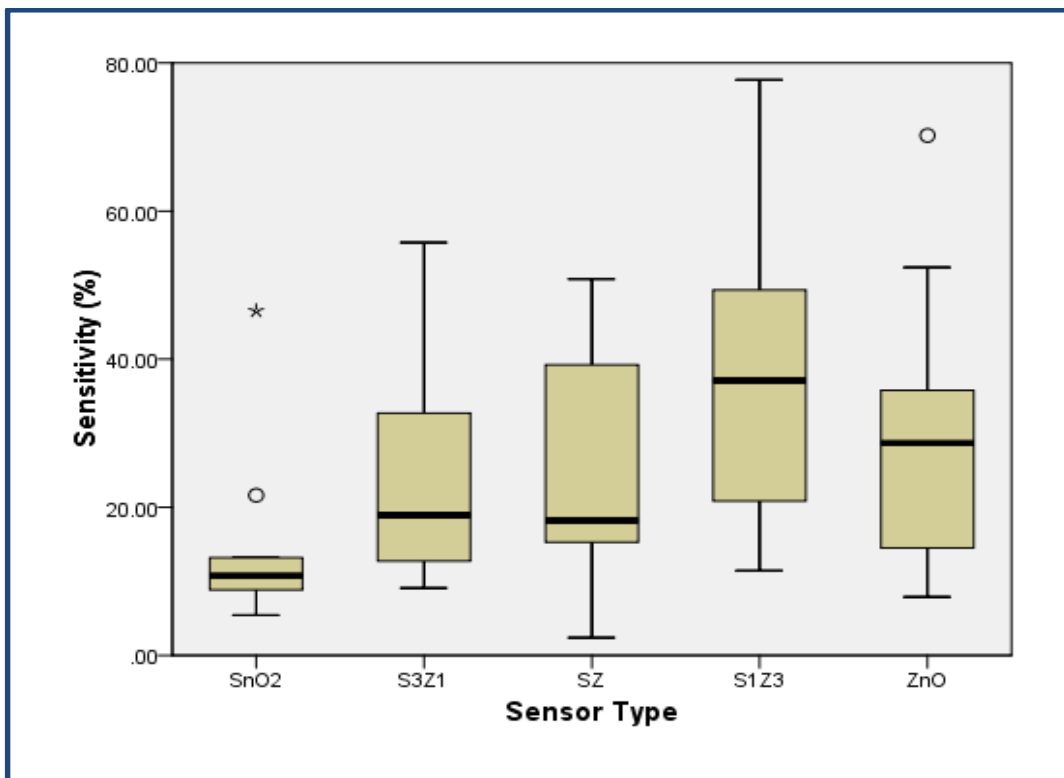


Figure 7-3: Boxplot of sensitivity versus sensor type (across all operating temperatures and methanol gas concentrations).

Temperature showed a significant main effect, $F(2, 30) = 19.542, p < 0.001 (\eta^2 = 0.849)$. The very strong effect size for temperature indicated its strong practical significance on the sensitivity at all operating temperatures (Figure 7-2). Although, the interaction between sensor type and temperature was marginally significant, $F(8, 30) = 0.496, p = 0.849 (\eta^2 = 0.117)$, the strong effect size for the interaction indicate their practical significance on the sensitivity. Across all sensor types and

concentrations (discussed in Section 6.2 and 6.3), temperature reflected a significant effect on sensitivity.

7.2.1.3 Factorial Analysis of Sensor Type and Gas Concentration

At particular operating temperature, the Levene's test of equality of error variances (across the levels of sensor type and gas concentration) indicated $p > 0.05$; therefore, the error of variance of sensitivity was equal across groups of sensor type and gas concentration. Analysis of the p -values for the main effects indicated $p < 0.05$ for only gas concentration. With $p > 0.05$ for sensor type and interaction of sensor type and gas concentration, their effects on sensitivity could not be ascertained as there was no unique combination of the factors that created significant effects on sensitivity.

There was a significant main effect for concentration, $F(2, 30) = 6.306$, $p < 0.001$ ($\eta^2 = 0.296$). As stated above, the strong effect size for concentration confirmed its practical significance on the sensitivity. The estimated marginal means indicated that the SZ sensor improved in sensitivity with increasing concentration (Figure 7-4).

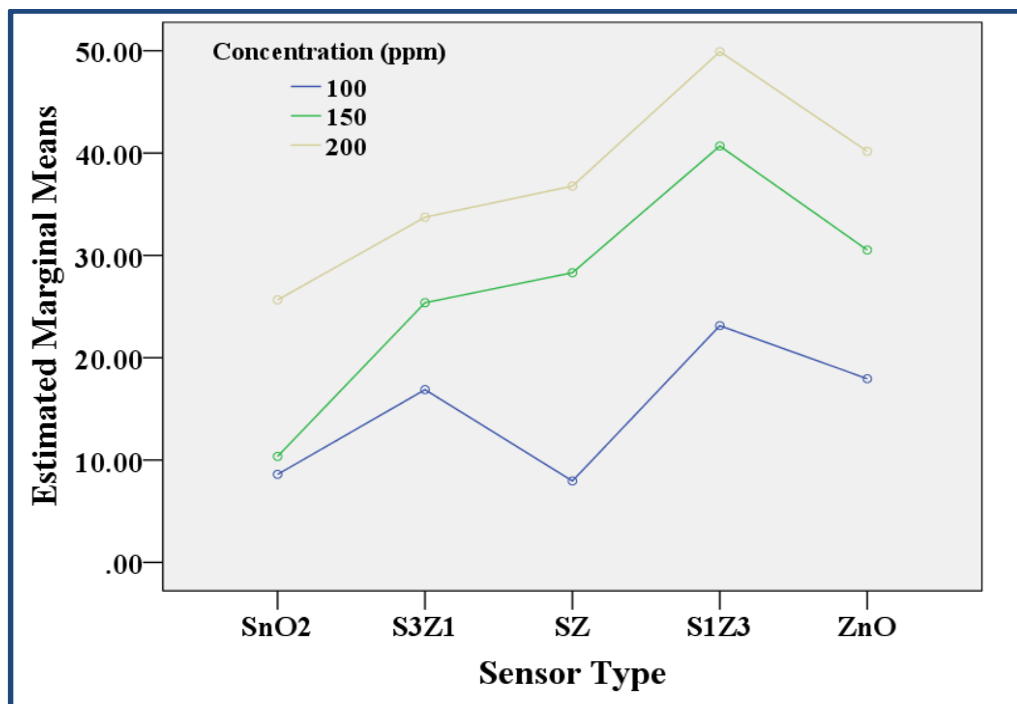


Figure 7-4: Estimated marginal mean of sensitivity to methanol.

This information is a robust improvement in the result (sensitivity difference) from the analysis in Chapter 6 (Section 6.2.1.3). Also, analysis of the Sheffe post hoc comparison and the boxplot analysis (Figure 7-1), confirmed that the 200 ppm affected sensitivity (by $M = 37.25$, $SD = 21.16$) more significantly than 100 ppm ($M = 14.91$, $SD = 9.81$). Other comparisons did not indicate significant difference.

7.2.2 Factorial Analysis of Sensitivity to Methanol and Ethanol Based on Sensor Type, Gas Type and Operating Temperature

The three-way interaction was run on the data set of sensor sensitivity to methanol and ethanol using tests of simple main-effects; i.e., the effect of sensor type across the levels of gas type and operating temperature, the effect of temperature across the levels of sensor type and gas type, and the effect of gas type across the levels of sensor type and operating temperature. The variation of sensitivity across different sensors is represented in Figure 7-5.

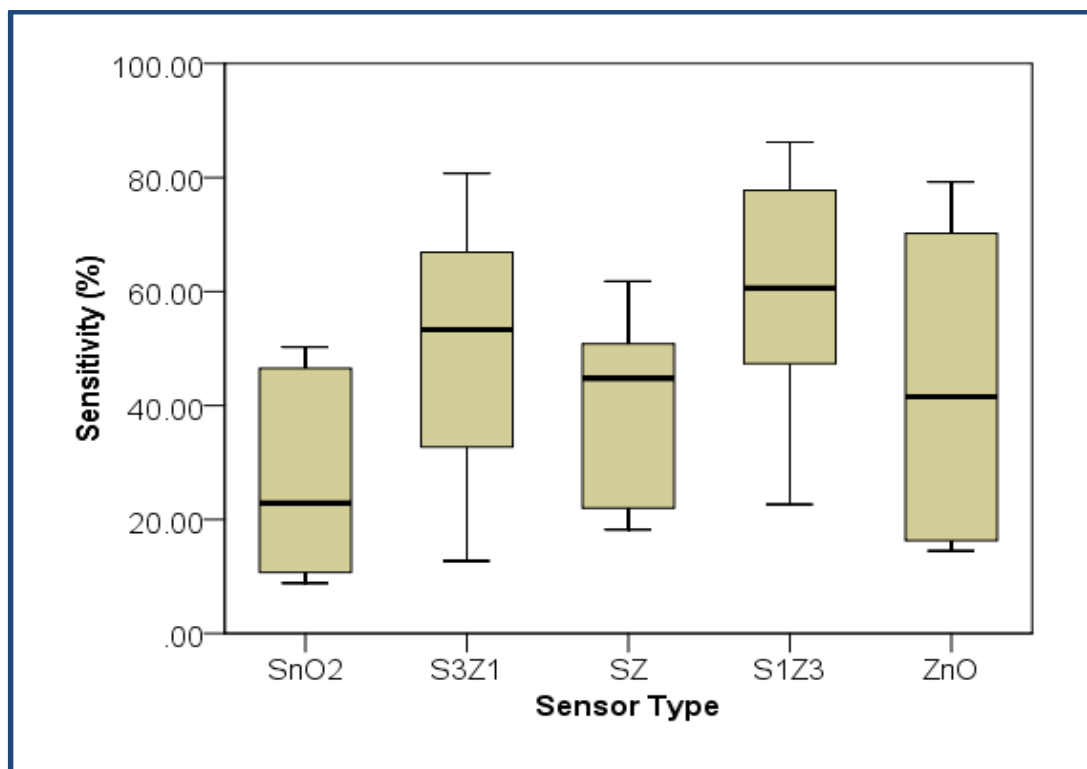


Figure 7-5: Boxplot of sensitivity versus sensor type with 200 ppm methanol and ethanol.

7.2.2.1 Factorial Analysis of Gas Type and Operating Temperature

Individual effects of methanol and ethanol with 200 ppm were analysed with respect to a particular sensor type. The Levene's test of equality of error variances (across the levels of gas type and temperature) indicated $p > 0.05$; thus, the error of variance of sensitivity was not violated across groups of the factors. From the descriptive statistics, the p -values for the main effects indicated $p < 0.05$ for both gas type and temperature.

There was a significant main effect for gas type, $F(1, 24) = 6.825$, $p < 0.05$ ($\eta^2 = 0.221$). The moderate effect size for gas type indicates it has some practical significance on the sensitivity of gas with 200 ppm. The post hoc test was not performed for gas type because there were fewer than 2 groups (of concentration levels), but the boxplot represents a fair variation (Figure 7-6 and Figure 7-7). However, ethanol indicated significant effect on sensitivity ($M = 50.93$, $SD = 24.13$) than methanol ($M = 37.25$, $SD = 21.16$).

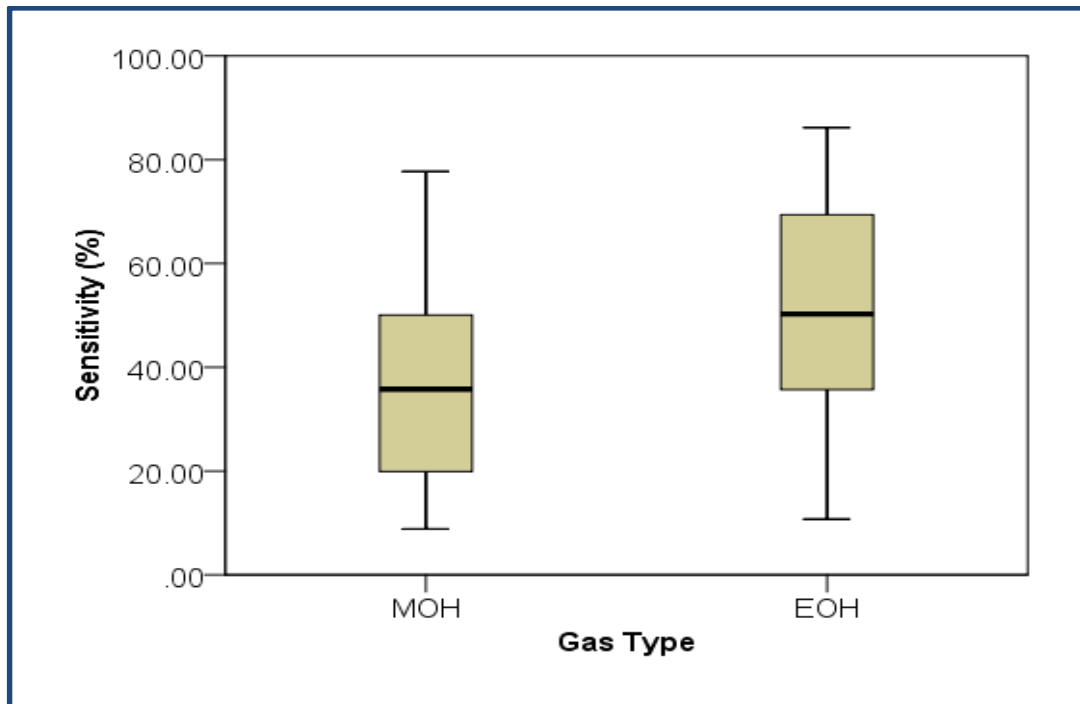


Figure 7-6: Boxplot of sensitivity versus gas type with 200 ppm methanol and ethanol.

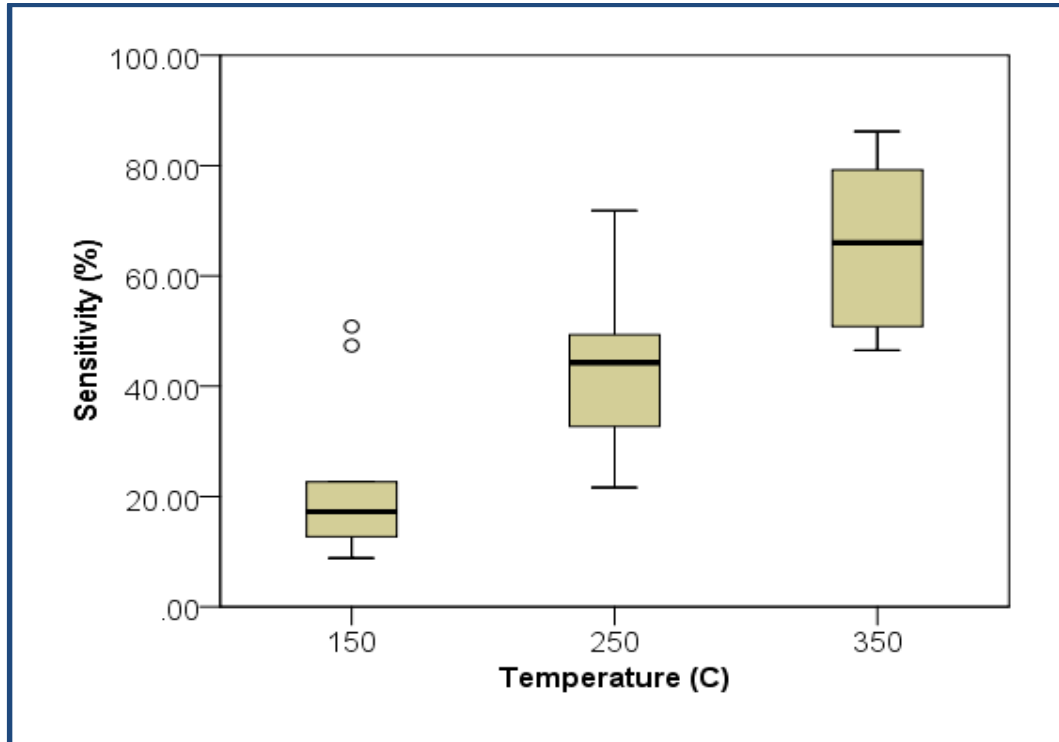


Figure 7-7: Boxplot of sensitivity versus temperature with 200 ppm methanol and ethanol.

For temperature, the Sheffe's post hoc comparison indicated that all operating temperatures have significant effect on sensitivity. Operating temperature 350 °C ($M = 65.93$, $SD = 14.66$) affected sensitivity more significantly than 250 °C ($M = 43.92$, $SD = 16.53$) and 150 °C ($M = 22.41$, $SD = 14.77$). The gas type by temperature interaction was not significant, $F(2, 24) = 0.053$, $p = 0.949$ ($\eta^2 = 0.004$). However, the moderate effect size indicated possible effects of the interaction on sensitivity.

7.2.2.2 Factorial Analysis of Sensor Type and Gas Type

At constant operating temperature, the Levene's test of equality of error variances (across the levels of sensor type and gas type) indicated $p = 0.979$; therefore, the error of variance of sensitivity was equal across groups of the factors. Analysis of the p -values for the main effects indicated $p > 0.05$ for sensor type, gas type, and interaction of sensor type and gas type. Therefore, it was difficult to determine their significance on sensitivity. The sensor type by gas type interaction effect is represented by Figure 7-8.

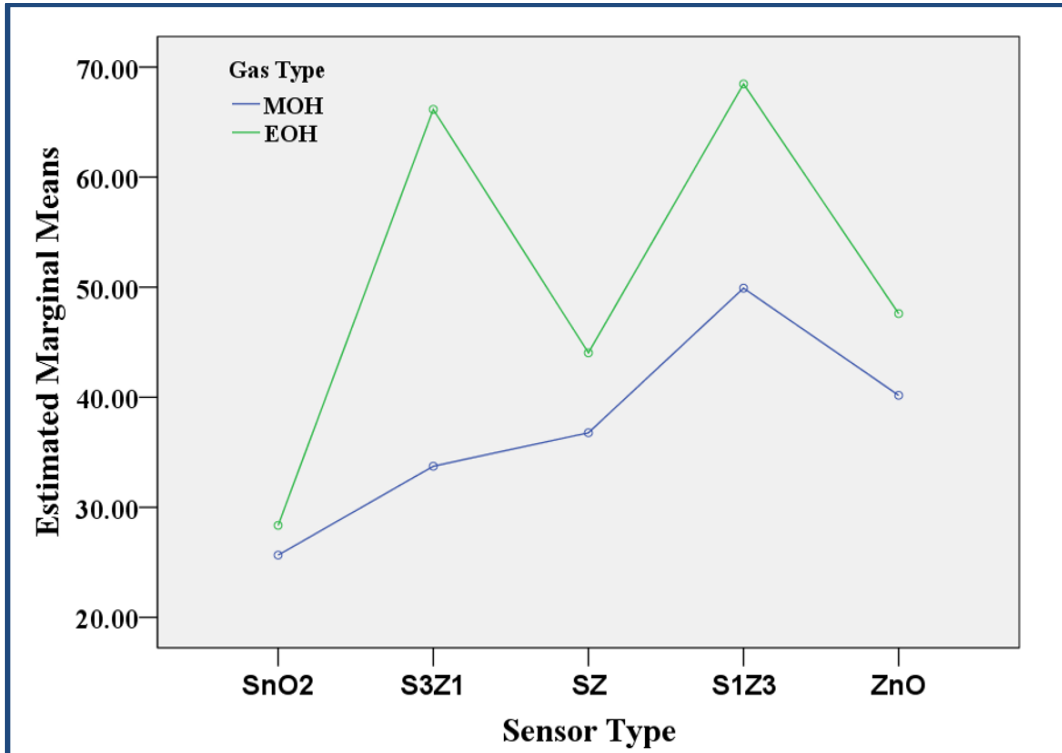


Figure 7-8: Plot of estimated marginal means of sensitivity with 200 ppm methanol and ethanol.

This figure represents the estimated marginal means of sensitivity across sensor types, and confirmed the high response of S_3Z_1 and S_1Z_3 sensors than the pure metal oxides for ethanol observed in Chapter 6. It also enhanced the sensitivity behaviour of SZ to methanol than initially observed in Section 6.2.

7.2.2.3 Factorial Analysis of Sensor Type and Operating Temperature

With a particular gas type at 200 ppm, the individual effects of methanol and ethanol were analysed. The Levene's test of equality of error variances (across the levels of sensor type and operating temperature) was not calculated; therefore, the null hypothesis was tested to determine that the error of variance of sensitivity was equal across groups of sensor type and operating temperature. Analysis of the p -values for the main effects indicated $p < 0.05$ for only temperature. But, for both sensor type and interaction of sensor type and temperature, $p > 0.05$; thus, their effects on sensitivity could not be ascertained as there was no unique combination of the factors.

There was a significant main effect for temperature, $F(2, 15) = 29.229$, $p < 0.001$ ($\eta^2 = 0.796$). The temperature at 350 °C ($M = 65.93$, $SD = 14.66$) affected sensitivity more than 250 °C ($M = 43.92$, $SD = 16.53$) and 150 °C ($M = 22.41$, $SD = 14.77$) with some variability within each group, as observed in Figure 7-2. The sensor type and temperature interaction was not significant, $F(8, 15) = 0.402$, $p = 0.903$ ($\eta^2 = 0.176$). However, the strong effect size for interaction of sensor type and temperature, indicated possible practical significance on the sensitivity.

The Sheffe's post hoc comparison also confirmed that there was significant difference in all temperatures. The post hoc comparison showed that the S₃Z₁ sensor exhibited highly significant sensitivity (by $M = 49.95$, $SD = 24.30$) than the pure SnO₂ sensor ($M = 27.00$, $SD = 17.63$). Other sensor pairs were not significantly different as observed the boxplot analysis (Figure 7-5).

Figure 7-9 shows the boxplot of sensitivity versus sensor type with 200 ppm ethanol.

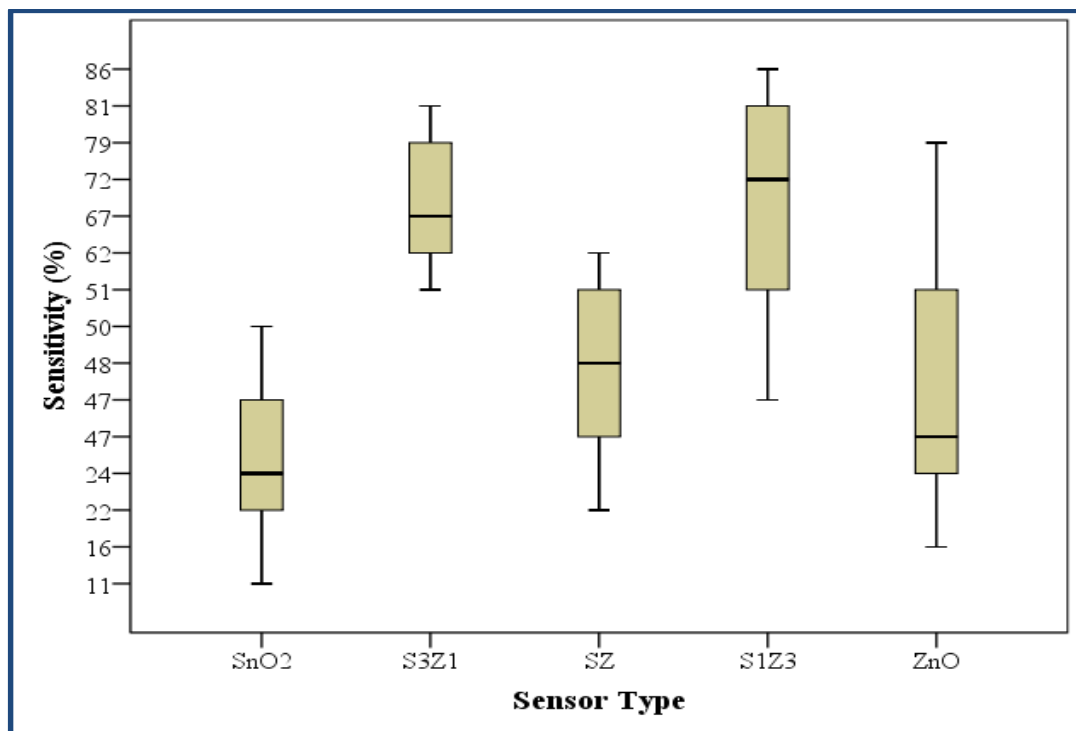


Figure 7-9: Boxplot of sensitivity versus sensor type with 200 ppm ethanol.

As stated in Section 6.2.1.4, further analysis of sensitivity to ethanol confirmed that S_1Z_3 sensor was most sensitive, closely followed by S_3Z_1 sensor, across all temperatures (Figure 7-9).

A similar behaviour was observed with methanol (Figure 7-10). Across all temperatures, sensitivity to methanol revealed that S_1Z_3 sensor was more sensitive than other sensors. However, SZ sensor indicated marginal increase in sensitivity than SnO_2 , ZnO and S_3Z_1 sensors.

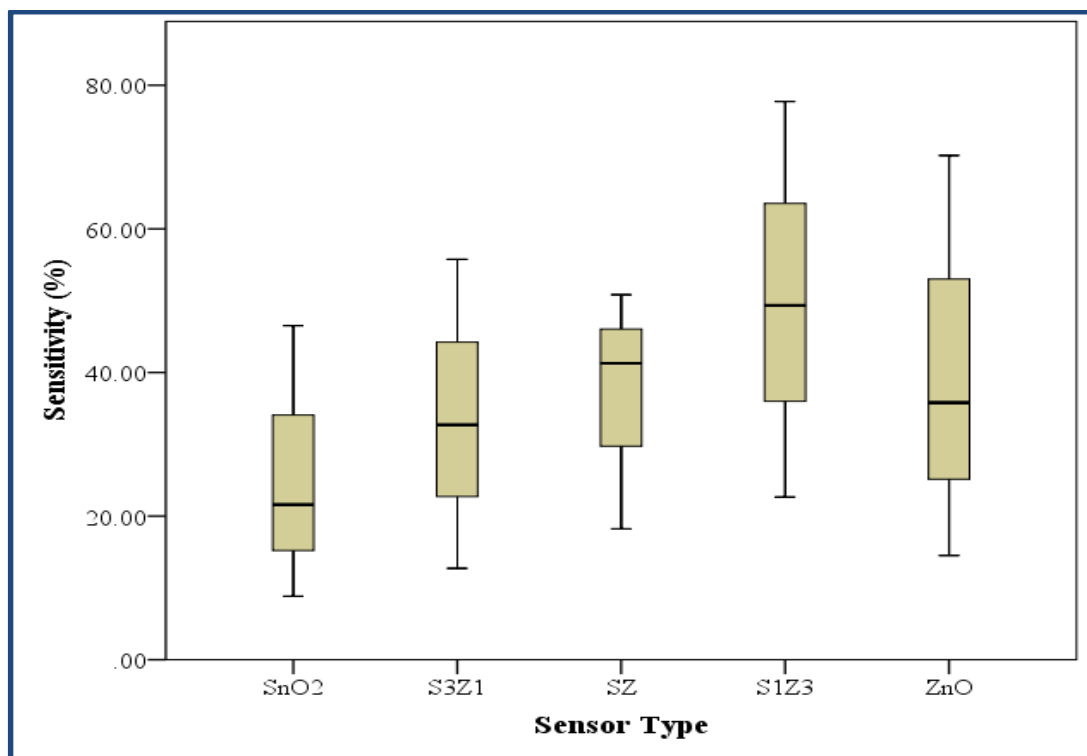


Figure 7-10: Boxplot of sensitivity versus sensor type with 200 ppm methanol.

7.3 Modified Chemisorption Model

The overall sensing mechanism of metal oxide semiconductors is based on the surface reactions, the resulting charge transfer processes, and the transport phenomena within the sensing layer (see Chapter 3 for details). Like a typical n -type semiconductor, the gas sensing mechanism of SnO_2 , ZnO and their nanocomposites is based on the changes of the electrical response before and after exposure to the target gas (Figure 7-11).

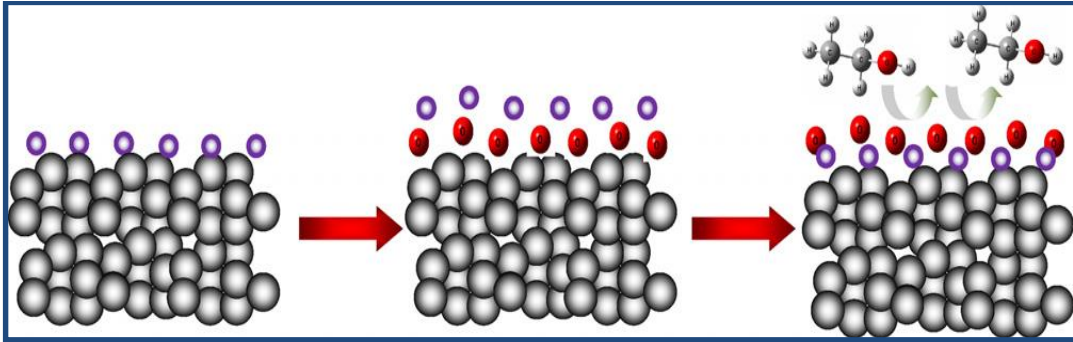
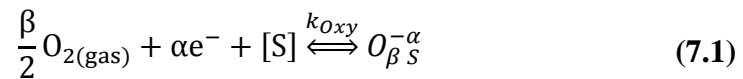


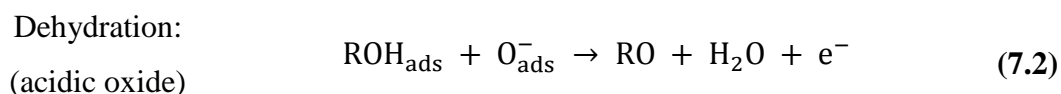
Figure 7-11: Schematic of sensing reaction process on the surface of metal oxide semiconductor (Zeng et al. 2012).

Firstly, the oxygen adsorbs on the surface in two ways, depending on the operating temperature. When SnO₂ or ZnO nanostructure is heated at 100–200 °C, oxygen molecules (O₂) in air adsorbed onto the surface of the nanostructure forming oxygen ion molecules O₂⁻. At high temperature (250–350 °C), oxygen molecules in air are dissociated to become oxygen ions with single or double negative electric charge due to the attraction of an electron from the conduction band of the SnO₂ or ZnO nanostructure. Thus, the oxygen adsorption reaction can be represented as:

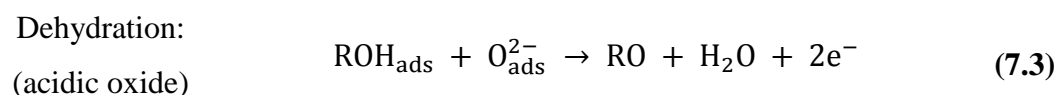


where O_{2(gas)} is an oxygen molecule in the ambient atmosphere and e⁻ is an electron on the surface that is depleted from the conduction band of the SnO₂ or ZnO nanostructure. The concentration of free charge carriers (electrons) is n_S, S is an unoccupied chemisorption (MOX) site for oxygen (i.e., oxygen vacancy or tin zinc interstitial), k_{Oxy} is the reaction rate constant or reaction rate coefficient, O_{βS}^{α-} is a chemisorbed oxygen species with: α = 1 for singly ionised forms, α = 2 for doubly ionised forms, β = 1 for atomic forms, β = 2 for molecular forms.

The sensing of methanol and ethanol by the sensor is considered an adsorption (dehydration) reaction. On the surface of the SnO₂, ZnO or coupled SnO₂–ZnO nanocomposites, the general chemical reaction between reducing molecule and oxygen ions is represented as:

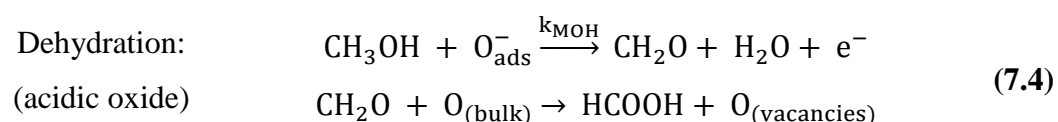


or

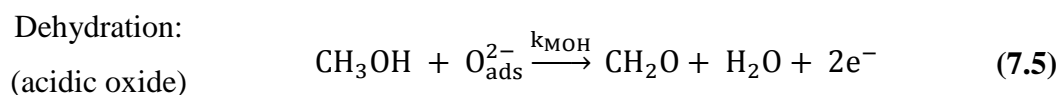


The products are alkoxy group and water; where R is the alkyl group for ethanol (i.e., CH₃CH) or methanol (i.e., CH₂) group.

Particularly for methanol (or ethanol) molecules, the chemical reaction mechanism is described. The methanol sensing mechanism with O⁻ and O²⁻ is as follows:

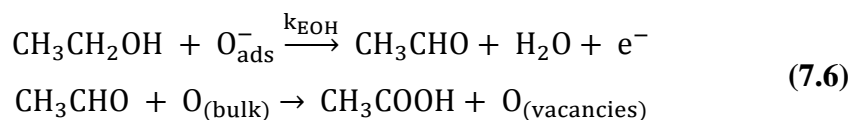


and



From the surface chemistry (see Sections 3.2 and 3.6), as methanol is oxidised to formaldehyde (CH₂O) and subsequently formic acid (HCOOH), it liberates electrons into the conduction band, thereby increasing the conductance (i.e., decreasing resistance) of the sensor upon exposure to methanol vapour ([Mishra and Sahay 2012](#)).

The ethanol sensing mechanism with O⁻ and O²⁻ is as follows ([Cheong and Lee 2006](#); [Hongsith et al. 2010](#); [Mishra and Sahay 2012](#)):

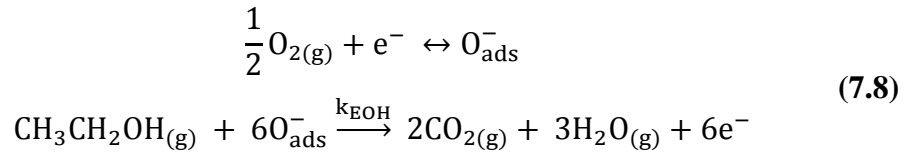


and



The formation of acetaldehyde (CH_3CHO), and subsequently acetic acid (CH_3COOH), due to the oxidation of ethanol, leads to the liberation of electrons into the conduction band, resulting in a decrease in the sample resistance ([Mishra and Sahay 2012](#)). See Chapter 3 (Sections 3.2, 3.4 and 3.6) for review of conduction models.

However, the full oxidation of $\text{C}_2\text{H}_5\text{OH}$ by O_{ads}^- in gas-sensing reactions can be considered to follow the adsorption of oxygen as ([Zeng et al. 2012](#)):



A similar mechanism by a *p*-type semiconductor is described by [Yoon et al. \(2012\)](#).

Therefore, using the general reduction equation, Equations (7.2) and (7.3), the rate equation of electron density is represented as:

$$\begin{aligned} \frac{dn}{dt} &= k_{\text{R}}(\text{T})[\text{O}_{\text{ads}}^{\alpha-}]^b[\text{ROH}]^b \\ \text{i.e.,} \\ \frac{dn}{dt} &= k_{\text{R}}(\text{T})[\text{O}_{\text{ads}}^{\alpha-}]^2[\text{ROH}]^2 \\ \frac{dn}{dt} &= k_{\text{R}}(\text{T})[\text{O}_{\text{ads}}^-]^1[\text{ROH}]^1 \\ \frac{dn}{dt} &= k_{\text{R}}(\text{T})[\text{O}_{\text{ads}}^{2-}]^{\frac{1}{2}}[\text{ROH}]^{\frac{1}{2}} \end{aligned} \quad (7.9)$$

where n is the electron density or electron concentration under the methanol or ethanol atmosphere, b is a charge parameter having value of 0.5 for O^{2-} , 1 for O^- and 2 for O_2^- and $k_{\text{R}}(\text{T})$ is the reaction rate coefficient described as:

$$k_{\text{R}} = A \exp\left(-\frac{E_{\text{A}}}{k_{\text{B}}T}\right) \quad (7.10)$$

where E_{A} is the activation energy of reaction, k_{B} is the Boltzmann constant and T is absolute temperature.

Integrating Equation (7.9) yields ([Hongstith et al. 2010](#)):

$$n = k_R(T) [O_{ads}^{\alpha-}]^b [ROH]^b t + n_0 \quad (7.11)$$

where n_0 is the electron concentration of sensor at an operating temperature in the air atmosphere (i.e., just before exposing the target gas). As the system becomes saturated (at equilibrium under the atmosphere of target gas and synthetic air), carrier concentration n and n_0 can be considered to be constant with time. Thus, Equation (7.11) can be rewritten as ([Hongstith et al. 2010](#)):

$$n = \Gamma_t k_R(T) [O_{ads}^{\alpha-}]^b [ROH]^b + n_0 \quad (7.12)$$

where Γ_t is a time constant. The carrier concentration is defined as $n = \gamma/R$, where R is a resistance and γ is a proportional constant. Substituting γ in Eq. (7.12) gives:

$$\frac{1}{R_g} = \frac{\Gamma_t k_R(T) [O_{ads}^{\alpha-}]^b [ROH]^b}{\gamma} + \frac{1}{R_a} \quad (7.13)$$

Rearranging,

$$S_g = \frac{R_a}{R_g} = \frac{\Gamma_t k_R(T) [O_{ads}^{\alpha-}]^b [ROH]^b}{n_0} + 1 \quad (7.14)$$

Redefining the sensor response (i.e., sensitivity), S , as ([Ahlers et al. 2005](#); [Tricoli et al. 2009](#)):

$$S = S_g - 1 = \left(\frac{R_a}{R_g} - 1 \right) = \left(\frac{R_a - R_g}{R_g} \right) = \left(\frac{R_a - R_g}{R_g} \right) \quad (7.15)$$

where R_a is the electrical resistance of the sensor in air, and R_g is the electrical resistance of the sensor in target gas. Therefore, the sensor response (fractional change in resistance) can be related as:

$$S = \left(\frac{R_a - R_g}{R_g} \right) = \frac{\Gamma_t k_R(T) [O_{ads}^{\alpha-}]^b C^b}{n_0} \quad (7.16)$$

During the sensing process, the temperature dependence of sensor response is controlled by two parameters; **reaction rate coefficient, $k_R(T)$** , between adsorbed

oxygen ions with the target gas (methanol or ethanol) molecules, and **electron density of the sensor, n_0** , ([Hongstith et al. 2010](#)). With rising temperature, the reaction rate coefficient and electron density increases exponentially. Therefore, sensor response, S , is proportional to reaction rate coefficient but inversely proportional to electron density. These two parameters compete with each other and result in maximum sensor response at optimum operating temperature.

$$S \propto \frac{k_R(T)}{n_0} \quad (7.17)$$

Empirically, the sensor response to target gas adsorption on the surface in relation to gas concentration, C , can be represented as ([Hongstith et al. 2010](#); [Wongrat et al. 2012](#)):

$$S_g = 1 + aC^b \quad (7.18)$$

Rearranging,

$$S = S_g - 1 = aC^b \quad (7.19)$$

where C represents the concentration of methanol or ethanol, and the sensor response, S , is characterised by the constants a and b .

Taking logarithmic function of both sides of Equation (7.19),

$$\begin{aligned} \log(S_g - 1) &= \log a + b \log C \\ \log S &= \log a + b \log C \end{aligned} \quad (7.20)$$

The **plot of $\log S$ against $\log C$ is a linear relationship**. Constant a is a controllable parameter ([Hongstith et al. 2010](#)). The slope, constant b , represents oxygen ion species on the surface of the metal oxide semiconductor sensor; its value depends on the sensor material, the type of gas sensor and the charge state of the surface ion. Thus, for O^{2-} , charge parameter, b is approximately 0.5; for O^- , b approximately 1; and for O_2^- , b is approximately 2. Usually, O_2^- (with b approximately 2) occurs at temperature equal or less than 150 °C ([Rothschild and Komem 2003](#)). The log-log plots of the relationships of the different sensors are shown in Figure 7-12.

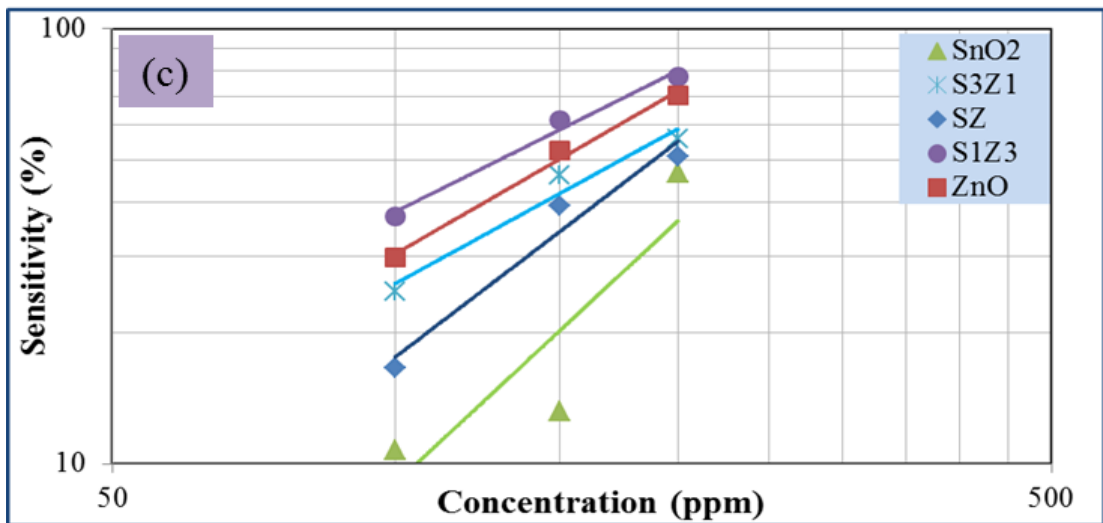
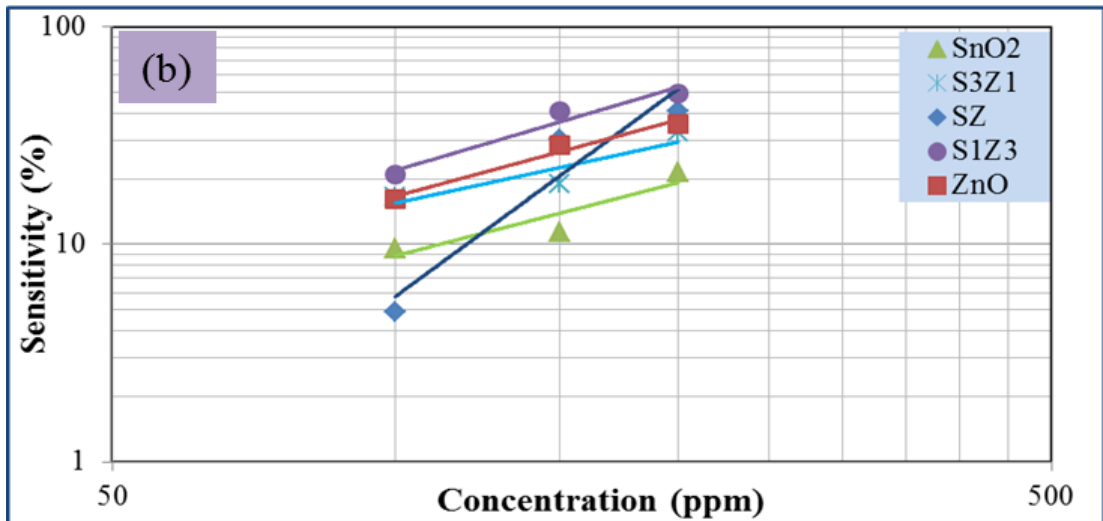
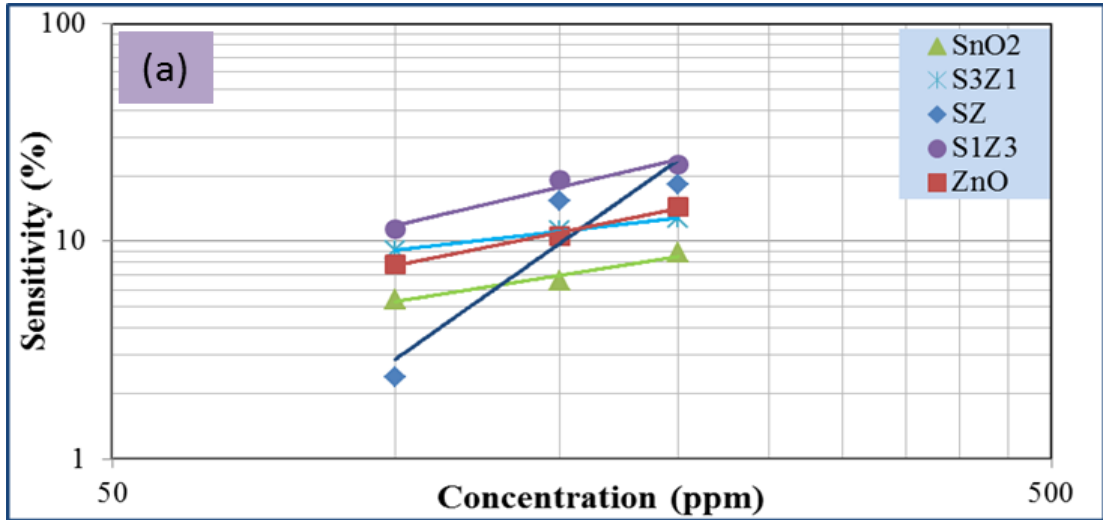


Figure 7-12: Log-log plot of sensitivity versus concentration at (a) 150 °C, (b) 250 °C, and (c) 350 °C.

7.3.1 Parameter Identification

All the sensor samples presented some linear dependence based on the log-log plots of sensitivity versus gas concentration (Figure 7-12). The log-log parameters could be transformed into a power model as given in Equation (7.19). The slope from the power regression analysis of the sensor sensitivity versus gas concentration data are presented in Table 7-1. Detail simulation of the power model is presented in Section 7.4.2 (see Figure 7-13).

Table 7-1: Table of power model parameters

| Parameter | T (°C) | SnO ₂ | S ₃ Z ₁ | SZ | S ₁ Z ₃ | ZnO |
|-----------|--------|------------------|-------------------------------|---------|-------------------------------|---------|
| b | 150 | 0.68651 | 0.4903 | 3.0422 | 1.00657 | 0.86985 |
| | 250 | 1.11711 | 0.93319 | 3.17074 | 1.27124 | 1.16748 |
| | 350 | 2.00634 | 1.18359 | 1.64767 | 1.07892 | 1.24503 |

7.3.2 Simulation of Sensor Behaviour Using the Modified Chemisorption (Power) Simulation

Using the charge parameters obtained from the power models (Table 7-1), the models were fitted excellently with experimental data. To demonstrate the application of the chemisorption model, the sensitivity of the sensor was simulated by fitting this model, and using it to predict the optimal sensitivities of the different sensors at different gas concentrations and operating temperatures. Typical result of the simulated sensitivity data is presented in Figure 7-13.

The model gave excellent simulation of the sensitivity behaviour for gas concentration of 100–200 ppm at operating temperatures of 150, 250 and 350 °C. But on expanding the concentration range, the best simulation was obtained at operating temperature of 350 °C for gas concentration between 0 and 500 ppm. This confirmed that the S₁Z₃ and S₃Z₁ samples produce better results than the pure MOXs (i.e., SnO₂ and ZnO) and the SZ sensors at all concentrations. However, from the simulation, the SZ sensors show promising sensitivity above 350 ppm methanol. Comparing the pure samples, the ZnO sensors produce better sensitivity than SnO₂ samples at most conditions, except for 500 ppm at 350 °C.

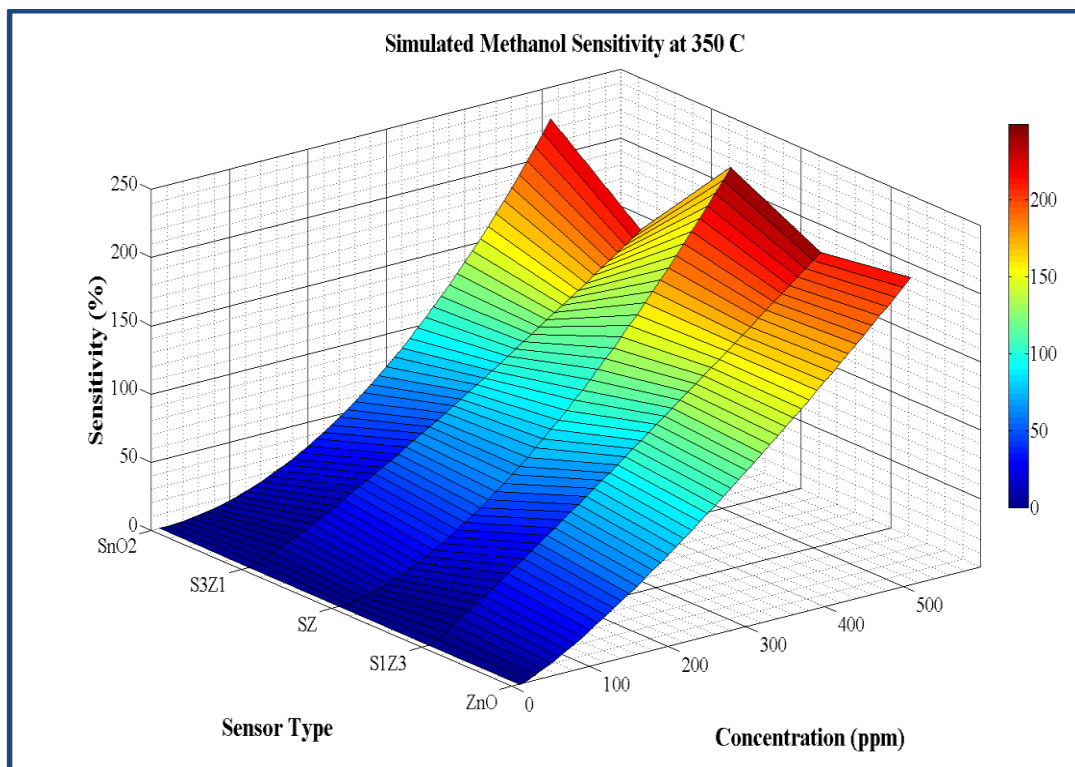


Figure 7-13: Simulated sensitivity at 350 °C (power model).

On individual sensor behaviour, the sensitivity increased with increasing temperature (see Figure 7-14 for SnO₂ Sensors). However, the model for SZ sensors indicated that the sensitivity at 250 °C could be better than at 150 and 350 °C (Figure 7-15). This abnormality could be in correlation with the high grain size and film heights of the SZ samples (discussed in Sections 5.3 and 5.4).

The simulated results (line plot) compared very well with the experimental values (dot plots), as indicated by the coefficient of determination, R^2 , (Table 7-2). The best curve fitting was demonstrated by S₃Z₁ at 150 °C, while the worst was exhibited by SnO₂ at 350 °C. In terms of temperature, there was no peculiar temperature with unique fitness. However, at all operating temperatures, the curve fitting tended to improve in fitting as the molar concentration of ZnO increased in the sensors.

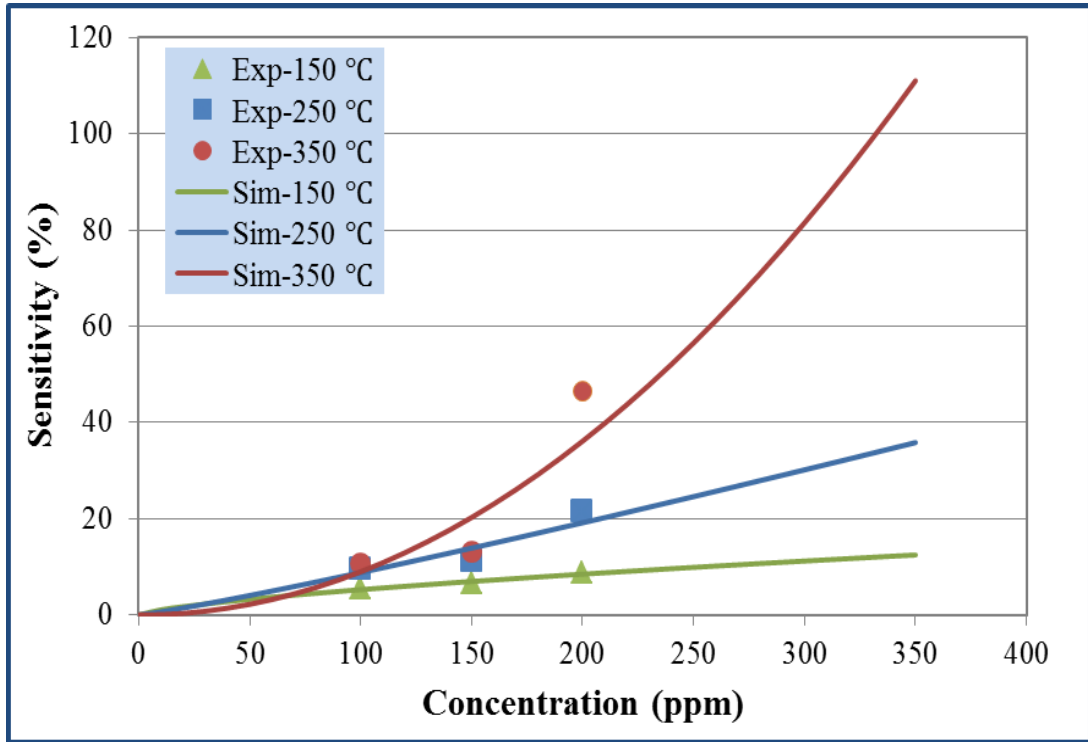


Figure 7-14: Simulated sensitivity of SnO₂ sensors (power model).

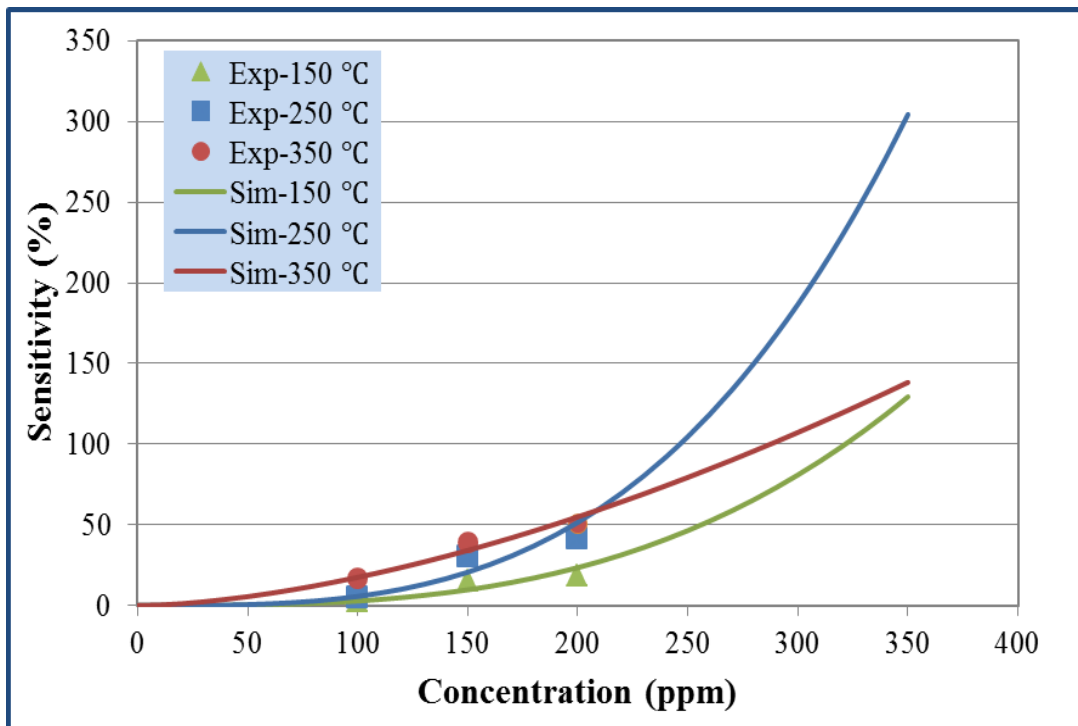


Figure 7-15: Simulated sensitivity of SZ sensors (power model).

Table 7-2: Coefficient of determination (power model)

| Parameter | T (°C) | SnO ₂ | S ₃ Z ₁ | SZ | S ₁ Z ₃ | ZnO |
|----------------|--------|------------------|-------------------------------|--------|-------------------------------|--------|
| R ² | 150 | 0.9488 | 0.9978 | 0.8838 | 0.9606 | 0.9838 |
| | 250 | 0.8285 | 0.8189 | 0.9167 | 0.9522 | 0.9769 |
| | 350 | 0.7753 | 0.9628 | 0.9594 | 0.9864 | 0.9932 |

With this, it can be confirmed that, apart from gas concentration and operating temperature, other factors could play some major roles in sensitivity profile. Other power plots are shown in Appendix B.6.

7.4 Linear Regression Model

For a particular sensor and particular gas, sensitivity can be modelled as a function of combination of gas concentration and operating temperature (as proposed in Section 6.4). The sensitivity profile describing the sensor response to the target gas was analysed, and standard curves prepared for each sensor at different concentrations, using Equation (6.3).

7.4.1 Linear Modelling of Sensitivity to Methanol

Data from particular sensor sensitivity to methanol was used to simulate the respective sensor behaviour as a function of gas concentration and operating temperature using the linear regression. Linearly, the sensitivity model, Equation (6.3), can be represented as given in Equation (7.21):

$$S(ST) = \nu + \rho * C + \eta * T \quad (7.21)$$

where ST = sensor type, C = gas concentration, T = operating temperature, ν = intercept, ρ = coefficient for concentration and η = coefficient for temperature.

Following a linear regression analysis of the sensor sensitivity using Equation (7.21), the coefficients of concentration and temperature, along with the R², are presented in Table 7-3. Detailed simulation of the linear relationship of sensor sensitivity to gas concentration and operating temperature is presented in Section 7.4.2 (see Figure 7-16).

Table 7-3: Table of linear model parameters

| Parameter | SnO ₂ | S ₃ Z ₁ | SZ | S ₁ Z ₃ | ZnO |
|----------------|------------------|-------------------------------|---------|-------------------------------|---------|
| ρ | 0.08526 | 0.08426 | 0.14407 | 0.13391 | 0.11113 |
| η | 0.08274 | 0.15607 | 0.11795 | 0.20542 | 0.19922 |
| R ² | 0.6500 | 0.8800 | 0.9100 | 0.9330 | 0.9040 |

7.4.2 Simulation of Sensor Behaviour Using the Linear Simulation

Typical linear relationship, based on gas concentration and operating temperature, is represented for all sensors in Figure 7-16.

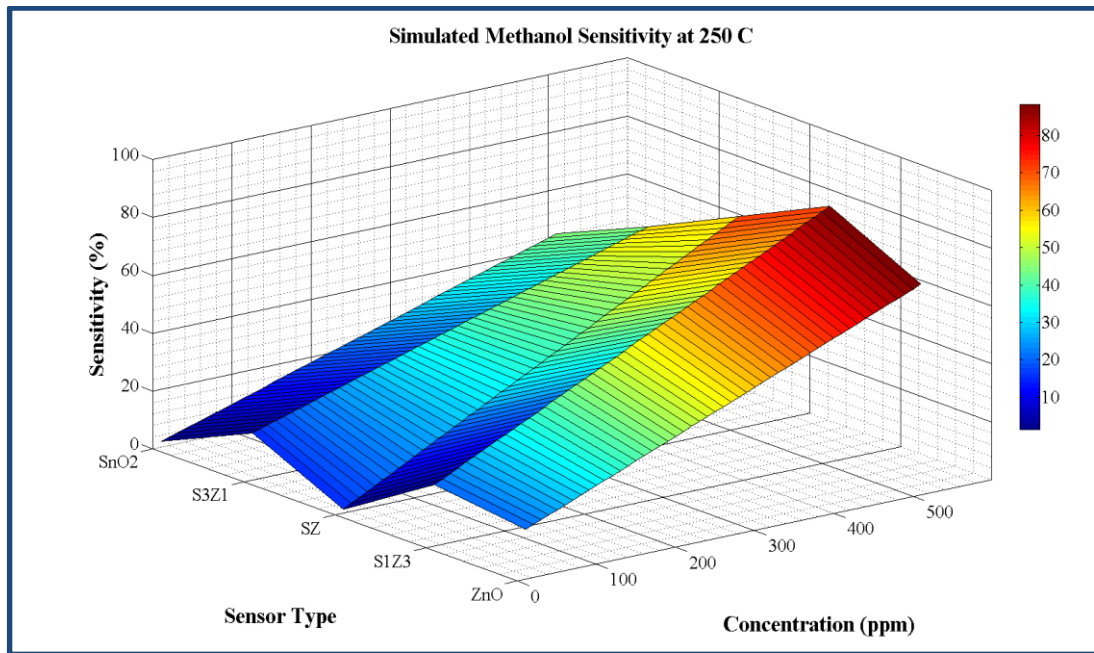


Figure 7-16: Simulated sensitivity at 250 °C (linear model).

In the linear simulation, SZ sensors indicated an improvement above the SnO₂ and S₃Z₁ sensors in sensitivity with increase in concentration of methanol at all operating temperatures. The simulated sensitivity from S₁Z₃ sensors was still better than all other sensors. This behaviour support the profile obtained from the power model, and confirmed the sensitivity profile observed in Section 6.2. However, the model did not support simulation of the low operational temperatures.

In the literature, relating to this research domain, there is apparently no evidence of previously published work that reflects linear regression analysis of sensitivity as a function of gas concentration and operational temperature. The results reported in this thesis, therefore, serves as a baseline for linear simulation of gas sensors based on gas concentration and operating temperature. This assertion is reflected in Chapter 8 where it is proposed that the results described in this thesis importantly inform the state-of-knowledge in this research domain.

7.5 Thermodynamics of Sensor - Gas Interaction

To analyse the thermodynamic and kinetic behaviour of the sensing mechanism, the Arrhenius relationship is applied for each of the sensors ([Karimi et al. 2013](#)):

$$\ln R_g = \ln R_a + \frac{E_A}{k_B T} \quad (7.22)$$

where, the Boltzmann constant, $k_B = 8.6173324 \times 10^{-5} \text{ eV K}^{-1}$ ($= 1.3806488 \times 10^{-23} \text{ J K}^{-1}$).

Therefore, the resistance versus temperature linear plot in the form of $\ln R_g$ versus $1/T$ was therefore used to determine the activation energy of the sensing reaction (Figure 7-17). The slope of the line is given as E_A/k_B , from which the activation energy, E_A , was calculated. The temperature region, 150 to 350 °C, was treated as a single linear zone.

Consistent with our observation, the activation energy for electronic conduction of SnO_2 and ZnO nanostructures was reported to increase with an increase in temperatures ([Yadav et al. 2008](#)). The activation energy for different sensors is presented in Figure 7-18. This indicated that the activation energy increases with increasing methanol concentration; but decreases with increase in molar composition of SnO_2 and ZnO in the fabricated sensors. The activation energy of SnO_2 was higher than that of ZnO for both methanol and ethanol. The activation energy of S_1Z_3 sensor devices was the lowest with methanol and ethanol. This behaviour confirms the high sensitivity exhibited by S_1Z_3 sensors across sensing conditions (Section 6.2). With SZ

sensor, the activation energy of ethanol is higher than that of methanol; this could be attributed to the effect of molecular mass of target gas on chemical reactivity (Figure 7-18).

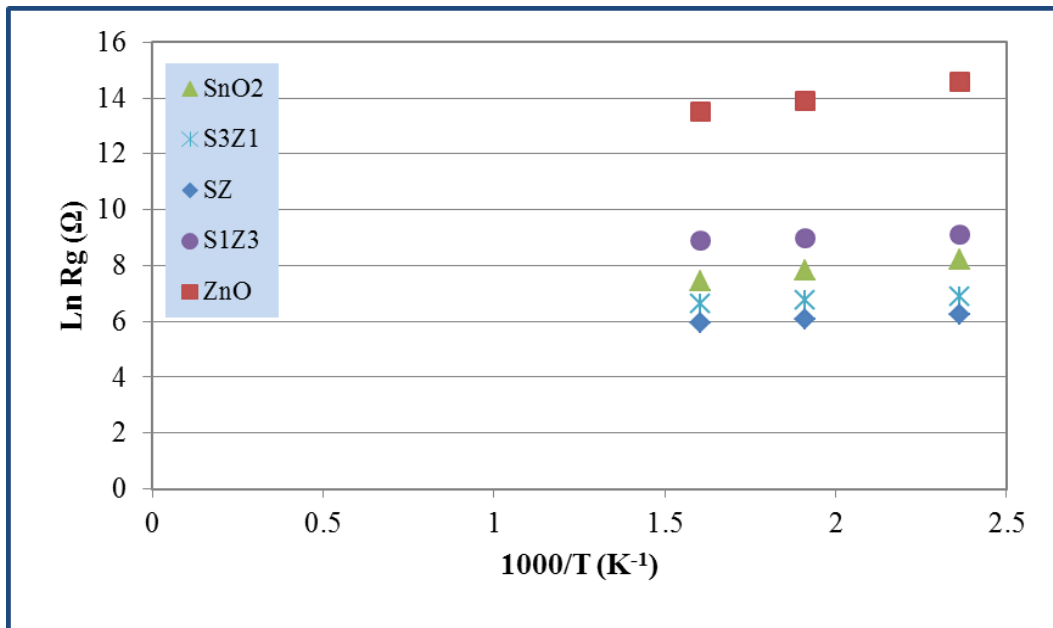


Figure 7-17: Resistance versus temperature plot of 200 ppm ethanol.

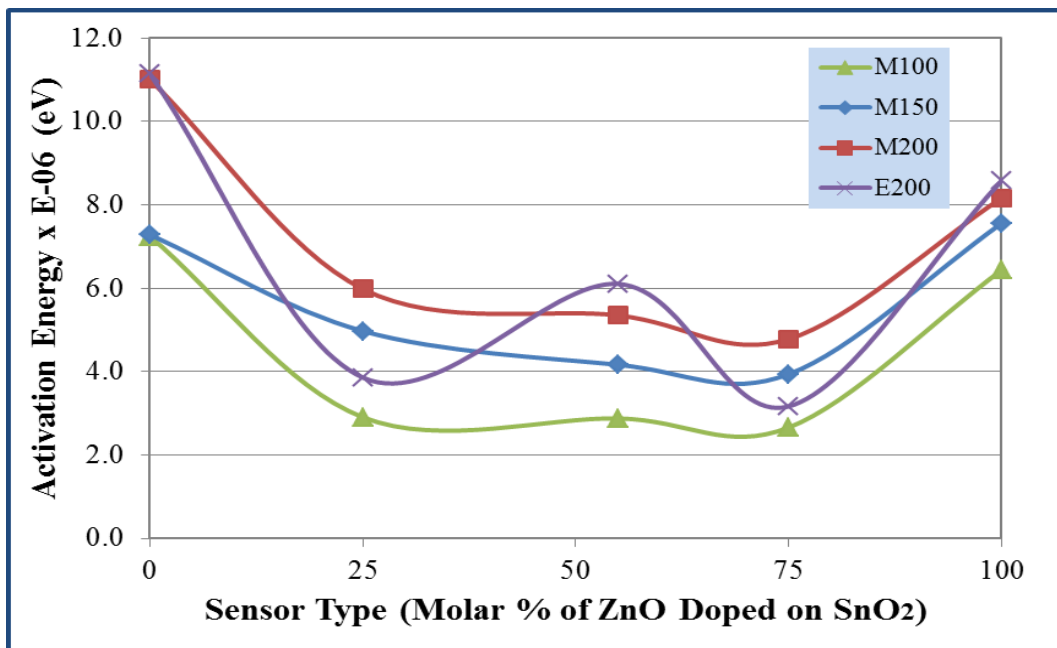


Figure 7-18: Plot of activation energy versus sensor type.

7.6 Adsorption-Desorption Kinetics

The kinetics process of gas-sensor interaction is modelled by the adsorption and desorption cycle (see Chapter 3). The adsorption and desorption processes are statistical in nature. In these processes, there could be fluctuations attributed to randomness associated with the kinetics of gas adsorption, desorption and diffusion ([Yadava and Verma 2014](#)). These fluctuations are intrinsic to the specific sensor and sensing experiment; that is, to the specific thin film, type and concentration of target gas, and film morphology. The adsorption rate on the film surface depends on the rate at which target gas molecules impinges on the film surface and the probability of sticking. The impingement depends on the gas concentration in vapour phase, while the probability of sticking depends on the affinity for the gas molecules to the film surface. Similarly, the rate of desorption depends on the concentration and binding energy of analyte molecules on the sensor surface. Usually, the net diffusion of gas molecules in and out of the sensor surface overlay on the sensitive area will create random fluctuations in the gas loading due to Brownian motion. This will have contributions from both normal (in and out of film surface) and lateral (in and out of sensitive area boundary) diffusive flows ([Yadava and Verma 2014](#)). As the gas-film surface interaction processes are taking place over time, the kinetic and randomness results in fluctuations of film mass density over the sensor sensitive area. This results in some fluctuations (noise) in the sensor output signals.

The reaction of target gas with sensor surface can be described as a dynamic system. The study of dynamical systems is greatly improved when signals are described in a representation space formed by a minimal set of canonical variables ([Martinelli et al. 2003](#)). As a central concept in the analysis of dynamics systems, the phase space phenomenon can be used for the description of the adsorption-desorption kinetics of the gas sensor interaction ([Martinelli et al. 2003](#); [Vergara et al. 2007](#)). In the phase space, the temporal evolution of any system is represented by time parametric trajectories; both the state and evolution of systems are described by the observed response and its first derivative. And, the feature extracted in the phase space leads to

higher classification performance with respect to the standard features calculated in the time domain ([Pardo and Sberveglieri 2007](#)).

7.6.1 Feature Extraction

Analogous with mechanical systems, the chemical sensor signal and its time derivatives are considered as canonical variables. In the phase space, the sensor signal behaviour is described by a response curve; the response curve is represented by the sensor response (or sensitivity), S , and the first derivative of sensor response, dS/dt (Figure 7-19).

The sensitivity, S , may reflect the concentration level of ionosorbed oxygen, while the first derivative of S , i.e. dS/dt , may reflect the concentration change rate of ionosorbed oxygen. The sensor response and the first derivative of S could be used to represent the reaction kinetic process.

The response curve can be described by six parameters. The adsorption process is represented by the curve above the blue line, while the desorption process is represented by the curve below the blue line (Figure 7-19). Part A represent the gas sensing response due to increasing adsorption of target gas for contact reactions on the sensor surface, with the release of captured electrons. As the chamber is saturated with the target gas, the surface reactions attend equilibrium as illustrated with the max (dS/dt), an indication of the rate of adsorption.

As the target gas competes with the synthetic gas over the gas sensor surface, the increase of response slows down gradually, as observed in part B. After the flow of the target gas is shut off, the gas-sensing reactions is predominated by initiation of the desorption process. The gas desorption process is characterised by the replacement of adsorbed target gas molecules by synthetic gas, leading to the recovery of gas sensor back to initial state finally. Part A' represents the increasing desorption of the target gas, and capture of electrons. The min (dS/dt) represents the equilibrium saturation of the chamber with both the target and synthetic gases, in which there is an equilibrium

capture and release of electrons from the system. This could be an indication of the rate of desorption. As the concentration of synthetic gas increases more than the target gas, the desorption process completes with part B', and the system returns to its initial stable state under the influence of synthetic gas.

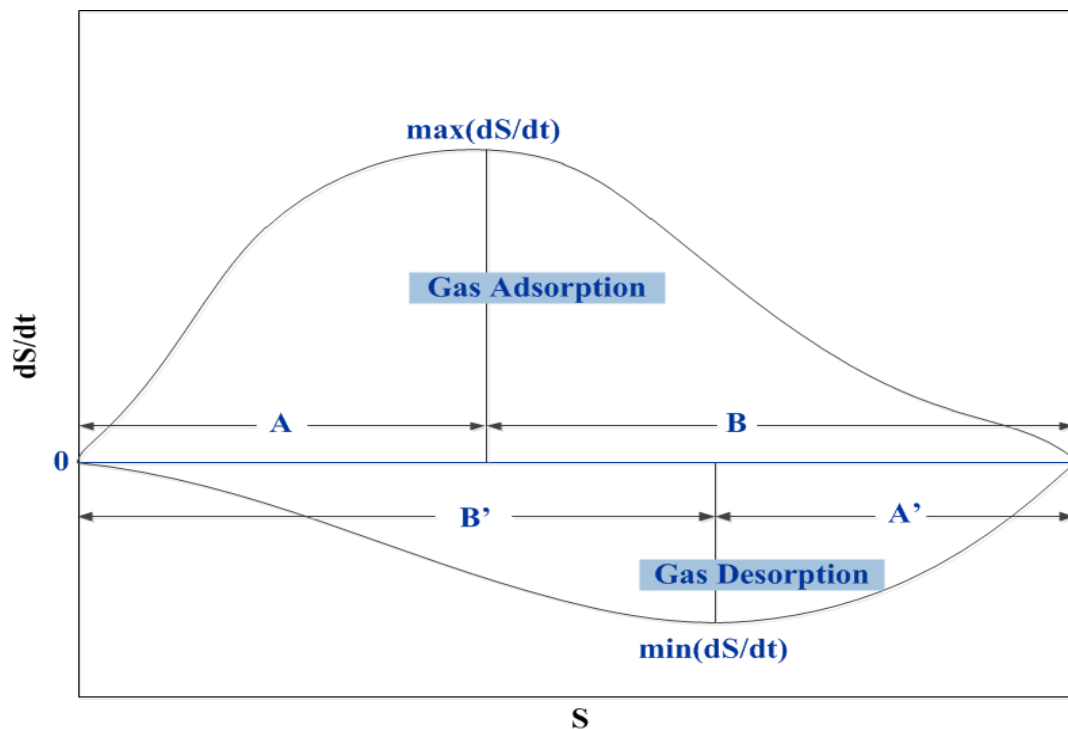


Figure 7-19: Gas adsorption-desorption cycle.

In the feature extraction process, the transformation of the response curve could result in the application of sensitivity, S , $\max(dS/dt)$, $\min(dS/dt)$, parts A, B, A' and B' in pattern recognition of target gases based on discriminant analysis, operating conditions, system configuration and optimisation process of gas sensor array.

Typical plots of the dS/dt versus S are presented in Figure 7-20. From our analyses, the shape of the phase space trajectories is dependent on the sensor type, operating temperature, gas type and concentration. As the phase-space model extracts the features that describe sensor trajectories, these parameters can be used to characterise the adsorption-desorption behaviour of the gas-sensor interaction process.

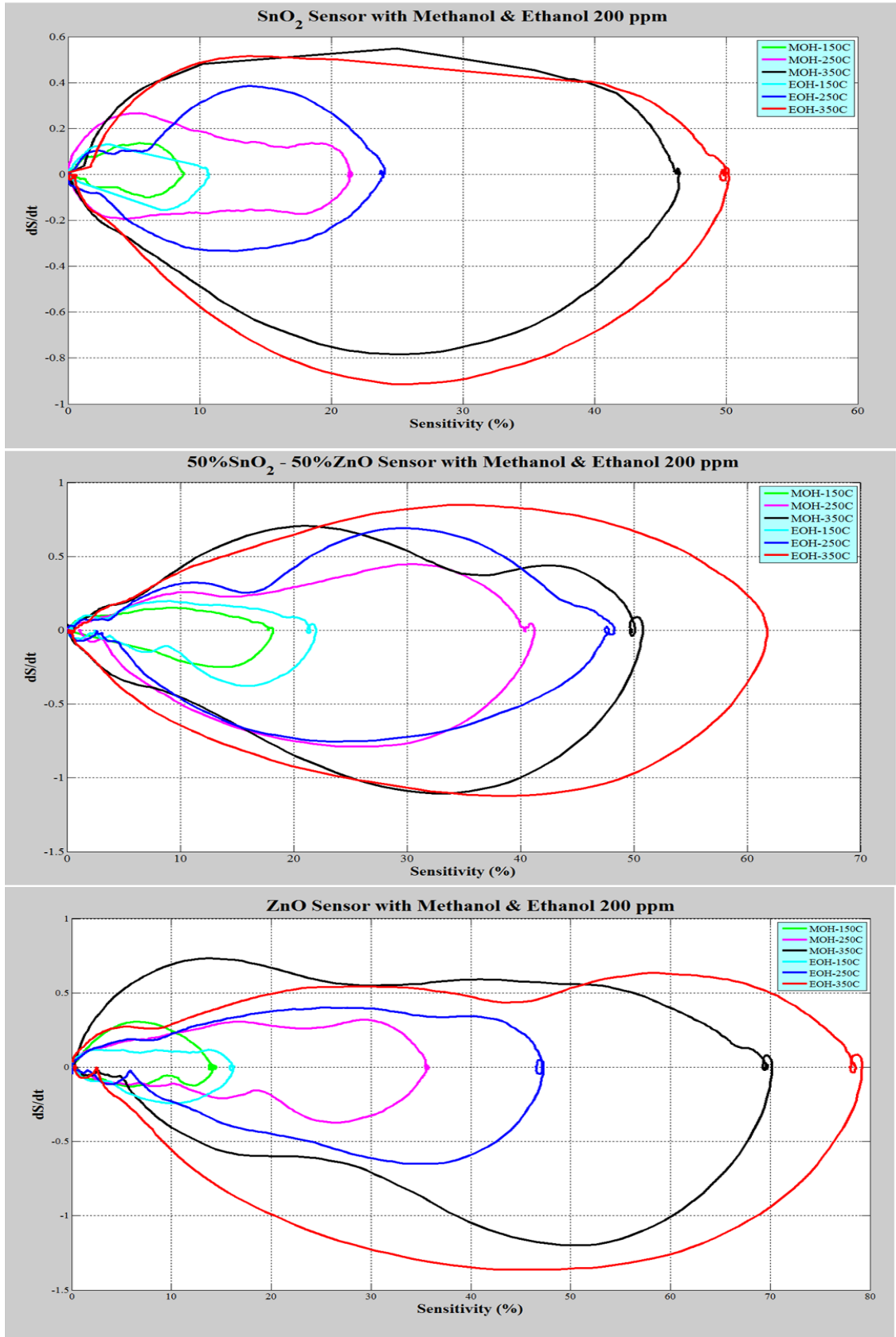


Figure 7-20: Adsorption-desorption cycles of SnO_2 , SZ and ZnO sensors.

Using these six parameters therefore, the application of the phase space phenomenon can be extended to the process of reaction kinetic modelling. This involves the adsorption-desorption mechanism that occurs in gas-sensor interaction leading to an analysis of the response behaviour of each sensor at different operating temperatures and gas concentrations.

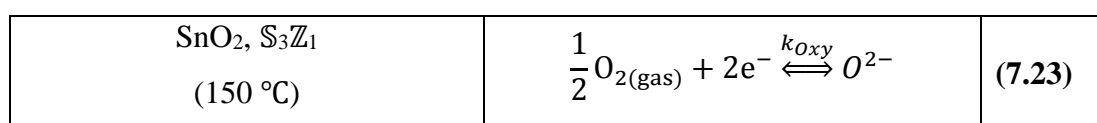
Faster response time at higher temperatures might be due to the faster rates of adsorption desorption (Yang et al. 2014). We have observed a strong correlation of $\max(dS/dt)$ and response time. However, despite this strong individual correlation, there were different trends in the $\max(dS/dt)$ versus response time behaviour for different sensors at different conditions.

From the adsorption-desorption kinetic parameters, it can be concluded that the reduction in response time at higher temperatures might be due to the faster rates of adsorption, while the reduction in recovery time could be attributed to faster rate of desorption.

7.7 Sensing Mechanism

At operating temperature of 150 °C, the SnO₂ and S₃Z₁ samples have average charge parameter of 0.5, indicating that they reacted in the atmosphere of O²⁻ species, while ZnO and S₁Z₃ (with $b \approx 1$) reacted in the atmosphere of O⁻. At operating temperature of 250 and 350 °C, S₃Z₁, S₁Z₃ and ZnO samples have average charge parameter of 1, indicating that they reacted in the atmosphere of O⁻. SnO₂ samples have $b \approx 1$ at 250 °C and $b \approx 2$ at 350 °C, indicating that they reacted in the atmosphere of O⁻ and O₂⁻ species, respectively.

Based on Equation (7.1), we can clearly state the sensing mechanism of the different sensors at different operating temperatures as follows:



| | | | | |
|--|------------------------------|---|---|--------|
| ZnO, S ₁ Z ₃ (150 °C) | SnO ₂ (250 °C) | S ₃ Z ₁ , S ₁ Z ₃ , ZnO (250, 350 °C) | $\frac{1}{2} O_{2(gas)} + e^{-} \xrightleftharpoons{k_{Oxy}} O^{-}$ | (7.24) |
|--|------------------------------|---|---|--------|

| | | |
|---|---|--------|
| SnO ₂ , S _Z (350 °C) | $O_{2(gas)} + e^{-} \xrightleftharpoons{k_{Oxy}} O_2^{-}$ | (7.25) |
|---|---|--------|

The S_Z samples have $b \approx 2$ at 350 °C. Although, exhibiting a very good linear dependence, the S_Z samples behaved very abnormally at temperatures of 150 and 250 °C. This behaviour by the S_Z samples could also be attributed to the high heterogeneity of the prepared sample, in correlation with its surface morphology (see Sections 5.2 and 5.3).

Nevertheless, there have been some abnormal b values reported in the literature. ZnO nanostructured sensors at 300 - 500 °C operating temperature had b of between 0.22 and 0.32 ([Khranovskyy et al. 2008](#)), while SnO₂ at operating temperature of 350 – 500 °C had $b = 0.25$ ([Xu et al. 2000](#)). For analysis of CO, CH₄, and H₂ using SnO₂ sensor, [Coles et al. \(1991\)](#) reported b values of between 0.2 and 0.5. These values are quite low.

This abnormal behaviour could be attributed to complication in the defect chemistry of metal oxides; i.e., the occurrence of associated species, such as oxygen vacancies and the acceptor defect ([Kamp et al. 2005](#)). Also, the method of preparation could be another factor in the sensitivity of the sensor. A linear dependence of sensitivity and concentration is explained by [Chen et al. \(2006c\)](#) in relationship with particle size and ethanol concentration. However, they did not relate the sensitivity with the oxygen concentration.

From this charge parameter behaviour and results of this study, it can therefore, be confirmed that gas concentration and operating temperature are not the only conditions

affecting the gas sensor sensitivity. A vital factor is the molar composition of the sensor materials. Other factors, such as, nanostructure, morphology, film fabrication process/conditions, post-fabrication processes, and testing conditions, could also influence sensor sensitivity.

7.8 Practical Application of Sensor Devices

This approach described in this study assumed that the nature of the volatile hydrocarbon gases is known, and requires a pre-calibration of the sensing system for each target gas. Laboratory applicability of the approach was validated with several experiments. The sensor devices were observed to fully recover to their initial baseline resistance after each exposure to the target gases. Therefore, each sensor response mechanism was confirmed to be fully reversible.

Practical implementation of the research findings will require the initial pre-treatment of the sensor devices as described in Section 4.9, to recalibrate and ascertain its sensing mechanism. The linear and power simulation models provided in Sections 7.3 and 7.4, respectively, have provided insights into the possible behaviours of different sensors at different operating conditions. Then the sensors could be applied and validated in uncontrolled environment in real-time with variable gas concentrations, using several experiments both inside and outside the laboratory. Some of the major issues that could affect real-life sensing of the sensors could be cross-sensitivity, because of the different volatility of environmental gases ([Zhang and Mo 2009](#)). However, the use of synthetic gas (i.e., ambient air) as a carrier gas in our research has prepared the sensors to respond to real-life environmental conditions. Also, to improve sensor sensitivity, gases of similar classes should be characterised at similar conditions, and the operating conditions modified for different hydrocarbon classes. In order to ascertain that the sensor response results from interested target gases and reveal measurement artifacts during the sensitivity analysis of target gases, it may be desirable to monitor other related gases and relevant conditions that could influence the measurement process, and gas sensitivity behaviours.

Generally, the detection, response and recovery times could be reduced by increasing the operating temperature of the sensor. Higher concentration and lower molecular composition of the target gases could also reduce the detection, response and recovery times.

7.9 Summary and Conclusion

Sensitivity analysis was undertaken to determine the effect of sensor type, gas concentration and operating temperature on sensor sensitivity, along with their relationship to sensor sensitivity itself. A modified chemisorption model was presented. As observed in the coefficient of determination, it gave excellent simulation of the sensitivity behaviour for gas concentration of 100–200 ppm at operating temperatures of 150, 250 and 350 °C. Extension of this model has produced robust simulation of sensitivity behaviour at gas concentration of 0-500 ppm. The best sensors were the S_1Z_3 and S_3Z_1 sensors. However, SZ sensor was observed to improve at higher concentration. Application of a linear model to the simulation of SZ sensor confirmed this behaviour at higher concentration.

The application SnO_2 and ZnO nanocomposite was supported by the thermodynamics of their surface interaction with gas. From analysis of their activation energies, electronic conduction of SnO_2 and ZnO nanostructures was reported to increase with increase in gas concentration and operating temperatures.

With the phase space response curves, it is easy to describe the gas sensing trajectory according the effects of target gas, gas concentration and operating temperature on adsorption-desorption and reaction kinetics. As a feature extraction procedure, the phase space methods are very vital in the analysis of the dynamic transient response of metal oxide sensors to a step change in sensor type (based on component contributions), gas concentration or temperature modulation. An interesting feature of the phase space model is that it takes into account both static and dynamic information at the same time. Along with the time space domain model (discussed in Sections 6.2.2 and 6.2.4), the phase space model enhanced information extraction about the gas-

sensor response dynamics. This is because feature extracted in the phase space leads to higher classification performance with respect to the standard features calculated in the time domain.

This report could serve as a baseline for linear regression analysis of sensitivity as a function of gas concentration and operational temperature. Further and future research would analyse the magnitude of the contributing effects of gas concentration and operational temperature in the light of their sensitivity.

Chapter Eight

Summary, Conclusion and Outlook

8.1 Summary and Conclusion

This research has explored the component features and dynamics of sensing mechanisms for different combinations of coupled SnO₂ and ZnO nanocomposite nanostructures. A primary research question formulated was to investigate the effects of variations in molar compositions of the combining metal oxides on the sensitivity of the chemical sensors. This question was applied as the baseline motivation for the research, and the ensuing investigation and experiments, with their results described in this thesis.

In order to develop an understanding of the dynamic relationship between the effective parameters and variables intrinsic to the domain of investigation, five sensors were fabricated; the sensors were pure SnO₂ and pure ZnO sensor devices, along with three sensors nanocomposites fabricated by gradual changes in the molar composition of SnO₂ and ZnO. The fabrication process involved sputtering of the MOX onto Si/SiO₂ substrate to form thin films. Both as-fabricated and annealed samples were characterised using FE-SEM, EDS and AFM.

The grain size was observed to increase from pure SnO₂ and ZnO samples toward the SZ samples. The grain height and surface roughness however, did not indicate a particular trend among the sensors. The SZ samples were observed to reflect the lowest surface roughness parameters, while the S₁Z₃ samples showed the highest surface roughness values. The structural analysis revealed the nanocrystalline images to have minor hillocks on a relatively dense film surface. The unannealed samples exhibited more rounded protrusions than the annealed samples. The grain heights of the as-fabricated samples were higher than the annealed samples, while there was reduction

in surface roughness as a result of annealing. Between the pure samples, SnO₂ samples were less rough than the ZnO samples.

The raw sensor signals were recorded in their quantised form. After smoothing the raw signal response using the Savitzky-Golay filter, the gas response was characterised to determine the sensitivity of the sensors. Laboratory investigation proved that gas sensitivity increases with increasing gas concentration and increasing temperature for all sensors. Thermodynamic analysis indicated that the sensitivity increased with activation energy of each sensor. The best sensitivities were displayed by S₁Z₃, followed by S₃Z₁ sensor devices, while ZnO was more sensitive than SnO₂. This behaviour was attributed to the high photocatalytic activity of pure ZnO and coupled SnO₂-ZnO nanocomposites than pure SnO₂. Also, sensitivity to ethanol was more than sensitivity to methanol, indicating a possibility for good selectivity of the sensors.

The adsorption-desorption kinetic process was studied by the response and recovery time of the sensors with particular target gases. The ZnO sensor had the best response to methanol exposure while the best recovery was exhibited by S₃Z₁ sensor when exposed to ethanol. Consistent with its sensitivity behaviour, the worst response and recovery was exhibited by S₁Z₃ sensors.

A sensitivity analysis undertaken to observe the dynamics of the response to methanol and ethanol indicated that sensor type, gas concentration and temperature influenced respective sensor sensitivity; but the effects were varied depending on the sensing conditions. Across all sensor types, S₃Z₁ and S₁Z₃ sensors confirmed higher response of than other sensors, while across all temperatures, sensitivity to methanol revealed that S₁Z₃ sensor was more sensitive than other sensors. The strong effect size for interaction of gas concentration and operating temperature indicated their possible practical significance on the sensor sensitivity.

With modified chemisorption and linear models, excellent sensitivity behaviours were simulated with concentration of 100–200 ppm at operating temperatures of 150, 250 and 350 °C. With extended concentration range, the simulation results collaborated the

facts that S_1Z_3 and S_3Z_1 sensors were the best sensors. At higher concentrations however, the SZ sensors were observed to improve in sensitivity.

The models produced from the analyses reflect proof that, apart from gas concentration and operating temperatures, a range of nanocomposites of SnO_2 and ZnO sensors can exhibit different sensing mechanisms or behaviours. This could be attributed to the presence of other surface species and other uncharacterised surface reactions taking place on the film surface.

The successful fabrication and application of these sensors has the valuable advantage of providing a robust array of micro chemical sensor systems with on-chip data-evaluation ability for established microelectronic and micro-technological bio- and geo-chemical processes. Therefore, with the behaviours of these sensors, they provide an excellent platform for real-time signal response logging, and quantitative and qualitative identification of volatile and semi-volatile hydrocarbons and other gases for effective environmental monitoring.

The results from the research conducted in this thesis have provided significant insights that inform answers to the primary research question posed at the outset of the work, and demonstrate the underlying science and technology relating to a method for answering associated questions concerning the dynamics of the sensor technology investigated and reported here. It is proposed therefore, that the report of this work in this thesis contributes significantly to the state-of-knowledge for this domain of scientific endeavour.

8.2 Outlook for Future Work

Although, this research has explored and established the sensing behaviour of SnO_2 and ZnO nanocomposites, further research could be undertaken to improve the sensing mechanisms of the fabricated sensors by:

- expanding the range (lower and higher) of gas concentration and operating temperature of the sensor to improve the model

- increasing target gas (e.g., more hydrocarbons, alcohols, H₂, CO, CO₂, etc.) variety to ascertain the selectivity of the sensors
- studying the effects of deposition duration on the behaviour of gas sensitivity
- deriving surface reaction models combining the intrinsic and extrinsic reactions to form a system of equations for the as-fabricated sensors

With the behaviour of surface roughness and film thickness, a transition model between an epitaxial regime and a roughening regime could be developed to simulate a smoothening-roughening transition in film growth. Also, application of the fabricated chemical sensors as sensor array in industrial or environmental analysis will prove the chemical sensor microsystem for commercialisation.

References

- Abouzar, M. H., Poghossian, A., Razavi, A., Williams, O. A., Bijmens, N., Wagner, P., and Schöning, M. J. (2009). "Characterisation of capacitive field-effect sensors with a nanocrystalline-diamond film as transducer material for multi-parameter sensing." *Biosensors and Bioelectronics*, 24(5), 1298-1304.
- Achmann, S., Hagen, G., Kita, J., Malkowsky, I., Kiener, C., and Moos, R. (2009). "Metal-Organic Frameworks for Sensing Applications in the Gas Phase." *Sensors*, 9(3), 1574-1589.
- Adhikari, B., and Majumdar, S. (2004). "Polymers in sensor applications." *Progress in Polymer Science*, 29(7), 699-766.
- Ahlers, S., Müller, G., and Doll, T. (2005). "A rate equation approach to the gas sensitivity of thin film metal oxide materials." *Sensors and Actuators B: Chemical*, 107(2), 587-599.
- Ahsanulhaq, Q., Kim, J. H., Reddy, N. K., and Hahn, Y. B. (2008). "Growth mechanism and characterization of rose-like microspheres and hexagonal microdisks of ZnO grown by surfactant-free solution method." *Journal of Industrial and Engineering Chemistry*, 14(5), 578-583.
- Al-Hardan, N. H., Abdullah, M. J., Abdul Aziz, A., Ahmad, H., and Low, L. Y. (2010). "ZnO thin films for VOC sensing applications." *Vacuum*, 85(1), 101-106.
- Aliofkhazraei, M., and Sabour Rouhaghdam, A. (2010). "Synthesis and Processing of Nanostructured Films, and Introduction to and Comparison with Plasma Electrolysis", *Fabrication of Nanostructures by Plasma Electrolysis*. Wiley-VCH Verlag GmbH & Co. KGaA, pp. 1-22.
- Alterkop, B., Parkansky, N., Goldsmith, S., and Boxman, R. L. (2003). "Effect of air annealing on opto-electrical properties of amorphous tin oxide films." *Journal of Physics D: Applied Physics*, 36(5), 552.
- Alvarez, R., González, J. C., Espinós, J. P., González-Elipé, A. R., Cueva, A., and Villuendas, F. (2013). "Growth of silver on ZnO and SnO₂ thin films intended for low emissivity applications." *Applied Surface Science*, 268, 507-515.
- An'chkov, D. G., Davydov, S. Y., and Troshin, S. V. (2007). "Effect of adsorption on the surface conductivity and work function." *Technical Physics Letters*, 33(9), 782-784.
- An'chkov, D. G., Davydov, S. Y., and Troshin, S. V. (2008). "Adsorption of hydrogen atoms and oxygen molecules on zinc oxide and titanium oxide on the surface conductivity and work function." *Technical Physics Letters*, 34(9), 795-797.

- Ang, G. T., Toh, G. H., Bakar, M. Z. A., Abdullah, A. Z., and Othman, M. R. (2011). "High sensitivity and fast response SnO₂ and La-SnO₂ catalytic pellet sensors in detecting volatile organic compounds." *Process Safety and Environmental Protection*, 89(3), 186-192.
- Anta, J. A. (2012). "Electron transport in nanostructured metal-oxide semiconductors." *Current Opinion in Colloid & Interface Science*.
- Anzai, J.-i. (2004). "Biosensors", in J. L. Atwood and J. W. Steed, (eds.), *Encyclopedia of Supramolecular Chemistry*. Taylor & Francis, pp. 115-119.
- Arnold, S. P., Prokes, S. M., Perkins, F. K., and Zaghoul, M. E. (2009). "Design and performance of a simple, room-temperature Ga₂O₃ nanowire gas sensor." *Applied Physics Letters*, 95(10), 1-3.
- Arshak, K., and Gaidan, I. (2005). "Development of a novel gas sensor based on oxide thick films." *Materials Science and Engineering: B*, 118(1-3), 44-49.
- Artursson, T., Spångeus, P., and Holmberg, M. (2002). "Variable reduction on electronic tongue data." *Analytica Chimica Acta*, 452(2), 255-264.
- Asar, N., Erol, A., Okur, S., and Arikan, M. C. (2012). "Morphology-dependent humidity adsorption kinetics of ZnO nanostructures." *Sensors and Actuators A: Physical*, 187, 37-42.
- Ashby, M. F., Ferreira, P. J., and Schodek, D. L. (2009). "Nanomaterials: Properties", *Nanomaterials, Nanotechnologies and Design*. Boston: Butterworth-Heinemann, pp. 199-255.
- Asokan, K., Park, J., Choi, S.-W., and Kim, S. S. (2010). "Nanocomposite ZnO-SnO₂ Nanofibers Synthesized by Electrospinning Method." *Nanoscale Research Letters*, 5(4), 747 - 752.
- Bai, Z., Xu, W., Xie, C., Dong, M., Zhang, S., Xu, J. I. E., and Xiao, S. (2013). "Preparation and gas-sensing property of parallel-aligned ZnO nanofibrous films." *Bulletin of Materials Science*, 36(4), 505-511.
- Baleanu, D., Okur, Y., Okur, S., and Ocakoglu, K. (2011). "Parameter Identification of the Langmuir Model for Adsorption and Desorption Kinetic Data", in J. A. T. Machado, D. Baleanu, and A. C. J. Luo, (eds.), *Nonlinear and Complex Dynamics: Applications in Physical, Biological and Financial Systems*. New York: Springer, pp. 97-106.
- Baltes, H., Fujita, H., and Liepmann, D. (2005). *Integrated Chemical Microsensor Systems in CMOS Technology*: Springer Berlin Heidelberg.
- Bârsan, N. (2011). "Transduction in Semiconducting Metal Oxide Based Gas Sensors - Implications of the Conduction Mechanism." *Procedia Engineering*, 25, 100-103.

- Barsan, N., Koziej, D., and Weimar, U. (2007). "Metal oxide-based gas sensor research: How to?" *Sensors and Actuators B: Chemical*, 121(1), 18-35.
- Barsan, N., Schweizer-Berberich, M., and Göpel†, W. (1999). "Fundamental and practical aspects in the design of nanoscaled SnO₂ gas sensors: a status report." *Fresenius' Journal of Analytical Chemistry*, 365(4), 287-304.
- Bârsan, N., Stetter, J. R., Findlay, M., and Göpel, W. (1999). "High-Performance Gas Sensing of CO: Comparative Tests for Semiconducting (SnO₂-Based) and for Amperometric Gas Sensors." *Analytical Chemistry*, 71(13), 2512-2517.
- Barsan, N., and Weimar, U. (2001). "Conduction Model of Metal Oxide Gas Sensors." *Journal of Electroceramics*, 7(3), 143-167.
- Bârsan, N., and Weimar, U. (2003). "Understanding the fundamental principles of metal oxide based gas sensors; the example of CO sensing with SnO₂ sensors in the presence of humidity." *Journal of Physics: Condensed Matter*, 15(20), R813.
- Bassey, E., Whalley, J., Sallis, P., and Prasad, K. (2014). "Wavelet transform smoothing filters for metal oxide gas sensor signal cleaning" *8th International Conference on Sensing Technology (ICST 2014)*. September 2-4, Liverpool John Moores University, United Kingdom, pp. 5.
- Batzill, M. (2006). "Surface Science Studies of Gas Sensing Materials: SnO₂." *Sensors*, 6(10), 1345-1366.
- Beckers, N. A., Taschuk, M. T., and Brett, M. J. (2013). "Selective room temperature nanostructured thin film alcohol sensor as a virtual sensor array." *Sensors and Actuators B: Chemical*, 176, 1096-1102.
- Bejaoui, A., Guerin, J., and Aguir, K. (2013). "Modeling of a p-type resistive gas sensor in the presence of a reducing gas." *Sensors and Actuators B: Chemical*, 181, 340-347.
- Bertazzi, F., Goano, M., and Bellotti, E. (2007). "Electron and Hole Transport in Bulk ZnO: A Full Band Monte Carlo Study." *Journal of Electronic Materials*, 36(8), 857-863.
- Bhargavi, K. S., and Kubakaddi, S. S. (2013). "Scattering mechanisms and diffusion thermopower in a bilayer graphene." *Physica E: Low-dimensional Systems and Nanostructures*, 52, 116-121.
- Bochenkov, V. E., and Sergeev, G. B. (2010). "Sensitivity, Selectivity, and Stability of Gas-Sensitive Metal-Oxide Nanostructures", in A. Umar and Y.-B. Hahn, (eds.), *Metal Oxide Nanostructures and Their Applications*. American Scientific Publishers, pp. 31-52.

- Boeker, P., Wallenfang, O., and Horner, G. (2002). "Mechanistic model of diffusion and reaction in thin sensor layers—the DIRMAS model." *Sensors and Actuators B: Chemical*, 83(1–3), 202-208.
- Brunauer, S., Emmett, P. H., and Teller, E. (1938). "Adsorption of Gases in Multimolecular Layers." *Journal of the American Chemical Society*, 60(2), 309-319.
- Bubphamala, T. (2006). *Ultra-thin oxide films as gas microsensors*, 3196423, The University of Texas at El Paso, United States -- Texas.
- Calvo, E. J., and Otero, M. (2008). "Chemical Sensors", in A. A. Vives, (ed.), *Piezoelectric Transducers and Applications*. pp. 241-257.
- Cao, G., and Wang, Y. (2004). "Zero-Dimensional Nanostructures: Nanoparticles", *Nanostructures and Nanomaterials: Synthesis, Properties, and Applications*. Imperial College Press (distributed by (World Scientific), pp. 61-141.
- Capone, S., Forleo, A., Francioso, L., Rella, R., Siciliano, P., Spadavecchia, J., Presicce, D. S., and Taurino, A. M. (2003). "Solid state gas sensors: State of the art and future activities." *Journal of Optoelectronics and Advanced Materials*, 5(5), 1335-1348.
- Çetinörgü, E. (2007). "Characteristics of filtered vacuum arc deposited ZnO–SnO₂ thin films on room temperature substrates." *Optics Communications*, 280(1), 114-119.
- Çetinörgü, E., Goldsmith, S., and Boxman, R. L. (2007a). "The effect of substrate temperature on filtered vacuum arc deposited zinc oxide and tin oxide thin films." *Journal of Crystal Growth*, 299(2), 259-267.
- Çetinörgü, E., Goldsmith, S., Rosenberg, Y., and Boxman, R. L. (2007b). "Influence of annealing on the physical properties of filtered vacuum arc deposited tin oxide thin films." *Journal of Non-Crystalline Solids*, 353(26), 2595-2602.
- Cha, C.-N., Choi, M.-H., and Ma, T.-Y. (2012). "Highly transparent and resistive nanocrystalline ZnO-SnO₂ films prepared by rf magnetron sputtering." *Journal of Electrical Engineering & Technology*, 7(4), 596~600.
- Chang, H.-P., Wang, F.-H., Chao, J.-C., Huang, C.-C., and Liu, H.-W. (2011). "Effects of thickness and annealing on the properties of Ti-doped ZnO films by radio frequency magnetron sputtering." *Current Applied Physics*, 11(1, Supplement), S185-S190.
- Chen, M., Wang, Z., Han, D., Gu, F., and Guo, G. (2011). "Porous ZnO Polygonal Nanoflakes: Synthesis, Use in High-Sensitivity NO₂ Gas Sensor, and Proposed Mechanism of Gas Sensing." *The Journal of Physical Chemistry C*, 115(26), 12763-12773.

- Chen, W., Qiu, Y., Zhong, Y., Wong, K. S., and Yang, S. (2009). "High-Efficiency Dye-Sensitized Solar Cells Based on the Composite Photoanodes of SnO₂ Nanoparticles/ZnO Nanotetrapods[†]." *The Journal of Physical Chemistry A*, 114(9), 3127-3138.
- Chen, Y., Zhu, C., and Wang, T. (2006a). "The enhanced ethanol sensing properties of multi-walled carbon nanotubes/SnO₂ core/shell nanostructures." *Nanotechnology*, 17(12), 3012-3017.
- Chen, Y., Zhu, C. L., and Xiao, G. (2006b). "Reduced-temperature ethanol sensing characteristics of flower-like ZnO nanorods synthesized by a sonochemical method." *Nanotechnology*, 17(18), 4537.
- Chen, Y. J., Nie, L., Xue, X. Y., Wang, Y. G., and Wang, T. H. (2006c). "Linear ethanol sensing of SnO₂ nanorods with extremely high sensitivity." *Applied Physics Letters*, 88(8), 083105-3.
- Cheong, H. W., and Lee, M. J. (2006). "Sensing characteristics and surface reaction mechanism of alcohol sensors based on doped SnO₂." *Journal of Ceramic Processing Research*, 7(3), 183-191.
- Chiu, H.-C., and Yeh, C.-S. (2007). "Hydrothermal Synthesis of SnO₂ Nanoparticles and Their Gas-Sensing of Alcohol." *The Journal of Physical Chemistry C*, 111(20), 7256-7259.
- Choi, S.-W., Katoch, A., Sun, G.-J., and Kim, S. S. (2013). "Synthesis and gas sensing performance of ZnO–SnO₂ nanofiber–nanowire stem-branch heterostructure." *Sensors and Actuators B: Chemical*, 181, 787-794.
- Chwieroth, B., Patton, B. R., and Wang, Y. (2001). "Conduction and Gas–Surface Reaction Modeling in Metal Oxide Gas Sensors." *Journal of Electroceramics*, 6(1), 27-41.
- Coleman, V. A., and Jagadish, C. (2006). "Basic Properties and Applications of ZnO", in J. Chennupati and P. Stephen, (eds.), *Zinc Oxide Bulk, Thin Films and Nanostructures*. Oxford: Elsevier Science Ltd, pp. 1-20.
- Coles, G. S. V., Williams, G., and Smith, B. (1991). "The effect of oxygen partial pressure on the response of tin (IV) oxide based gas sensors." *Journal of Physics D: Applied Physics*, 24(4), 633.
- Comini, E., Baratto, C., Faglia, G., Ferroni, M., Vomiero, A., and Sberveglieri, G. (2009a). "Quasi-one dimensional metal oxide semiconductors: Preparation, characterization and application as chemical sensors." *Progress in Materials Science*, 54(1), 1-67.
- Comini, E., Faglia, G., and Sberveglieri, G. (2009b). "Electrical-Based Gas Sensing", in E. Comini, G. Faglia, and G. Sberveglieri, (eds.), *Solid State Gas Sensing*. Springer US, pp. 1-61.

- Comini, E., Guidi, V., Malagù, C., Martinelli, G., Pan, Z., Sberveglieri, G., and Wang, Z. L. (2004). "Electrical Properties of Tin Dioxide Two-Dimensional Nanostructures." *The Journal of Physical Chemistry B*, 108(6), 1882-1887.
- Cun, W., Jincai, Z., Xinming, W., Bixian, M., Guoying, S., Ping'an, P., and Jiamo, F. (2002a). "Preparation, characterization and photocatalytic activity of nano-sized ZnO/SnO₂ coupled photocatalysts." *Applied Catalysis B: Environmental*, 39(3), 269-279.
- Cun, W., Xinming, W., Jincai, Z., Bixian, M., Guoying, S., Ping'an, P., and Jiamo, F. (2002b). "Synthesis, characterization and photocatalytic property of nano-sized Zn₂SnO₄." *Journal of Materials Science*, 37(14), 2989-2996.
- Damaschio, C. J., Berengue, O. M., Stroppa, D. G., Simon, R. A., Ramirez, A. J., Herwig Schreiner, W., Chiquito, A. J., and Leite, E. R. (2010). "Sn₃O₄ single crystal nanobelts grown by carbothermal reduction process." *Journal of Crystal Growth*, 312(20), 2881-2886.
- de Lacy Costello, B. P. J., Ewen, R. J., Guernion, N., and Ratcliffe, N. M. (2002). "Highly sensitive mixed oxide sensors for the detection of ethanol." *Sensors and Actuators B: Chemical*, 87(1), 207-210.
- Delgado, R. D. (2002). *Tin Oxide Gas Sensors: An Electrochemical Approach*, Doctoral Dissertation, Universität Tübingen, Barcelona - Spain.
- Deng, G., Ding, A., Cheng, W., Zheng, X., and Qiu, P. (2005). "Two-dimensional zinc oxide nanostructure." *Solid State Communications*, 134(4), 283-286.
- Di Giulio, M., Manno, D., Micocci, G., Rella, R., Siciliano, P., and Tepore, A. (1993). "Growth and characterization of tin oxide thin films prepared by reactive sputtering." *Solar Energy Materials and Solar Cells*, 31(2), 235-242.
- Di Natale, C., Buchholt, K., Martinelli, E., Paolesse, R., Pomarico, G., D'Amico, A., Lundström, I., and Lloyd Spetz, A. (2009). "Investigation of quartz microbalance and ChemFET transduction of molecular recognition events in a metalloporphyrin film." *Sensors and Actuators B: Chemical*, 135(2), 560-567.
- Ding, J., McAvoy, T. J., Cavicchi, R. E., and Semancik, S. (2001). "Surface state trapping models for SnO₂-based microhotplate sensors." *Sensors and Actuators B: Chemical*, 77(3), 597-613.
- Ding, J., Yan, X., and Xue, Q. (2012). "Study on field emission and photoluminescence properties of ZnO/graphene hybrids grown on Si substrates." *Materials Chemistry and Physics*, 133(1), 405-409.
- Elangovan, E., Singh, M. P., and Ramamurthi, K. (2004). "Studies on structural and electrical properties of spray deposited SnO₂:F thin films as a function of film thickness." *Materials Science and Engineering: B*, 113(2), 143-148.

- Ellmer, K. (2011). "Transparent Conductive Zinc Oxide and Its Derivatives", in D. S. Ginley, (ed.), *Handbook of Transparent Conductors*. Springer US, pp. 193-263.
- Elokhin, V., Matveev, A., Gorodetskii, V., and Latkin, E. (2007). "Hysteresis in Oscillatory Behaviour in CO Oxidation Reaction over Pd(110) Revealed by Asynchronous Cellular Automata Simulation", in V. Malyshekin, (ed.), *Parallel Computing Technologies*. Springer Berlin Heidelberg, pp. 401-409.
- Erhart, P., Juslin, N., Goy, O., Nordlund, K., Müller, R., and Albe, K. (2006). "Analytic bond-order potential for atomistic simulations of zinc oxide." *Journal of Physics Condensed Matter*, 18(29), 6585-6605.
- Errana, G. (2011). "Nanostructured Metal Oxides and Gas-Sensing Devices", *Metal Oxide Nanostructures as Gas Sensing Devices*. Taylor & Francis, pp. 41-190.
- Fahrner, W. R. (2006). *Nanotechnology and nanoelectronics: materials, devices, measurement techniques*, DE: Springer Verlag.
- Falabretti, B., and Robertson, J. (2007). "Electronic structures and doping of SnO₂, CuAlO₂, and CuInO₂." *Journal of Applied Physics*, 102(12), 123703.
- Feng, P., Wan, Q., and Wang, T. H. (2005). "Contact-controlled sensing properties of flowerlike ZnO nanostructures." *Applied Physics Letters*, 87(21), 213111.
- Fergus, J. W. (2007). "Solid electrolyte based sensors for the measurement of CO and hydrocarbon gases." *Sensors and Actuators B: Chemical*, 122(2), 683-693.
- Fort, A., Rocchi, S., Serrano-Santos, M. B., Mugnaini, M., Vignoli, V., Atrei, A., and Spinicci, R. (2006). "CO sensing with SnO₂-based thick film sensors: Surface state model for conductance responses during thermal-modulation." *Sensors and Actuators B: Chemical*, 116(1-2), 43-48.
- Fraden, J. (2004). "Chemical Sensors", *Handbook of Modern Sensors*. pp. 499-532.
- Franke, M. E., Koplín, T. J., and Simon, U. (2006). "Metal and Metal Oxide Nanoparticles in Chemiresistors: Does the Nanoscale Matter?" *Small*, 2(1), 36-50.
- Gas'kov, A. M., and Romyantseva, M. N. (2001). "Nature of Gas Sensitivity in Nanocrystalline Metal Oxides." *Russian Journal of Applied Chemistry*, 74(3), 440-444.
- Gautam, M., and Jayatissa, A. H. (2012). "Adsorption kinetics of ammonia sensing by graphene films decorated with platinum nanoparticles." *Journal of Applied Physics*, 111(9), -.
- Geistlinger, H. (1993). "Electron theory of thin-film gas sensors." *Sensors and Actuators B: Chemical*, 17(1), 47-60.

- Geurts, J. (2010). "Crystal Structure, Chemical Binding, and Lattice Properties", *Zinc Oxide*. Springer Berlin Heidelberg, pp. 7-37.
- Giefers, H., Porsch, F., and Wortmann, G. (2005). "Kinetics of the disproportionation of SnO." *Solid State Ionics*, 176(1–2), 199-207.
- Gleiter, H. (2000). "Nanostructured materials: basic concepts and microstructure." *Acta Materialia*, 48(1), 1-29.
- Goano, M., Bertazzi, F., Penna, M., and Bellotti, E. (2007). "Electronic structure of wurtzite ZnO: Nonlocal pseudopotential and ab initio calculations." *Journal of Applied Physics*, 102(8), 083709.
- Gomez De Arco, L. (2010). *Graphene and carbon nanotubes: synthesis, characterization and applications for beyond silicon electronics*, Ph.D., University of Southern California, United States -- California.
- Gomri, S., Seguin, J.-L., Guerin, J., and Aguir, K. (2006). "Adsorption–desorption noise in gas sensors: Modelling using Langmuir and Wolkenstein models for adsorption." *Sensors and Actuators B: Chemical*, 114(1), 451-459.
- Gopel, W. (1985). "Chemisorption and charge transfer at ionic semiconductor surfaces: Implications in designing gas sensors." *Progress in Surface Science*, 20(1), 9-103.
- Gründler, P. (2007). *Chemical Sensors: An Introduction for Scientists and Engineers*: Springer Berlin Heidelberg.
- Gu, H., Wang, Z., and Hu, Y. (2012). "Hydrogen Gas Sensors Based on Semiconductor Oxide Nanostructures." *Sensors*, 12(5), 5517-5550.
- Guérin, J., Aguir, K., and Bendahan, M. (2006). "Modeling of the conduction in a WO₃ thin film as ozone sensor." *Sensors and Actuators B: Chemical*, 119(1), 327-334.
- Guo, J., Zhang, J., Ju, D., Xu, H., and Cao, B. (2013). "Three-dimensional SnO₂ microstructures assembled by porous nanosheets and their superior performance for gas sensing." *Powder Technology*, 250, 40-45.
- Gurlo, A. (2006). "Interplay between O₂ and SnO₂: Oxygen Ionosorption and Spectroscopic Evidence for Adsorbed Oxygen." *ChemPhysChem*, 7(10), 2041-2052.
- Gurlo, A., Barsan, N., and Weimar, U. (2005). "Gas Sensors Based on Semiconducting Metal Oxides", in J. L. G. Fierro, (ed.), *Metal Oxides: Chemistry and Application*. CRC Press, pp. 683-738.

- Gurlo, A., and Riedel, R. (2007). "In Situ and Operando Spectroscopy for Assessing Mechanisms of Gas Sensing." *Angewandte Chemie International Edition*, 46(21), 3826-3848.
- Habibzadeh, S., Khodadadi, A. A., and Mortazavi, Y. (2010). "CO and ethanol dual selective sensor of Sm₂O₃-doped SnO₂ nanoparticles synthesized by microwave-induced combustion." *Sensors and Actuators B: Chemical*, 144(1), 131-138.
- Hackner, A., Habauzit, A., and Müller, G. (2010). "Resistive and surface ionisation response of SnO₂ gas sensing layers." *Sensors and Actuators B: Chemical*, 146(2), 433-439.
- Hafaiedh, I., Helali, S., Cherif, K., Abdelghani, A., and Tournier, G. (2008). "Characterization of tin dioxide film for chemical vapors sensor." *Materials Science and Engineering: C*, 28(5–6), 584-587.
- Hamrouni, A., Lachheb, H., and Houas, A. (2013). "Synthesis, characterization and photocatalytic activity of ZnO-SnO₂ nanocomposites." *Materials Science and Engineering: B*, 178(20), 1371-1379.
- Harbeck, S. (2005). *Characterisation and functionality of SnO₂ gas sensors using vibrational spectroscopy*, Doctoral Dissertation, Universität Tübingen, Tübingen.
- Hemmati, S., Anaraki Firooz, A., Khodadadi, A. A., and Mortazavi, Y. (2011). "Nanostructured SnO₂-ZnO sensors: Highly sensitive and selective to ethanol." *Sensors and Actuators B: Chemical*, 160(1), 1298-1303.
- Henrich, V. E., and Cox, P. A. (1993). "Fundamentals of gas-surface interactions on metal oxides." *Applied Surface Science*, 72(4), 277-284.
- Heo, Y. W., Tien, L. C., Norton, D. P., Kang, B. S., Ren, F., Gila, B. P., and Pearton, S. J. (2004). "Electrical transport properties of single ZnO nanorods." *Applied Physics Letters*, 85(11), 2002-2004.
- Hierlemann, A., and Baltes, H. (2006). "Semiconductor-Based Chemical Microsensors", in J. Korvink and O. Paul, (eds.), *MEMS: A Practical Guide to Design, Analysis, and Applications*. Springer Berlin Heidelberg, pp. 567-666.
- Hildenbrand, J. (2003). *Simulation and Characterisation of a Micromachined Gas Sensor and Preparation for Model Order Reduction*, Diploma Thesis, Albert Ludwig University, Freiburg, Germany.
- Ho, R. (2013). "Handbook of Univariate and Multivariate Data Analysis with IBM SPSS, Second Edition". Taylor and Francis: Hoboken.
- Höganäs, A. B. (2012). *Compacting of Metal Powders*. Höganäs AB, Sweden.

- Holmberg, M., Davide, F. A. M., Di Natale, C., D'Amico, A., Winquist, F., and Lundström, I. (1997). "Drift counteraction in odour recognition applications: lifelong calibration method." *Sensors and Actuators B: Chemical*, 42(3), 185-194.
- Hongsith, N., Wongrat, E., Kerdcharoen, T., and Choopun, S. (2010). "Sensor response formula for sensor based on ZnO nanostructures." *Sensors and Actuators B: Chemical*, 144(1), 67-72.
- Hosseini-Babaei, F., and Ghafarinia, V. (2010). "Compensation for the drift-like terms caused by environmental fluctuations in the responses of chemoresistive gas sensors." *Sensors and Actuators B: Chemical*, 143(2), 641-648.
- Hosseini-Babaei, F., and Orvatina, M. (2003). "Analysis of thickness dependence of the sensitivity in thin film resistive gas sensors." *Sensors and Actuators B: Chemical*, 89(3), 256-261.
- Hu, H., Trejo, M., Nicho, M. E., Saniger, J. M., and García-Valenzuela, A. (2002). "Adsorption kinetics of optochemical NH₃ gas sensing with semiconductor polyaniline films." *Sensors and Actuators B: Chemical*, 82(1), 14-23.
- Huang, H., Tan, O. K., Lee, Y. C., and Tse, M. S. (2006). "Preparation and characterization of nanocrystalline SnO₂ thin films by PECVD." *Journal of Crystal Growth*, 288(1), 70-74.
- Huang, J., Wu, Y., Gu, C., Zhai, M., Yu, K., Yang, M., and Liu, J. (2010). "Large-scale synthesis of flowerlike ZnO nanostructure by a simple chemical solution route and its gas-sensing property." *Sensors and Actuators B: Chemical*, 146(1), 206-212.
- Huang, M. H., Mao, S., Feick, H., Yan, H., Wu, Y., Kind, H., Weber, E., Russo, R., and Yang, P. (2001). "Room-Temperature Ultraviolet Nanowire Nanolasers." *Science*, 292(5523), 1897-1899.
- Hübner, M., Simion, C. E., Tomescu-Stănoiu, A., Pokhrel, S., Bârsan, N., and Weimar, U. (2011). "Influence of humidity on CO sensing with p-type CuO thick film gas sensors." *Sensors and Actuators B: Chemical*, 153(2), 347-353.
- Iglesias, Y., Peiteado, M., de Frutos, J., and Caballero, A. C. (2007). "Current–voltage characteristic behaviour of dense Zn₂SnO₄-ZnO ceramics." *Journal of the European Ceramic Society*, 27(13–15), 3931-3933.
- Iijima, S. (1991). "Helical microtubules of graphitic carbon." *Nature*, 354(6348), 56-58.
- IUPAC. (1997). *Compendium of Chemical Terminology (the "Gold Book")*, Oxford: Blackwell Scientific Publications.

- Iwuoha, E. I., Al-Ahmed, A., Sekota, M., Waryo, T., and Baker, P. (2007). "Amperometric Sensors", in J. L. Atwood and J. W. Steed, (eds.), *Encyclopedia of Supramolecular Chemistry*. Taylor & Francis, pp. 1-18.
- Jain, G. H., Patil, L. A., and Gaikwad, V. B. (2007). "Studies on gas sensing performance of (Ba_{0.8}Sr_{0.2})(Sn_{0.8}Ti_{0.2})O₃ thick film resistors." *Sensors and Actuators B: Chemical*, 122(2), 605-612.
- Jakšić, O. M., Jakšić, Z. S., Čupić, Ž. D., Randjelović, D. V., and Kolar-Anić, L. Z. (2014). "Fluctuations in transient response of adsorption-based plasmonic sensors." *Sensors and Actuators B: Chemical*, 190, 419-428.
- Janata, J. í. (2009). "Potentiometric Sensors", *Principles of Chemical Sensors*. pp. 119-199.
- Janotti, A., Varley, J. B., Lyons, J. L., and Walle, C. G. (2012). "Controlling the Conductivity in Oxide Semiconductors", in J. Wu, J. Cao, W.-Q. Han, A. Janotti, and H.-C. Kim, (eds.), *Functional Metal Oxide Nanostructures*. Springer New York, pp. 23-35.
- Jin, C., Hong, C., Park, S., and Lee, C. (2010). "Annealing behaviors of SnO₂-ZnO coaxial nanowires." *Thin Solid Films*, 519(4), 1351-1355.
- Jing, Z., and Zhan, J. (2008). "Fabrication and Gas-Sensing Properties of Porous ZnO Nanoplates." *Advanced Materials*, 20(23), 4547-4551.
- Jinkawa, T., Sakai, G., Tamaki, J., Miura, N., and Yamazoe, N. (2000). "Relationship between ethanol gas sensitivity and surface catalytic property of tin oxide sensors modified with acidic or basic oxides." *Journal of Molecular Catalysis A: Chemical*, 155(1-2), 193-200.
- Johnson, J. L., Behnam, A., An, Y., Pearton, S. J., and Ural, A. (2011). "Experimental study of graphitic nanoribbon films for ammonia sensing." *Journal of Applied Physics*, 109(12), -.
- Kalantar-zadeh, K., and Fry, B. (2008). "Characterization Techniques for Nanomaterials", *Nanotechnology-Enabled Sensors*. Springer US, pp. 211-281.
- Kale, G. M., Wang, L., Hayes, J. E., Congjin, J., and Hong, Y. R. (2003). "Solid-state sensors for in-line monitoring of NO₂ in automobile exhaust emission." *Journal of Materials Science*, 38(21), 4293-4300.
- Kamp, B., Merkle, R., Lauck, R., and Maier, J. (2005). "Chemical diffusion of oxygen in tin dioxide: Effects of dopants and oxygen partial pressure." *Journal of Solid State Chemistry*, 178(10), 3027-3039.
- Kamp, B., Merkle, R., and Maier, J. (2001). "Chemical diffusion of oxygen in tin dioxide." *Sensors and Actuators B: Chemical*, 77(1-2), 534-542.

- Kapustianyk, V., Turko, B., Kostruba, A., Sofiani, Z., Derkowska, B., Dabos-Seignon, S., Barwiński, B., Eliyashevskiy, Y., and Sahraoui, B. (2007). "Influence of size effect and sputtering conditions on the crystallinity and optical properties of ZnO thin films." *Optics Communications*, 269(2), 346-350.
- Karazhanov, S. Z., Ravindran, P., Grossner, U., Kjekshus, A., Fjellvåg, H., and Svensson, B. G. (2006a). "Strong Coulomb correlation effects in ZnO." *Solid State Communications*, 139(8), 391-396.
- Karazhanov, S. Z., Ravindran, P., Kjekshus, A., Fjellvåg, H., Grossner, U., and Svensson, B. G. (2006b). "Electronic structure and band parameters for Zn (X=O, S, Se, Te)." *Journal of Crystal Growth*, 287(1), 162-168.
- Karimi, M., Saydi, J., Mahmoodi, M., Seidi, J., Ezzati, M., Shamsi Anari, S., and Ghasemian, B. (2013). "A comparative study on ethanol gas sensing properties of ZnO and Zn_{0.94}Cd_{0.06}O nanoparticles." *Journal of Physics and Chemistry of Solids*, 74(10), 1392-1398.
- Kassier, G. H. (2006). *The characterization of bulk as-grown and annealed ZnO by Hall effect*, University of Pretoria, Pretoria, South Africa.
- Kazaryan, A., Wang, Y., and Patton, B. R. (1999). "Generalized phase field approach for computer simulation of sintering: incorporation of rigid-body motion." *Scripta Materialia*, 41(5), 487-492.
- Khranovskyy, V., Eriksson, J., Lloyd-Spetz, A., and Yakimova, R. "Oxygen absorption effect on the sensitivity and material stability of ZnO nanostructured films." *Presented at Sensors, 2008 IEEE*.
- Kim, H., Park, H.-H., Chang, H. J., Jeon, H., and Park, H.-H. (2008). "Carbon nanotube-incorporated direct-patternable SnO₂ thin films formed by photochemical metal-organic deposition." *Thin Solid Films*, 517(3), 1072-1076.
- Kim, I.-D., Rothschild, A., and Tuller, H. L. (2013). "Advances and new directions in gas-sensing devices." *Acta Materialia*, 61(3), 974-1000.
- Kim, K.-W., Cho, P.-S., Kim, S.-J., Lee, J.-H., Kang, C.-Y., Kim, J.-S., and Yoon, S.-J. (2007). "The selective detection of C₂H₅OH using SnO₂-ZnO thin film gas sensors prepared by combinatorial solution deposition." *Sensors and Actuators B: Chemical*, 123(1), 318-324.
- Kissine, V. V., Sysoev, V. V., and Voroshilov, S. A. (2001). "Conductivity of SnO₂ thin films in the presence of surface adsorbed species." *Sensors and Actuators B: Chemical*, 79(2-3), 163-170.
- Klein, A. (2013). "Transparent Conducting Oxides: Electronic Structure-Property Relationship from Photoelectron Spectroscopy with in situ Sample Preparation." *Journal of the American Ceramic Society*, 96(2), 331-345.

- Klein, A., Körber, C., Wachau, A., Säuberlich, F., Gassenbauer, Y., Schafranek, R., Harvey, S. P., and Mason, T. O. (2009). "Surface potentials of magnetron sputtered transparent conducting oxides." *Thin Solid Films*, 518(4), 1197-1203.
- Ko, H., Park, S., An, S., and Lee, C. (2013). "Enhanced ethanol sensing properties of TeO₂/In₂O₃ core-shell nanorod sensors." *Current Applied Physics*, 13(5), 919-924.
- Kohl, D., Heinert, L., Bock, J., Hofmann, T., and Schieberle, P. (2000). "Systematic studies on responses of metal-oxide sensor surfaces to straight chain alkanes, alcohols, aldehydes, ketones, acids and esters using the SOMMSA approach." *Sensors and Actuators B: Chemical*, 70(1-3), 43-50.
- Koinkar, P. M., Mahajan, J. R., Patil, P. P., and More, M. A. (2005). "Field emission characteristics of chemical vapor deposited diamond thin films with SnO₂ as overlayer on silicon." *Thin Solid Films*, 474(1-2), 275-278.
- Kolev, S. D., Ádám, M., Bársony, I., van den Berg, A., Cobianu, C., and Kulinyi, S. (1998). "Mathematical modelling of a porous silicon-based pellistor-type catalytic flammable gas sensor." *Microelectronics Journal*, 29(4-5), 235-239.
- Kolmakov, A., and Moskovits, M. (2004). "Chemical Sensing and Catalysis by One-Dimensional Metal-Oxide Nanostructures." *Annual Review of Materials Research*, 34(1), 151-180.
- Kong, X. Y., Ding, Y., Yang, R., and Wang, Z. L. (2004). "Single-Crystal Nanorings Formed by Epitaxial Self-Coiling of Polar Nanobelts." *Science*, 303(5662), 1348-1351.
- Kopparthy, V. L., Tangutooru, S. M., Nestorova, G. G., and Guilbeau, E. J. (2012). "Thermoelectric microfluidic sensor for bio-chemical applications." *Sensors and Actuators B: Chemical*, 166-167, 608-615.
- Körber, C., Ágoston, P., and Klein, A. (2009). "Surface and bulk properties of sputter deposited undoped and Sb-doped SnO₂ thin films." *Sensors and Actuators B: Chemical*, 139(2), 665-672.
- Korotcenkov, G. (2005). "Gas response control through structural and chemical modification of metal oxide films: state of the art and approaches." *Sensors and Actuators B: Chemical*, 107(1), 209-232.
- Korotcenkov, G. (2007). "Metal oxides for solid-state gas sensors: What determines our choice?" *Materials Science and Engineering: B*, 139(1), 1-23.
- Korotcenkov, G. (2008). "The role of morphology and crystallographic structure of metal oxides in response of conductometric-type gas sensors." *Materials Science and Engineering: R: Reports*, 61(1-6), 1-39.

- Korotcenkov, G. (2011). "Chemical Sensors : Comprehensive Sensor Technologies Volume 4: Solid State Devices". Momentum Press: New York.
- Korotcenkov, G. (2012). "Chemical Sensors : Simulation and Modeling Volume 3: Solid-State Devices". Momentum Press: New York.
- Korotcenkov, G., Han, S. D., Cho, B. K., and Brinzari, V. (2009). "Grain Size Effects in Sensor Response of Nanostructured SnO₂- and In₂O₃-Based Conductometric Thin Film Gas Sensor." *Critical Reviews in Solid State and Materials Sciences*, 34(1-2), 1-17.
- Krivetskiy, V. V., Rumyantseva, M. N., and Gaskov, A. M. (2013). "Chemical modification of nanocrystalline tin dioxide for selective gas sensors." *Russian Chemical Reviews*, 82(10), 917.
- Kuchibhatla, S. V. N. T., Karakoti, A. S., Bera, D., and Seal, S. (2007). "One dimensional nanostructured materials." *Progress in Materials Science*, 52(5), 699-913.
- Kumar, M., Kumar, A., and Abhyankar, A. C. (2014). "SnO₂ based sensors with improved sensitivity and response-recovery time." *Ceramics International*, 40(6), 8411-8418.
- Kustov, E. F., and Nefedov, V. I. (2008). "Nanostructures: Compositions, structure, and classification." *Russian Journal of Inorganic Chemistry*, 53(14), 2103-2170.
- Kwoka, M., Ottaviano, L., and Szuber, J. (2007). "AFM study of the surface morphology of L-CVD SnO₂ thin films." *Thin Solid Films*, 515(23), 8328-8331.
- Kykyneshi, R., Zeng, J., and Cann, D. (2011). "Transparent Conducting Oxides Based on Tin Oxide", in D. S. Ginley, (ed.), *Handbook of Transparent Conductors*. Springer US, pp. 171-191.
- Li, C. C., Du, Z. F., Li, L. M., Yu, H. C., Wan, Q., and Wang, T. H. (2007a). "Surface-depletion controlled gas sensing of ZnO nanorods grown at room temperature." *Applied Physics Letters*, 91(3), 032101.
- Li, G.-R., Lu, X.-H., Qu, D.-L., Yao, C.-Z., Zheng, F.-l., Bu, Q., Dawa, C.-R., and Tong, Y.-X. (2007b). "Electrochemical Growth and Control of ZnO Dendritic Structures." *The Journal of Physical Chemistry C*, 111(18), 6678-6683.
- Licznanski, B. (2004). "Thick-film gas microsensors based on tin dioxide." *Bulletin of the Polish Academy of Sciences: Technical Sciences*, 52(1), 37-42.
- Liewhiran, C., and Phanichphant, S. (2007). "Influence of Thickness on Ethanol Sensing Characteristics of Doctor-bladed Thick Film from Flame-made ZnO Nanoparticles." *Sensors*, 7(2), 185-201.

- Litton, C. W., Collins, T. C., Reynolds, D. C., Capper, P., Kasap, S., and Willoughby, A. (2011). "Zinc Oxide Materials for Electronic and Optoelectronic Device Applications". Wiley: Hoboken.
- Liu, D., Liu, M., Liu, G., Zhang, S., Wu, Y., and Zhang, X. (2009). "Dual-Channel Sensing of Volatile Organic Compounds with Semiconducting Nanoparticles." *Analytical Chemistry*, 82(1), 66-68.
- Liu, H., Ma, H., Zhou, W., Liu, W., Jie, Z., and Li, X. (2012). "Synthesis and gas sensing characteristic based on metal oxide modification multi wall carbon nanotube composites." *Applied Surface Science*, 258(6), 1991-1994.
- Liu, J., and Ning, W. (2009). "Influence of ZnO addition on the sintering properties of SnO₂ electrodes." *Journal of Materials Science*, 44(10), 2520-2524.
- Liu, R., Huang, Y., Xiao, A., and Liu, H. (2010). "Preparation and photocatalytic property of mesoporous ZnO/SnO₂ composite nanofibers." *Journal of Alloys and Compounds*, 503(1), 103-110.
- Lorenz, H., Friedrich, M., Armbrüster, M., Klötzer, B., and Penner, S. (2013). "ZnO is a CO₂-selective steam reforming catalyst." *Journal of Catalysis*, 297, 151-154.
- Lu, G., Xu, J., Sun, J., Yu, Y., Zhang, Y., and Liu, F. (2012). "UV-enhanced room temperature NO₂ sensor using ZnO nanorods modified with SnO₂ nanoparticles." *Sensors and Actuators B: Chemical*, 162(1), 82-88.
- Lu, X., Zhang, W., Wang, C., Wen, T.-C., and Wei, Y. (2010). "One-dimensional conducting polymer nanocomposites: Synthesis, properties and applications." *Progress in Polymer Science*, In Press, Corrected Proof.
- Lyashkov, A. Y., and Tonkoshkur, A. S. (2013). "Gas sensitivity of ZnO-based ceramics to vapors of saturated monohydric alcohols." *Materials Chemistry and Physics*, 140(1), 31-36.
- Ma, X., Song, H., and Guan, C. (2013a). "Enhanced ethanol sensing properties of ZnO-doped porous SnO₂ hollow nanospheres." *Sensors and Actuators B: Chemical*, 188, 193-199.
- Ma, Y., Qu, Y., and Zhou, W. (2013b). "Surface engineering of one-dimensional tin oxide nanostructures for chemical sensors." *Microchimica Acta*, 1-20.
- Madelung, O., Rössler, U., and Schulz, M. (1998). "Tin dioxide (SnO₂) transport properties", in O. Madelung, U. Rössler, and M. Schulz, (eds.), *Non-Tetrahedrally Bonded Elements and Binary Compounds I*. Springer Berlin Heidelberg, pp. 1-5.

- Maekawa, T., Suzuki, K., Takada, T., Kobayashi, T., and Egashira, M. (2001). "Odor identification using a SnO₂-based sensor array." *Sensors and Actuators B: Chemical*, 80(1), 51-58.
- Martinelli, E., Falconi, C., D'Amico, A., and Di Natale, C. (2003). "Feature Extraction of chemical sensors in phase space." *Sensors and Actuators B: Chemical*, 95(1-3), 132-139.
- Martins, R., Barquinha, P., Pimentel, A., Pereira, L., Fortunato, E., Kang, D., Song, I., Kim, C., Park, J., and Park, Y. (2008). "Electron transport in single and multicomponent n-type oxide semiconductors." *Thin Solid Films*, 516(7), 1322-1325.
- Martyniuk, M. (2006). *Low-temperature micro-opto-electro-mechanical technologies for temperature sensitive substrates*, PhD, University of Western Australia.
- Matsui, S. (2010). "Three-Dimensional Nanostructure Fabrication by Focused Ion Beam Chemical Vapor Deposition", in B. Bhushan, (ed.), *Springer Handbook of Nanotechnology*. Springer Berlin Heidelberg, pp. 211-229.
- Matsunaga, N., Sakai, G., Shimanoe, K., and Yamazoe, N. (2003). "Formulation of gas diffusion dynamics for thin film semiconductor gas sensor based on simple reaction-diffusion equation." *Sensors and Actuators B: Chemical*, 96(1-2), 226-233.
- Mattox, D. M. (2010). "Non-Elemental Characterization of Films and Coatings", in P. M. Martin, (ed.), *Handbook of Deposition Technologies for Films and Coatings (Third Edition)*. Boston: William Andrew Publishing, pp. 716-748.
- Mazloom, J., and Ghodsi, F. E. (2012). "Nanostructured Metal Oxide Gas Sensor: Response Mechanism and Modeling", *Nanoscience and Advancing Computational Methods in Chemistry: Research Progress*. IGI Global, pp. 180-221.
- McDonagh, C., Burke, C. S., and MacCraith, B. D. (2008). "Optical Chemical Sensors." *Chemical Reviews*, 108(2), 400-422.
- Mei, L., Deng, J., Yin, X., Zhang, M., Li, Q., Zhang, E., Xu, Z., Chen, L., and Wang, T. (2012). "Ultrasensitive ethanol sensor based on 3D aloe-like SnO₂." *Sensors and Actuators B: Chemical*, 166-167, 7-11.
- Michahelles, F., and Schiele, B. (2003). "Sensing Opportunities for Physical Interaction", A. Schmidt, (ed.) *Physical Interaction (PI03) Workshop on Real World User Interfaces, Fifth International Symposium on Human Computer Interaction (HCI) with Mobile Devices and Services*. September 8-11, Udine, Italy.
- Min, Y. (2003). *Properties and sensor performance of zinc oxide thin films*, 0805790, Massachusetts Institute of Technology, United States -- Massachusetts.

- Mishra, R. K., Pandey, S. K., and Sahay, P. P. (2013). "Influence of In doping on the structural, photo-luminescence and alcohol response characteristics of the SnO₂ nanoparticles." *Materials Research Bulletin*, 48(10), 4196-4205.
- Mishra, R. K., and Sahay, P. P. (2012). "Synthesis, characterization and alcohol sensing property of Zn-doped SnO₂ nanoparticles." *Ceramics International*, 38(3), 2295-2304.
- Mohammadi, A. S., Baizae, S. M., and Salehi, H. (2011). "Density Functional Approach to Study Electronic Structure of ZnO Single Crystal." *World Applied Sciences Journal* 14(10), 1530-1536.
- Mondal, B., Basumatari, B., Das, J., Roychaudhury, C., Saha, H., and Mukherjee, N. (2014). "ZnO–SnO₂ based composite type gas sensor for selective hydrogen sensing." *Sensors and Actuators B: Chemical*, 194, 389-396.
- Morin, S. A., Forticaux, A., Bierman, M. J., and Jin, S. (2011). "Screw Dislocation-Driven Growth of Two-Dimensional Nanoplates." *Nano Letters*, 11(10), 4449-4455.
- Moseley, P. T. (1997). "Solid state gas sensors." *Measurement Science and Technology*, 8(3), 223.
- Mukherjee, K., and Majumder, S. B. (2009). "Analyses of response and recovery kinetics of zinc ferrite as hydrogen gas sensor." *Journal of Applied Physics*, 106(6), 064912-10.
- Nakamura, C., Inuyama, Y., Shirai, K., Sugimoto, N., and Miyake, J. (2001). "Detection of porphyrin using a short peptide immobilized on a surface plasmon resonance sensor chip." *Biosensors and Bioelectronics*, 16(9–12), 1095-1100.
- Neri, G., Bonavita, A., Micali, G., Rizzo, G., Callone, E., and Carturan, G. (2008). "Resistive CO gas sensors based on In₂O₃ and InSnO_x nanopowders synthesized via starch-aided sol–gel process for automotive applications." *Sensors and Actuators B: Chemical*, 132(1), 224-233.
- Neri, G., Bonavita, A., Rizzo, G., Galvagno, S., Capone, S., and Siciliano, P. (2006). "Methanol gas-sensing properties of CeO₂–Fe₂O₃ thin films." *Sensors and Actuators B: Chemical*, 114(2), 687-695.
- Nikan, E., Khodadadi, A. A., and Mortazavi, Y. (2013). "Highly enhanced response and selectivity of electrospun ZnO-doped SnO₂ sensors to ethanol and CO in presence of CH₄." *Sensors and Actuators B: Chemical*, 184, 196-204.
- Oberhüttinger, C., Habauzit, A., Hackner, A., and Müller, G. (2011). "A rate equation approach towards surface ionisation gas detection." *Sensors and Actuators B: Chemical*, 160(1), 981-990.

- Oprea, A., Moretton, E., Barsan, N., Becker, W. J., Wollenstein, J., and Weimar, U. (2006). "Conduction model of SnO₂ thin films based on conductance and Hall effect measurements." *Journal of Applied Physics*, 100(3), 033716-10.
- Ozgur, U., Alivov, Y. I., Liu, C., Teke, A., Reshchikov, M. A., Dogan, S., Avrutin, V., Cho, S. J., and Morkoc, H. (2005). "A comprehensive review of ZnO materials and devices." *Journal of Applied Physics*, 98(4), 041301-103.
- Padilla, M., Perera, A., Montoliu, I., Chaudry, A., Persaud, K., and Marco, S. (2010). "Drift compensation of gas sensor array data by Orthogonal Signal Correction." *Chemometrics and Intelligent Laboratory Systems*, 100(1), 28-35.
- Palmer, G. B., and Poeppelmeier, K. R. (2002). "Phase relations, transparency and conductivity in Ga₂O₃-SnO₂-ZnO." *Solid State Sciences*, 4(3), 317-322.
- Pan, J., Shen, H., and Mathur, S. (2012). "One-Dimensional SnO₂ Nanostructures: Synthesis and Applications." *Journal of Nanotechnology*, 2012.
- Pan, X. Q., Fu, L., and Dominguez, J. E. (2001). "Structure-property relationship of nanocrystalline tin dioxide thin films grown on (1012) sapphire." *Journal of Applied Physics*, 89(11), 6056-6061.
- Panchapakesan, B. (2001). *Nanoparticle engineering and control of microhotplate gas sensor performance*, 3024959, University of Maryland College Park, United States -- Maryland.
- Panchapakesan, B., DeVoe, D. L., Widmaier, M. R., Cavicchi, R., and Semancik, S. (2001). "Nanoparticle engineering and control of tin oxide microstructures for chemical microsensor applications." *Nanotechnology*, 12(3), 336.
- Pardo, M., and Sberveglieri, G. (2007). "Comparing the performance of different features in sensor arrays." *Sensors and Actuators B: Chemical*, 123(1), 437-443.
- Park, H.-H., Park, H.-H., and Hill, R. H. (2006). "Direct-patterning of SnO₂ thin film by photochemical metal-organic deposition." *Sensors and Actuators A: Physical*, 132(2), 429-433.
- Park, J. (2010). *Nanostructured semiconducting metal oxides for use in gas sensors*, Ph.D., University of Wollongong, Wollongong, Australia.
- Park, K., Seong, J. K., Kwon, Y., Nahm, S., and Cho, W. S. (2008). "Influence of SnO₂ addition on the thermoelectric properties of Zn_{1-x}Sn_xO (0.01 ≤ x ≤ 0.05)." *Materials Research Bulletin*, 43(1), 54-61.
- Patel, H. (2014a). "Sensor", *The Electronic Nose: Artificial Olfaction Technology*. Springer India, pp. 27-66.

- Patel, H. (2014b). "Sensor Used in E-nose", *The Electronic Nose: Artificial Olfaction Technology*. Springer India, pp. 143-180.
- Patil, L. A., Shinde, M. D., Bari, A. R., and Deo, V. V. (2010). "Highly sensitive ethanol sensors based on nanocrystalline SnO₂ thin films." *Current Applied Physics*, 10(5), 1249-1254.
- Peiteado, M., Iglesias, Y., de Frutos, J., Fernández, J. F., and Caballero, A. C. (2006). "Preparation of ZnO-SnO₂ ceramic materials by a coprecipitation method." *Boletín de la Sociedad Española de Cerámica y Vidrio*, 45(3), 158-162.
- Pokropivny, V. V., and Skorokhod, V. V. (2007). "Classification of nanostructures by dimensionality and concept of surface forms engineering in nanomaterial science." *Materials Science and Engineering: C*, 27(5–8), 990-993.
- Ponzoni, A., Comini, E., Sberveglieri, G., Zhou, J., Deng, S. Z., Xu, N. S., Ding, Y., and Wang, Z. L. (2006). "Ultrasensitive and highly selective gas sensors using three-dimensional tungsten oxide nanowire networks." *Applied Physics Letters*, 88(20), 203101-3.
- Puzzovio, D. (2009). *Surface interaction mechanisms in metal-oxide semiconductors for alkane detection*, Ph.D., Università degli Studi di Ferrara, Ferrara, Italy.
- Rachut, K., Körber, C., Brötz, J., and Klein, A. (2014). "Growth and surface properties of epitaxial SnO₂." *physica status solidi (a)*, n/a-n/a.
- Ramírez, M. A., Rubio-Marcos, F., Fernández, J. F., Lengauer, M., Bueno, P. R., Longo, E., and Varela, J. A. (2008). "Mechanical Properties and Dimensional Effects of ZnO- and SnO₂-Based Varistors." *Journal of the American Ceramic Society*, 91(9), 3105-3108.
- Ravi, N. (2006). *Pulsed adsorption gas sensor system*, M.S., State University of New York at Buffalo, Ann Arbor.
- Raymo, F. M. (2010). "Nanomaterials Synthesis and Applications: Molecule-Based Devices", in B. Bhushan, (ed.), *Springer Handbook of Nanotechnology*. Springer Berlin Heidelberg, pp. 17-45.
- Rehrl, M. (2011). *Differential Equation Models for Surface Reactions of SnO₂ Nanowire Gas Sensors and their Inverse Modeling*, Diploma Thesis, University of Vienna, Vienna.
- Reichel, P. (2005). *Development of a chemical gas sensor system*, Doctoral Dissertation, Universität Tübingen, Tübingen.
- Ren, C.-Y., Chiou, S.-H., and Hsue, C.-S. (2004). "Ga-doping effects on electronic and structural properties of wurtzite ZnO." *Physica B: Condensed Matter*, 349(1–4), 136-142.

- Rickerby, D. G., and Serventi, A. M. (2010). "Nanostructured Metal Oxide Gas Sensors for Air-Quality Monitoring", in F. Maohong, H. Chin-Pao, E. B. Alan, W. Zhonglin, S. Rachid, C.-P. H. A. E. B. Z. W. R. S. Ian WrightA2 - Maohong Fan, and W. Ian, (eds.), *Environanotechnology*. Amsterdam: Elsevier, pp. 99-136.
- Romain, A. C., and Nicolas, J. (2010). "Long term stability of metal oxide-based gas sensors for e-nose environmental applications: An overview." *Sensors and Actuators B: Chemical*, 146(2), 502-506.
- Rothschild, A., and Komem, Y. (2003). "Numerical computation of chemisorption isotherms for device modeling of semiconductor gas sensors." *Sensors and Actuators B: Chemical*, 93(1-3), 362-369.
- Rothschild, A., and Komem, Y. (2004). "On the Relationship Between the Grain Size and Gas-Sensitivity of Chemo-Resistive Metal-Oxide Gas Sensors with Nanosized Grains." *Journal of Electroceramics*, 13(1-3), 697-701.
- Russell, R. M., Boehm, J. E., Carim, A. H., Merzbacher, C. I., Holdridge, G. M., and Teague, E. C. (2007). *National Nanotechnology Initiative Strategic Plan 2007*. National Science and Technology Council, USA.
- Sahay, P. P., and Nath, R. K. (2008). "Al-doped ZnO thin films as methanol sensors." *Sensors and Actuators B: Chemical*, 134(2), 654-659.
- Sahm, T., Gurlo, A., Bârsan, N., and Weimar, U. (2006). "Basics of oxygen and SnO₂ interaction; work function change and conductivity measurements." *Sensors and Actuators B: Chemical*, 118(1-2), 78-83.
- Sahner, K., and Tuller, H. (2010). "Novel deposition techniques for metal oxide: Prospects for gas sensing." *Journal of Electroceramics*, 24(3), 177-199.
- Sakai, G., Matsunaga, N., Shimano, K., and Yamazoe, N. (2001). "Theory of gas-diffusion controlled sensitivity for thin film semiconductor gas sensor." *Sensors and Actuators B: Chemical*, 80(2), 125-131.
- Santarossa, G., Hahn, K., and Baiker, A. (2013). "Free Energy and Electronic Properties of Water Adsorption on the SnO₂(110) Surface." *Langmuir*, 29(18), 5487-5499.
- Savitzky, A., and Golay, M. J. E. (1964). "Smoothing and Differentiation of Data by Simplified Least Squares Procedures." *Analytical Chemistry*, 36(8), 1627-1639.
- Schmid, W. (2004). *Consumption measurements on SnO₂ sensors in low and normal oxygen concentration*, Doctoral Dissertation, Universität Tübingen, Tübingen.

- Schmid, W., Bârsan, N., and Weimar, U. (2004). "Sensing of hydrocarbons and CO in low oxygen conditions with tin dioxide sensors: possible conversion paths." *Sensors and Actuators B: Chemical*, 103(1–2), 362-368.
- Schmidt-Mende, L., and MacManus-Driscoll, J. L. (2007). "ZnO – nanostructures, defects, and devices." *Materials Today*, 10(5), 40-48.
- Scott, R. W. J., Yang, S. M., Chabanis, G., Coombs, N., Williams, D. E., and Ozin, G. A. (2001). "Tin Dioxide Opals and Inverted Opals: Near-Ideal Microstructures for Gas Sensors." *Advanced Materials*, 13(19), 1468-1472.
- Sedlak, P., Sikula, J., Majzner, J., Vrnata, M., Fitl, P., Kopecky, D., Vyslouzil, F., and Handel, P. H. (2012). "Adsorption–desorption noise in QCM gas sensors." *Sensors and Actuators B: Chemical*, 166–167, 264-268.
- Semonin, O. E., Luther, J. M., and Beard, M. C. (2012). "Quantum dots for next-generation photovoltaics." *Materials Today*, 15(11), 508-515.
- Šetkus, A. (2012). "Numerical Simulation of Electrical Responses to Gases in Advanced Structures", G. Korotchenkov, (ed.) *Chemical Sensors: Simulation and Modeling. Volume 2: Conductometric-Type Sensors*. Momentum Press: New York, pp. 1-50.
- Shah, A. V., Vaněček, M., Meier, J., Meillaud, F., Guillet, J., Fischer, D., Droz, C., Niquille, X., Faÿ, S., Vallat-Sauvain, E., Terrazzoni-Daudrix, V., and Bailat, J. (2004). "Basic efficiency limits, recent experimental results and novel light-trapping schemes in a-Si:H, μ c-Si:H and 'micromorph tandem' solar cells." *Journal of Non-Crystalline Solids*, 338–340, 639-645.
- Shen, G., and Chen, D. (2009). "One-Dimensional Nanostructures and Devices of II–V Group Semiconductors." *Nanoscale Research Letters*, 4(8), 779-788.
- Shevchenko, V. Y., Samoilovich, M. I., Talis, A. L., and Madison, A. E. (2004). "Nanostructures with coherent boundaries and the local approach." *Glass Physics and Chemistry*, 30(6), 537-550.
- Sikula, J., Pavelka, J., Tacano, M., Hashiguchi, S., and Toita, M. (2005). "RTS in Quantum Dots and MOSFETs: Experimental Set-Up with Long-Time Stability and Magnetic Field Compensation", in J. Sikula and M. Levinshtein, (eds.), *Advanced Experimental Methods For Noise Research in Nanoscale Electronic Devices*. Springer Netherlands, pp. 227-236.
- Smulko, J. M., Ederth, J., Li, Y., Kish, L. B., Kennedy, M. K., and Kruis, F. E. (2005). "Gas sensing by thermoelectric voltage fluctuations in SnO₂ nanoparticle films." *Sensors and Actuators B: Chemical*, 106(2), 708-712.
- Solanki, P. R., Kaushik, A., Agrawal, V. V., and Malhotra, B. D. (2011). "Nanostructured metal oxide-based biosensors." *NPG Asia Materials*, 3, 17-24.

- Solovyov, L. A. (2013). "Diffraction analysis of mesostructured mesoporous materials." *Chemical Society Reviews*, 42(9), 3708-3720.
- Song, X., and Liu, L. (2009). "Characterization of electrospun ZnO–SnO₂ nanofibers for ethanol sensor." *Sensors and Actuators A: Physical*, 154(1), 175-179.
- Sree Harsha, K. S. (2006). "Structure and Properties of Films", *Principles of Vapor Deposition of Thin Films*. Oxford: Elsevier, pp. 961-1072.
- Stanca, S. E., Popescu, I. C., and Oniciu, L. (2003). "Biosensors for phenol derivatives using biochemical signal amplification." *Talanta*, 61(4), 501-507.
- Sun, S., Meng, G., Zhang, G., and Zhang, L. (2007). "Controlled Growth and Optical Properties of One-Dimensional ZnO Nanostructures on SnO₂ Nanobelts." *Crystal Growth & Design*, 7(10), 1988-1991.
- Sun, Y.-F., Liu, S.-B., Meng, F.-L., Liu, J.-Y., Jin, Z., Kong, L.-T., and Liu, J.-H. (2012). "Metal Oxide Nanostructures and Their Gas Sensing Properties: A Review." *Sensors*, 12(3), 2610-2631.
- Swartz, C. H. (2012). "Transport and surface conductivity in ZnO." *Journal of Materials Research*, 27(17), 2205-2213.
- Tang, W., Wang, J., Yao, P., and Li, X. (2014). "Hollow hierarchical SnO₂-ZnO composite nanofibers with heterostructure based on electrospinning method for detecting methanol." *Sensors and Actuators B: Chemical*, 192, 543-549.
- Tang, Y. (2004). *Synthesis and characterization of tin oxide for thin film gas sensor applications*, Ph.D., Case Western Reserve University, United States -- Ohio.
- Tennakone, K., and Bandara, J. (2001). "Photocatalytic activity of dye-sensitized tin(IV) oxide nanocrystalline particles attached to zinc oxide particles: long distance electron transfer via ballistic transport of electrons across nanocrystallites." *Applied Catalysis A: General*, 208(1-2), 335-341.
- Thanh Le, D. T., Trung, D. D., Chinh, N. D., Thanh Binh, B. T., Hong, H. S., Van Duy, N., Hoa, N. D., and Van Hieu, N. (2013). "Facile synthesis of SnO₂-ZnO core-shell nanowires for enhanced ethanol-sensing performance." *Current Applied Physics*, 13(8), 1637-1642.
- Thornton, E. W., and Harrison, P. G. (1975a). "Tin oxide surfaces. Part 1.-Surface hydroxyl groups and the chemisorption of carbon dioxide and carbon monoxide on tin(IV) oxide." *Journal of the Chemical Society, Faraday Transactions 1: Physical Chemistry in Condensed Phases*, 71, 461-472.
- Thornton, E. W., and Harrison, P. G. (1975b). "Tin oxide surfaces. Part 3.-Infrared study of the adsorption of some small organic molecules on tin(IV) oxide." *Journal of the Chemical Society, Faraday Transactions 1: Physical Chemistry in Condensed Phases*, 71, 2468-2477.

- Tian, S., Gao, Y., Zeng, D., and Xie, C. (2012). "Effect of Zinc Doping on Microstructures and Gas-Sensing Properties of SnO₂ Nanocrystals." *Journal of the American Ceramic Society*, 95(1), 436-442.
- Tianshu, Z., Hing, P., Jiancheng, Z., and Lingbing, K. (1999). "Ethanol-sensing characteristics of cadmium ferrite prepared by chemical coprecipitation." *Materials Chemistry and Physics*, 61(3), 192-198.
- Tiwari, J. N., Tiwari, R. N., and Kim, K. S. (2012). "Zero-dimensional, one-dimensional, two-dimensional and three-dimensional nanostructured materials for advanced electrochemical energy devices." *Progress in Materials Science*, 57(4), 724-803.
- Tosun, B. S., Feist, R. K., Gunawan, A., Mkhoyan, K. A., Campbell, S. A., and Aydil, E. S. (2012). "Sputter deposition of semicrystalline tin dioxide films." *Thin Solid Films*, 520(7), 2554-2561.
- Tricoli, A., Righettoni, M., and Pratsinis, S. E. (2009). "Minimal cross-sensitivity to humidity during ethanol detection by SnO₂-TiO₂ solid solutions." *Nanotechnology*, 20(31), 315502.
- Tricoli, A., Righettoni, M., and Teleki, A. (2010). "Semiconductor Gas Sensors: Dry Synthesis and Application." *Angewandte Chemie International Edition*, 49(42), 7632-7659.
- Tsuda, N., Nasu, K., Fujimori, A., and Siratori, K. (2000). "Representative Conducting Oxides", in N. Tsuda, K. Nasu, A. Yanase, and K. Siratori, (eds.), *Electronic Conduction in Oxides*. Springer Berlin Heidelberg, pp. 157-319.
- Tu, Y.-F., Fu, Q.-M., Sang, J.-P., Tan, Z.-J., and Zou, X.-W. (2012). "Effects of annealing temperature on the properties of ZnO/SnO₂ core/shell nanorod arrays." *Materials Letters*, 86, 80-83.
- Tvrdikova, J., Danhel, A., Barek, J., and Vyskocil, V. (2012). "Voltammetric and amperometric determination of selected dinitronaphthalenes using single crystal silver amalgam based sensors." *Electrochimica Acta*, 73, 23-30.
- Uddin, M. T., Nicolas, Y., Olivier, C., Toupance, T., Servant, L., Müller, M. M., Kleebe, H.-J., Ziegler, J., and Jaegermann, W. (2012). "Nanostructured SnO₂-ZnO Heterojunction Photocatalysts Showing Enhanced Photocatalytic Activity for the Degradation of Organic Dyes." *Inorganic Chemistry*, 51(14), 7764-7773.
- Urschey, J., Kühnle, A., and Maier, W. F. (2003). "Combinatorial and conventional development of novel dehydrogenation catalysts." *Applied Catalysis A: General*, 252(1), 91-106.

- Vaezi, M. R. (2008). "SnO₂/ZnO double-layer thin films: A novel economical preparation and investigation of sensitivity and stability of double-layer gas sensors." *Materials Chemistry and Physics*, 110(1), 89-94.
- Vaezi, M. R. (2011). "Coupled Semiconductor Metal Oxide Nanocomposites: Types, Synthesis Conditions and Properties", in B. Attaf, (ed.), *Advances in Composite Materials for Medicine and Nanotechnology*. Rijeka, Croatia: InTech, pp. 365-400.
- Vander Wal, R. L., Hunter, G. W., Xu, J. C., Kulis, M. J., Berger, G. M., and Ticich, T. M. (2009). "Metal-oxide nanostructure and gas-sensing performance." *Sensors and Actuators B: Chemical*, 138(1), 113-119.
- Velasco-Vélez, J.-J. (2012). "Co-Adsorption Processes and Quantum Mechanical Modeling of Gas-Sensing Effects", in G. Korotchenkov, (ed.), *Chemical Sensors: Simulation and Modeling. Volume 2: Conductometric-Type Sensors*. [New York, N.Y.] (222 East 46th Street, New York): Momentum Press, pp. 51-96.
- Velasco-Velez, J. J., Chaiboun, A., Wilbertz, C., Scheinert, S., and Doll, T. (2008). "Drift Modeling of Electrically Controlled Nanoscale Metal-Oxide Gas Sensors." *Electron Device Letters, IEEE*, 29(7), 677-680.
- Vergara, A., Llobet, E., Martinelli, E., Di Natale, C., D'Amico, A., and Correig, X. (2007). "Feature extraction of metal oxide gas sensors using dynamic moments." *Sensors and Actuators B: Chemical*, 122(1), 219-226.
- Vrňata, M., Myslík, V., Vysloužil, F., Jelínek, M., Lančok, J., and Zemek, J. (2000). "The response of tin acetylacetonate and tin dioxide-based gas sensors to hydrogen and alcohol vapours." *Sensors and Actuators B: Chemical*, 71(1-2), 24-30.
- Wagh, M. S., Patil, L. A., Seth, T., and Amalnerkar, D. P. (2004). "Surface cupricated SnO₂-ZnO thick films as a H₂S gas sensor." *Materials Chemistry and Physics*, 84(2-3), 228-233.
- Wang, C., Yin, L., Zhang, L., Xiang, D., and Gao, R. (2010). "Metal Oxide Gas Sensors: Sensitivity and Influencing Factors." *Sensors*, 10(3), 2088-2106.
- Wang, X., Song, J., and Wang, Z. L. (2007). "Nanowire and nanobelt arrays of zinc oxide from synthesis to properties and to novel devices." *Journal of Materials Chemistry*, 17(8), 711-720.
- Wang, Y., Liu, Y., Ciobanu, C., and Patton, B. R. (2000). "Simulating Microstructural Evolution and Electrical Transport in Ceramic Gas Sensors." *Journal of the American Ceramic Society*, 83(9), 2219-2226.

- Wang, Z. L. (2003). "Nanobelts, Nanowires, and Nanodiskettes of Semiconducting Oxides—From Materials to Nanodevices." *Advanced Materials*, 15(5), 432-436.
- Wang, Z. L. (2004). "Zinc oxide nanostructures: growth, properties and applications." *Journal of Physics: Condensed Matter*, 16(25), R829.
- WebElements™. (2013). "Tin Dioxide" *WebElements: The periodic table on the web*. WebElement Nexus.
- Weimann, T., Hinze, P., Schlenker, E., Bakin, A., Mofor, A. C., Behrends, A., and Waag, A. (2008). "Electrical and structural characterisation of single ZnO nanorods." *Microelectronic Engineering*, 85(5–6), 1248-1252.
- Weimar, U., and Barsan, N. (2009). "n and p-type Semiconducting Metal Oxides Based Gas Sensors; Influence of Conduction Type on Sensitivity" *215th ECS Meeting, The Electrochemical Society Meeting Abstracts, May 24 - May 29*. San Francisco, CA, USA, pp. 1553.
- White, M. E., Bierwagen, O., Tsai, M. Y., and Speck, J. S. (2009). "Electron transport properties of antimony doped SnO₂ single crystalline thin films grown by plasma-assisted molecular beam epitaxy." *Journal of Applied Physics*, 106(9), 093704-093710.
- White, R. M. (1987). "A Sensor Classification Scheme." *Ultrasonics, Ferroelectrics and Frequency Control, IEEE Transactions on*, 34(2), 124-126.
- Winquist, F. (2008). "Voltammetric electronic tongues – basic principles and applications." *Microchimica Acta*, 163(1), 3-10.
- Wolf, D. E., Brendel, L., Fendrich, M., and Zinetullin, R. (2012). "Nanopowder Sintering", in A. Lorke, M. Winterer, R. Schmechel, and C. Schulz, (eds.), *Nanoparticles from the Gasphase*. Springer Berlin Heidelberg, pp. 161-183.
- Wongrat, E., Hongstith, N., Wongratanaphisan, D., Gardchareon, A., and Choopun, S. (2012). "Control of depletion layer width via amount of AuNPs for sensor response enhancement in ZnO nanostructure sensor." *Sensors and Actuators B: Chemical*, 171–172, 230-237.
- Wongrat, E., Pimpang, P., and Choopun, S. (2009). "Comparative study of ethanol sensor based on gold nanoparticles: ZnO nanostructure and gold: ZnO nanostructure." *Applied Surface Science*, 256(4), 968-971.
- Wu, F., Fang, L., Pan, Y. J., Zhou, K., Ruan, H. B., Liu, G. B., and Kong, C. Y. (2011). "Effect of annealing treatment on structural, electrical, and optical properties of Ga-doped ZnO thin films deposited by RF magnetron sputtering." *Thin Solid Films*, 520(2), 703-707.

- Xu, K., Zeng, D., Tian, S., Zhang, S., and Xie, C. (2014). "Hierarchical porous SnO₂ micro-rods topologically transferred from tin oxalate for fast response sensors to trace formaldehyde." *Sensors and Actuators B: Chemical*, 190, 585-592.
- Xu, Y., Zhou, X., and Toft Sørensen, O. (2000). "Oxygen sensors based on semiconducting metal oxides: An overview." *Sensors and Actuators, B: Chemical*, 65(1), 2-4.
- Yadav, B. C., Srivastava, R., Dwivedi, C. D., and Pramanik, P. (2008). "Moisture sensor based on ZnO nanomaterial synthesized through oxalate route." *Sensors and Actuators B: Chemical*, 131(1), 216-222.
- Yadava, L., Verma, R., and Dwivedi, R. (2010). "Sensing properties of CdS-doped tin oxide thick film gas sensor." *Sensors and Actuators B: Chemical*, 144(1), 37-42.
- Yadava, R. D. S., and Verma, V. K. (2014). "A diffusion limited sorption–desorption noise model for polymer coated SAW chemical sensors." *Sensors and Actuators B: Chemical*, 195, 590-602.
- Yamazoe, N., Fuchigami, J., Kishikawa, M., and Seiyama, T. (1979). "Interactions of tin oxide surface with O₂, H₂O and H₂." *Surface Science*, 86, 335-344.
- Yamazoe, N., Sakai, G., and Shimanoe, K. (2003). "Oxide Semiconductor Gas Sensors." *Catalysis Surveys from Asia*, 7(1), 63-75.
- Yang, D. (2011). "Nanocomposite Films for Gas Sensing", in B. Reddy, (ed.), *Advances in Nanocomposites - Synthesis, Characterization and Industrial Applications*. Rijeka, Croatia: InTech, pp. 857-882.
- Yang, H. G., and Zeng, H. C. (2004). "Self-Construction of Hollow SnO₂ Octahedra Based on Two-Dimensional Aggregation of Nanocrystallites." *Angewandte Chemie*, 116(44), 6056-6059.
- Yang, L., Zhang, S., Li, H., Zhang, G., Zhan, C., and Xie, C. (2013). "Conduction model of coupled domination by bias and neck for porous films as gas sensor." *Sensors and Actuators B: Chemical*, 176, 217-224.
- Yang, P., and Kim, F. (2002). "Langmuir–Blodgett Assembly of One-Dimensional Nanostructures." *ChemPhysChem*, 3(6), 503-506.
- Yang, T., Zhang, Y., and Li, C. (2014). "Large scale production of spherical WO₃ powder with ultrasonic spray pyrolysis assisted by sol–gel method for hydrogen detection." *Ceramics International*, 40(1, Part B), 1765-1769.
- Yang, Z., Huang, Y., Chen, G., Guo, Z., Cheng, S., and Huang, S. (2009). "Ethanol gas sensor based on Al-doped ZnO nanomaterial with many gas diffusing channels." *Sensors and Actuators B: Chemical*, 140(2), 549-556.

- Yao, M., Hu, P., Cao, Y., Xiang, W., Zhang, X., Yuan, F., and Chen, Y. (2013). "Morphology-controlled ZnO spherical nanobelt-flower arrays and their sensing properties." *Sensors and Actuators B: Chemical*, 177, 562-569.
- Yıldırım, M. A., Akaltun, Y., and Ateş, A. (2012). "Characteristics of SnO₂ thin films prepared by SILAR." *Solid State Sciences*, 14(9), 1282-1288.
- Yoon, J.-W., Choi, J.-K., and Lee, J.-H. (2012). "Design of a highly sensitive and selective C₂H₅OH sensor using p-type Co₃O₄ nanofibers." *Sensors and Actuators B: Chemical*, 161(1), 570-577.
- Yoon, J. H., Lee, H. J., and Kim, J. S. (2010). "Formaldehyde gas-sensing characteristics of SnO₂-ZnO materials." *Journal of Korean Institute of Metals and Materials*, 48(2), 169-174.
- Young, D. L., Coutts, T. J., Kaydanov, V. I., and Mulligan, W. P. "Direct measurement of density-of-states effective mass and scattering parameter in transparent conducting oxides using second-order transport phenomena." *Presented at American Vacuum Society (AVS) 46th International Symposium*, 25-29 October, Washington State Convention Center, Seattle, WA., USA.
- Young, D. L., Williamson, D. L., and Coutts, T. J. (2002). "Structural characterization of zinc stannate thin films." *Journal of Applied Physics*, 91(3), 1464-1471.
- Youssef, S., Combette, P., Podlecki, J., Asmar, R. A., and Foucaran, A. (2008). "Structural and Optical Characterization of ZnO Thin Films Deposited by Reactive rf Magnetron Sputtering." *Crystal Growth & Design*, 9(2), 1088-1094.
- Yu, J. H., and Choi, G. M. (1998). "Electrical and CO gas sensing properties of ZnO–SnO₂ composites." *Sensors and Actuators B: Chemical*, 52(3), 251-256.
- Yu, P., and Cardona, M. (2005). "Electronic Band Structures", *Fundamentals of Semiconductors: Physics and Materials Properties*. Springer Berlin Heidelberg, pp. 17-105.
- Zabels, R., Muktepavela, F., Grigorjeva, L., Tamanis, E., and Mishels-Piesins, M. (2010). "Nanoindentation and photoluminescence characterization of ZnO thin films and single crystals." *Optical Materials*, 32(8), 818-822.
- Zeng, W., Liu, T.-m., and Lin, L.-y. (2012). "Ethanol gas sensing property and mechanism of ZnSnO₃ doped with Ti ions." *Materials Science in Semiconductor Processing*, 15(3), 319-325.
- Zhang, B. P., Wakatsuki, K., Binh, N. T., Segawa, Y., and Usami, N. (2004a). "Low-temperature growth of ZnO nanostructure networks." *Journal of Applied Physics*, 96(1), 340-343.

- Zhang, D. H., and Ma, H. L. (1996). "Scattering mechanisms of charge carriers in transparent conducting oxide films." *Applied Physics A: Materials Science & Processing*, 62(5), 487.
- Zhang, G., and Liu, M. (2000). "Effect of particle size and dopant on properties of SnO₂-based gas sensors." *Sensors and Actuators B: Chemical*, 69(1–2), 144–152.
- Zhang, M., An, T., Hu, X., Wang, C., Sheng, G., and Fu, J. (2004b). "Preparation and photocatalytic properties of a nanometer ZnO–SnO₂ coupled oxide." *Applied Catalysis A: General*, 260(2), 215–222.
- Zhang, W.-H., and Zhang, W.-D. (2008). "Fabrication of SnO₂-ZnO nanocomposite sensor for selective sensing of trimethylamine and the freshness of fishes." *Sensors and Actuators B: Chemical*, 134(2), 403–408.
- Zhang, Y., and Mo, J. (2009). "Real-Time Monitoring of Indoor Organic Compounds", *Organic Indoor Air Pollutants*. Wiley-VCH Verlag GmbH & Co. KGaA, pp. 65–99.
- Zhao, H., Su, X., Xiao, F., Wang, J., and Jian, J. (2011). "Synthesis and gas sensor properties of flower-like 3D ZnO microstructures." *Materials Science and Engineering: B*, 176(7), 611–615.
- Zheng, L., Chen, C., Zheng, Y., Zhan, Y., Cao, Y., Lin, X., Zheng, Q., Wei, K., and Zhu, J. (2014). "Photocatalytic activity of ZnO/Sn_{1-x}Zn_xO_{2-x} nanocatalysts: A synergistic effect of doping and heterojunction." *Applied Catalysis B: Environmental*, 148–149, 44–50.
- Zheng, L., Zheng, Y., Chen, C., Zhan, Y., Lin, X., Zheng, Q., and Wei, K. (2012). "Facile One-Pot Synthesis of ZnO/SnO₂ Heterojunction Photocatalysts with Excellent Photocatalytic Activity and Photostability." *ChemPlusChem*, 77(3), 217–223.
- Zhu, M. W., Huang, N., Gong, J., Zhang, B., Wang, Z. J., Sun, C., and Jiang, X. (2011). "Growth of ZnO nanorod arrays by sol–gel method: transition from two-dimensional film to one-dimensional nanostructure." *Applied Physics A*, 103(1), 159–166.
- Zook, J. D., and Schroeder, N. (2006). "Sensors as Information Transducers ", in C. A. Grimes, E. C. Dickey, and M. V. Pishko, (eds.), *Encyclopedia of Sensors*. Stevenson Ranch, California: American Scientific Publisher, pp. 329–359.
- Zumbühl, D. (2007). *Semiconductor Surfaces and Interfaces*. Basel University, Department of Physics, Quantum Coherence Lab - Zumbühl Group.

Appendix A

Gas Sensor Signal Pre-Processing and Processing

A.1 Data Description and Sensor Response Normalisation

The basic architecture of a data processing system can be represented in an array of sensors. In this research, there is an array of five discrete sensors, where each sensor i produces a time-dependent output signal $X_{ij}(t)$ in response to an analyte j . The electrical sensor signal (e.g. resistance) depends on several physical parameters (e.g. target gas concentration and operating temperature), but the sensor outputs are expected to reach constant asymptotic values when presented with a constant input stimulus.

Since each sensor was tested independent of the others and with one target gas at a time, $X_{ij}(t)$ can be simply equated to time-independent parameter, sensor resistance, $R_g(t)$. One common practice is use only the static or steady-state values of the sensor signals, where the response is then simply a time-independent parameter, $R_g(t) \rightarrow \max[R_g(t)]$. But it is preferable to use dynamic or transient responses, and represent the response as time-independent, $R_g(t)$ because of the ease of visualising the response behaviour of the sensor signals during the sensing process.

In this study, to extract relevant key features from the data in terms of the static change of the sensor parameter (e.g. resistance), a fractional difference model was used to normalise the sensor response, determine the sensitivity of the target gas by the sensor ([Ahlers et al. 2005](#)):

$$S (\%) = \left(\frac{R_a - R_g}{R_g} \right) \times 100 \quad (\text{A.1})$$

where R_a is the sensor resistance in synthetic air, and R_g is the sensor resistance in the presence of the test gas.

A.2 Digital Signal Processing and Pattern Recognition

In order to improve the interpretability of the sensitivity and selectivity behaviour of an array of sensors, pattern recognition techniques have become a critical component of signal processing in the successful implementation of chemical sensor arrays and electronic noses ([Shaffer et al. 1999](#)). This involves coupling an array of sensors with pattern recognition algorithms to interpret the complex sensor signals and provide automated decision-making capabilities (i.e. presence or absence, of the targeted analyte).

The signal processing of gas sensor data can be categorized into a number of steps ([Gutierrez-Osuna 2002](#)): (1) pre-processing, for further processing of sensor signal (e.g., drift compensation, concentration normalization); (2) dimensionality reduction (of the input signal to avoid problems associated with high dimensionality data); (3) prediction (of the interesting properties of the sample, e.g., class membership, related odour samples); and (4) validation, where model and parameter settings are selected in order to optimize a criterion function (e.g., classification rate, mean-squared error). Pre-processing can further be divided into baseline manipulation, compression, and normalization ([Gutierrez-Osuna et al. 2004](#); [Jurs et al. 2000](#)). A summary of statistical and optimisation methods can be broadly classified into three categories: dimensionality reduction, classifiers, and clustering methods.

A.2.1 Sensor Signal Data Pre-processing

Usually, the raw signals acquired as sensor response is contaminated by noise (and outliers). At various stages of gas sensor measurement process, the sources of noise include the quantity under measurement itself, the sensors, the analogue processing system, the data acquisition stage and the digital signal processing system ([Gutierrez-Osuna et al. 2004](#)). Clearly, noise in the early measurement stages is most harmful as it propagates and can be potentially amplified through the subsequent stages in the signal pathway. Several forms of noise are irreducible; such sources as thermal and

shot noise are inherent to the underlying physics of the sensors or electronic components.

The typical raw digital signal observed in our results is represented in Figure A-1. Therefore, with signal acquired in its noisy forms, data pre-processing must be implemented in order to extract a desired digital signal before further analysis. Signal pre-processing, the first computational stage in data analysis, is aimed to extract relevant information from the sensor responses and prepare the data for multivariate pattern analysis and decision making. This could involve application of low-pass filter to prevent aliasing (i.e., signal distortion) in subsequent processing steps.

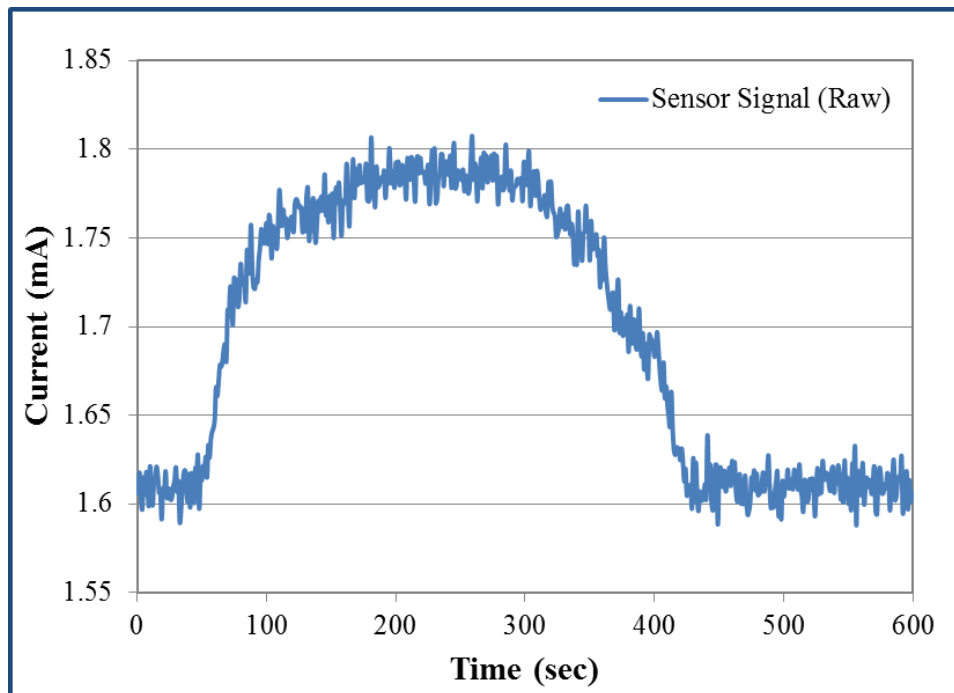


Figure A-1: Typical sensor digital signal.

Generally, the observed signal can be represented as p -dimensional model of the form ([Aminghafari et al. 2006](#); [Yang and Ren 2011](#)):

$$Y(t) = f(t) + \varepsilon(t); t = 1, \dots, n \quad (\text{A.2})$$

where $Y(t)$, $f(t)$, $\varepsilon(t)$ are of 1 by p . $f(t)$ is the deterministic signal to be recovered, $\varepsilon(t)$ is a spatially correlated noise of unknown covariance matrix \sum_{ε} . This kind of model is well suited for situations for which such additive, spatially correlated noise is realistic ([MathWorks 2014](#)). For $1 \leq i \leq p$, each component of $Y(t)$ is of the following form:

$$Y^i(t) = f^i(t) + \varepsilon^i(t); t = 1, \dots, n \quad (\text{A.3})$$

the covariance matrix \sum_{ε} , supposed to be positive definite, captures the stochastic link between the components of $Y(t)$ and models the spatial correlation.

The process of signal pre-processing facilitates noise elimination, data smoothing/filtering and signal enhancement, with the sole aim of increasing the signal-to-noise ratio without greatly distorting the signal. The choice of signal pre-processing is very vital, and has a significant impact on the results and performance of the pattern analysis system.

In the selection of appropriate pre-processing algorithm, three principles must be considered ([Johnson et al. 2003](#)):

- (1) The algorithm must preserve the chemical selectivity differences between different profiles and limit run-to-run retention/migration time shift.
- (2) The algorithm must be fast and less memory-demanding to deal with large number of data sets in a short period of time.
- (3) The resulting precision of retention/migration time estimation should be significantly improved in comparison with that initially provided by the instrumentation.

Wavelet transforms appear to meet all these requirements. Wavelets are a family of basis functions, well-localized in both the time and frequency domains ([Perrin et al. 2001](#)). They have a compact support (i.e., they differ from zero only in a limited time domain); and easily represent the different features of a signal, especially sharp signals and discontinuities. Wavelet transforms in processing analytical signals have advantages such as simple procedure, short operation time, little memory, high precision, and good reproducibility ([Bao et al. 1997](#)). Examples of wavelet transforms for denoising signals include Savitzky–Golay filtering (SGF), fast Fourier transform (FFT), multivariate wavelet denoising (MWD), discrete wavelet transform (DWT), and continuous wavelet transform (CWT). Details of their algorithms are presented by ([Orfanidis 1996](#); [Press et al. 2007](#)). Some of the methods are summarised here before the actual implementation.

A.2.2 Moving Average Filtering

A moving average filter, equivalent to low-pass filtering, smooths data by replacing each data point with the average of the neighbouring data points defined within the span ([MathWorks 2014](#)). This process is described by the difference equation:

$$y_s(i) = \frac{1}{2N + 1} (y(i + N - 1) + \dots + y(i - N)) \quad (\text{A.4})$$

where $y_s(i)$ is the smoothed value for the i th data point, N is the number of neighbouring data points on either side of $y_s(i)$, and $2N+1$ is the span.

A.2.3 Local Regression: Lowess and Loess

Local regression uses locally weighted linear least squares to smooth data, and are termed locally weighted scatter plot smooth. The local regression first and second degree polynomial models are lowess and loess, respectively. The robust local regression method (rlowess and rloess) assign lower weight to outliers in the regression, and assign zero weight to data outside six mean absolute deviations.

Like the moving average method, the lowess and loess smoothed value is determined by neighbouring data points defined within the span ([MathWorks 2014](#)). The process is weighted because a regression weight function is defined for the data points contained within the span. In addition to the regression weight function, a robust weight function can be used; this makes the process resistant to outliers. The methods are differentiated by the model used in the regression: lowess uses a linear polynomial, while loess uses a quadratic polynomial.

A.2.4 Savitzky–Golay Smoothing Filter

The Savitzky-Golay (SG) smoothing filter is based on local least-squares polynomial approximation ([Savitzky and Golay 1964](#)). It is a generalization of the finite-impulse response (FIR) or moving average filter with filter coefficients determined by an unweighted linear least-squares regression and a polynomial model of specified degree. The process, equivalent to discrete convolution with a fixed impulse response, involves fitting a polynomial to a set of input data and evaluating the resulting polynomial at a single point within the approximation interval. The Savitzky-Golay

smoothing procedure consists of replacing the central point of a window (containing an odd number of points, $2M + 1$) by the value obtained from the polynomial fit. The window is moved one data point until the whole signal is scanned; thus, creating a new, smoothed value for each data point. The smoothed signal is calculated by convolving the signal $f(t)$ with a smoothing (or convolution) function $h(t)$ ([Perrin et al. 2001](#)):

$$g(t) = f(t) * h(t) = \frac{\sum f(m)h(m - t)}{\sum h(m)} \quad (\text{A.5})$$

for all m for which $f(m)$ is defined and $h(m - t) \neq 0$. The convolution functions $h(t)$ is defined for each combination of degree of the polynomial and window size.

A typical digital filter can be applied to a series of equally spaced data values $f_i \equiv f(t_i)$, where $t_i \equiv t_0 + i\Delta$ for some constant sample spacing Δ and $i = \dots -2, -1, 0, 1, 2, \dots$. The SG smoothing operations consist of replacement of each data f_i by a linear combination g_i of itself and some number of nearby neighbours ([Press et al. 2007](#)):

$$g_i = \sum_{n=-nL}^{nR} c_n f_{i+n} \quad (\text{A.6})$$

where nL is the number of points used “to the left” of a data point i , i.e., earlier than it, while nR is the number used to the right, i.e., later than it. The coefficients c_n are called weights of the linear combination. A causal filter would have $nR = 0$ ([Press et al. 2007](#)). For the simplest possible averaging smoothing filter (like the moving average window), the smoothed point is the average of an odd number of neighbouring data points. This moving window average is computed as g_i , i.e., as the average of the data points from f_{i-nL} to f_{i+nR} , for some fixed $nL = nR = M$; and the weights $c_n = 1/(nL + nR + 1)$ ([Zuppa et al. 2004](#)):

$$g_i = \sum_{n=-M}^M \frac{f_{i+n}}{2M + 1} \quad (\text{A.7})$$

The weights c_n are chosen in such a way that the smoothed data point g_i is the value of a polynomial fitted by least-squares to all $(nL + nR + 1)$ points in the moving window. That is, for the group of $2M+1$ data centred at $n = 0$, the coefficient of the polynomial is obtained as ([Schafer 2011](#); [Thornley 2007](#)):

$$c_n = p(n) = \sum_{k=0}^N a_k n^k \quad (\text{A.8})$$

This minimises the mean-squared approximation error for the group of input samples centred on $n = 0$:

$$\varepsilon_N = \sum_{n=-M}^M (p(n) - x[n])^2 = \sum_{n=-M}^M \left(\sum_{k=0}^N a_k n^k - x[n] \right)^2 \quad (\text{A.9})$$

Therefore, the smoothed data point g_i by the Savitzky–Golay algorithm is given by the following equation ([Zuppa et al. 2004](#)):

$$g_i = \frac{\sum_{n=-nL}^{nR} c_n f_{i+n}}{\sum_{n=-nL}^{nR} c_n} \quad (\text{A.10})$$

The Savitzky-Golay filter method is a low-pass filter superior to other adjacent averaging FIR filters because it tends to preserve features of the data, such as peak height and width, which can be “washed out” by adjacent averaging ([OriginLab 2012](#)). To increase the smoothness of the result, one can increase the “window size,” or number of data points used in each local regression. Although Savitzky-Golay filters are less successful than standard averaging FIR filters at rejecting noise, they are more effective at preserving the pertinent high frequency components of the signal, and are optimal in minimising the least-squares error in fitting a polynomial to frames of noisy data ([MathWorks 2014](#)). It can preserve better the high-frequency content of the desired signal, at the expense of not removing as much noise as the average ([Orfanidis 1996](#)). Therefore, an optimum number of data points must be used in order for Savitzky-Golay to still preserve the height, width, amplitude and overall profile of the signal.

A.3 Smoothing Implementation and Curve Fitting

All the raw data were in quantised form. All other raw data were pre-processed before further analysis. But as example, presented are the implementation of pre-processing of two sets of data using local regression (and robust local regression), moving average and the Savitzky-Golay filters. These data are from SnO₂ and ZnO sensor devices, analysed with 150 ppm methanol at 250 °C. During exploratory analysis, the data were

visualised, and smoothed using multiple fitting algorithms. Parameters of the curve were analysed after residual analysis, fits generated, and the curve reconstructed to determine the accuracy of the models. Then an optimal model was selected for generating the best polynomial model.

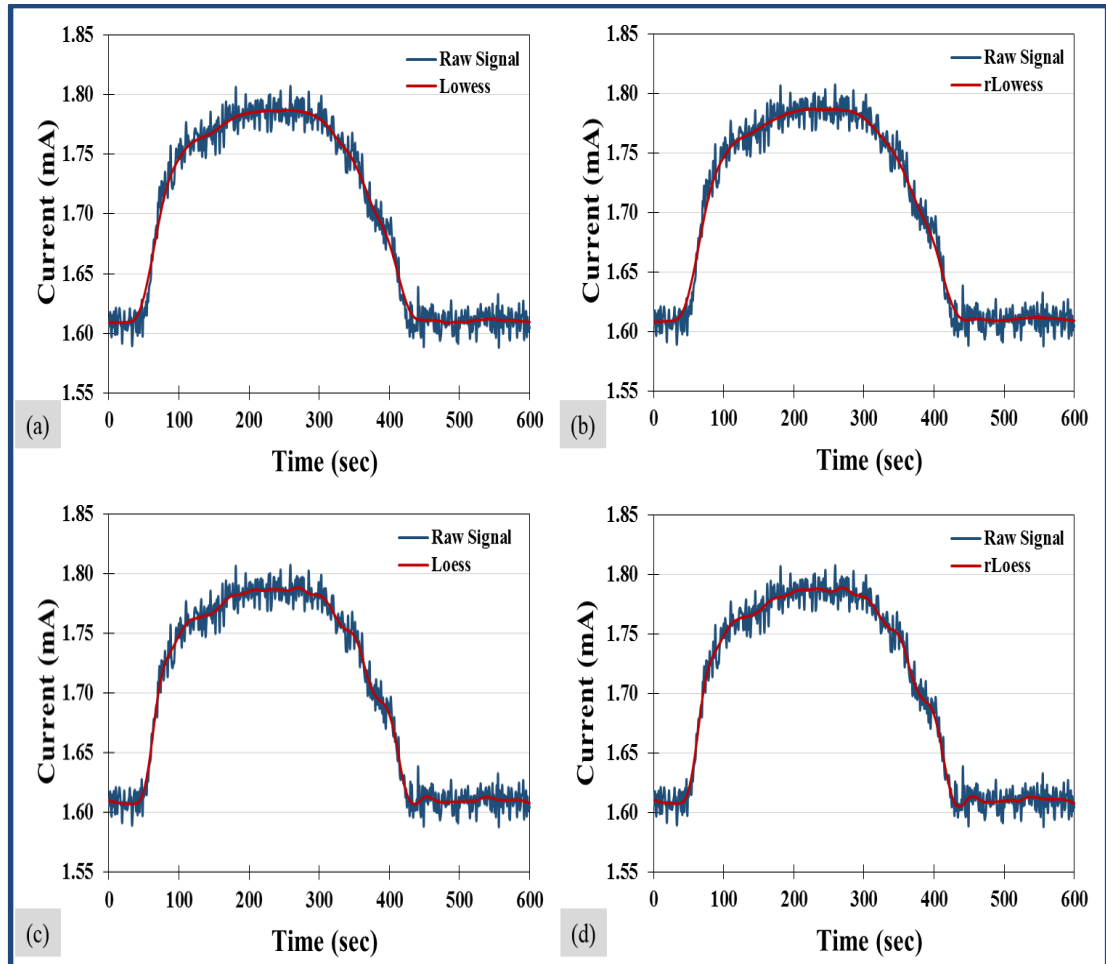


Figure A-2: SnO₂ Sensor local regression smoothing: (a) Lowess, (b) rLowess; and robust local regression smoothing (c) Loess, (d) rLoess.

The local regression smoothing (lowess and loess) and robust local regression (rloess and rloess) were used with a span of 10% of the data points. The moving average and Savitzky-Golay filters smooth the data using a span of 5 and 55. These values were chosen because they gave comparable results. The curve fitting parameters were obtained and compared for optimal model using reasonably optimal polynomial. These filtering processes were implemented using MATLAB.

The smoothing of raw data from SnO₂ sensor device is shown for local regression smoothing and robust local regression (Figure A-2) and moving average and Savitzky-Golay filters (Figure A-3). The results from local regression smoothing and robust local regression give relatively the same shape resolution (Figure A-2). The smoothing by moving average and Savitzky-Golay filters with span of 55 were better than span of 5 (Figure A-3).

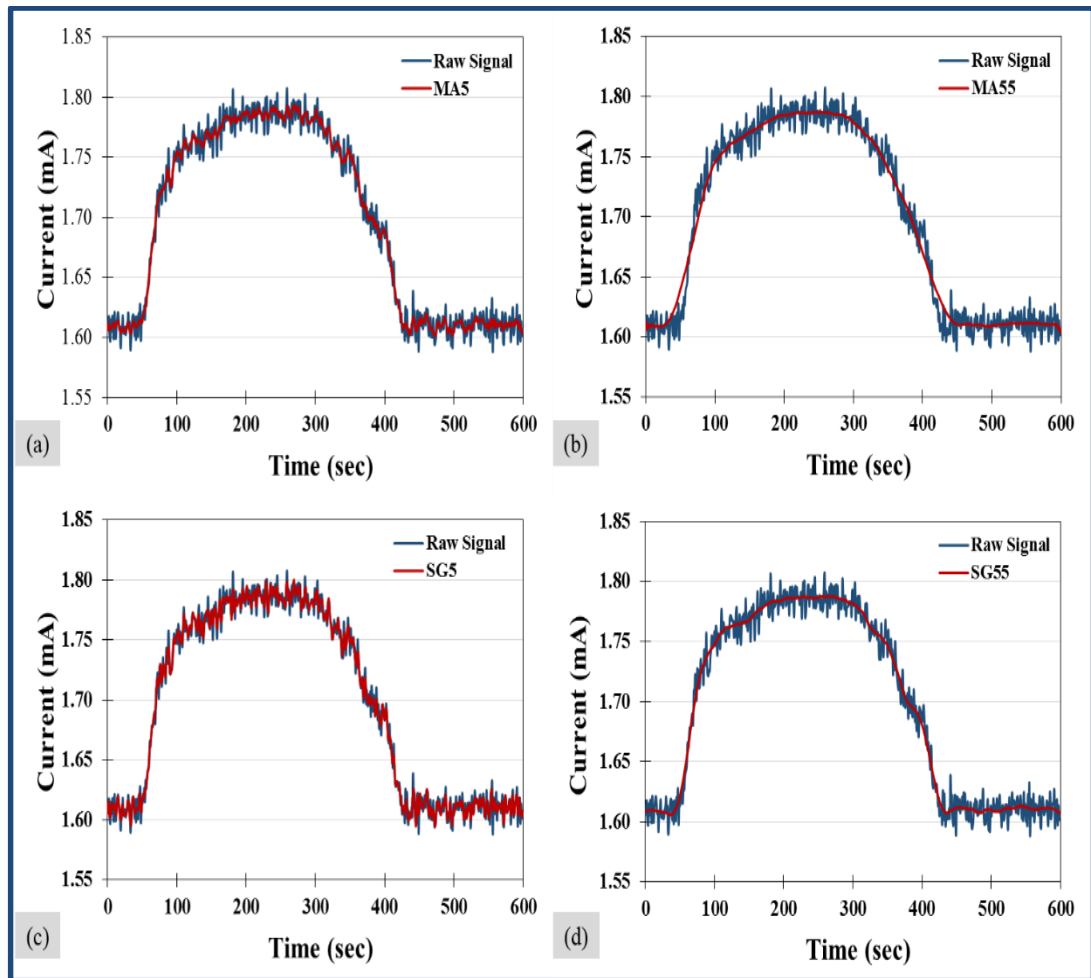


Figure A-3: SnO₂ sensor (a) Moving Average with span = 5, (b) Moving Average with span = 55, (c) Savitzky-Golay filters with span = 5, and (d) Savitzky-Golay filters with span = 55.

Similarly, the results from the ZnO device are presented in Figure A-4 and Figure A-5. The loess local regression smoothing and robust local regression gave a better shape resolution than the lowess (Figure A-4). The smoothing by moving average and Savitzky-Golay Filters with span of 55 were better than span of 5 (Figure A-5).

However, in the Savitzky–Golay smoothing filter, the heights and widths of narrow peaks are accurately captured by higher degree polynomials, but wider peaks are poorly smoothed.

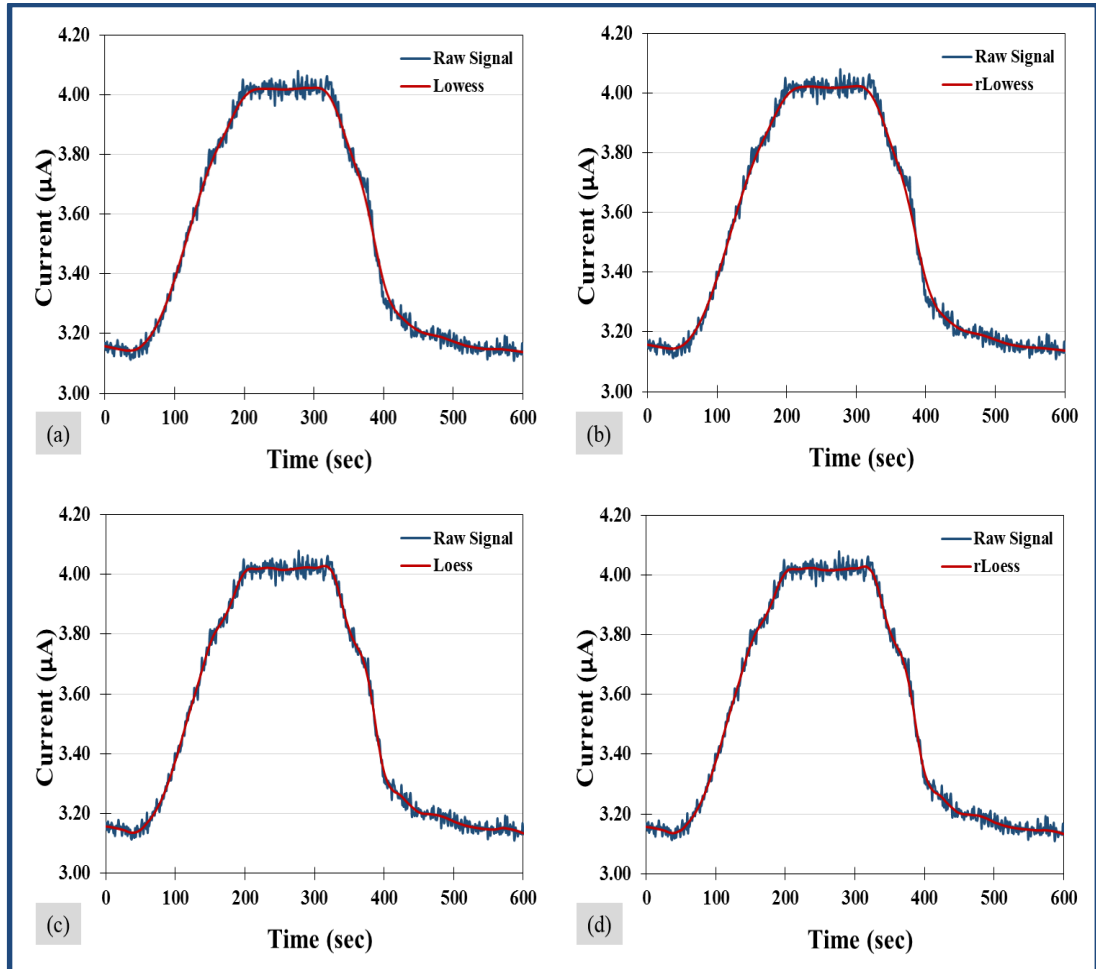


Figure A-4: ZnO Sensor local regression smoothing: (a) Lowess, (b) rLowess; and robust local regression smoothing (c) Loess (d) rLoess.

Curve fitting was undertaken using each of the smoothing processes, and the coefficient of determination (R-squared) calculated. The coefficient of determination (R^2) indicates the proportionate amount of variation in the response signal explained by the independent variables t in the polynomial model:

$$R^2 = \frac{SSR}{SST} = 1 - \frac{SSE}{SST} \quad (\text{A.11})$$

where SSE is the sum of squared error, SSR is the sum of squared regression; SST is the sum of squared total.

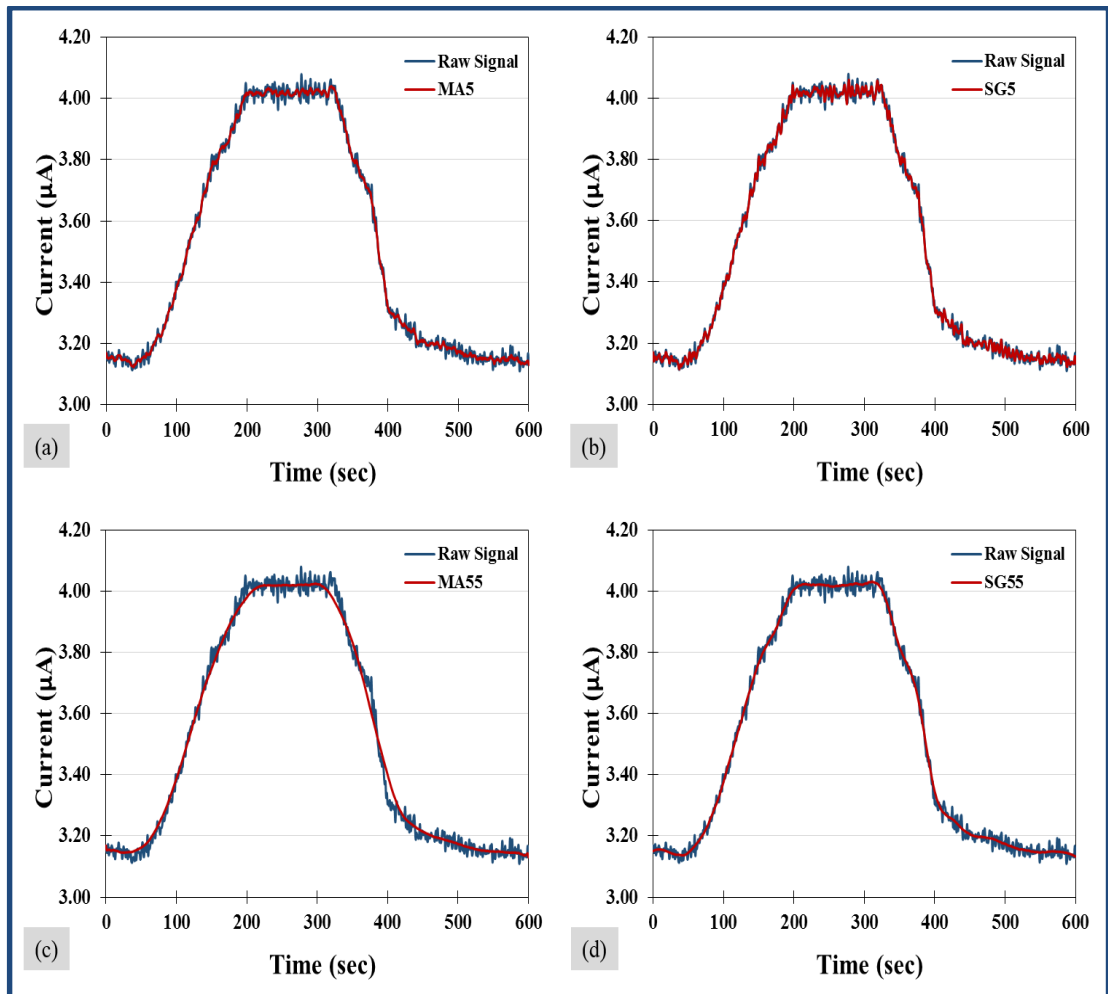


Figure A-5: ZnO sensor (a) Moving Average (span = 5), (b) Moving Average (span = 55), (c) Savitzky-Golay filters (span = 5), and (d) Savitzky-Golay filters (span = 55).

The R^2 (usually between 0 and 1) is proportional to the variability of the response signal in the polynomial model (see Figure A-6). These values were obtained using a polynomial of 3. Generally, the R^2 value of SnO_2 was greater than that of ZnO. The best value of R^2 was from the moving average (span = 55), followed by the loess local regression for both the SnO_2 and ZnO devices. But from visual observation of the smoothing results, the Savitzky-Golay and the loess methods gave a better shape resolution. The norms of residuals were the same for all smoothing methods for each device; the values were $5.25114\text{E-}04$ and $3.62\text{E-}06$ for SnO_2 and ZnO devices, respectively.

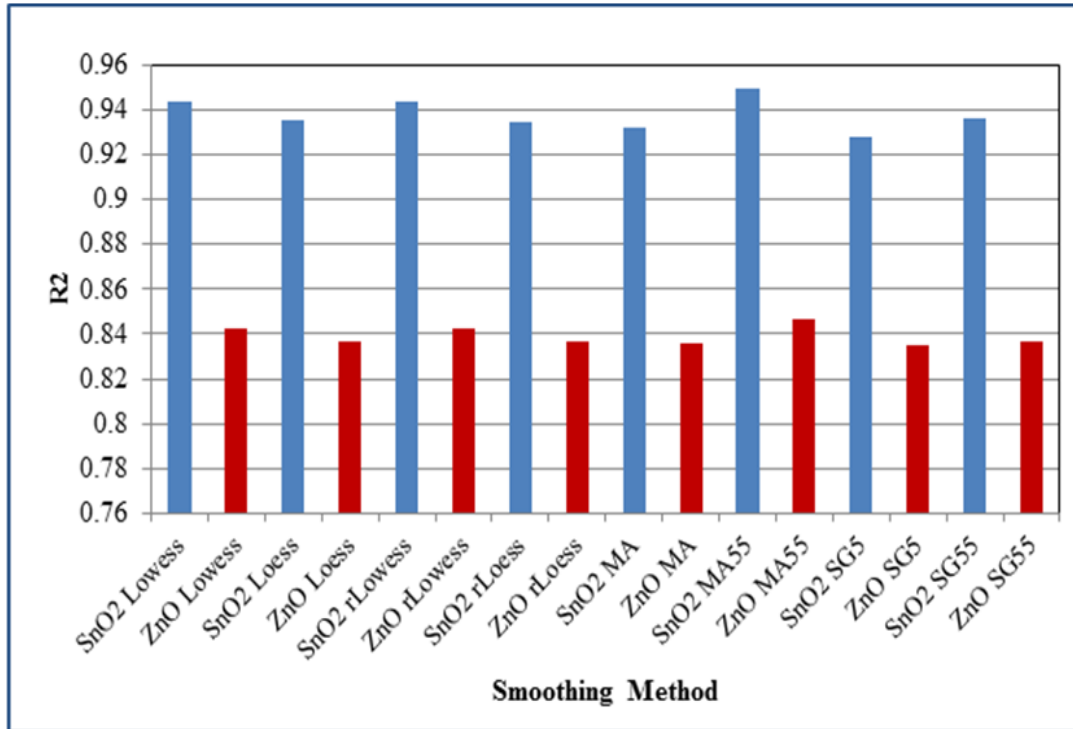


Figure A-6: Coefficient of determination (r-squared) from the curve fitting process.

To calibrate the model, different polynomial models were tested on the raw data to determine the best fit within the confidence bounds. An attempt to fit the data using a higher degree polynomial was presented using the Savitzky-Golay (span = 55) and the loess (span = 10%) methods. The best fit was found with polynomial degree of 9 for both loess and Savitzky-Golay methods. In the SnO₂ device, the norms of residuals were 1.8034E-04 and 1.714E-04 for loess and Savitzky-Golay methods, respectively. While the norms of residuals for ZnO devices were 8.47E-07 and 8.27E-07 for loess and Savitzky-Golay methods, respectively. The SnO₂ sensor response was fitted as shown in Figure A-7, while the ZnO sensor response as shown in Figure A-8.

Using a $\pm 2\Delta$ interval (i.e., 95% confidence interval), the fitted data and the smoothed data are observed to fall within the bounds.

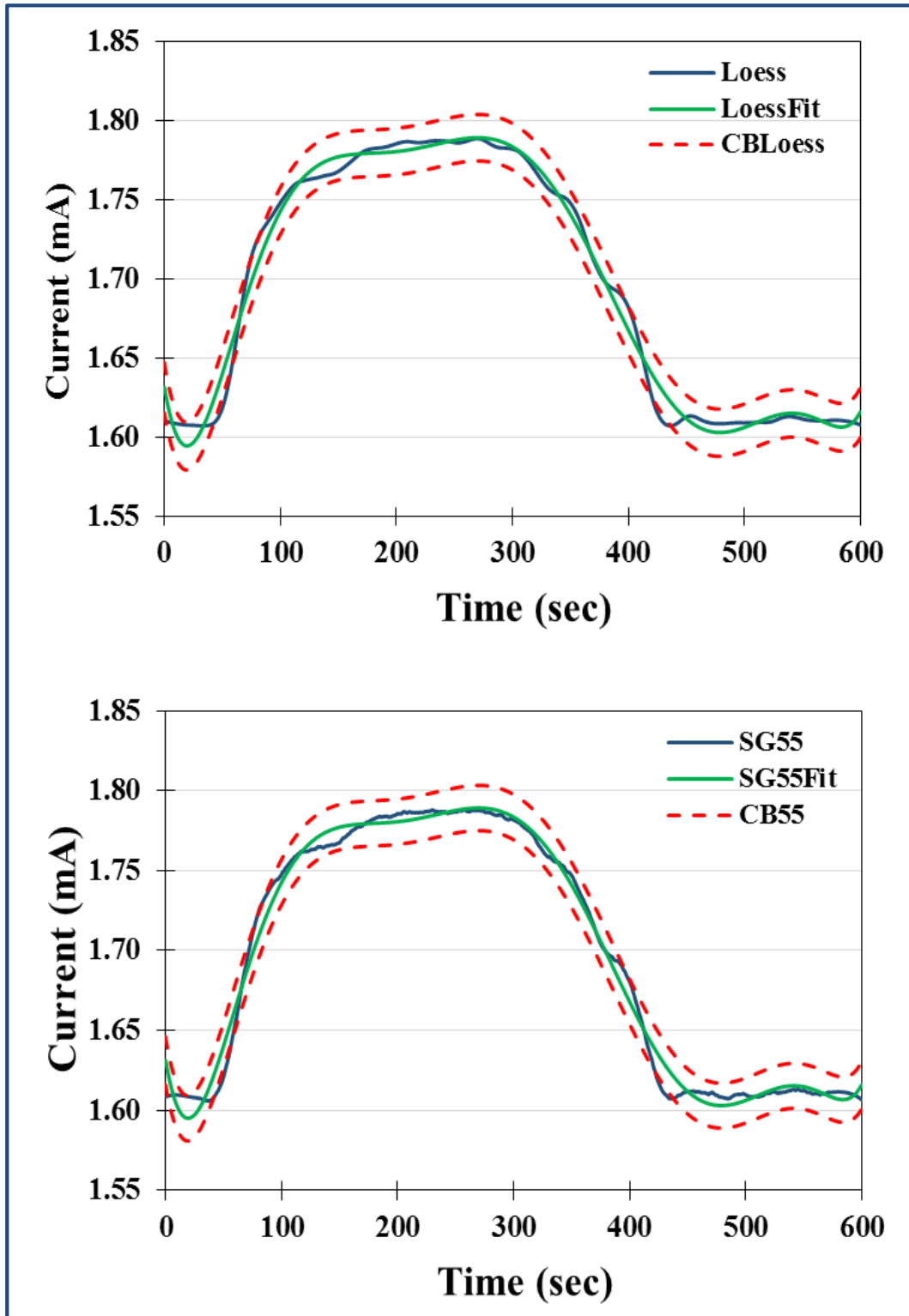


Figure A-7: Polynomial fit with confidence bounds and smoothed SnO₂ device data.

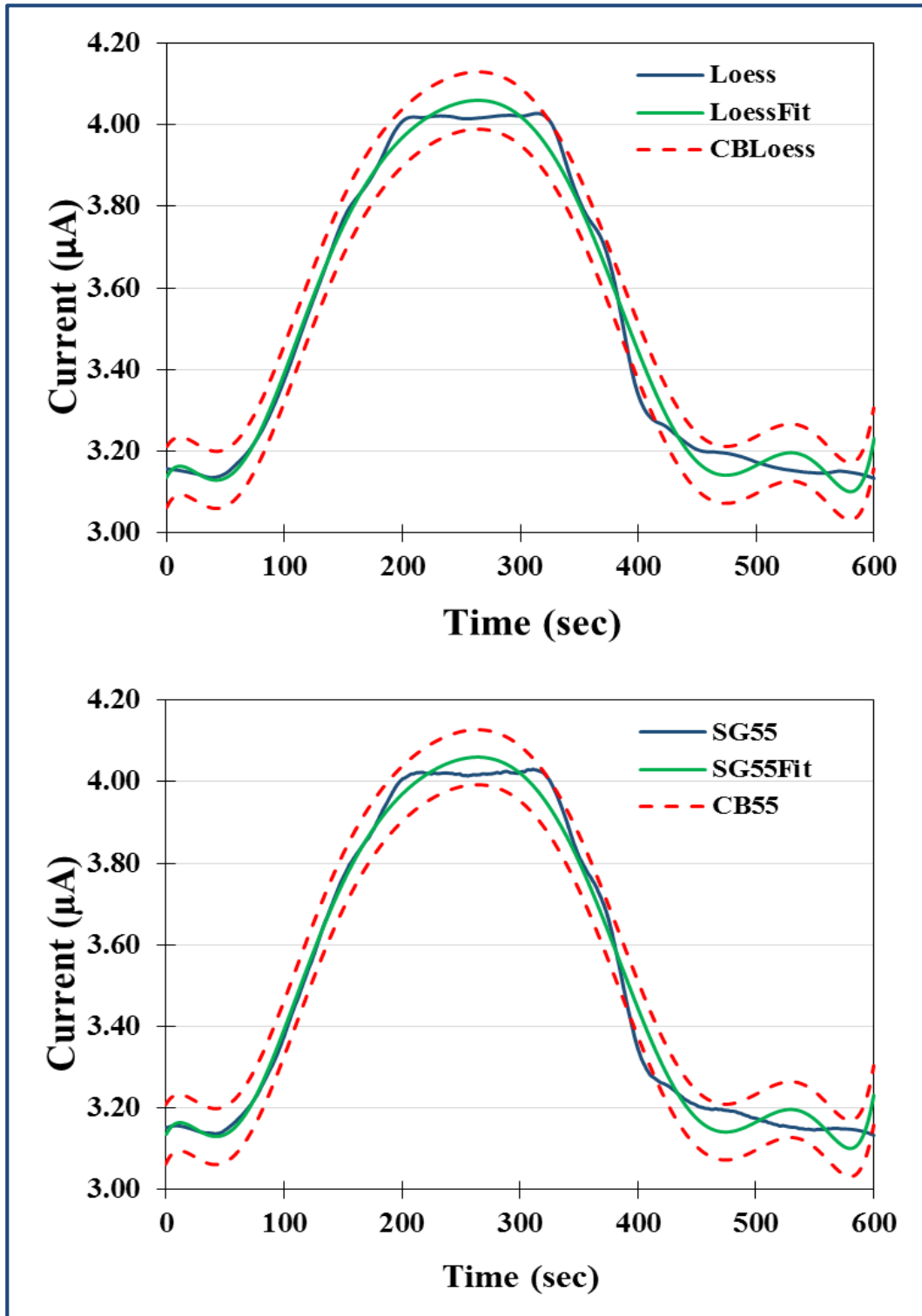


Figure A-8: Polynomial fit with confidence bounds and smoothed with ZnO device.

A further analysis of the raw data and the fitted data illustrated that the two smoothing methods (loess and Savitzky-Golay) present very good confidence bounds over the

raw data. The fitting of the confidence bounds over the SnO₂ and ZnO devices raw data are shown in Figure A-9 and Figure A-10, respectively.

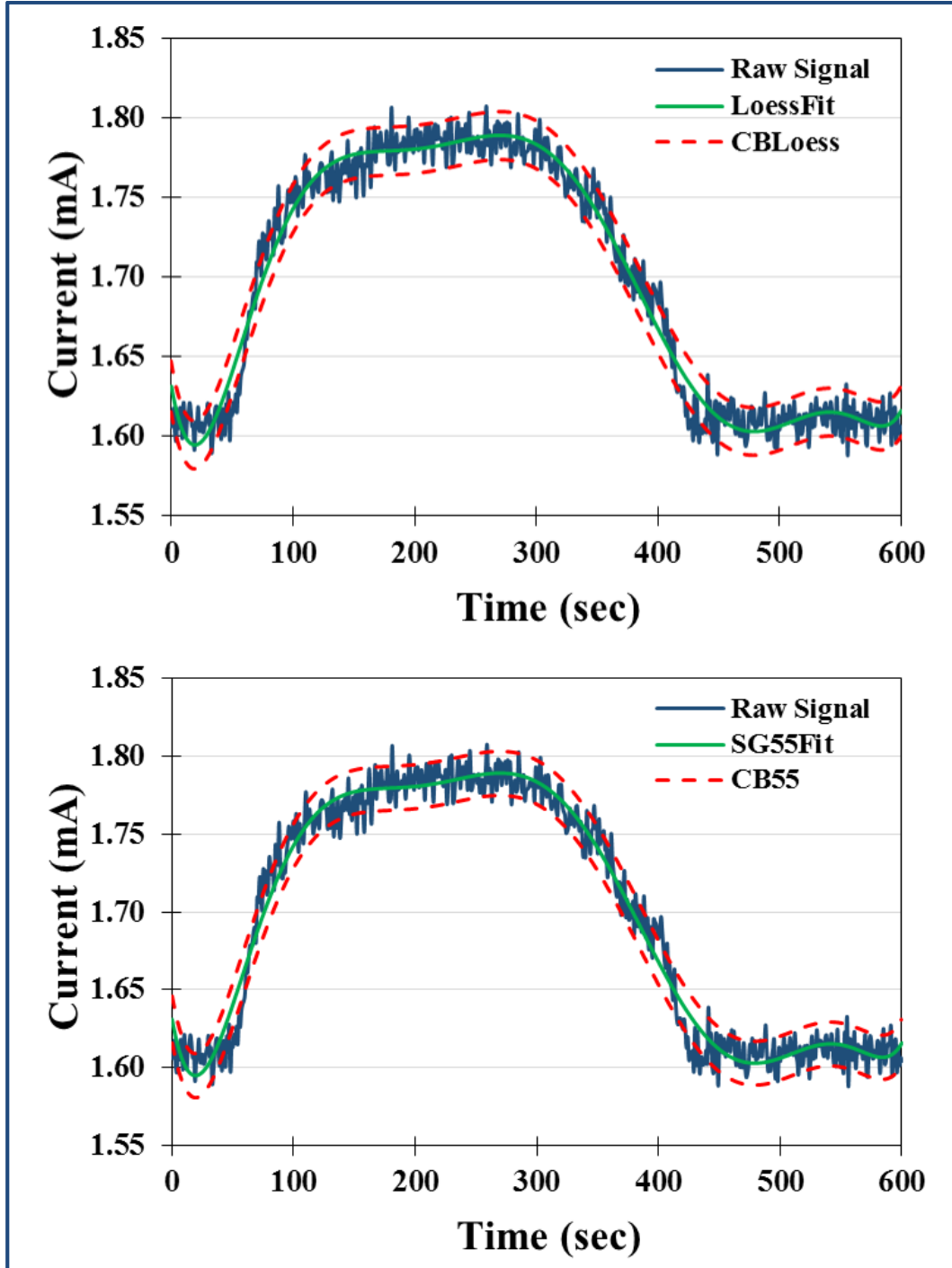


Figure A-9: Fitting the confidence bounds over the SnO₂ device raw data.

For both sensor devices, the raw data were observed to fall within the confidence bounds simulated from the polynomial models. These results are very good; and validate the methodology and the models.

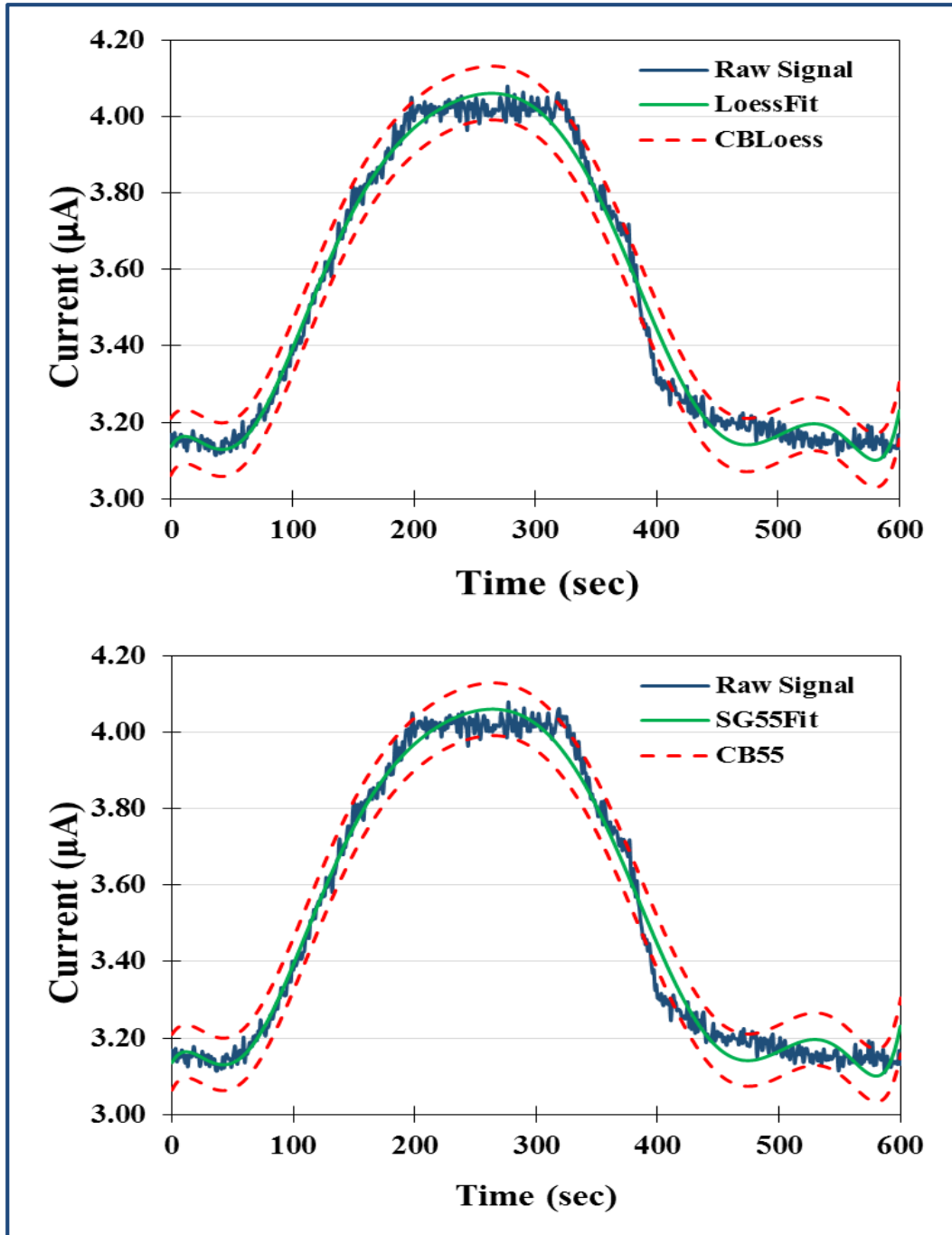


Figure A-10: Fitting the confidence bounds over the ZnO device raw data.

Thus, pre-processing (by smoothing) of the raw data improved the implementation and boosts confidence in the application of the data for further analysis.

References

- Ahlers, S., Müller, G., and Doll, T. (2005). "A rate equation approach to the gas sensitivity of thin film metal oxide materials." *Sensors and Actuators B: Chemical*, 107(2), 587-599.
- Aminghafari, M., Cheze, N., and Poggi, J.-M. (2006). "Multivariate denoising using wavelets and principal component analysis." *Computational Statistics & Data Analysis*, 50(9), 2381-2398.
- Bao, L., Mo, J., and Tang, Z. (1997). "The Application in Processing Analytical Chemistry Signals of a Cardinal Spline Approach to Wavelets." *Analytical Chemistry*, 69(15), 3053-3057.
- Gutierrez-Osuna, R. (2002). "Pattern analysis for machine olfaction: a review." *Sensors Journal, IEEE*, 2(3), 189-202.
- Gutierrez-Osuna, R., Nagle, H. T., Kermani, B., and Schiffman, S. S. (2004). "Signal Conditioning and Preprocessing", in T. C. Pearce, S. S. Schiffman, H. T. Nagle, and J. W. Gardner, (eds.), *Handbook of Machine Olfaction: Electronic Nose Technology*. Wiley-VCH Verlag GmbH & Co. KGaA, pp. 105-132.
- Johnson, K. J., Wright, B. W., Jarman, K. H., and Synovec, R. E. (2003). "High-speed peak matching algorithm for retention time alignment of gas chromatographic data for chemometric analysis." *Journal of Chromatography A*, 996(1-2), 141-155.
- Jurs, P. C., Bakken, G. A., and McClelland, H. E. (2000). "Computational Methods for the Analysis of Chemical Sensor Array Data from Volatile Analytes." *Chemical Reviews*, 100(7), 2649-2678.
- MathWorks. (2014). "Signal Processing Toolbox™ User's Guide 2014a" *MATLAB: Signal Processing Toolbox*. The MathWorks, Inc.: Natick, MA, USA.
- Orfanidis, S. J. (1996). *Introduction to Signal Processing*, New Jersey, USA: Prentice Hall, Inc.
- OriginLab. (2012). "Origin: Smoothing using Savitzky-Golay Filtering" *OriginLab^(R): Data Analysis and Graphing Software*. OriginLab Corporation: Northampton, MA USA.
- Perrin, C., Walczak, B., and Massart, D. L. (2001). "The Use of Wavelets for Signal Denoising in Capillary Electrophoresis." *Analytical Chemistry*, 73(20), 4903-4917.
- Press, W. H., Teukolsky, S. A., Vetterling, W. T., and Flannery, B. P. (2007). *Numerical Recipes: The Art of Scientific Computing*, Cambridge, New York Cambridge University Press.

- Savitzky, A., and Golay, M. J. E. (1964). "Smoothing and Differentiation of Data by Simplified Least Squares Procedures." *Analytical Chemistry*, 36(8), 1627-1639.
- Schafer, R. (2011). "What Is a Savitzky-Golay Filter?" *Signal Processing Magazine, IEEE*, 28(4), 111-117.
- Shaffer, R. E., Rose-Pehrsson, S. L., and McGill, R. A. (1999). "A comparison study of chemical sensor array pattern recognition algorithms." *Analytica Chimica Acta*, 384(3), 305-317.
- Thornley, D. J. "Novel Anisotropic Multidimensional Convolutional Filters for Derivative Estimation and Reconstruction." *Presented at Signal Processing and Communications, 2007. ICSPC 2007. IEEE International Conference on.*
- Yang, R., and Ren, M. (2011). "Wavelet denoising using principal component analysis." *Expert Systems with Applications*, 38(1), 1073-1076.
- Zuppa, M., Distanto, C., Siciliano, P., and Persaud, K. C. (2004). "Drift counteraction with multiple self-organising maps for an electronic nose." *Sensors and Actuators B: Chemical*, 98(2-3), 305-317.

Appendix B

More Gas Sensitivity Behaviour

B.1 SnO₂ Sensor Device (S)

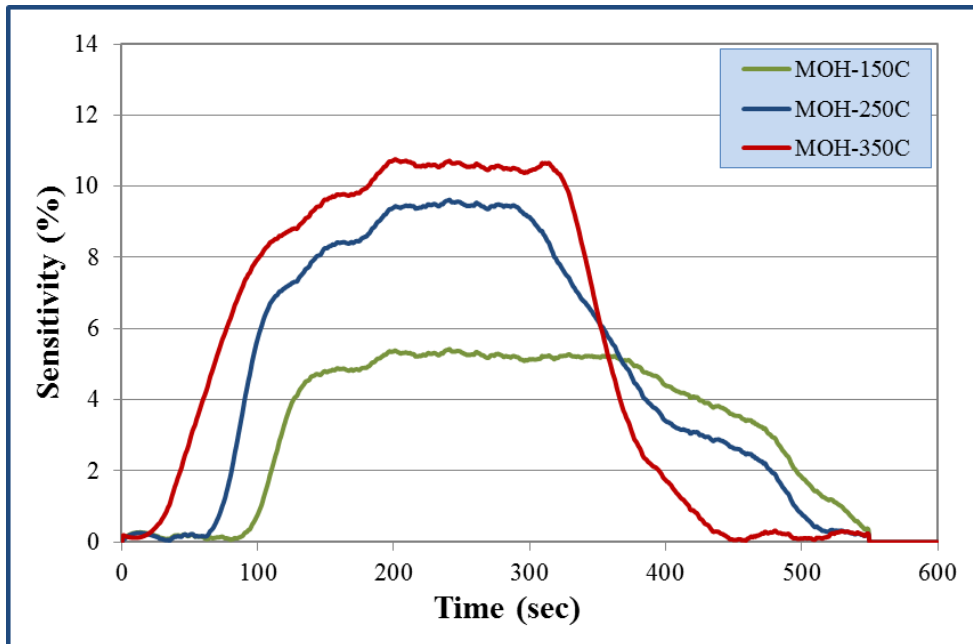


Figure B-1: SnO₂ sensor device (S) with 100 ppm methanol.

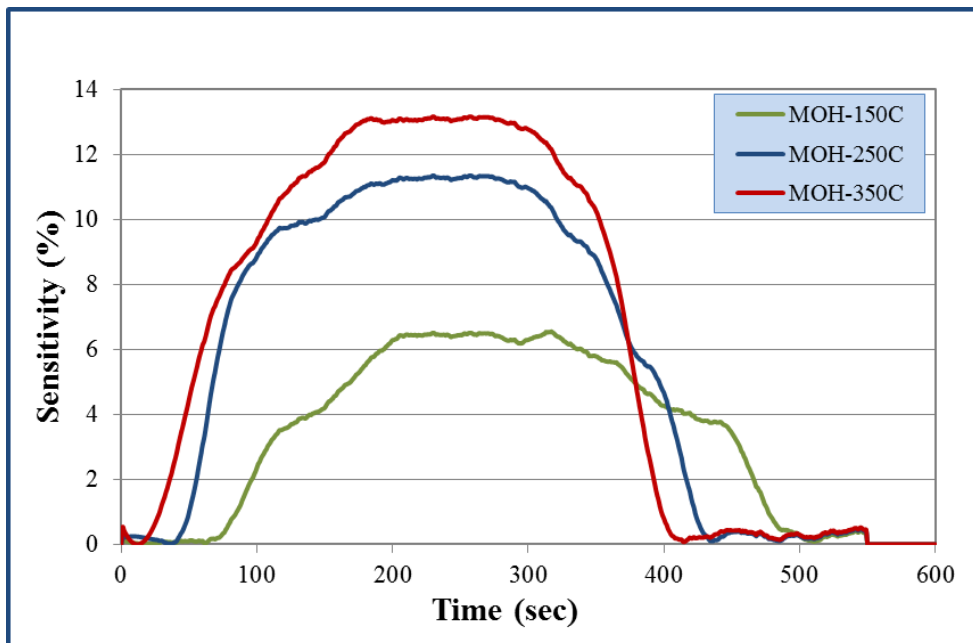


Figure B-2: SnO₂ sensor device (S) with 150 ppm methanol.

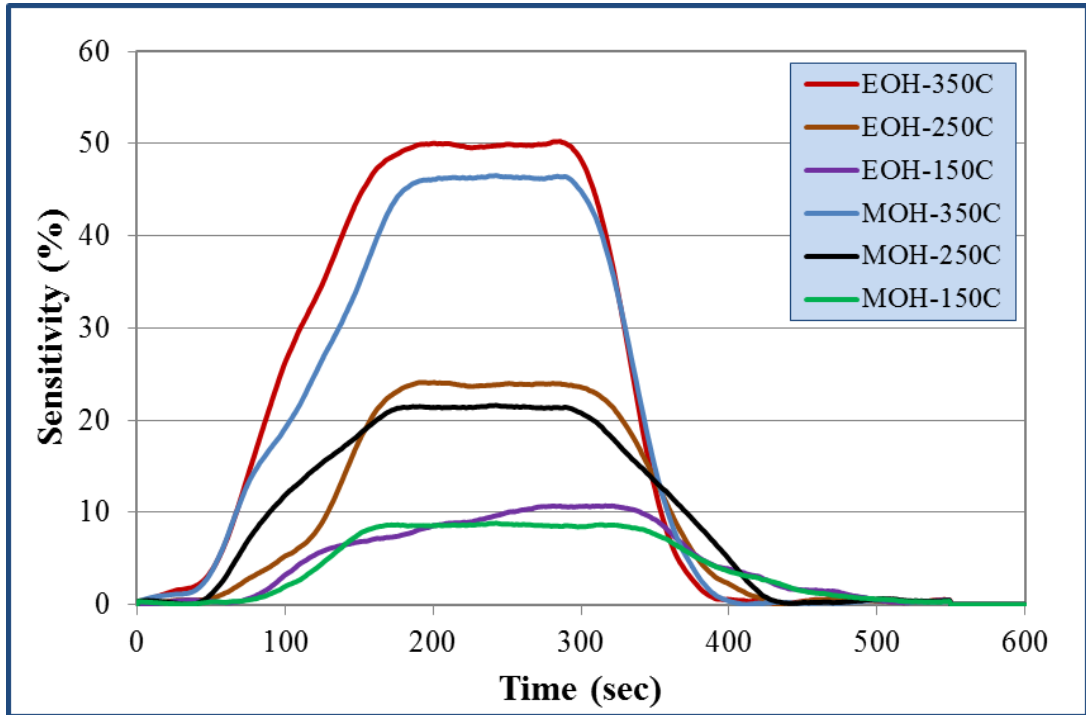


Figure B-3: SnO₂ sensor device (S) with 200 ppm methanol and ethanol.

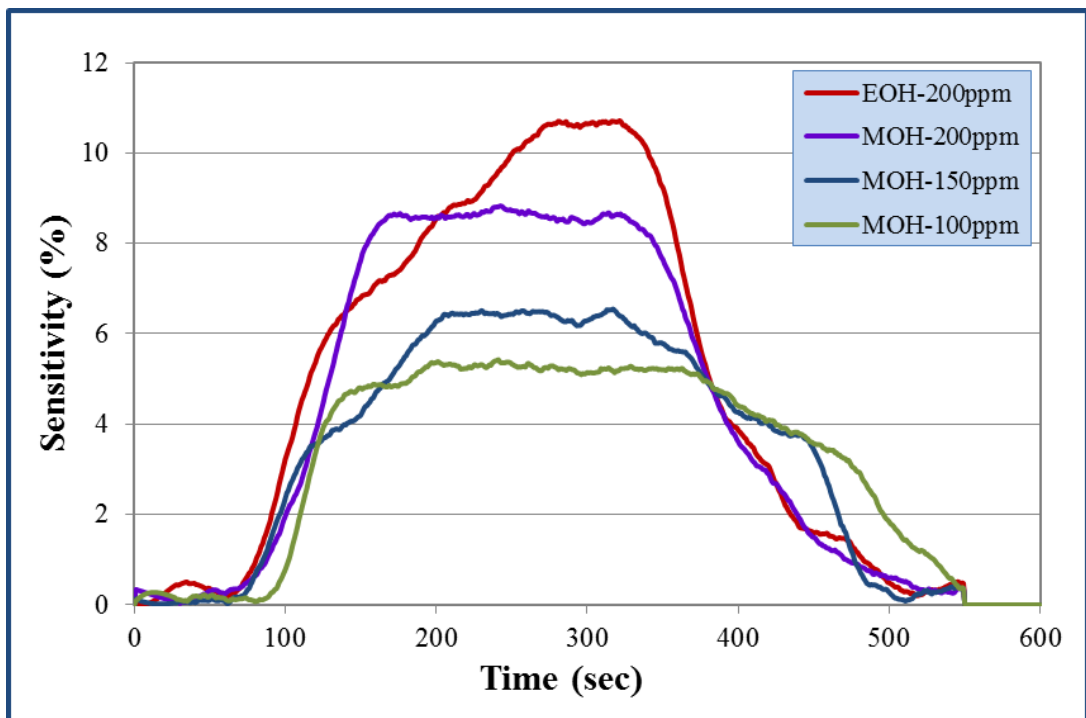


Figure B-4: SnO₂ sensor device (S) at 150 °C operating temperature.

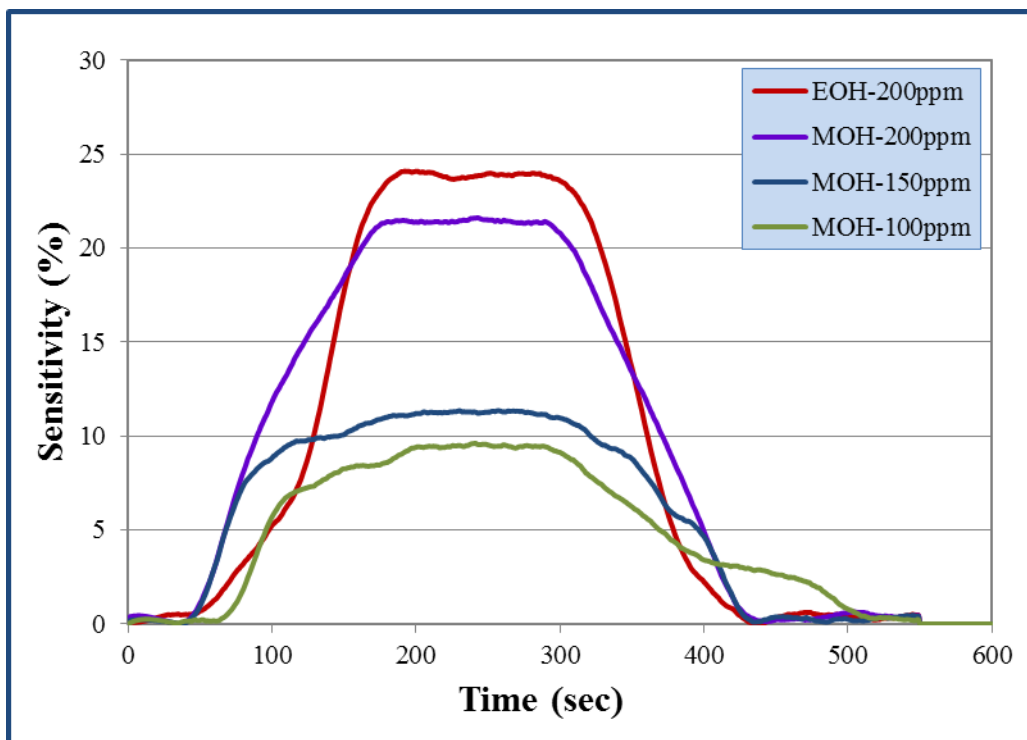


Figure B-5: SnO₂ sensor device (S) at 250 °C operating temperature.

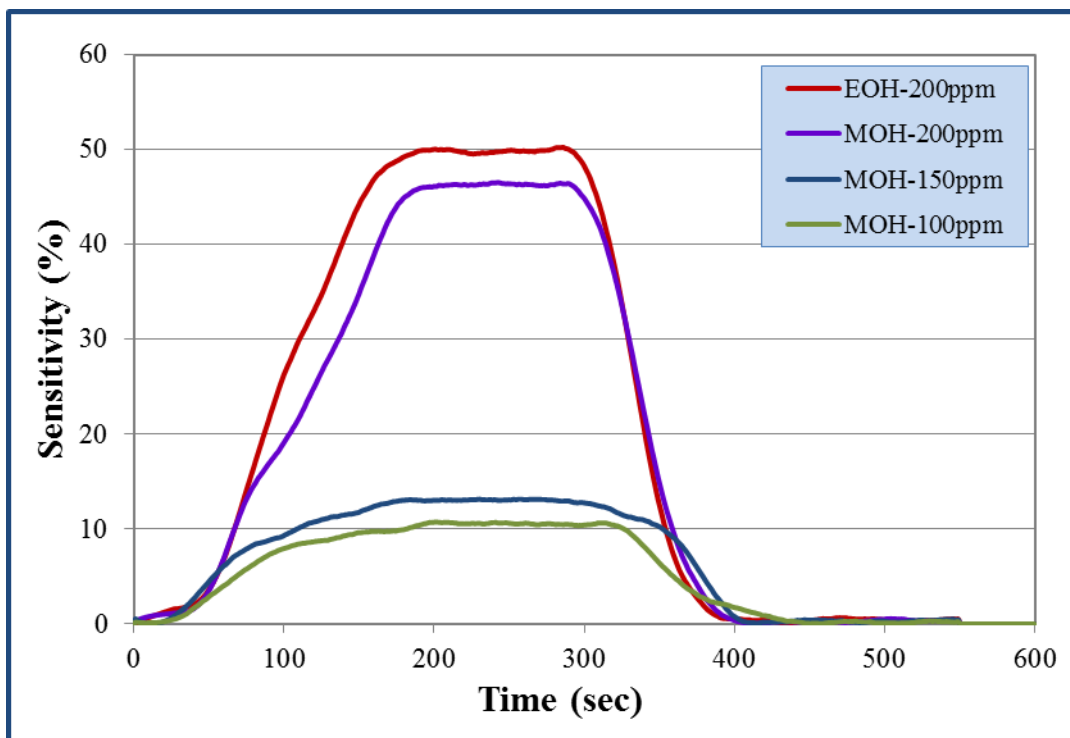


Figure B-6: SnO₂ sensor device (S) at 350 °C operating temperature.

B.2 SnO₂ (75%) - ZnO (25%) Sensor Device (S₃Z₁)

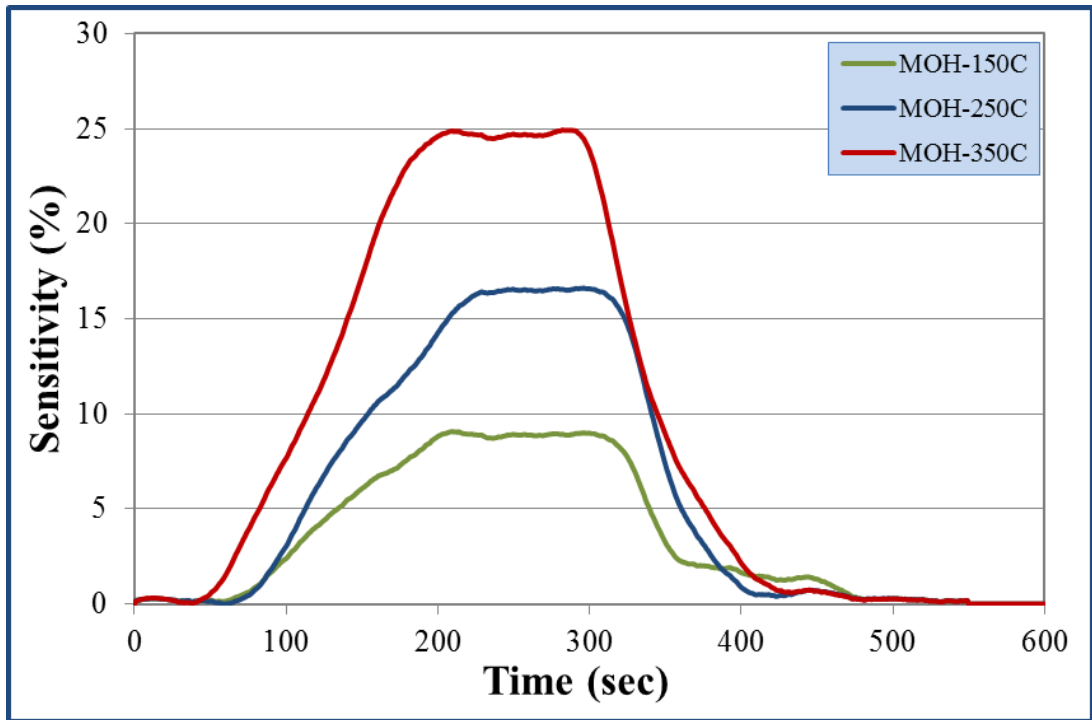


Figure B-7: S₃Z₁ sensor device with 100 ppm methanol.

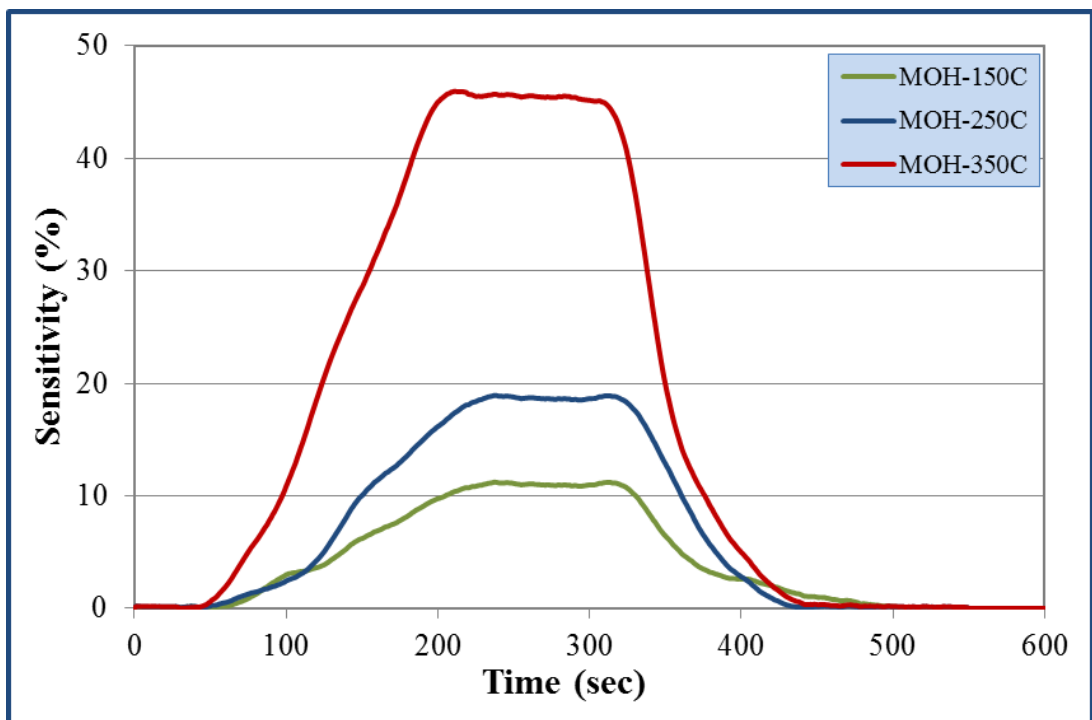


Figure B-8: S₃Z₁ sensor device with 150 ppm methanol.

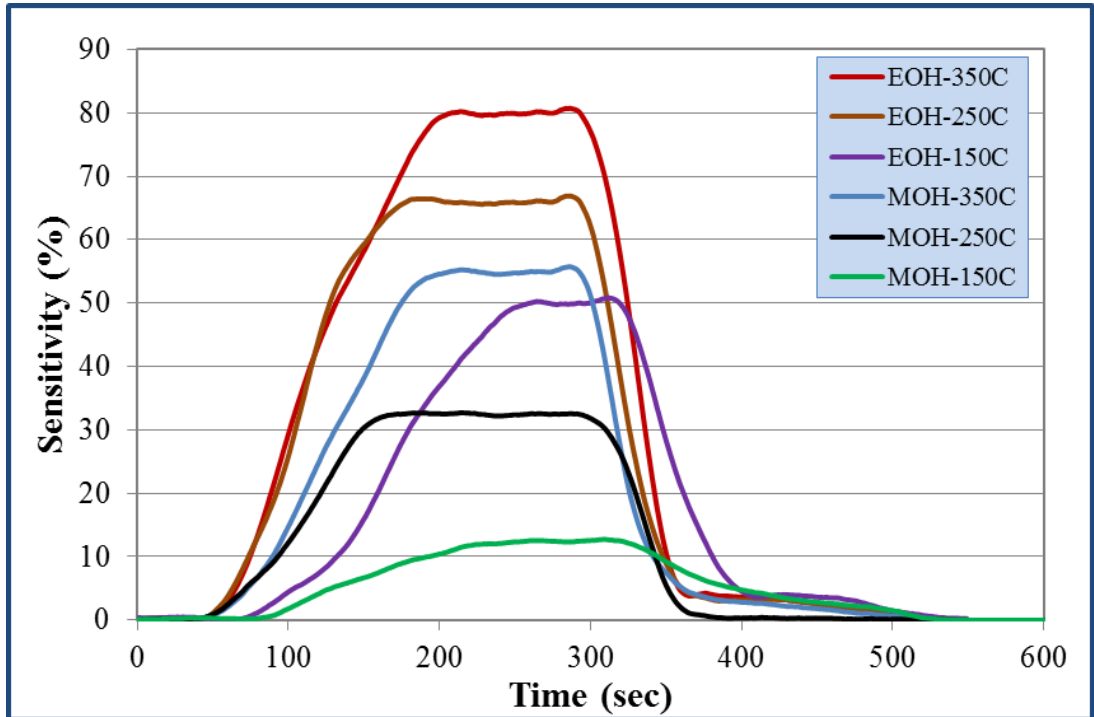


Figure B-9: S_3Z_1 sensor device with 200 ppm methanol and ethanol.

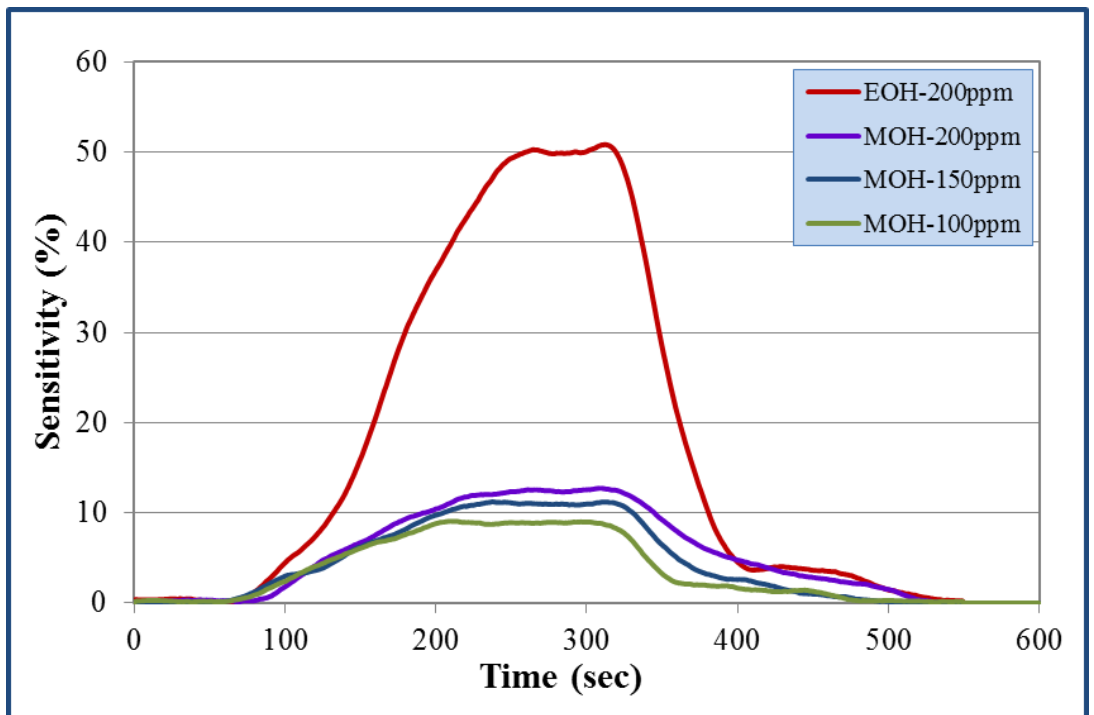


Figure B-10: S_3Z_1 sensor device at 150 °C operating temperature.

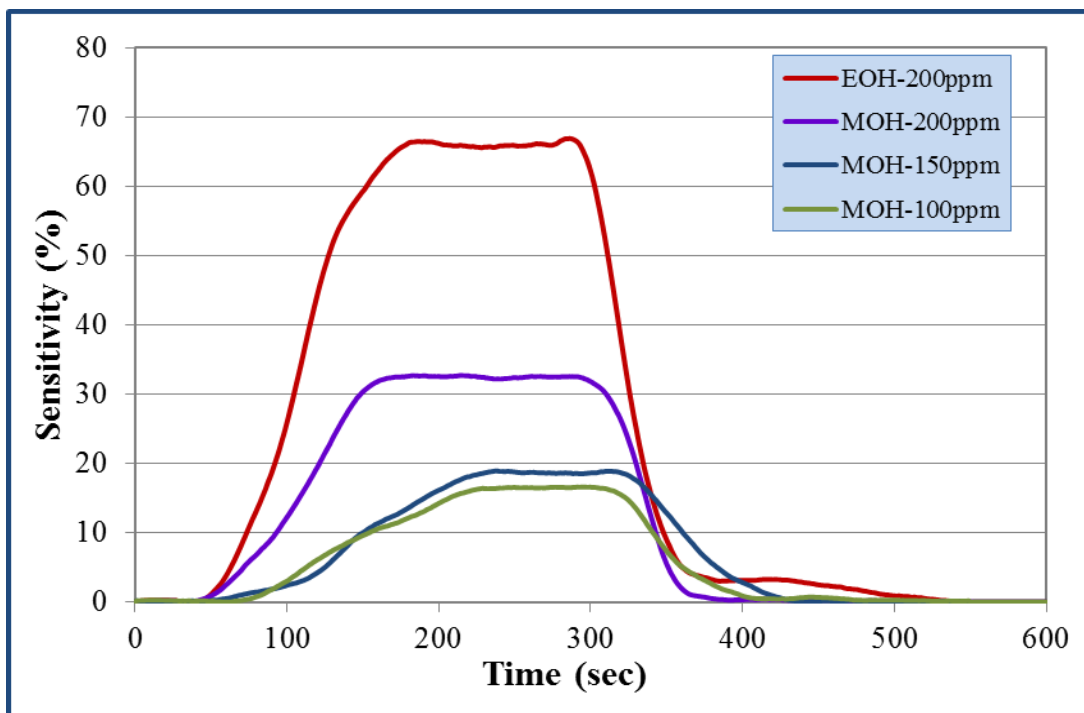


Figure B-11: S_3Z_1 sensor device at 250 °C operating temperature.

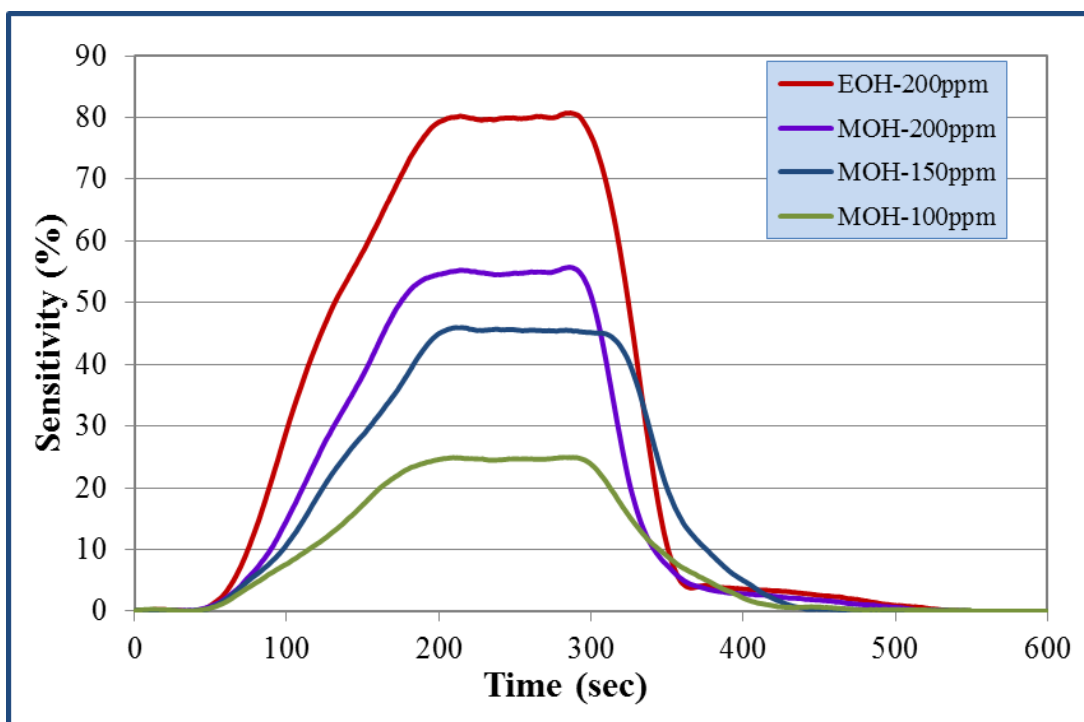


Figure B-12: S_3Z_1 sensor device at 350 °C operating temperature.

B.3 SnO₂ (50%) - ZnO (50%) Sensor Device (SZ)

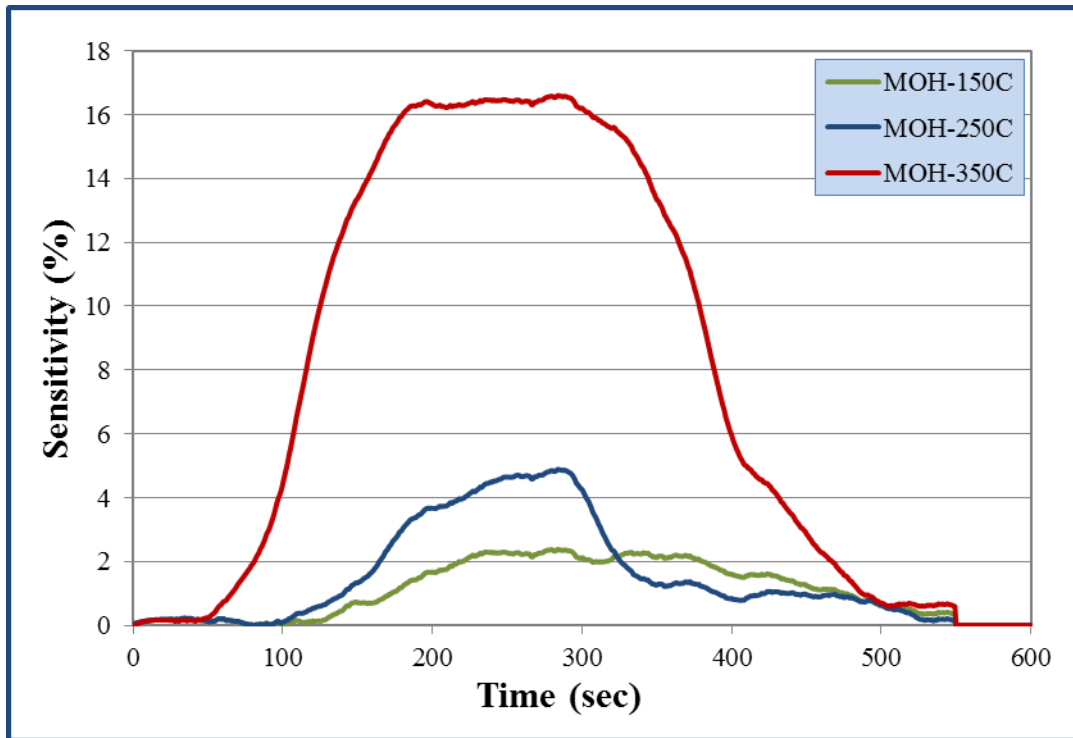


Figure B-13: SZ sensor device with 100 ppm methanol.

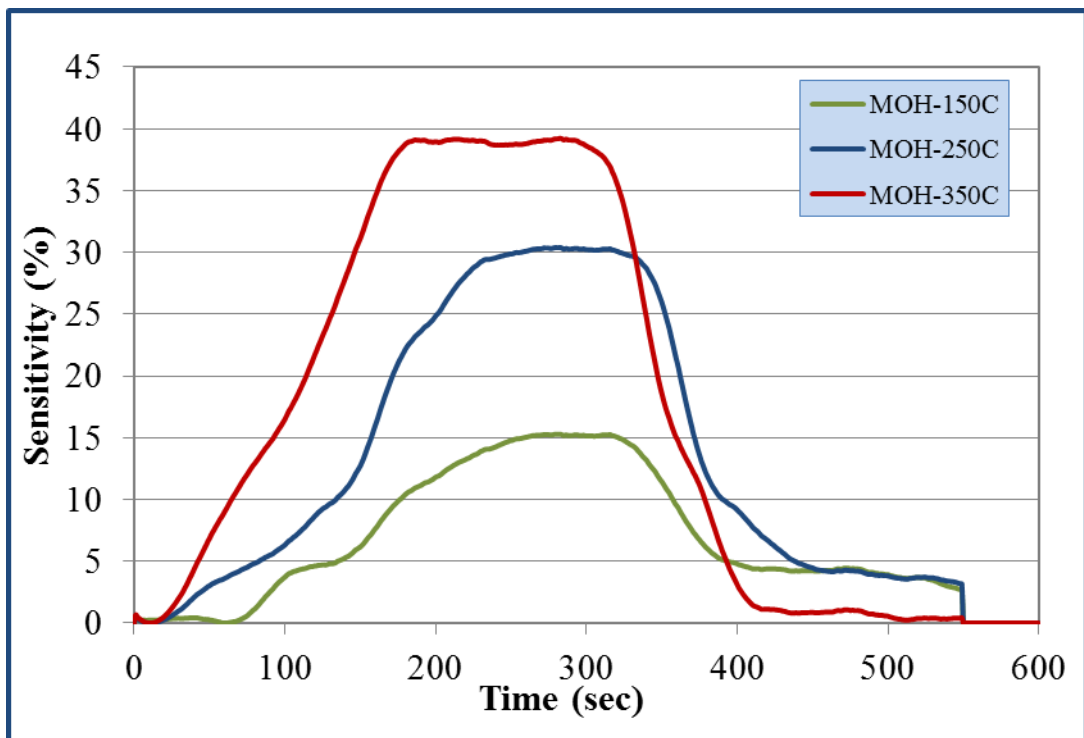


Figure B-14: SZ sensor device with 150 ppm methanol.

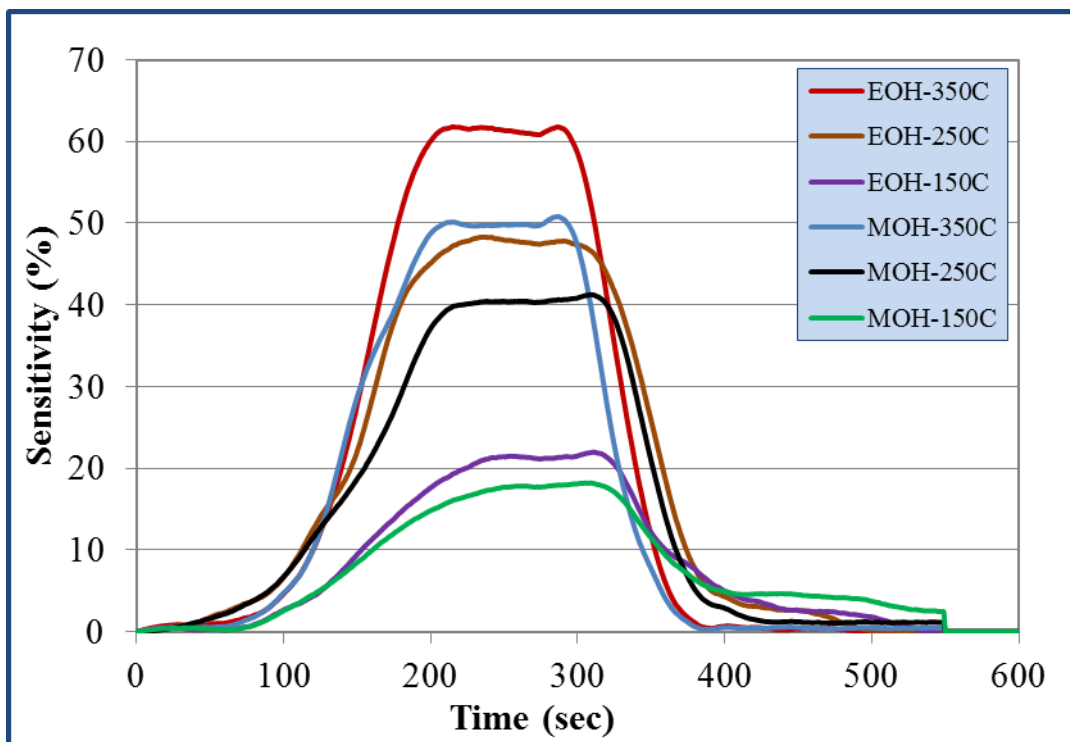


Figure B-15: SZ sensor device with 200 ppm methanol and ethanol.

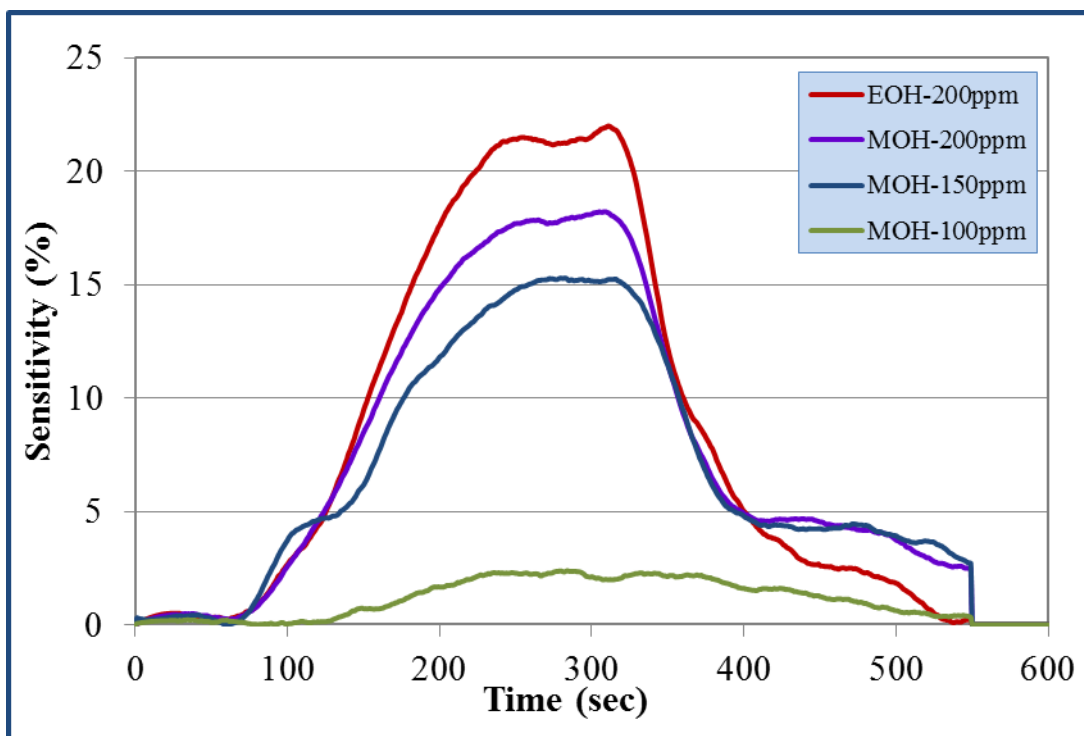


Figure B-16: SZ sensor device at 150 °C operating temperature.

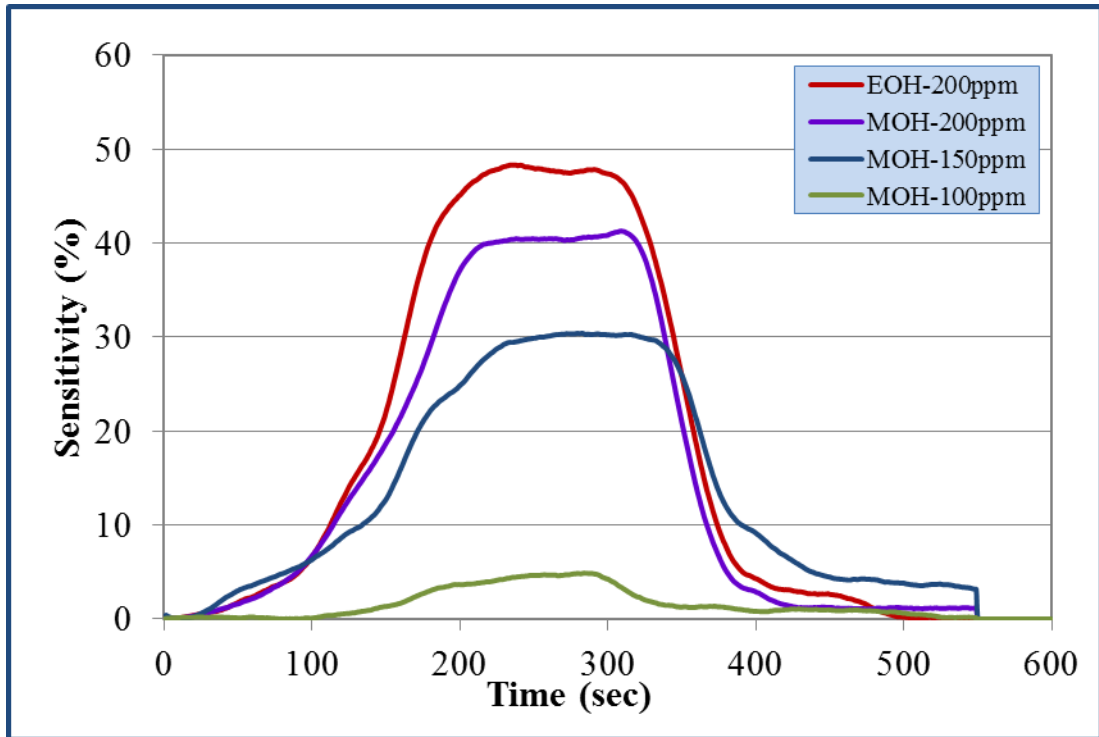


Figure B-17: SZ sensor device at 250 °C operating temperature.

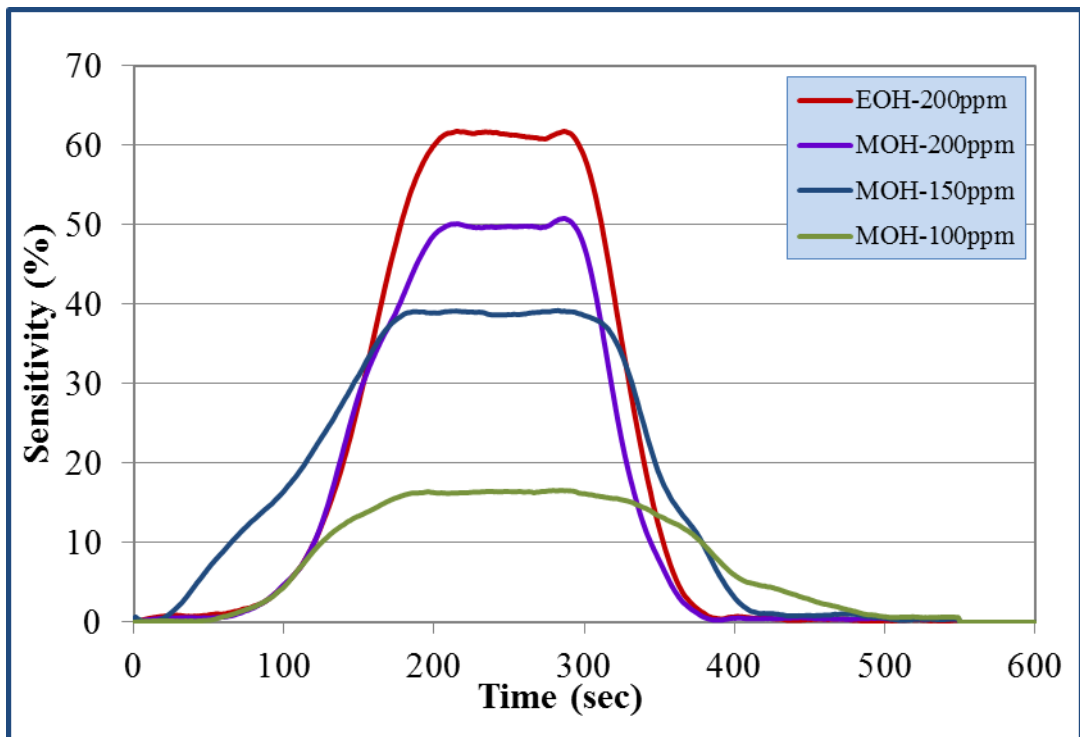


Figure B-18: SZ sensor device at 350 °C operating temperature.

B.4 SnO₂ (25%) - ZnO (75%) Sensor Device (S₁Z₃)

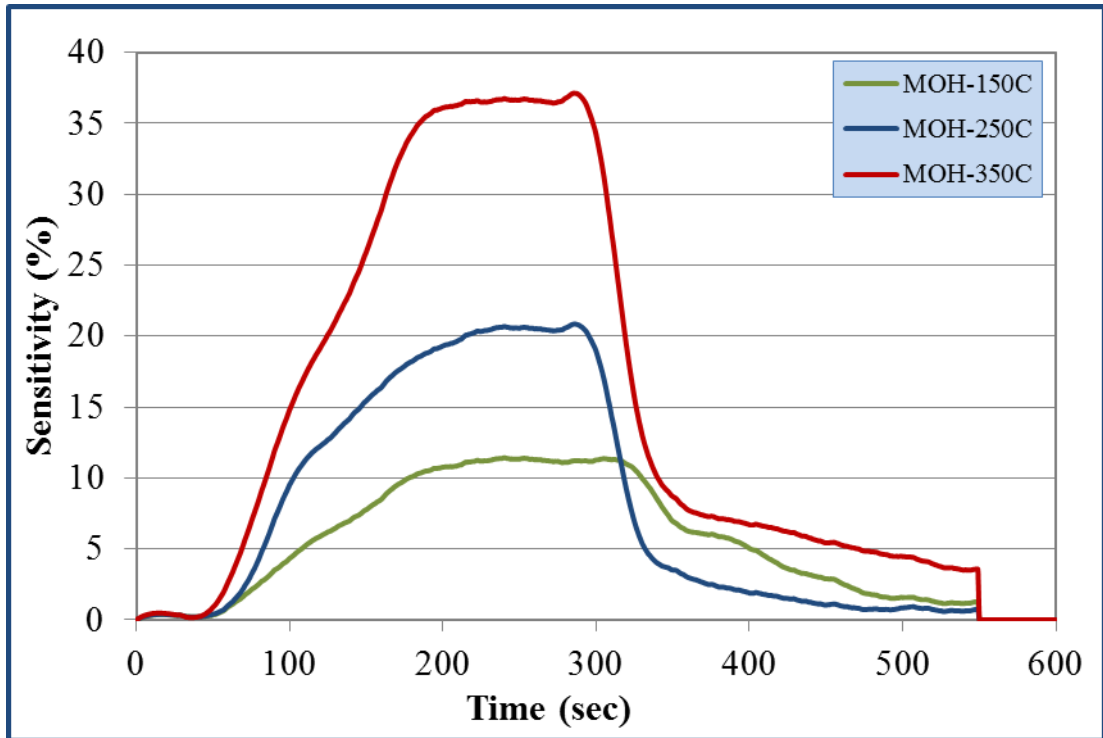


Figure B-19: S₁Z₃ sensor device with 100 ppm methanol.

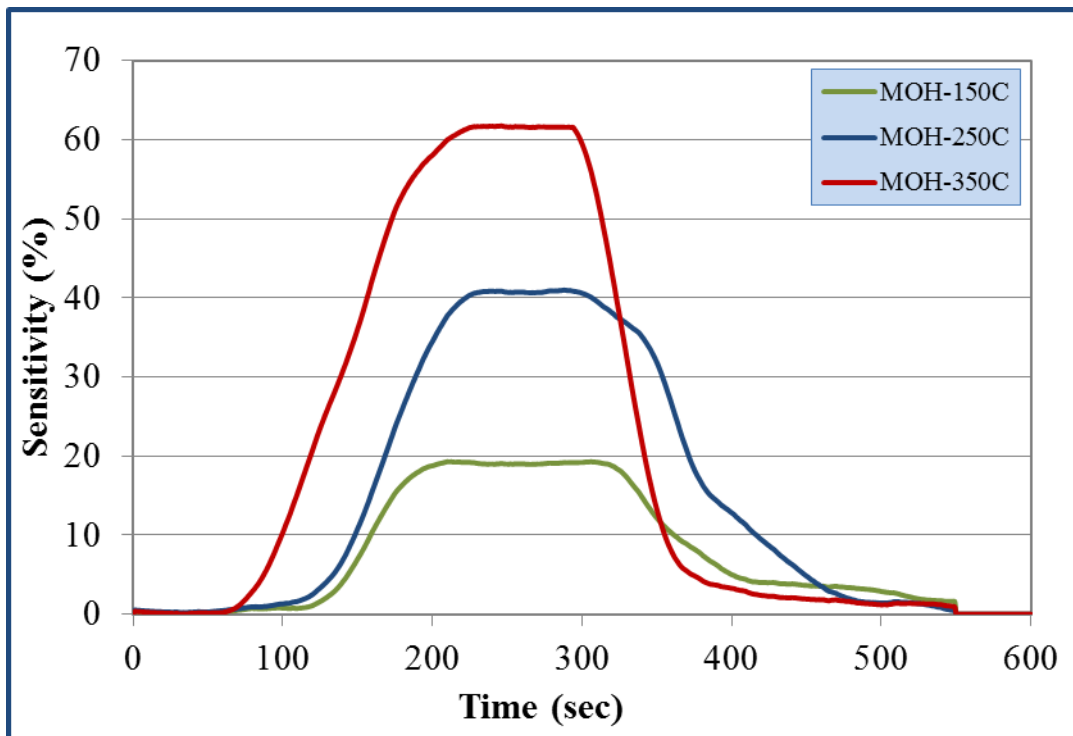


Figure B-20: S₁Z₃ sensor device with 150 ppm methanol.

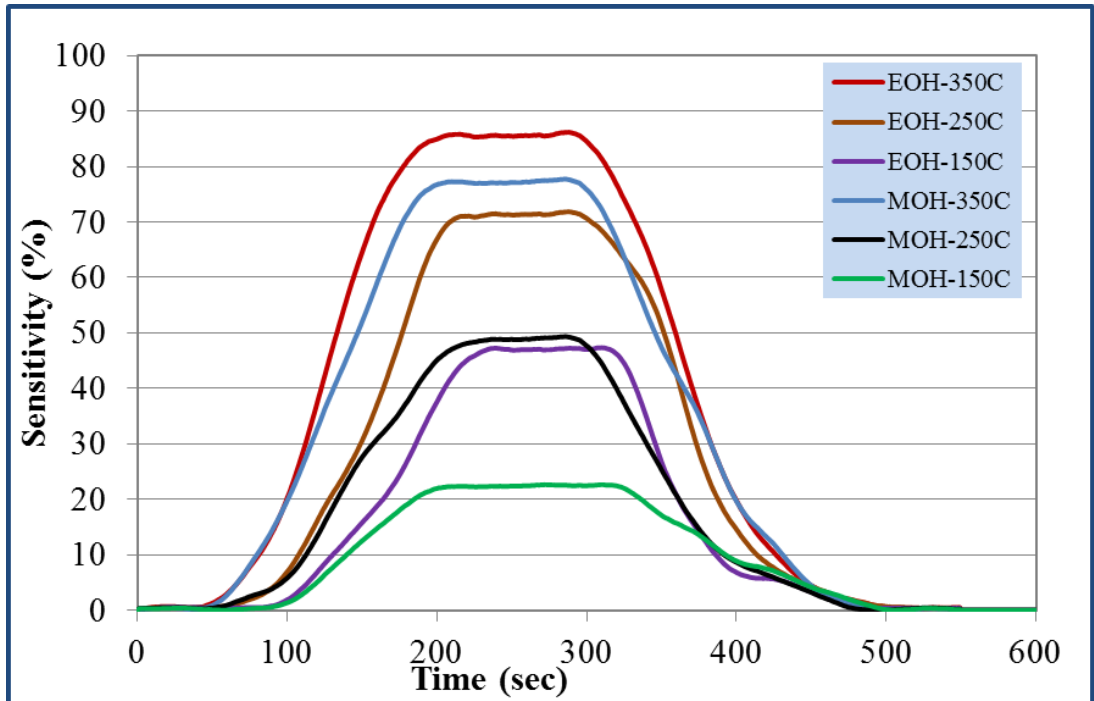


Figure B-21: SiZ_3 sensor device with 200 ppm methanol and ethanol.

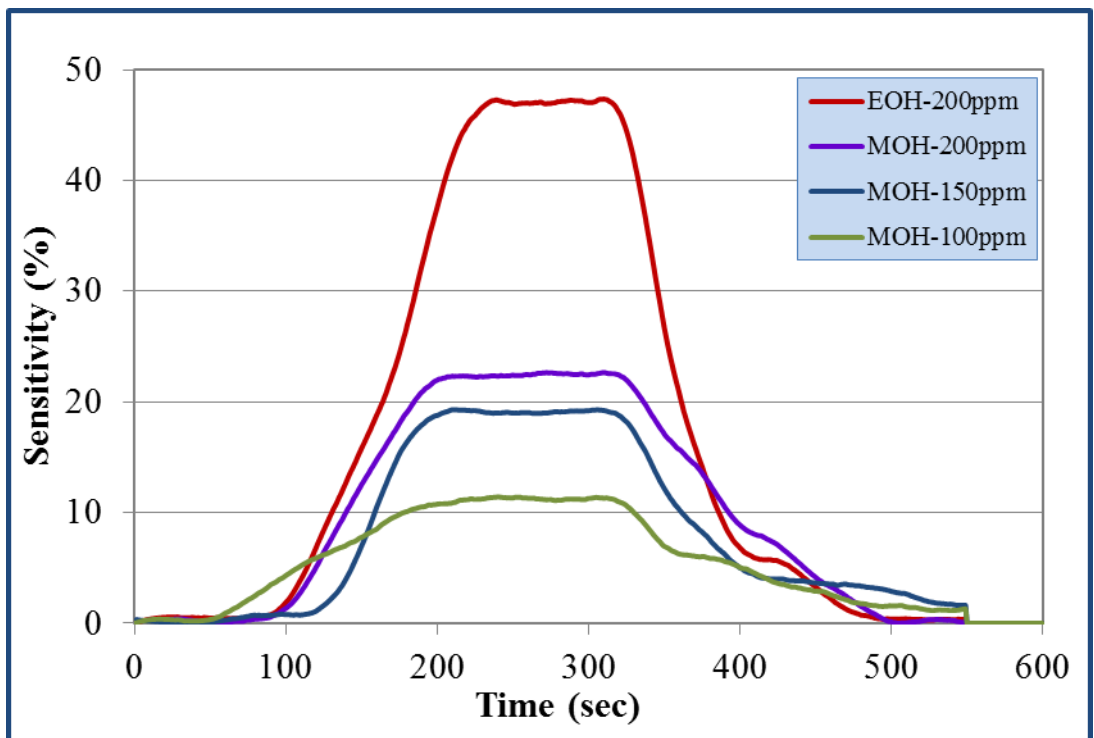


Figure B-22: SiZ_3 sensor device at 150 °C operating temperature.

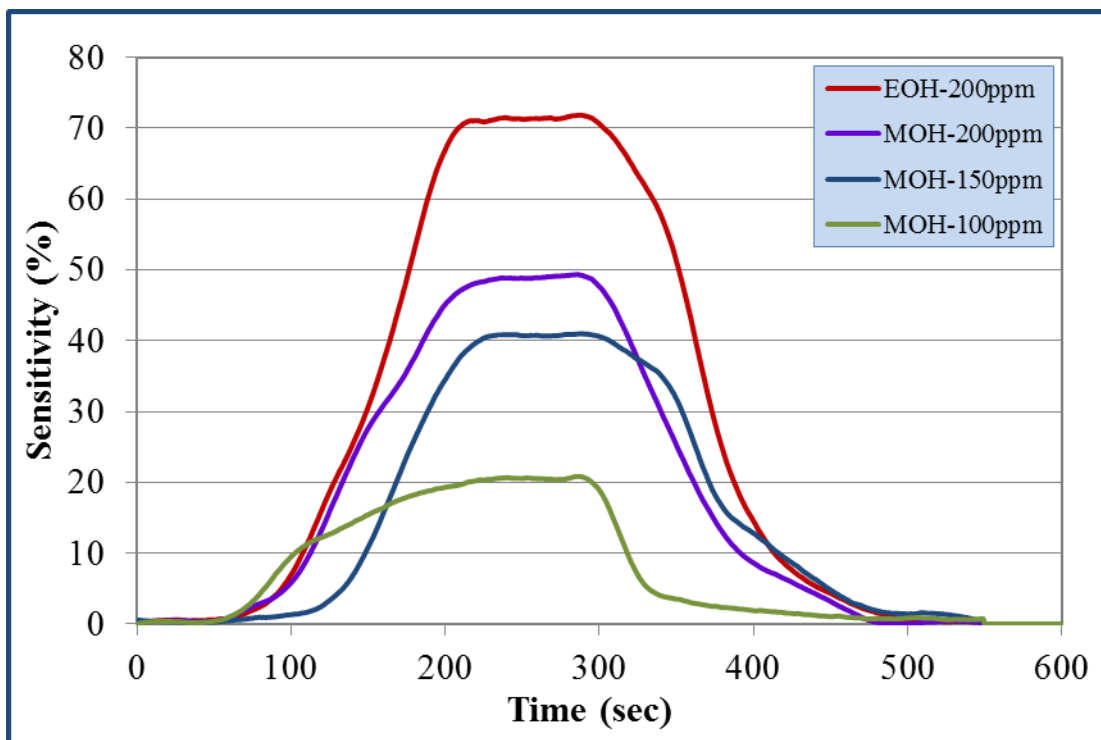


Figure B-23: SiZ_3 sensor device at 250 °C operating temperature.

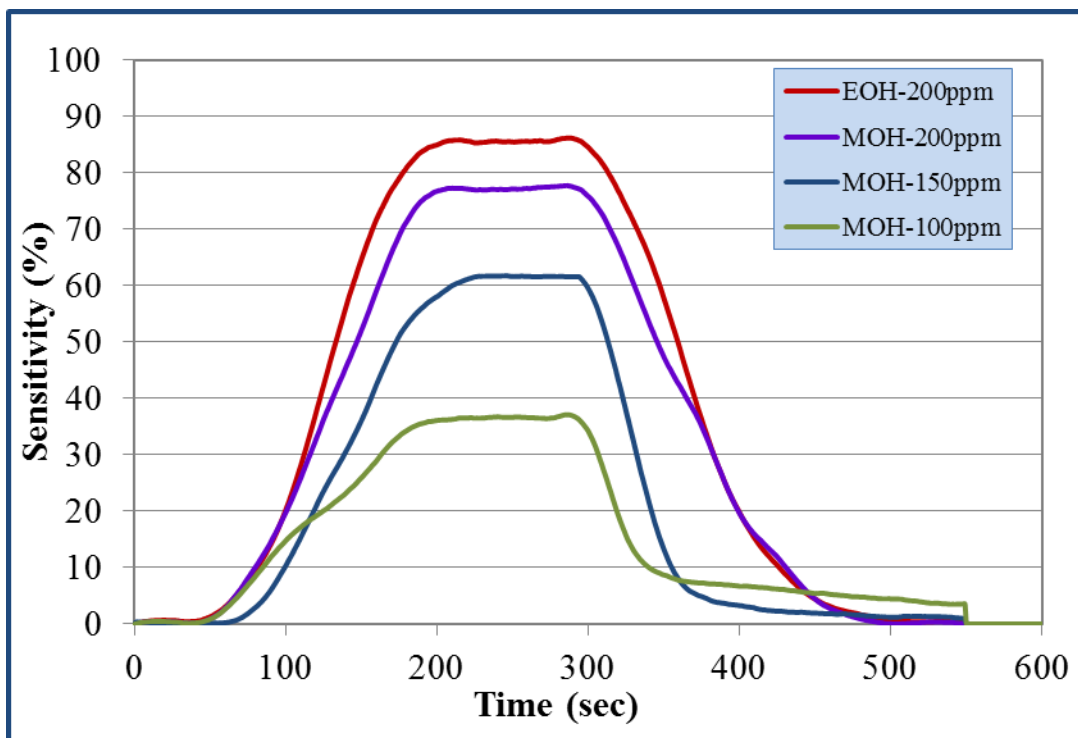


Figure B-24: SiZ_3 sensor device at 350 °C operating temperature.

B.5 ZnO Sensor Device (Z)

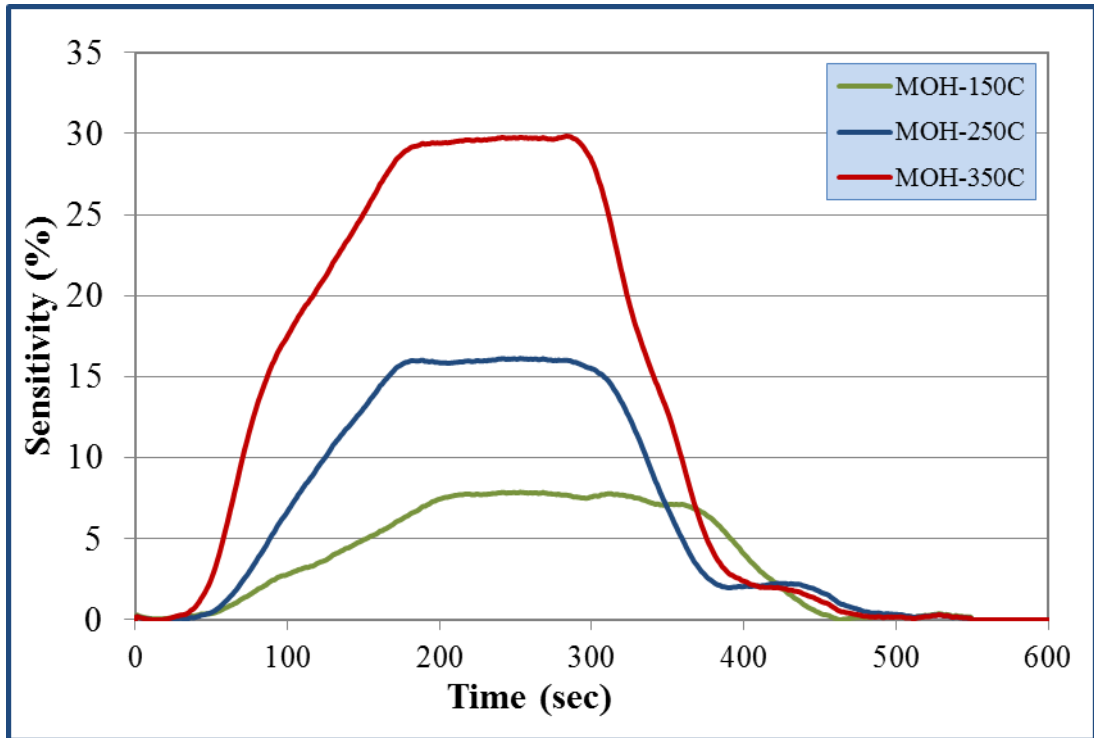


Figure B-25: ZnO sensor device with 100 ppm methanol.

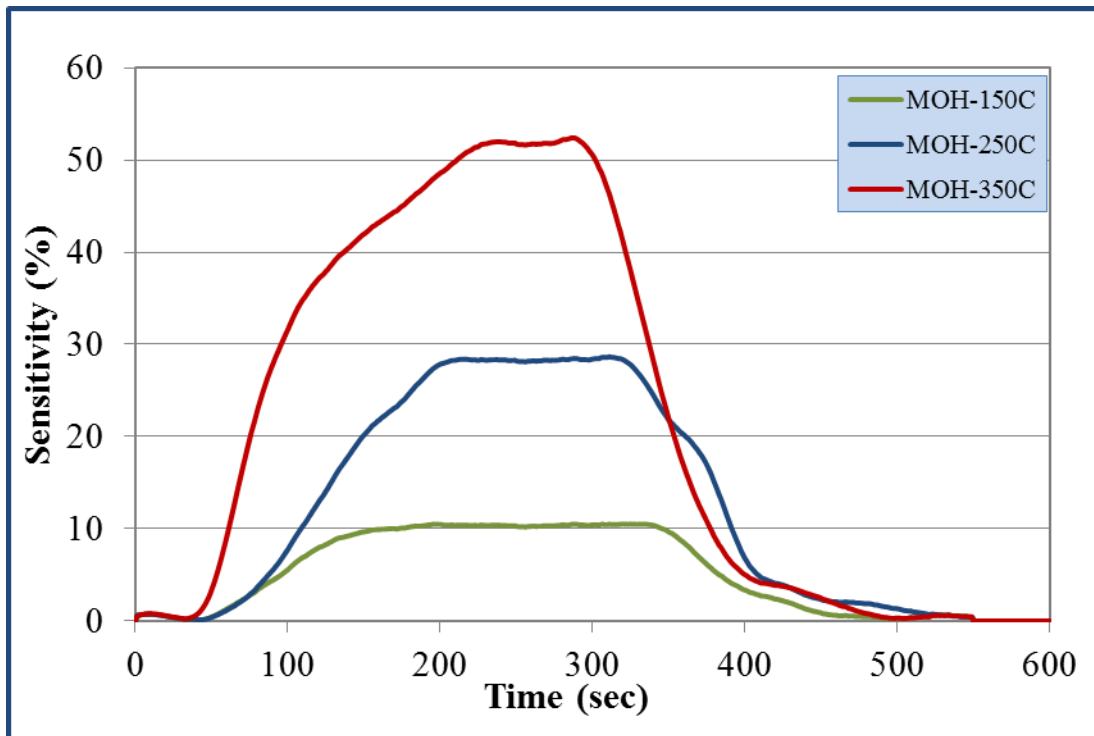


Figure B-26: ZnO sensor device with 150 ppm methanol.

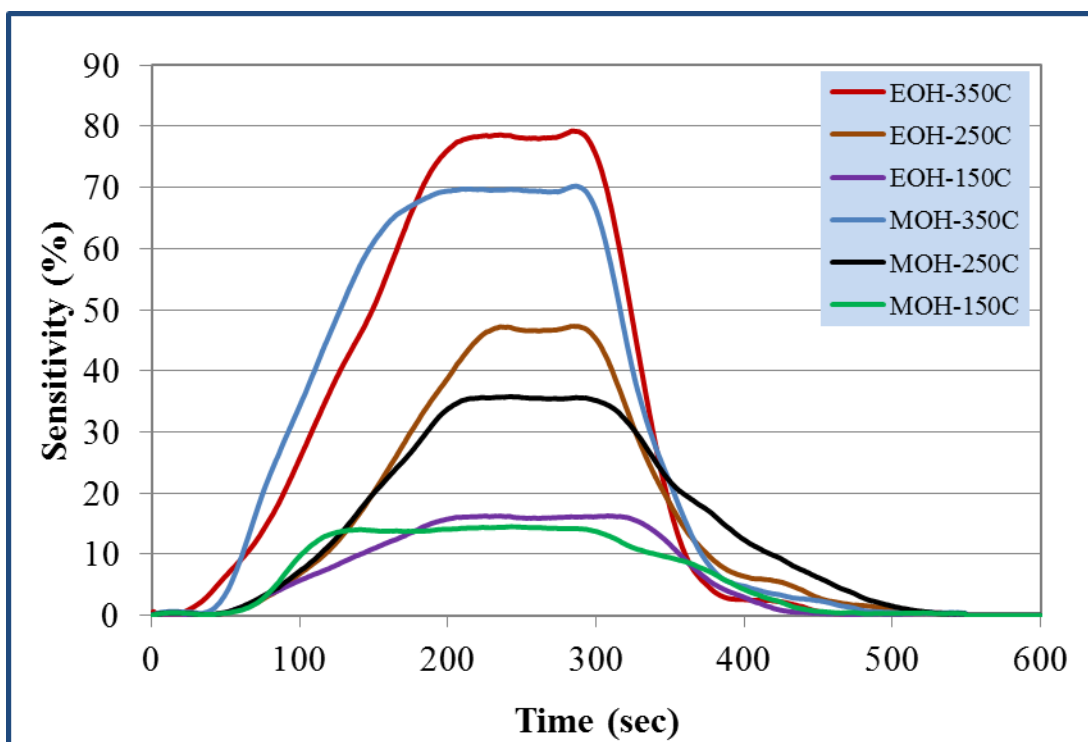


Figure B-27: ZnO sensor device with 200 ppm methanol and ethanol.

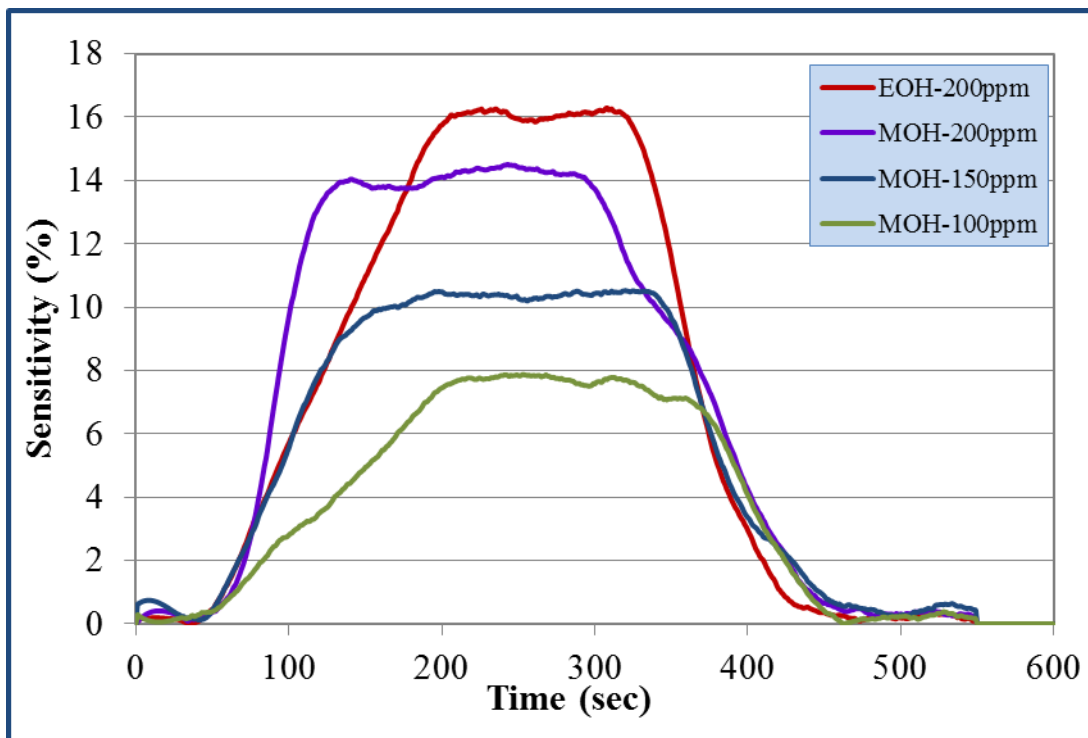


Figure B-28: ZnO sensor device at 150 °C operating temperature.

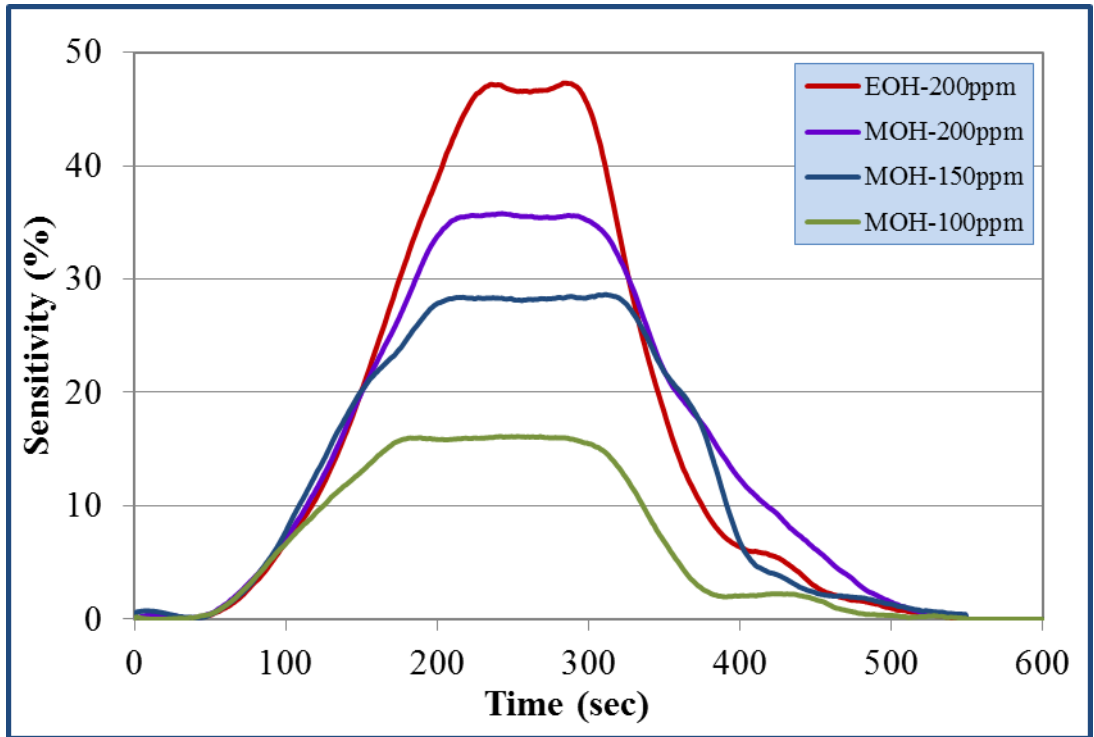


Figure B-29: ZnO at 250 °C operating temperature.

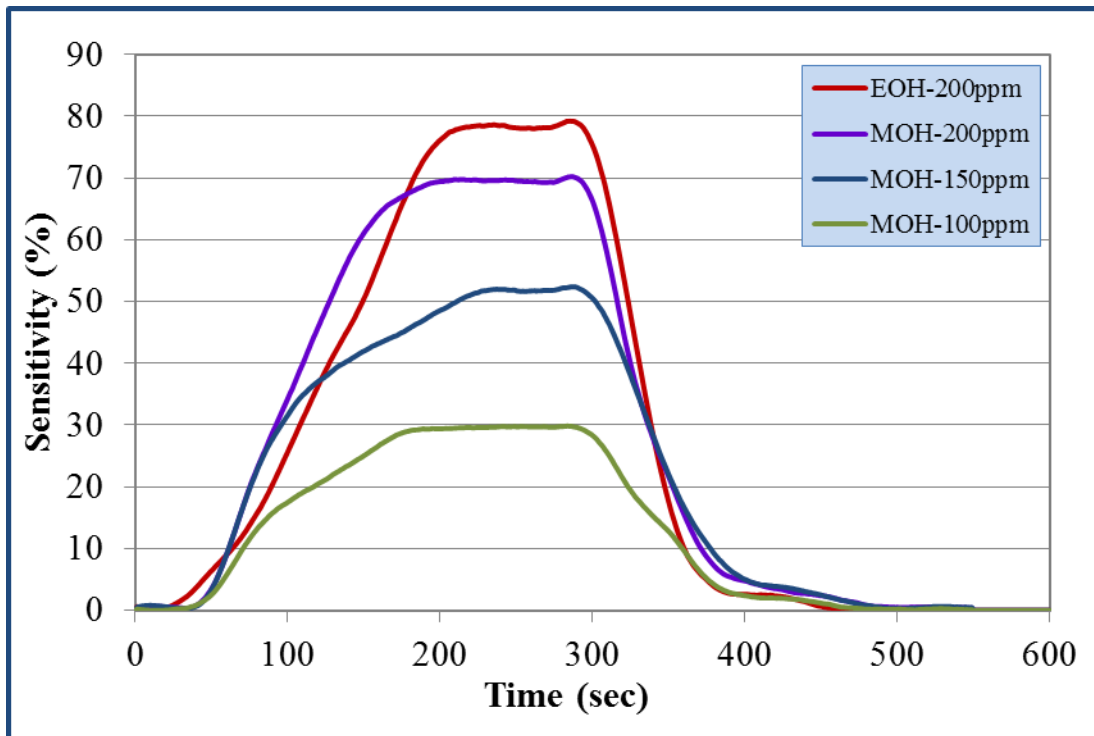


Figure B-30: ZnO at 350 °C operating temperature.

B.6 Power Model

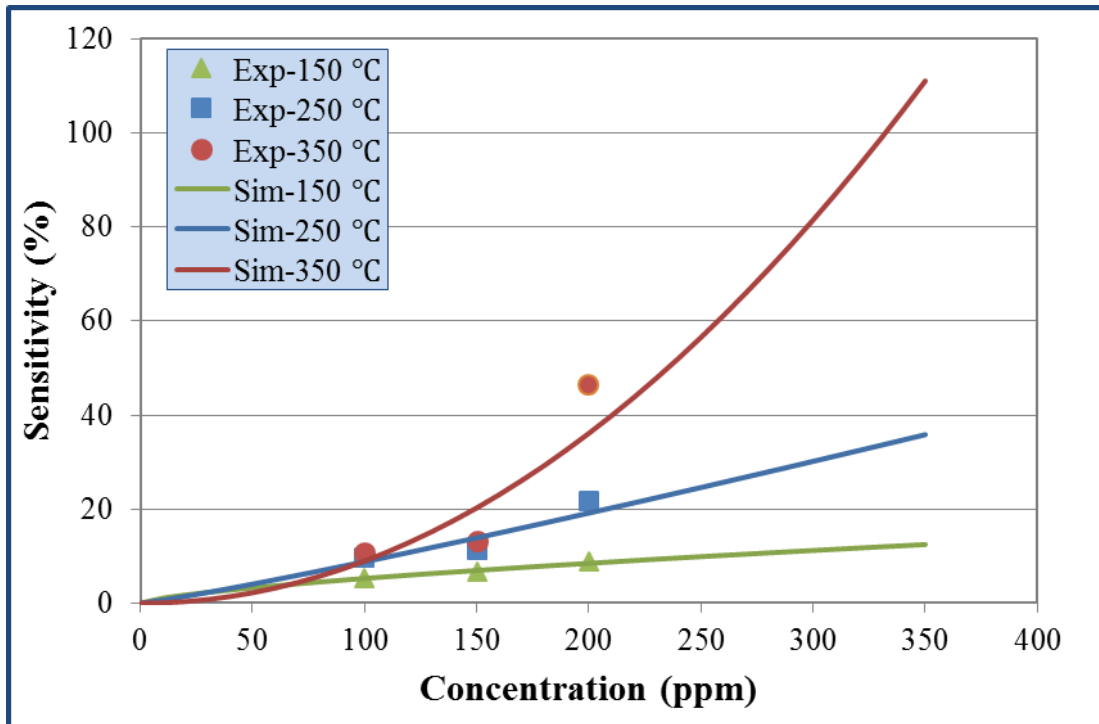


Figure B-31: Simulated sensitivity of SnO₂ sensors (Power Model).

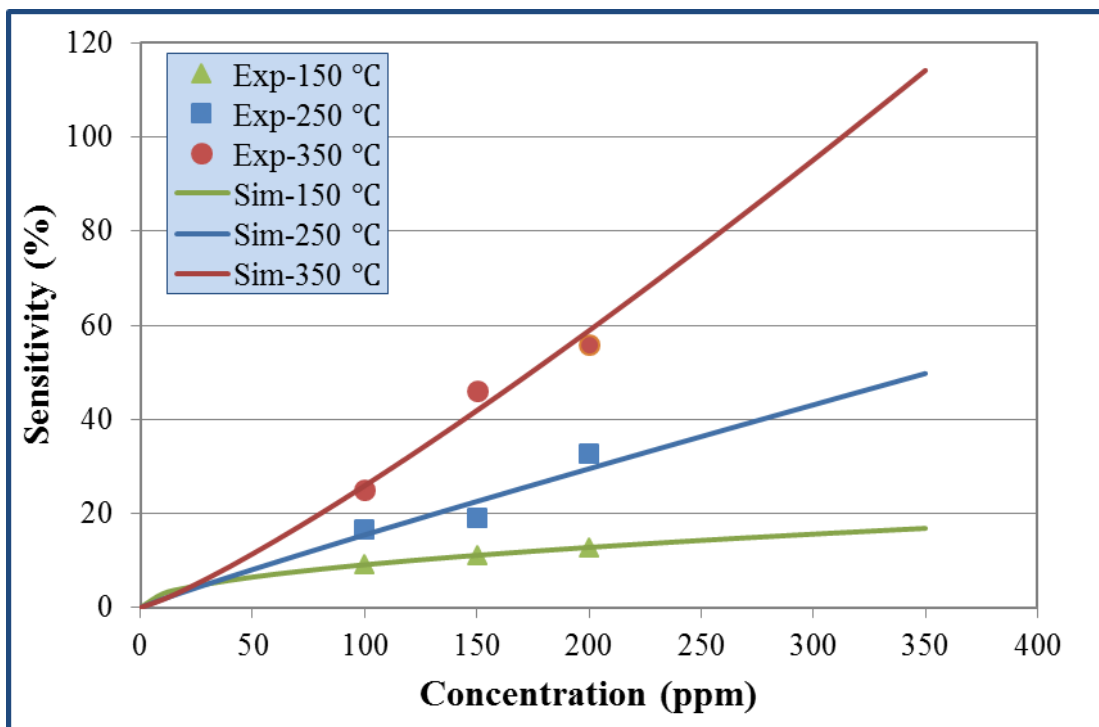


Figure B-32: Simulated sensitivity of S₃Z₁ sensors (Power Model).

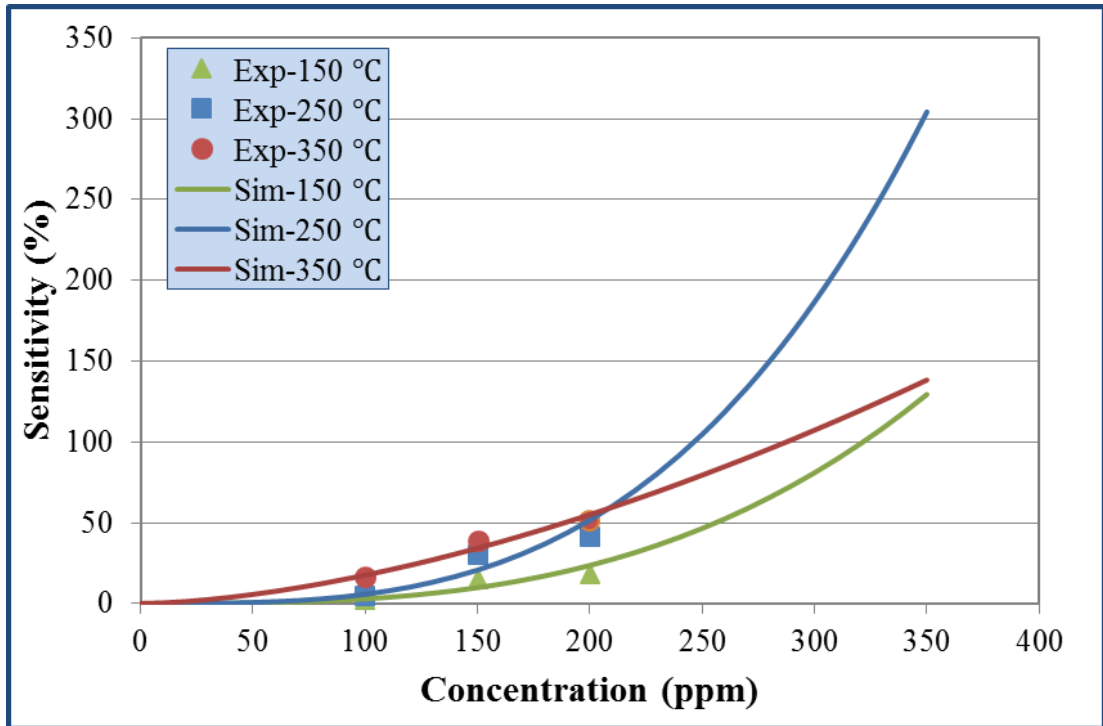


Figure B-33: Simulated sensitivity of SZ sensors (Power Model).

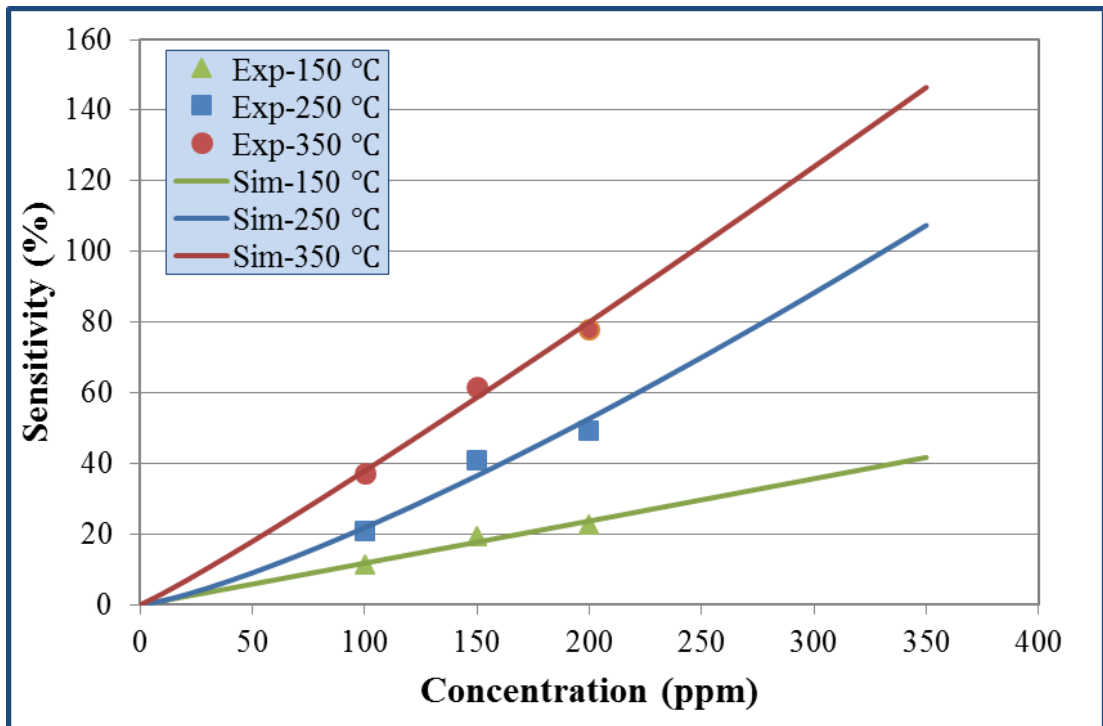


Figure B-34: Simulated sensitivity of S₃Z₁ sensors (Power Model).

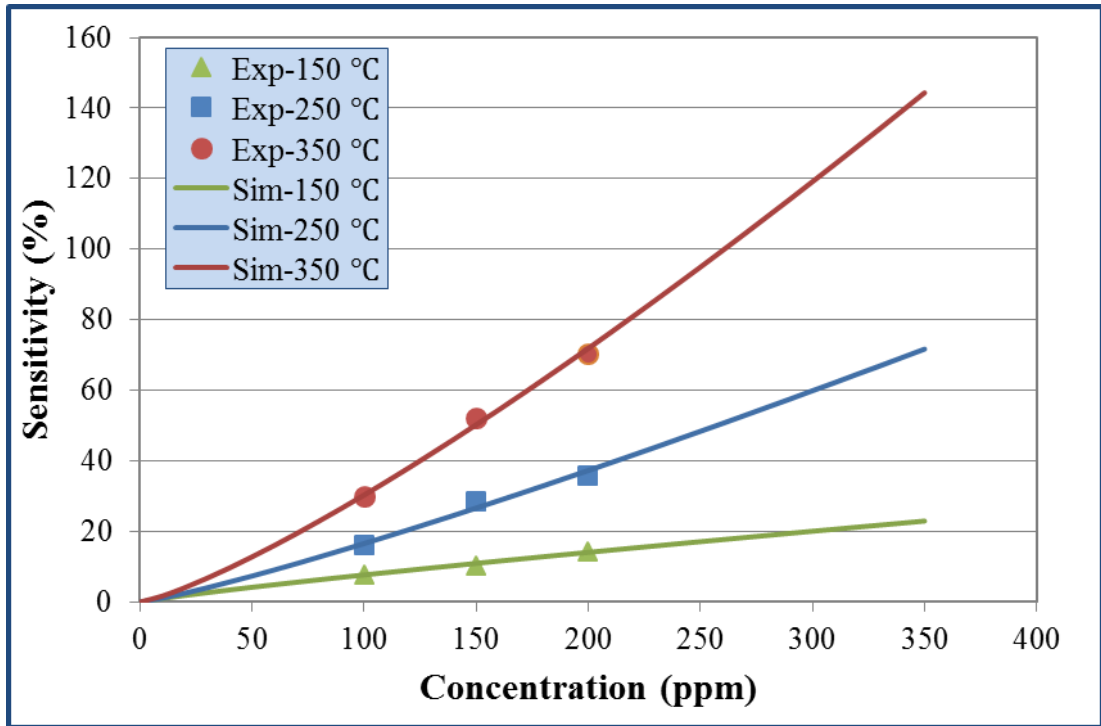


Figure B-35: Simulated sensitivity of ZnO sensors (Power Model).